Florida State University Libraries

2019

Understanding the Behavior and Structure of Nanocrystalline Material through the Interactions of Photons

David A. (David Allen) Hardy

FLORIDA STATE UNIVERSITY

COLLEGE OF ARTS AND SCIENCES

UNDERSTANDING THE BEHAVIOR AND STRUCTURE OF
NANOCRYSTALLINE MATERIAL THROUGH THE INTERACTIONS OF PHOTONS

By

DAVID A. HARDY

A Dissertation submitted to the
Department of Chemistry and Biochemistry
in the partial fulfillment of the
requirements for the degree of
Doctor of Philosophy

2019

David Hardy defended this dissertation on October 17, 2019.

The members of the supervisory committee were:

Geoffrey F. Strouse

Professor Directing Dissertation

William S. Oates

University Representative

Albert E. Stiegman

Committee Member

Kenneth Hanson

Committee Member

The Graduate School has verified and approved the above-named committee members, and certifies that the dissertation has been approved in accordance with university requirements.

To my wife, Sanja, you have been the foundation I needed to persevere throughout these past years. Without your constant love and support, the following work would not have been accomplished. I love you very much.

To Noah, you are already loved so much by your mom and me. We cannot wait to meet you very soon!

To my Mom & Dad, you two have always shown me how to work hard and dream big. You two have always and will forever be an inspiration.

ACKNOLWEDGMENTS

The work within this dissertation could not have been completed if not challenged and supported by current and former Strouse Group members. To all the former and current Strouse Group members, thank you for always engaging in scientific discussions which led to deeper thinking and intellectual growth. To Bridgett and Dave, thank you for writing a grant that funded my research and your contributions that resulted in the development of new research ideas. Rodney, you were an undeniable asset to the team during your year and half at FSU. I'm glad that we discussed that Dexter wins and I look forward to calling you on the 29 of March 2024 and hearing about your advancements to the Fe-U PBA field. Dr. Strouse, your guidance and pursuit of knowledge develops highly skilled scientist. Your ability to motivate students to dive into their science and to think deeper shows your capacity as an educator, scientist and a leader. You have many good years left to educate the next generation of scientist.

In addition, none of the work within this dissertation could not have been completed without the constant support from my family. Thank you all for the endless love and support over the past 4.5 years!

TABLE OF CONTENTS

LIST OF TABLES

LIST OF FIGURES

ABSTRACT

Ligand passivated nanoparticles have applications in solid-state lighting, plasmonics, and catalysis. At the nanoscale, the properties of these materials can be manipulated by reaction kinetics, allowing for systematic control to achieve desired functionalities and performance efficiencies. Analysis of these properties and evaluating their fundamental behavior is challenging due to the complex chemistry at the nanoscale. Therefore, a combination of analytical techniques such as TEM, SEM, pXRD, NMR, and optical methods are required to study the structure and properties of these materials. This dissertation consists of two topics covering nanoparticle synthesis and their applications. The first topic will discuss the synthesis and isolation of catalytic material from an iron-cobalt Prussian blue analogue (PBA). The isolated catalytic material retain elemental compositions and obey a scaling law with respect to the seed PBA, suggesting a templated interconversion. The second topic will discuss the use of 2 nm lanthanide doped nanospinels (Ln:ZnAl$_2$O$_4$, Ln = Tb, Eu) as down-shifting phosphors for solid-state lighting. Emission quantum yields up to 50% are achieved following energy transfer from a surface coordinating ligand. The nanophosphors provide crystallographic information of the lattice due the unique photophysical behavior of the lanthanides allowing for their use as an optical probe leading to identification of lattice strain and octahedral tilting within a nanophosphor. The material within the dissertation have applications in catalysis, photonics, and crystallography.

CHAPTER 1

INTRODUCTION

1.1 General Introduction.

Nanoparticles are routinely used in applications such as magnetism, lighting, plasmonics, and catalysis where enhanced performance can be achieved by reducing the size of the nanomaterial. For example, decreasing the size of a lanthanide doped nanoparticle allows for sensitization by a surface ligand due to minimization of the distance separating the donor and acceptor. In catalysis, it has been suggested that selectivity can be achieved due to preferential faceting of the nanocrystal, allowing for targeted isolation of hydrocarbons in the Fischer-Tropsch synthesis (FTS). The development of high-performance nanomaterials is essential to ensuring the nation's energy independence.

In the US alone, approximately 10% of the energy generated is consumed by lighting demands.[1] In 2019, over half of the available sockets use inefficient incandescent light bulbs due to the poor color quality of commercial solid state lighting (SSL) technology at a $5 price point.[1] To aid in the development of SSL technologies, the Department of Energy (DOE) has invested in academia and industry to increase color rendering, luminaire efficiencies, and stability of phosphor materials in efforts to reduce the overall energy consumption. To become energy independent, researchers are challenged with reducing the overall consumption, generating renewable energy, but also to produce hydrocarbon fuels from other chemical feedstocks not derived from petrochemical drilling and refining methods. This has led to the industrial adaptation of the Fischer-Tropsch Synthesis (FTS) where plants in Qatar, Malaysia, and South Africa, are operational. However, projects in Texas, Ohio, and Louisiana have been postponed due to the high

estimated capital cost needed to operate the gas-to-liquid facilities.[2] Further research and development is necessary for the implementation into the US energy sector.

FTS allows for the isolation of liquid fuels from biomass, natural gas, and coal, commonly written as $n\ CO + (2n + 1)\ H_2 \rightarrow C_nH_{(2n+2)} + n\ H_2O$ (1.1). This reaction was developed during the war efforts in World War II and has been investigated to enhance selectivity of products and reduce water gas shift side (WGS) reaction, $CO + H_2O \rightarrow H_2 + CO_2$ (1.2), and products. Industrial catalysts are iron carbide species which are formed by *in-situ* carburization of iron.[3] While iron carbides are the preferred catalyst, they are susceptible to the WGS (1.2) that causes the equilibrium to be shifted allowing the isolation of undesirable products.[3-7] Cobalt is less susceptible to the water gas reaction, but costs ~200x more as a catalyst than iron due to relative abundancies of the metals.[3, 8, 9] Isolation of a mixed-metal iron cobalt catalyst can enhance the selectivity of the reaction and reduce the sensitivity to the water gas reaction by incorporation of Co, while reducing the cost of a pure Co metal system. However, isolation of mixed-metal nanocrystals is difficult due to differences in reactivities of the precursors allowing for phase segregation.[10-12] Considering these technical obstacles, gas-to-liquid plants require the development of a robust catalyst that is not prone to the WGS, that can be isolated through a facile and scalable synthesis. Employing a templated precursor, such as a Prussian blue analogue (PBA), can aid in the isolation of mixed-metal species at the nanoscale following stepwise conversions to mixed-metal carbides and bimetallic nanocrystals.

The research within this dissertation is aimed to provide solutions to energy issues by employing ligand passivated nanomaterials isolated from facile and scalable synthesis protocols. Careful consideration was taken in the development of the material to reduce critical needs material without the sacrifice of performance. The work investigated two classes of nanomaterial focused

on tunable catalysts for FTS applications and earth abundant nanophosphors that are thermally and chemically stable. The foundation to extrapolate the material into industrial applications was described and the nanomaterial have immediate uses throughout multiple sectors of materials science.

1.2 General Nanoparticles Synthesis and Growth.

Isolation of ligand passivated nanoparticles is accomplished from decomposition of molecular precursors in the presence of a coordinating ligand that can be accomplished in either a round bottom reaction or microwave cavity. Alternatively, nanoparticles can be produced *via* top-down protocols that use mechanical forces to reduce grain sizes and boundaries at the expense of uniform material.[13] In this dissertation, two protocols were employed for the synthesis of oxide and mixed-metal nanocrystals. To produce ternary oxides, microwave (MW) induced thermal decomposition of stoichiometric amounts zinc(II) undecylenate and aluminum(III) acetylacetonate were reacted in a coordinating solvent. The MW couples to dipoles in the reaction media, allowing for selective absorption of MW photons leading to uniform heating throughout the solution.[14] The uniform heating produces nanoparticles with smaller size distributions when compared to convective round bottom synthesis techniques due to temperature differences between the exterior and interior of the reaction batch.[15, 16]

Mixed-metal carbides and bimetallic nanocrystals isolation was accomplished from thermal conversion of a PBA template mesocrystal.[17] The thermal conversion does not follow classical nucleation theory and is enhanced by the presence of oleylamine. The elemental composition, size, and crystallographic phase was shown to be templated by the initial PBA seed. Due to the slow kinetics of the reaction, these systems were isolated using common Schlenk line
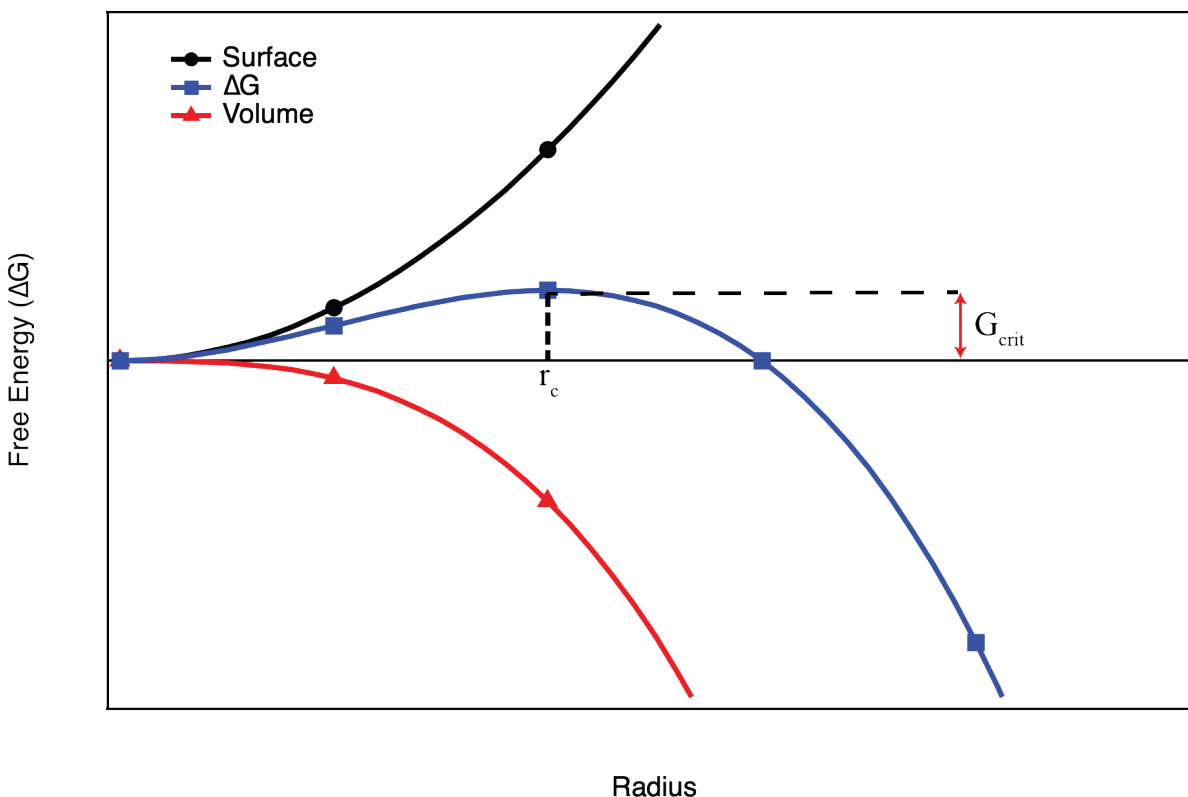
Figure 1.1. Free energy diagram illustrating the critical radius where the volume term begins to dominate the growth of the nuclei, avoiding the dissolution of the nuclei into the solution.

techniques. The versatility of an Fe-Co PBA mesocrsytal was demonstrated where controlled synthesis of catalytic material was achieved in the solid state and solution reactions.

1.2.1 Classic Nucleation and Growth Theories.

Bottom-up approaches undergo heterogenous or homogenous nucleation as reactive precursors become available within the reaction. In homogenous nucleation, rapid or burst nucleation occurs which leads to the monodisperse nanocrystals whereas heterogenous nucleation is random and nonuniform, yielding products with uncontrolled properties. Classical LaMer nucleation theory suggests that monomers form from atoms and begin to grow into nuclei.[18] At this point, some nuclei are dissolving into the solution while others are growing through collisions or coalescence
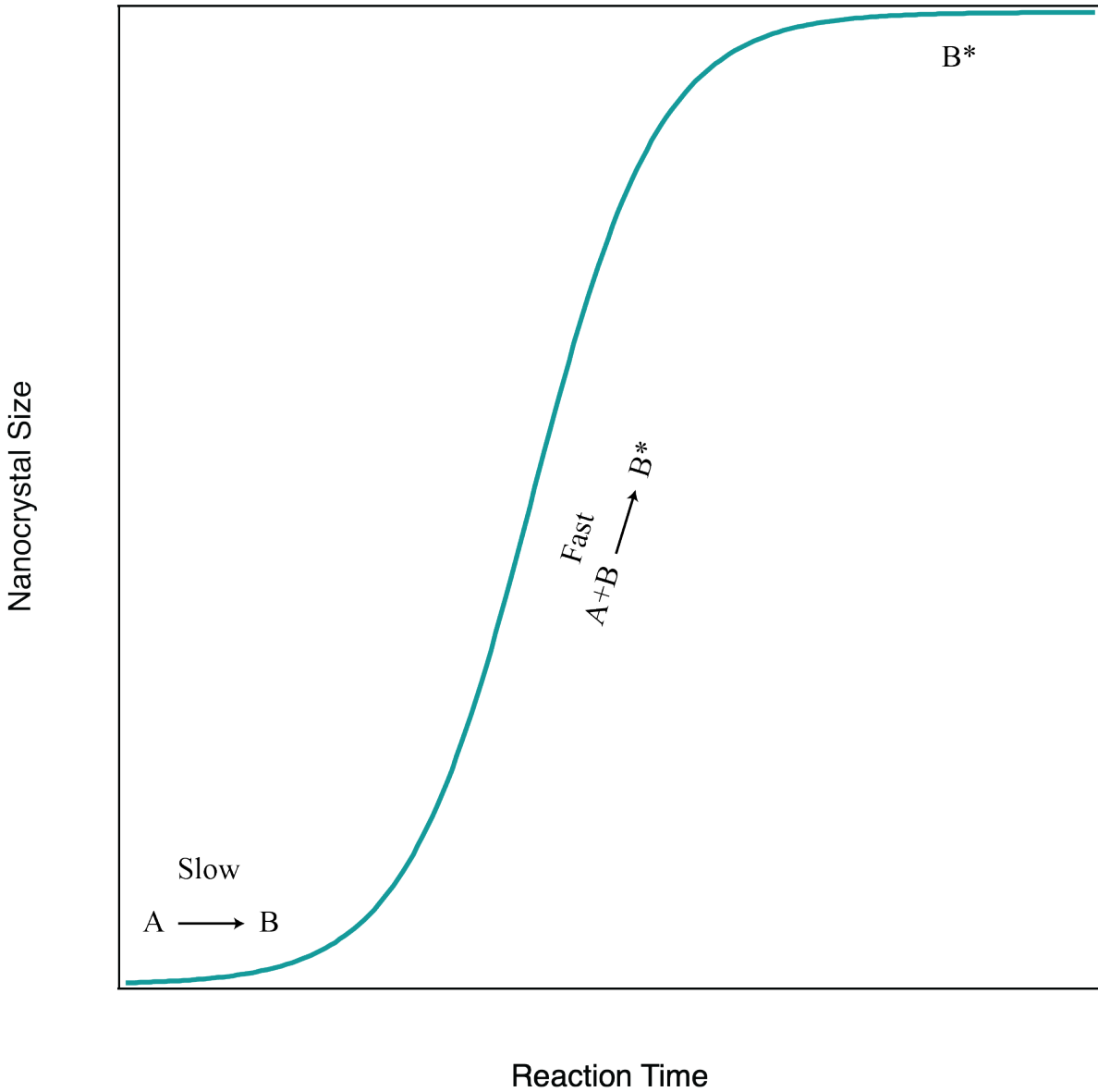
Figure 1.2. Autocatalytic growth of nanocrystal showing the two-step process where nucleation occurs slowly followed by rapid growth of the nanocrystal.

mechanisms to reach the critical radius.[18] Once the critical radius (r*) is reached, dissolution of the nuclei becomes unfavorable allowing for further nanocrystal growth. For a spherical system, this can be mathematically described by the total free energy ΔG, which is sum of the surface energy (γ) and bulk free energy (ΔG_v) as a function of the radius (r), shown in equation 1.3.

The bulk free energy is the product of Boltzmann's constant (k_B), temperature (T), and the natural log of the super saturation (S) over the molar volume (v), shown in equation 1.4.

$$\Delta G = 4\pi r^2 \gamma + \frac{4}{3}\pi r^3 \Delta G_v \tag{1.3}$$

$$\Delta G_v = \frac{-k_B T ln(S)}{v} \tag{1.4}$$

This is schematically represented in Figure 1.1, where r_c represents the critical radius where stable nuclei are formed as the bulk energy term begins to dominate. As the reaction progressed, the nuclei grow into nanocrystals until the precursor is depleted and form a size distribution through Ostwald ripening, coalescence, oriented addition, or autocatalytic surface growth.[18]

In Ostwald ripening, the smaller particles are redissolved into solution due to their higher surface energy, thus providing more precursor for the larger, more stable nanocrystals. This is known to reduce the size distribution of the nanocrystals at small time domains, however, if left too long, larger distributions are observed. Coalescence is the growth of nanocrystals by the random collisions within the reaction medium. This leads to multiple domains with crystallographic defects. In oriented addition, the growth of the nanocrystal is achieved along crystallographic planes with similar energies, producing more crystalline and less defective material.

Autocatalytic growth of nanoparticles occurs in reactions where the concentration of monomers is below the supersaturation limit. The model developed by Finke and Watzky dictates a two-step process where the first step is the slow nucleation followed by the faster growth on the surface of the seed in the second step.[19] These two processes are occurring simultaneously and fit a sigmoidal curve where the slow nucleation occurs followed by rapid growth of the nanocrystal, graphically represented in Figure 1.2 This model has been applied to transition metal nanoparticle

6

growth, such as Ni,[14] Pt,[20, 21] and Pd.[22, 23] Previous work out of our group has shown the autocatalytic growth of Ni nanoparticles in a microwave field.[14]

1.2.2 Microwave Assisted Growth of Nanocrystals.
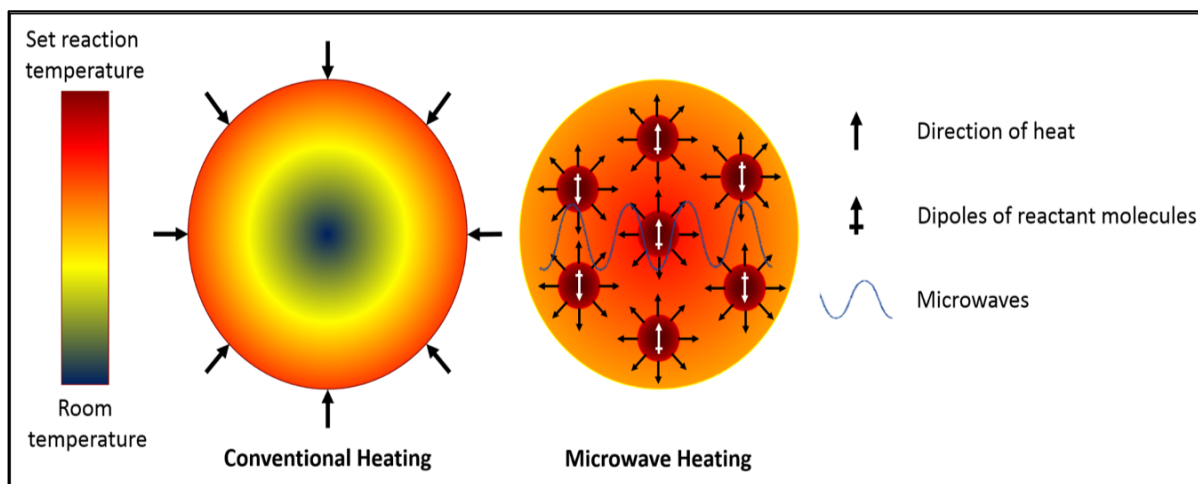
Figure 1.3. Convection *vs*. microwave heating methods. Convection heating generates a temperature gradient causing heterogenous nucleation whereas microwave heating allows for the isolation of monodisperse nanoparticles due to uniform heating throughout the reaction medium.

Microwaves are low energy electromagnetic waves with frequencies between 0.3 and 300 GHz. Frequencies that are used in household microwaves and microwave synthetic reactors are 2.45 GHz, which is approximately 10^{-5} eV. These low energy waves couple to dipoles or ions within solution causing molecular rotations which result in friction and thus heat. Microwave synthetic reactors have been adapted to many fields in chemistry such as catalysis,[24, 25] digestions, organic,[26, 27] solid state,[28] and nanoparticle reactions.[15, 16, 29-32] This technology offers many benefits such as batch-to-batch reproducibility, scalability, and requires less energy to operate than comparable convection methods.

In microwave assisted nanoparticle synthesis, organo-metallic precursors are employed due to their dielectric properties. In order for a MW to heat a material, it must be polarizable and

couple to the MW to convert the energy into heat. The ability for a species to absorb a MW photon is described by equation 1.5.

$$tan\delta = \frac{\varepsilon''}{\varepsilon'} \qquad (1.5)$$

Where ε'' is the dielectric loss, or absorption of the MW field while ε' is the scattering term. The $tan\delta$ is directly proportional to the MW cross-section and thus the ability for a species to generate heat within a given reaction. The MW cross-section is temperature and frequency dependent.

Selective absorption in a MW synthetic reactor can be achieved through experimental design. Many high-temperature solvents used in nanoparticle synthesis have a large scattering term and thus a small $tan\delta$, while the organo-metallic precursors have a larger $tan\delta$. This allows for the selective absorption of the soluble precursors producing uniform heating throughout the reaction batch. In contrast, convection methods are hottest near the source and cooler elsewhere. This theory is schematically represented in Figure 1.3. More advanced microwave synthetic strategies include the epitaxial growth on metals where the microwave cross section is larger for the metal than the solvent.[31, 33]

1.3 Crystallographic Structures.

Within this dissertation, the synthesis and properties of spinels (AB_2X_4) and Prussian blue analogues ($KCo_x[Fe_{2-x}(CN)_6]$) will be discussed in detail. This section aims to describe the crystallographic information of the structures. Hereafter, spinels isolated at 2 nm will be referred to as nanospinels while $KCo_x[Fe_{2-x}(CN)_6]$ Prussian blue analogues will be referred to as FeCo-PBAs.

1.3.1 Nanospinels.

Spinels are naturally occurring minerals having the general formula of AB_2X_4, where the A site is a tetrahedrally coordinated 2+ cation, B is an octahedrally coordinated 3+ cation, and X
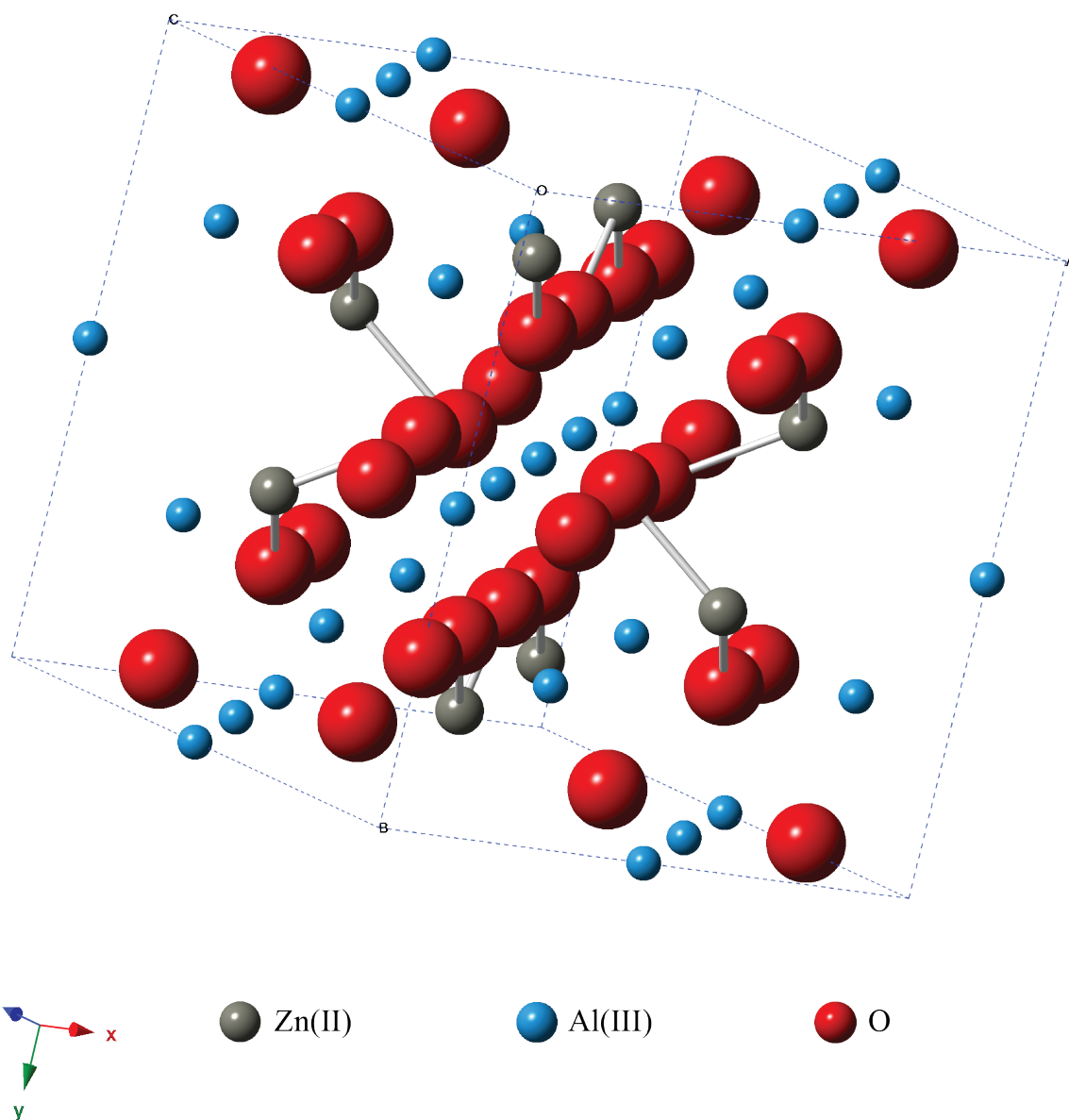
Figure 1.4. Unit cell of a $ZnAl_2O_4$ lattice where the grey spheres represent the tetrahedral Zn(II), blue spheres represent the octahedral Al(III), and red spheres represent the oxygen anion.

is a chalcogenide. Some examples of the spinels are Fe_3O_4 which has mixed valence of Fe^{II} and Fe^{III} species, $MgAl_2O_4$, a naturally occurring mineral, and $LiMn_2O_4$,[34] a potential cathode material. Oxide spinels exhibit thermal and chemical stability and thus provide applications from optical hosts[35,36,37] to uses in containment of nuclear waste[38, 39] and nuclear reactors.[40, 41] These properties arise from ability to have cation migration between the A and B sites of the spinel. When the B^{3+}

cation occupies the tetrahedral A site and *vice-versa*, the spinel becomes an 'inverted' spinel. At the nanoscale, the inversion parameter (degree of inversion, λ) is demonstrated to be larger than their bulk counterparts due to the kinetically trapped structure.[42-45] Investigating the degree of inversion (DOI) has been accomplished from neutron pair distribution function alysis,[46] EPR,[47] Mossbauer, pXRD,[44] and solid-state NMR,[42, 44, 48-51] however, at the nanoscale Rietveld refining patterns through pXRD is inaccurate due to the broadness of the reflections. Within this dissertation we probe the DOI by ^{27}Al magic angle spinning-NMR (MAS-NMR).

In 1915, the spinel was assigned to the *Fd*3*m* phase by Bragg[52] and Nishikawa,[53] independently where the octahedral inversion center is conserved in the B site. In this phase there is one tetrahedral and octahedral site and it is the most symmetric unit cell of all spinel phases. The unit cell is displayed in Figure 1.4. Since 1915, other symmetries have also been reported which result from minor distortions in the A or B sites.[46, 54] With two different sized octahedral sites, the symmetry is reduced to tetragonal *P*4$_1$22 whereas if two different tetrahedral sites are present then cubic *F*43*m* phase is assigned. Additional tetragonal phases (*I*4$_1$22 & *I*41/*amd*) have been studied in $ZnCr_2O_4$ and $ZnGa_2O_4$ with non-centrosymmetric B sites.[55, 56] In many of these systems, similarities in the X-ray cross-sections makes identification of the phase difficult.[46] However, bulk systems with narrow line-widths allow for the investigation of the pressure induced phase transitions from cubic to tetragonal systems by Rietveld refining the powder patterns in $ZnGa_2O_4$.[57] At 31.2 GPa a phase transition to the tetragonal phase of bulk $ZnGa_2O_4$ is reported due to a decrease in relative intensities and broadening of the reflections. However, similarities of the X-ray scattering of the cations in $ZnAl_2O_4$ and broadening of the reflections at the nanoscale provide ambiguous results. Determination of the proper phase must be made correlations of ^{27}Al MAS-NMR, pXRD, and optical probe data.
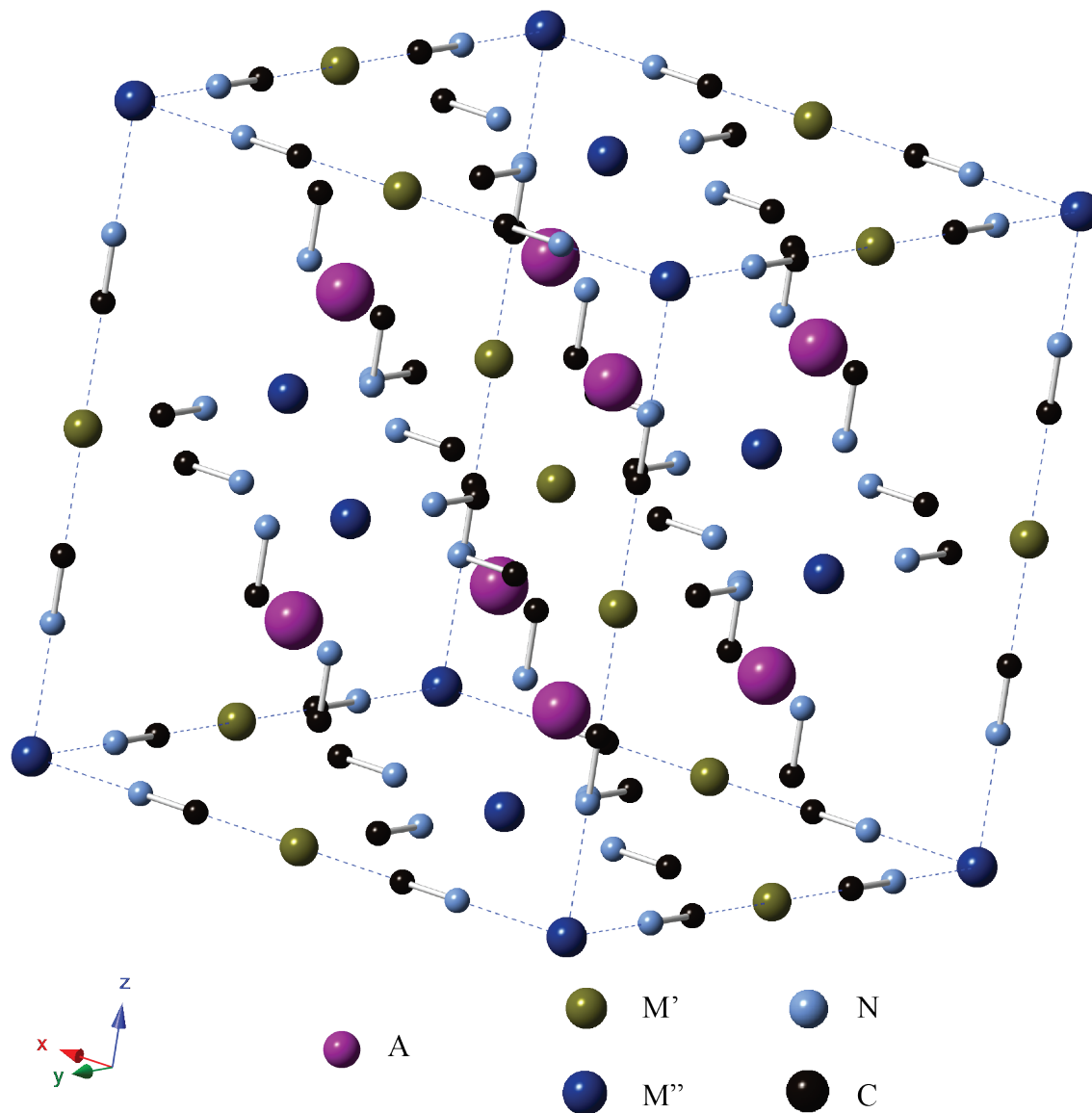
Figure 1.5. Unit cell of a Prussian blue (analogue) where M' and M" can be different transition metals or oxidation states. The general formula for a Prussian blue is AM'[M''(CN)6].

1.3.2 Prussian Blue and Prussian Blue Analogues.

Prussian blues (PB) belong to a class of compounds known as heterometallic coordination polymers. These materials provide control over coordination environments for *d*- and *f*-block metals that are bridged by a coordinating ligand. Within the PB itself, there are two metal (Fe^{II} and Fe^{III}) sites in an octahedral coordination that are bridged cyanide ligands. The metals are
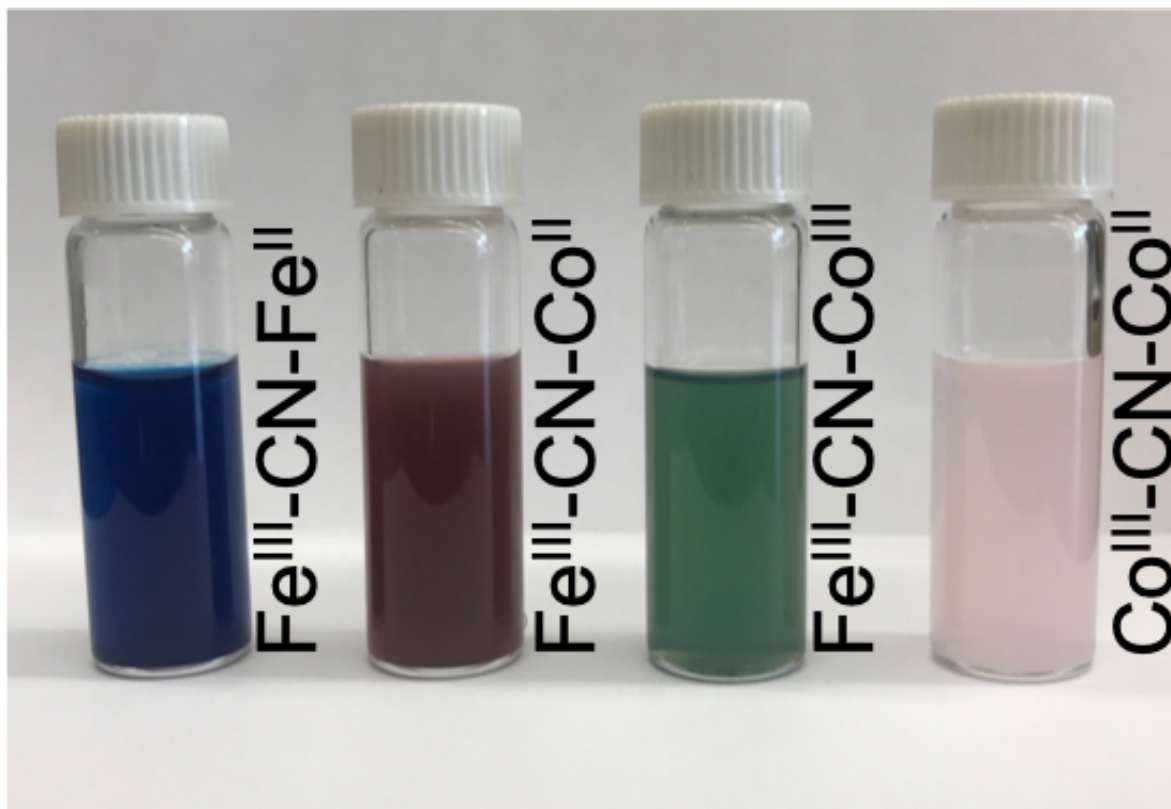
Figure 1.6. A series of Prussian blue analogues displaying the differences in the intervalence charge transfer bands. The blue is a typical Prussian blue, burgundy is an iron cobalt PBA, the green is an oxidized version of the iron cobalt PBA, and the pink is a cobalt cobalt PBA.

coordinated in an *fcc* open framework lattice with a unit cell length of ~10.8 Å, displayed in Figure 1.5. The lattice is balanced by an alkali cation ion and has a general formula of AM'[M''(CN)$_6$]. By mixing potash and oxblood, the PB was originally isolated as a vibrant blue pigment and led to its use in art, instigating the Prussian blue era.[58] During the 18th and 19th centuries, wide scale production of the pigment produced work like *The Stary Night* and *Great Wave off Kanagawa*.[58] This color was later found to arise from an intervalence charge transfer band, the Fe^{II}—CN—Fe^{III} metal centers.[59, 60] The intervalence charge transfer (IVCT) bands are altered by the oxidation state, metal used, and hydration of the lattice, shown in Figure 1.6. For example, oxidation of Prussian blue to Fe^{III}—CN—Fe^{III} yields a green product designated as Berlin green.
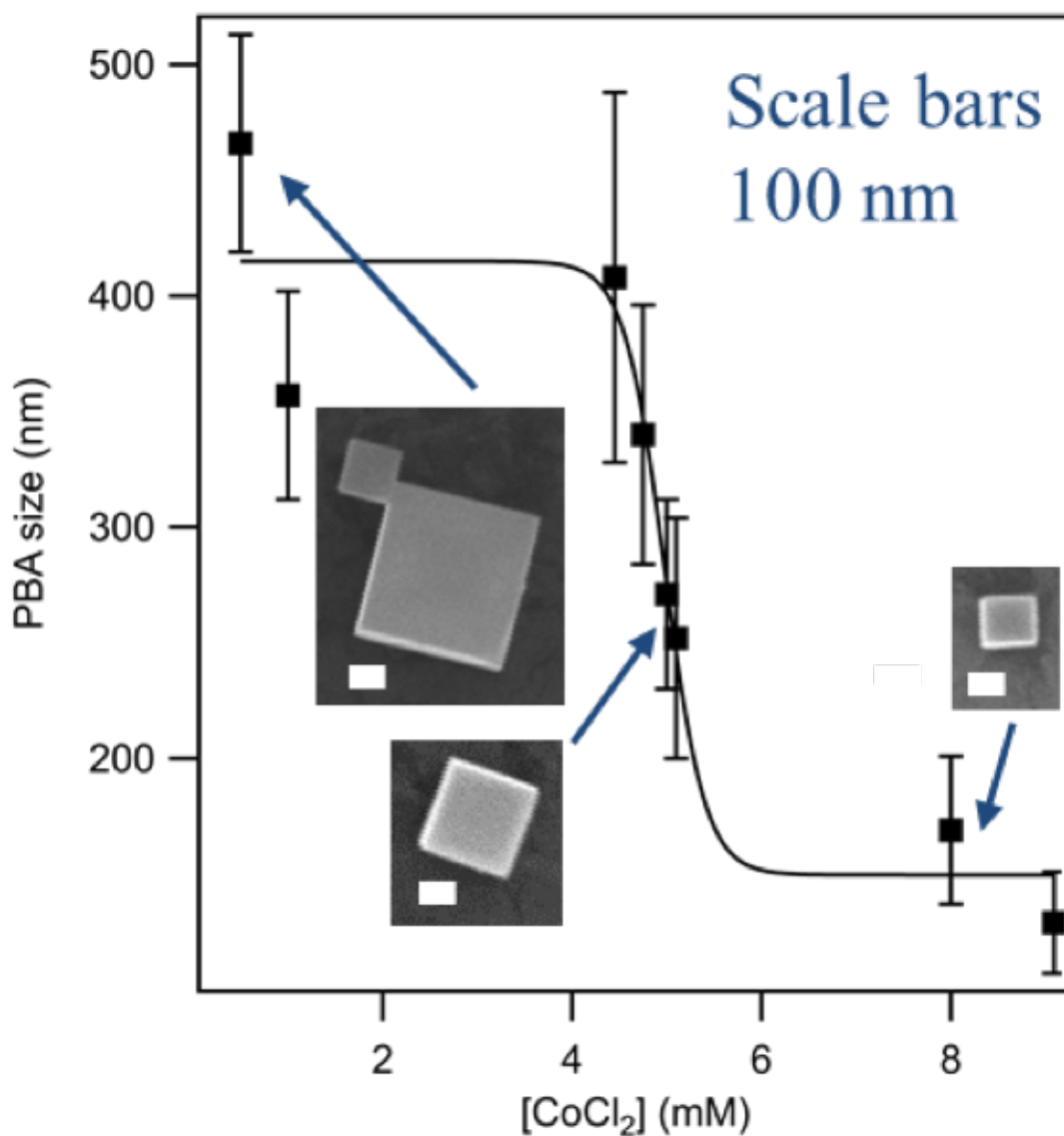
Figure 1.7. Size control of the $KCo_x[Fe_{2-x}(CN)_6]$ by manipulation of the $CoCl_2$ concentration. The $CoCl_2$ solutions contained 1 mmol of $CoCl_2$ inserted into 1 mmol, 20 mM $K_3Fe(CN)_6$ at a rate of 5 mL/min at room temperature. Scale bars are 100 nm.

PBAs are similar to PBs with the exception that the metals cations can be either *d*- or *f*-block elements. PBAs retain the same open framework *fcc* lattice with octahedrally coordinated metals bridged by cyanides. By substituting the metal cations, control over physical properties can be achieved which has given rise to the various applications ranging from catalysis,[61, 62] energy

storage,[63, 64] gas storage,[65-67] and medicinal use.[68-70] The changes in the physical properties can be seen upon isolation from the reaction mixture where products of different colors are observed. This is due to the changes of the IVCT band which can be seen in Figure 1.6.

PBAs are synthesized from drop wise addition of cyanide containing species to *d*- or *f*-block metal salts where sizes can be controlled by precursor concentrations[71] or by use of surfactants such as AOT (dioctyl sulfosuccinate soldium salt)[72] and Igapel[73].[74] When surfactants are employed, a reverse micelle yields <50 nm particles whereas simple drop-wise addition and shaping agents, like PVP, produce material with cube lengths greater than 100 nm.[74-76] Although surfactants and shaping agents have been used to control size and morphology, precursor concentration were altered to control the mesocrystal size within this dissertation. A series of $KCo_x[Fe_{2-x}(CN)_6]$ (FeCo PBAs) were synthesized at room temperature by dropwise addition of 1 mmol $CoCl_2$ into a 20 mM (1 mmol) solution of $K_3Fe(CN)_6$ in the presence of KCl. Changing the concentration of $CoCl_2$ from 0.5 mM to 9 mM produced FeCo PBAs with different sizes between 100 and 500 nm where the experimental results are shown in Figure 1.7. At dilute concentrations, larger FeCo PBAs were isolated, however, solubility was unfavorable which caused the larger PBAs to precipitate out of solution and allowing for nucleation of smaller mesocrystals. The resultant change in mesocrystal size with concentration follows classical nucleation theory and therefore are also dependent on temperature of the reaction mixture, drip rate, and KCl concentrations. Through the manipulation of mescocrystal size, a scaling behavior was developed for the conversion of a FeCo PBA to isolate desired nanomaterial for catalytic applications.

1.4 Nanoparticle Applications.

Materials science is the investigation of inorganic or organic compounds that can be employed in applications. At the nanoscale properties can be enhanced from tuning of emission

spectra by manipulating the size of a quantum dot,[77] to increasing carrier concentrations by adding aliovalent dopants to a semiconductor oxide nanoparticle.[78] Investigation of properties at the nanoscale requires precise synthetic strategies to systematically manipulate its properties. Through the use of library synthesis, lanthanide doped nanospinels were investigated as downshifting phosphors for solid state lighting where photoluminescence quantum yields (PLQY) up to 50% are achieved. Additionally, mixed-metal carbides and bimetallic nanocrystals were prepared as potential catalysts for the Fischer-Tropsch reaction to isolate liquid hydrocarbons from chemical feedstocks.

1.4.1 Solid State Lighting.

High-performance down-shifting phosphors are currently being developed to further advance the solidstate lighting industry and provide tunability with white light systems. Down-shifting materials absorb a higher energy photon which is converted to a single lower energy photon, as compared to down-conversion materials which emit two lower energy photons per one photon absorption event.[79] The Department of Energy (DOE) has provided a set of criteria that are needed for new state of the art phosphors which include, narrow emission features, high quantum efficiencies, and thermally stable materials.[80] An additional goal set by the DOE includes development of flexible material that would simplify the mass production of new luminaries which can be achieved by additive manufacturing.[80] Traditional one-component white light assemblies include cerium doped yttrium aluminum garnet (Ce^{3+}:$Y_3Al_5O_{12}$, Ce:YAG), which has an absorption band centered at 470 nm. When coupled to a GaN blue light emitting diode (LED), Ce:YAG absorbs the blue photon and converts the higher energy photon to a lower energy yellow photon.[81, 82] The blending of the yellow and residual blue photons from the phosphor and pump LED produces cool white light. To warm the color, a red phosphor is needed to enhance the
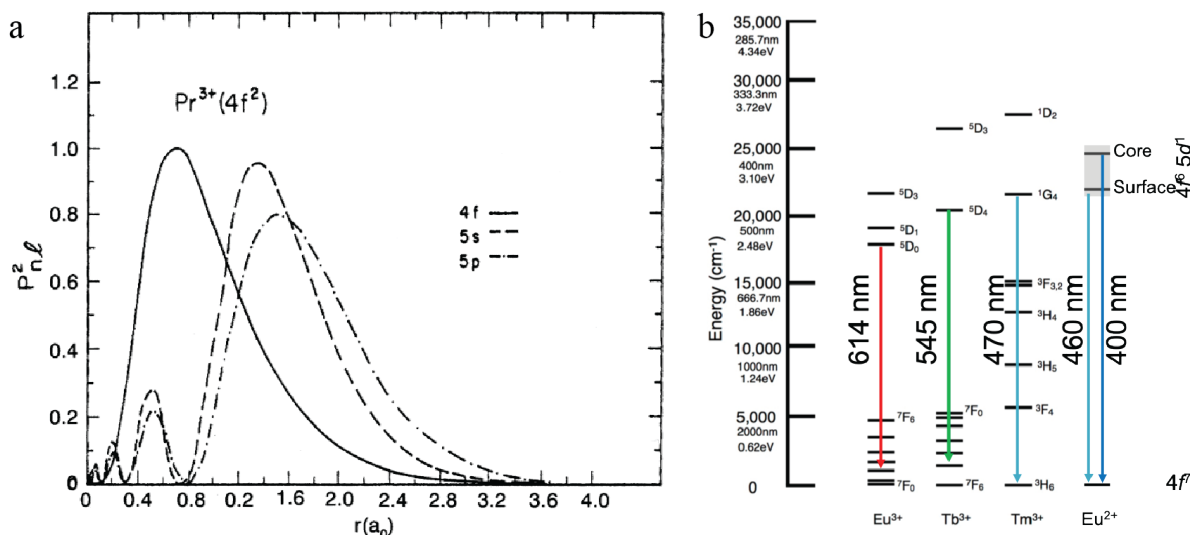
Figure 1.8. a) Radial distribution diagram of the Pr(III) cation showing the $4f$ orbitals shielded by the $5s$ and $5p$ orbitals[87] and b) an abridged Jablosnki diagram of Eu(III), Tb(III), Tm(III) and Eu(II) illustrating the excited states of the visible emitting lanthanides.

emission profile. In 2015, GE patented a red phosphor, $Mn^{4+}:K_2SiF_6$ which is a narrow line emitter centered at 630 nm.[83] The system has increased the tunability of LEDs employed through industry today; however, both systems aforementioned have critical issues which need to be addressed. First, both materials are produced in conventional solid-state reactions which yield bulk material reducing luminaire efficiencies by scattering rather than absorbing pump LED photons. In addition, the bulk material is insoluble in lens matrices such as poly (methyl methacrylate) (PMMA), polyacrylate, and polystyrene reducing homogeneity in the lens. By reducing the size of the phosphors to sub 1100 nm, scattering will be reduced to <10%, thus increasing luminaire efficiencies. Further reduction of the size below 5 nm allows for enhancement of nanoparticle solubility by ligand passivation, as well as sensitizing lanthanide emission by the molecular antenna effect.

Elemental composition of the host must also be considered when designing a host lattice that meets the DOE's R & D goals and prove to be economically viable. General Electric's TriGain
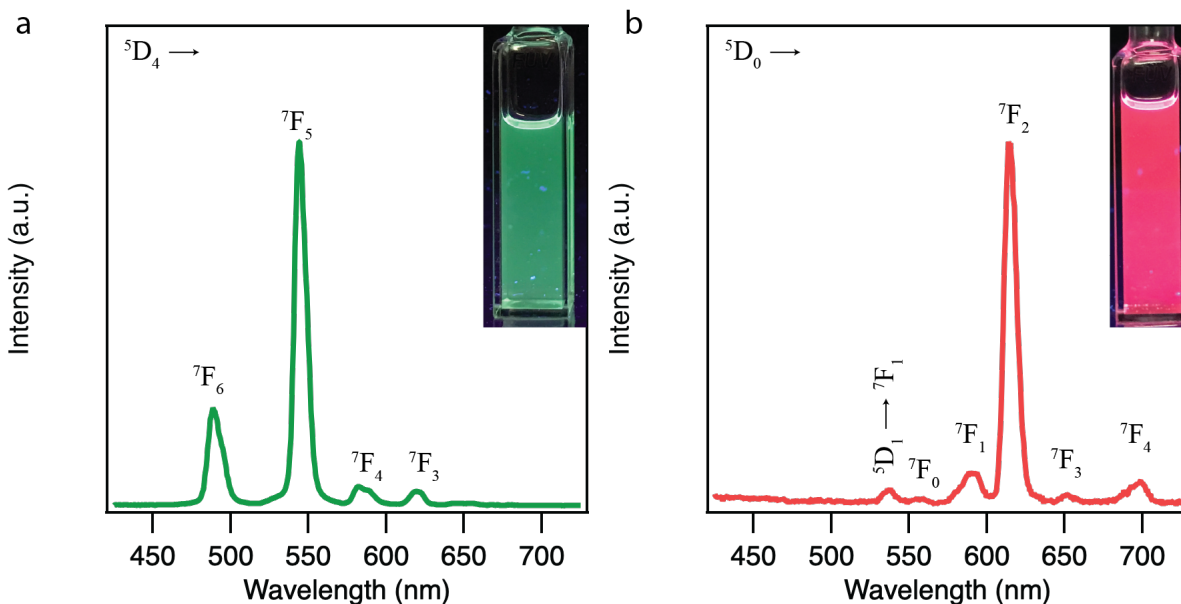
Figure 1.9. Photoluminesce emission spectra at 298 K of a) Tb(III) and b) Eu(III) when excited by a sensitizing ligand at 320 nm. The transitions are labeled and correspond to the abridged Jablonski diagram in Figure 1.8b.

phosphor[84, 85] has eliminated the use of critical material, such as Y(III); however, lattices for down-shifting material must be thermally and chemically stable to minimize thermal droop. Although these materials are currently employed throughout the world, advancements must be made to increase the efficiency and decrease the cost, aiding the transition to the new technology, ultimately reducing CO_2 emissions world-wide. The $ZnAl_2O_4$ nanospinel lattice is composed of earth abundant materials and given a typical solid-state reaction producing YAG *vs.* $ZnAl_2O_4$ using 99.99% pure oxide precursors (Y_2O_3/Al_2O_3 for YAG, ZnO/Al_2O_3 for $ZnAl_2O_4$), the spinel cost ~54% less to produce than YAG. By eliminating the use of yttrium and moving to earth abundant materials, costs of the host lattice can be reduced as well as eliminating harmful mining to the global environment.[86] Although Eu(III) and Tb(III) are on the critical needs material list, highest QY are typically achieved at concentrations below 10% therefore minimal amounts are necessary to reduce lighting energy consumption.

1.4.2 Lanthanide Photophysics.

Trivalent lanthanide, Ln(III), photophysics are well studied and understood. Ln(III) emitters have line like absorption and emission features which are defined by *f*-orbital characteristics. The *f*-orbitals are buried under the 5*s* and 5*p* orbitals resulting in the *f*-orbitals being unperturbed by the coordinating ligand and lattice effects.[87] This is shown in Figure 1.8a where the 4*f*, 5*s*, and 5*p* orbital wavefunctions are drawn.[88, 89] Due to the isolation of these orbitals, the only perturbations that arise when excited states are populated through direct excitation or other energy transfer mechanisms resulting in slightly broader emission features in comparison to the absorption features.[88, 90] In addition, the transitions between 4*f*-4*f* orbitals are both spin and Laporte forbidden which result in low extinction coefficients, ε, (~ 1 $M^{-1}cm^{-1}$) and micro- to milli- second lifetimes.[88]

Lanthanides emit from throughout the ultraviolet, visible, and near infrared spectrum. Within this dissertation, the work will focus on the Ln(III) with visible emission features such as Tb(III) and Eu(III). An abridged Jablonski diagram of Eu(III) and Tb(III) are displayed in Figure 1.8b. The emission spectra are displayed in Figure 1.9 for (a) Tb(III) and (b) Eu(III). Terbium(III) is a green emitter with transitions in the range of 450 and 650 nm. The dominant transition centered at 544 nm is assigned to the $^5D_4 \rightarrow {}^7F_5$. Europium(III) exhibits red emission with transitions between 525 and 725 nm with the dominant hypersensitive transition ($^5D_0 \rightarrow {}^7F_2$) is observed at 614 nm. The lanthanide emission spectrums are comprised of electronic and magnetic dipole transitions which allow for lanthanides. In an electronic dipole transition, the dipole has an odd parity while a magnetic dipole transition is even parity from the rotational displacement.[88, 91, 92] The transitions arise from differences between the charge displacements between the ground and excited states where ED transitions exhibit a linear displacement and MD transitions have a

rotational displacement. Given that the Laporte selection rule states that transitions with opposite parity (electronic transitions) are forbidden, many of the lanthanide emission features are deemed forbidden transitions.[88, 91] However, the Laporte selection rule only applies in centrosymmetric systems, allowing for the lanthanide ions to act as optical probes for site symmetry.

Europium(III) has two transitions which can interrogate the local environment, the hypersensitive electronic-dipole (ED, $^5D_0 \rightarrow ^7F_2$) transition centered 614 nm and the magnetic-dipole (MD, $^5D_0 \rightarrow ^7F_1$) transition centered at 590 nm. The ED transition is sensitive to site symmetry with an inversion center where the MD transition is independent of symmetry which allows red to orange ratio (R/O) to be extrapolated. Lower R/O ratios indicate the presence of an inversion center whereas, higher R/O ratios indicate asymmetry which is favorable to lanthanide emission.[92] Similarly, for the Tb(III) cation, a blue/green (b/g) ratio can be calculated by taking the ratio of the ($^5D_4 \rightarrow ^7F_6$)/($^5D_4 \rightarrow ^7F_5$) transitions.[93, 94] In this case, the lower the ratio, the more asymmetric the site. In spinels, cation migration is known to occur which causes distortion in the octahedron. This distortion is beneficial to lanthanide emission since it reduces the site symmetry, thus promoting the probability of the ED transitions of the *f*-elements.

Lanthanides are known to self-quench at higher concentrations and multiple mechanisms have been proposed to explain the self-quenching. Historically, the quenching mechanism was believed to occur *via* cross-relaxation through neighboring lanthanide ions, a mechanism similar to triplet-triplet annilhaiton.[95, 96] However, studies using upconverting lanthanide doped nanoparticles have shown concentration quenching through energy migration to surface defects is more detrimental to the QY than cross relaxation mechanisms.[97, 98] Adding an undoped shell to the nanoparticle reduces the observed quenching behavior by passivating surface defects through the epitaxial growth.[97] The increase in the concentration can allow for higher QY in new nanophosphor

technology, however, the growth of the shell will reduce the efficiency of energy transfer due to the increased distance between the donor and acceptor. When designing tomorrow's technology, consideration of the competitive processes is necessary to achieve the highest QY.

1.4.3 Quantum Yields.

The quantum yield (QY) is defined by $\Phi = \frac{P_{em}}{P_{abs}}$ which is the ratio of emitted photons (P_{em}) divided by absorbed photons (P_{abs}). The ratio defines how efficient the system is at producing photons rather than losing electrons through non-radiative decay pathways. To obtain relative quantum efficiencies, Eu(TTA)$_3$Phen (QY$_{Ethanol}$ = 35.6 %)[99, 100] is used as a reference for our β-diketonate passivated Ln$_x$ZnAl$_{2-x}$O$_4$ given the similarities in the absorption and emission spectra. Relative QY are determined by equation 1.6:

$$\frac{\Phi_S}{\Phi_R} = \frac{I_S}{I_R} \times \frac{1-10^{-A_R}}{1-10^{-A_S}} \times \frac{\eta_S^2}{\eta_R^2} \tag{1.6}$$

where $I_{S/R}$ is the integrated intensity of the sample/reference photoluminescence spectra at a given excitation wavelength, $A_{S/R}$ is the absorbance of the sample/reference at the excitation wavelength, and $\eta_{S/R}$ is the refractive index of solvent used.[89, 91, 101, 102] To increase accuracy of the reported quantum yields, a dilution method was employed where plotting the integrated intensities *vs.* the abs yields a linear regression. Comparison of the slopes between the standard and the sample, allow for determination of accurate QYs displayed in equation (1.7):

$$\Phi_s = \Phi_r \left(\frac{m_s}{m_r}\right)\left(\frac{\eta_s^2}{\eta_r^2}\right) \tag{1.7}$$

Where m is the slope and η is the refractive index of the solvent. Subscripts *r* indicate the reference while *s* indicates the sample. Achieving the highest quantum yield is important for solid state lighting applications due to the proportional relationship with luminaire efficiency. When sensitizing a Ln(III) by a ligand, the QY of the system is defined by equation 1.8:

$$\Phi_{Lanthanide}^{Ligand} = \eta_{sens} \times \Phi_{Lanthanide}^{Lanthanide} = \eta_{ISC} \times \eta_{ET} \times \Phi_{Lanthanide}^{Lanthanide} \qquad (1.8)$$

where $\Phi_{Lanthanide}^{Ligand}$ is the QY of the lanthanide emitter given excitation of the ligand ${}^1\pi^*$ state, η_{ISC} is the efficiency of intersystem crossing from the ${}^1\pi^* \rightarrow {}^3\pi^*$ of the ligand, η_{ET} is the efficiency of energy transfer, $\Phi_{Lanthanide}^{Lanthanide}$ is the intrinsic quantum efficiency defined by equation 4.[89, 91] The intrinsic quantum yield is the QY of the lanthanide following direct excitation which allows for extraction of radiative (k_R) and non-radiative rates (k_{NR}) inherent to the lanthanide ion.

$$\Phi_{Lanthanide}^{Lanthanide} = \frac{k_R}{k_R + k_{NR}} = \frac{k_R}{k_{exp}} = \frac{\tau_{exp}}{\tau_R} \qquad (1.9)$$

Given equation 1.8 and 1.9 the overall quantum yield can be manipulated by the efficiency of the intersystem crossing and efficiency of energy transfer which are described in the next section.

1.4.4 Time-Resolved Spectroscopy.

Time-resolved emission studies provide insight into site (in)homogeneity and quenching of emission. The data from the time-resolved studies are commonly referred to as lifetimes which describe the time it takes a photon to decay from a ground state to a lower lying state. The data acquired in lifetime studies can be fit to a mono-exponential, bi-exponential, or stretched exponential decay equations which are shown in equations 1.10, 1.11, and 1.12, respectively.

$$y = y_0 + A e^{-\frac{x}{\tau}} \qquad (1.10)$$

$$y = y_0 + A_1 e^{-\frac{x}{\tau_1}} + A_2 e^{-\frac{x}{\tau_2}} \qquad (1.11)$$

$$y = y_0 + A e^{\left(-\frac{x}{\tau}\right)^{\beta}} \qquad (1.12)$$

When the data best resembles a mono-exponential decay, the emitter occupies equivalent sites where the lifetime is τ, y_0 is a baseline correction term, A is a scaling factor, and x is time. If two inequivalent sites are known to exist, it is anticipated that the lifetime data could be fit to a bi-exponential equation where the percentages of the scaling terms (*i.e. $A_1/(A_1 + A_2)$*) is directly
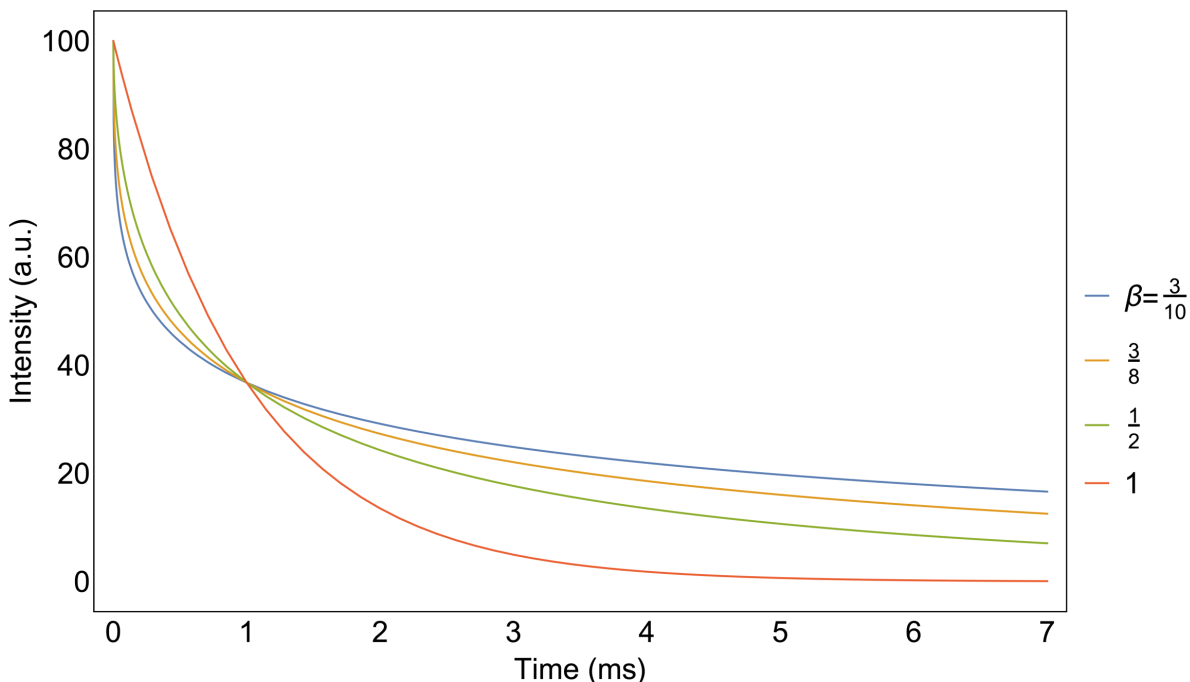
Figure 1.10. Simulated stretched exponential models with lifetimes of 1 ms. Values of β were changed to $^1/_2$, $^3/_8$, $^3/_{10}$, and 1, illustrating the differences between stretched exponential fits. The isosbestic point seen at 1 ms corresponds to the simulated lifetime value.

related to the occupation of the site. The stretched exponential equation is similar to the single exponential equation when β is 1. The value of β is between 0 and 1 and describes the quenching of the donor emission from energy transfer pathways when β is expanded to $β = d/s$.[103, 104] The nominator, d, is defined by the dimension of energy transfer (*1D, 2D,* or *3D*) systems whereas the denominator, s, relates the type of coupling that is occurring. For dipole-dipole, dipole-quadrupole, and quadrupole-quadrupole coupling, s is equal to 6, 8, and 10, respectively. For resonance energy transfer mechanisms within a nanoparticle system, values of $^1/_2$, $^3/_8$, $^3/_{10}$, and 1 are anticipated within *3D* systems.[105-107] Figure 1.10 shows a simulated lifetime of 1 ms for β values of $^1/_2$, $^3/_8$, $^3/_{10}$, and 1 where the isosbestic point shown is equal to the lifetime of the system.
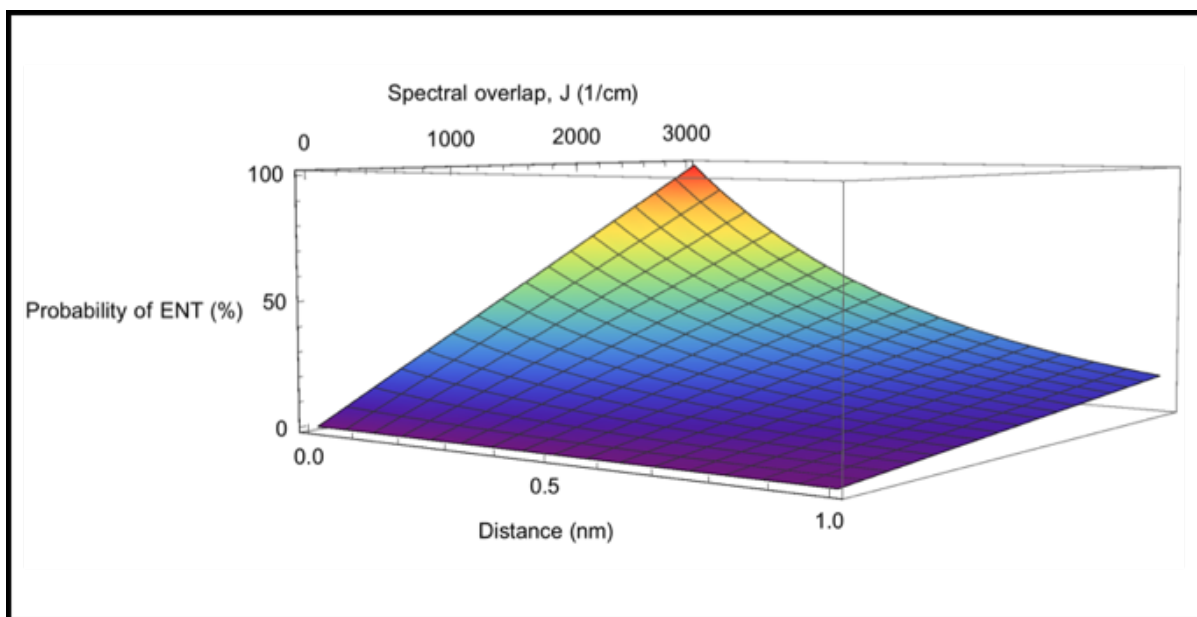
Figure 1.11. Probability of Dexter energy transfer as a function of distance between donor and accepter, R_{DA}, and spectral overlap, <J>. Energy transfer is maximized at small distances and large spectral overlap terms.

1.4.5 Molecular Antenna.

Lanthanide transitions are Loprte-parity forbidden which causes low extinction coefficients, typically on the order of 20 $cm^{-1}M^{-1}$.[88, 89] To circumvent these low extinction coefficients, a molecular antenna is employed where the extinction coefficients for the $^1\pi \rightarrow {}^1\pi^*$ states are orders of magnitude grater, typically around 10^5. This effect has been widely used in the field with lanthanide complexes,[101, 102, 108-111] however passivation of nanoparticles with a sensitizing ligand is a novel approach. In these systems, the ligand can be considered the donor and the lanthanide can be considered the acceptor. Once irradiated, the ligand will undergo a transition from the $^1\pi \rightarrow {}^1\pi^*$ state followed by intersystem crossing to the $^3\pi^*$. Intersystem crossing is achieved by the heavy-atom effect which states that the larger spin-orbit coupling term from the heavy-atom will relax the spin selection rule of the coordinated ligand, allowing triplet state formation.[108, 112-114] From the ligand's triplet state, the electron will undergo a Dexter energy

transfer to the excited state of the lanthanide followed by emission.[115] The probability of energy transfer is defined by the Dexter mechanism:

$$k_{ent} = K <J> e^{\frac{-2R_{DA}}{L}}$$ (1.13)

where K is the pre-exponential factor describing the probability of electron state population between donor and acceptor, $<J>$ is the spectral overlap integral (equation 1.8), R_{DA} is the separation distance from the ligand and lanthanide, and L is the sum of the van der Waals radii for the donor and acceptor.[116] To optimize energy transfer, ligand matching is needed to place the triplet state of the ligand and excited state of the lanthanide within 3000 cm^{-1} of each other, corresponding to the J, spectral overlap integral term.[116]

$$J(v) = \frac{\int F_D(v)\varepsilon_A(v) \, dv}{\int F_D(v)dv \int \varepsilon_A(v) \, dv}$$ (1.14)

In the Dexter energy transfer model, $<J>$ is taken as the integrated area of the overlap from the fluorescence of the donor (ligand) and extinction of the acceptor (lanthanide). Considering that the Dexter energy transfer model is an electron hoping mechanism and can occur through spin-forbidden systems, the emission and extinction spectra are normalized since the intensities correlate to the allowedness of the transitions.[117] This in contrast to FRET where dipole-dipole coupling require the intensities to be considered within $<J>$.

For high-efficient nanophosphors, the distance separating the donor and acceptor must be minimized, further increasing the probability of energy transfer. As noted in equation 5, Dexter energy transfer has and exponential dependency (*-2R$_{DA}$*) on distance between the donor and acceptor, giving rise to 'short range energy transfer.' Förster energy transfer (FRET) on the other hand has a R_{DA}^6 dependency, often noted as 'long range energy transfer.' Figure 1.11 shows the probability of Dexter energy transfer as a function of R_{DA} and spectral overlap, $<J>$. The synthetic route produces 2.0 nm particles which given stochastic distribution of dopant places most

lanthanides within the quenching sphere of the ligand. If matched to a ligand, the energy transfer would be highly efficient at sensitizing neighboring lanthanide ions.

1.4.6 Other Energy Transfer Pathways.

While the most common method to sensitize a lanthanide is through the molecular antenna effect, other pathways do occur. A common pathway to sensitize Eu(III) is from a neighboring Tb(III) cation. Due to the similar energies of the Eu(III) and Tb(III) excited states, the two ions can couple and transfer its energy to the lowest lying excited state of the $^5D_0$ of the Eu(III). It has been reported from various authors that sensitization does occur between the two lanthanide cations, however, the actual energy transfer mechanism is still elusive. Authors have suggested a dipole-dipole coupling[118-120] energy transfer best describes the behavior, however, it is unlikely due to the fact that the dipole-dipole coupling cannot occur since no *f-f* transitions are dipole allowed. However, it has been proposed that a similar resonance energy transfer mechanism can occur through the coupling of two quadrupoles.[105-107] This energy transfer pathway behaves like FRET with the exception that distance dependence term is R_{DA}^{-10}, rather than R_{DA}^{-6}. Considering the electronic quadrupole transitions are weak in the lanthanides, this energy pathway may only partially contribute to the overall energy transfer process. By coupling lifetime data and fitting the PLQY to the Perrin model, an energy transfer model can be generated.

1.4.7 The Perrin Model.

In order to understand the energy transfer processes, the Perrin model was explored to elucidate the critical radii for energy transfer within the quenching sphere. The critical radii is donor dependent and is given by the following equation:

$$\ln\left(\frac{QY}{Q_0}\right) = -VN_A[Ln^{3+}] \tag{1.15}$$

where QY is the quantum yield of the system, Q_0 is the quantum yield within the quenching sphere, assumed to be 1, N_A is avagadro's number, $[Ln^{3+}]$ is the concentration of the lanthanide in mol/L, and V is the volume of a sphere.[121] The volume term can be related to the R_0 (50% quenching radius) in other diffusional energy transfer models, however in the Perrin model energy transfer is assumed to be 100% efficient within the sphere. Plotting the $\ln\left(\frac{QY}{Q_0}\right)$ vs. $N_A[Ln^{3+}]$ produces a linear regression where the slope is equal to the volume of the sphere. From the volume, a percentage of accessible lanthanide ions was extrapolated, assuming a stochastic distribution. This model can be applied to any donor acceptor pair and therefore was applied to dual-doped systems to understand the energy transfer between Tb(III) and Eu(III) as well as ligand sensitization of Tb(III) cations.

1.4.8 Scattering.

The scattering of light is a problem with current state of the art phosphors. Current phosphors used are made by commercial solid state synthetic routes which are later ball-milled to reduce the particle sizes.[82] Although ball-milling reduces the scattering of lower energy photons, blue and UV photons continue to be scattered reducing luminaire efficiency. Rayleigh scattering becomes prominent over Mie scattering when the particle size is 1/10 of the wavelength of light
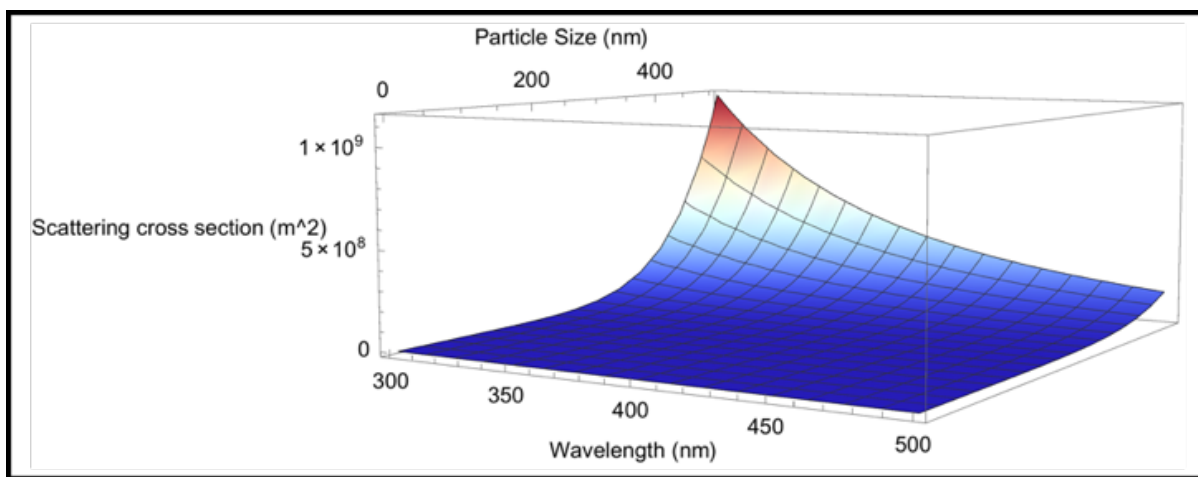
Figure 1.12. The scattering cross section as a function of nanoparticle size and wavelength as predicted from Rayleigh scattering.

which applies to the nanotechnology described in this dissertation. The Rayleigh scattering cross section is given by equation 1.16:

$$\sigma = \frac{2\pi^5}{3}\frac{D^6}{\lambda^4}\left(\frac{\eta^2-1}{\eta^2+2}\right)^2 \tag{1.16}$$

where D is the particle diameter in meters, λ is wavelength in meters, and η is the refractive index of the material which is 1.7940 for $ZnAl_2O_4$.[122, 123] Figure 1.12 shows the scattering cross section as a function of particle size and pump LED wavelengths, which demonstrate the importance of particle size reduction to increase luminaire efficiency. Additionally, the larger products are more difficult to become soluble in the lens increasing the scattering from the pump LED when embedded into a lens matrix. Reducing the size to 2.0 nm scattering of the pump LED is minimized. By producing soluble 2.0 nm nanoparticles passivated with a sensitizing ligand, high efficient down-shifting nanophosphors can be manufactured using additive manufacturing protocols as a new technology aimed to reduce lighting energy consumption, consistent with the DOE goals.

1.4.9 Fischer-Tropsch Synthesis.

The Fischer-Tropsch synthesis (FTS) isolates liquid hydrocarbon fuels from biomass, natural gas, and coal feedstocks by converting syngas to hydrocarbons.[124] The FTS reaction is shown in equation 1.1 .Originally commercialized prior to World War II, interest in the FTS has recently increased since coal and natural gas reserves are 25 and 1.5 times more abundant than petrochemical feedstocks, respectively.[3, 124]

$$n\,CO + (2n+1)\,H_2 \rightarrow C_nH_{(2n+2)} + n\,H_2O \tag{1.1}$$

$$CO + H_2O \rightarrow H_2 + CO_2 \tag{1.2}$$
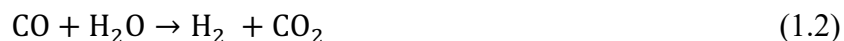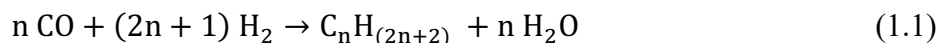
The FTS is already used at industrial scales to isolate the liquid fuels on a global level with plants in Malaysa, South Africa and Qatar, however, facilities in the United States have been postponed

due to the significant cost associated with the process. Using iron or cobalt containing catalysts, plants around the globe produce millions of barrels of diesel and gasoline from the chemical feedstocks. At the industrial scale, iron carbide catalysts are frequently generated by the *in-situ* carburization of α-Fe prior to the catalytic activity. However, common issues arise from iron-based systems such the susceptibility to the water gas shift (equation 1.2), limiting the application of iron-based catalysts. The water gas shift causes the isolation of longer and undesired hydrocarbons and production of CO_2. While the mechanism is not understood by the literature, it is suggested that formation of intermediate formate complexes shift the equilibrium of the reaction, resulting in the longer hydrocarbons.[125] Even though iron is more active to the water gas shift, it is employed as the catalyst for feedstocks with low water content at plants around the world since cobalt containing systems are approximately 200 times more costly to operate.[126]

Product tunability can be achieved by controlling the elemental ratios of the alloyed material. Ralston *et al.*[127] isolated a series of *d*-block alloys of Co-M (M = Mn, Cu, Ru, Rh, Re) through solvent assisted decomposition of M-carbonyl complexes that produced bimetallic nanocrystals. The bimetallic nanocrystals demonstrated enhanced selectivity for ethanol, albeit the study indicates that changes in nanocrystal size may also contribute to differences in the catalytic behavior. Similar observations were seen by Davis *et al.*[128] in ternary alloys of $M_xFe_2Co_{1-x}$ (M= Cu, Zn, Mn). Lower CO and H_2 conversions were observed for Mn doped systems, while Zn and Cu doped systems exhibited higher conversions rates. Selectivity for alcohol isolation was accomplished with the Mn and Fe systems and water-gas shift activity was reduced when Cu and Zn were incorporated into the material. The studies aforementioned investigated the alloyed material in the FTS, however, it has been suggested that the carbide species are more stable against deactivation, yet isolation of mixed metal carbides is difficult.[128] The difficulty stems from the

complex phase diagrams of the Fe-C, where most Fe_xC_y species are metastable and are isolated as mixed phases, especially at the nanoscale. Controlling the elemental composition for the mixed metal carbides at the nanoscale requires advanced synthetic strategies where reactivities are similar for each metal species.

In addition to elemental composition, nanoparticle size and phase have been observed to have selectivity towards product isolation. At sizes below 6 nm, reduced turnover frequencies (TOF) and increased selectivity was observed for CH_4 products, however, the olefin TOF was independent of nanocrystal size in metal carbide and metal alloy systems.[127-131] Many of the systems studied are the iron-carbide catalysts are isolated from sol-gel,[132-134] hydrothermal,[6, 135, 136] and recently by thermal conversion of a Prussian blue analogue.[74, 137-139] These protocols typically require post-annealing steps to enhance crystallinity, however, fusing of the grain boundaries are common during annealing which result in aggregated or bulk material.[140] Due to the synthetic protocol, the results are ambiguous and often conflicting between reports. For implementation into the US markets, further research is necessary to control phase, size, and elemental composition of the catalyst to control product in the FTS.

1.5 Conclusion.

The following chapters within in this dissertation describe the application and synthesis of nanoparticles. Chapter 2 presents a novel method to isolate size, phase, and composition-controlled metal carbide and metal nanocrystals from a single-source precursor. It is anticipated that the material isolated from the results found in Chapter 2 can be employed as potential catalyst for the selective isolation of products generated during the Fischer-Tropsch Synthesis. Chapter 3, 4, and 5 investigate the properties of lanthanide doped nanospinels (Ln:$ZnAl_2O_4$) where quantum yields of 37% are achieved from sensitizing Tb(III) with heaxfluoroacetylacetonate (hfacac). The QY

were enhanced by understanding the spectral overlap between the donor and acceptor, as well as probing the strain dependent behavior. Spectral engineering was accomplished by incorporation of two lanthanide ions into a single nanospinel and sensitized by hfacac. The results found within this dissertation are aimed to secure energy independence and reduce overall energy consumption within the USA.

CHAPTER 2

PRUSSIAN BLUE IRON-COBALT MESOCRYSTALS AS A TEMPLATE FOR THE GROWTH OF FE/CO CARBIDE (CEMENTITE) AND FE/CO NANOCRYSTALS

The work in this chapter is available on pubs.acs.org[141]

Controlling the composition, size, and morphology of transition metal carbides and metals is important for product selectivity in industrial catalytic processes, such as in the Fischer-Tropsch synthesis (FTS). Formation of iron-cobalt carbide nanocatalysts can enhance selectivity in the FTS process if the iron to cobalt ratios are controlled. Unfortunately, this is difficult to achieve in nanocrystals due to ion migration, differences in formation rates, and the requirement of a perfect critical nuclei to form prior to growth of the nanocrystal in colloidal synthesis. In this chapter, a mixed metal iron-cobalt Prussian blue analogue (PBA) mesocrystal is shown to act as a template for isolating pure phase iron-cobalt carbide and iron-cobalt alloy nanocrystals. The formation of the individual nanocrystals from the heterometallic mesocrystal occurs through sequential decomposition and recrystallization events. The steps in the inter-conversion are observed by *in-situ* and *ex-situ* analytical techniques allowing a mechanism for carbide and metal formation to be proposed. The synthetic route is scalable, and likely to be extendable to a wider range of bimetallic materials using the diverse range of Prussian blue analogues (PBAs) reported in the literature.

2.1 Introduction.

The increasing demand for chemical feedstocks has promoted the investigation of catalytic material and the role of elemental composition, phase, and nanocrystal size in product selectivity. High surface area, nanocrystal metal carbides are finding increased application in catalysis, but can be difficult to isolate as a pure phase due to carbon diffusivity.[3, 142-144] An important industrial

catalyst used in the Fischer-Tropsch Synthesis (FTS) is iron carbide and its transition metal carbide variants.[3-7] FTS converts syngas to alkanes at the surface of transition metal carbides (Fe_5C_2, Fe_7C_3, Fe_3C, or Fe_2C) to produce hydrocarbons and olefins. Recent studies have shown the chain length of the alkane depends on the transition metal carbide composition due to contributions from a side reaction known as the water-gas shift (WGS). [3-5, 8, 128] The WGS is the reaction between H_2O and CO allowing for the formation of H_2 and CO_2. This reaction is catalyzed in pure iron carbide systems, resulting in isolation of longer and less desirable hydrocarbons with increasing water content.[3-5] Incorporation of cobalt into the iron carbide inhibits the WGS side-reaction; [3, 8, 9] enhances catalyst stability, [4, 5] but unfortunately the pure Co_xC_y is unreactive and Co is more expensive.[3, 8] Generating catalysts of known Co composition can allow the balance of selectivity and cost to be assessed for the FTS, however, to date, few reports have shown the successful incorporation of Co into Fe_xC_y nanometals.[10-12] Translation of the bulk catalysts to nanocrystal metal carbides can allow exploration of catalytic activity through control of composition, crystallographic phase, and faceting.[3, 4, 145]

In this chapter, we explore the controlled conversion of an iron-cobalt Prussian Blue Analogue (Fe-Co PBA) mesocrystal to form FeCo nanocarbides ($Fe_{3-x}Co_xC$) and FeCo nanometals ($Fe_{2-x}Co_x$) selectively. The conversion process is monitored using *in-situ* and *ex-situ* methods to elucidate the steps that lead to isolating the FeCo carbide over FeCo metal. When carried out in oleylamine, precise size and shape control is achieved. The size of the isolated nanocrystals scale linearly with the initial PBA size. The growth of the nanocrystal from the PBA is believed to occur *via* a template process involving the growth of the carbide on the wall of the PBA, followed by a kinetically slow diffusion of carbon to the nanocrystal surface forming the mixed metal alloy. Although no catalysis studies are reported in this chapter, it is envisioned that

the described strategy to prepare mixed metal carbides and metals wherein the nanocrystal size, phase, and elemental composition are controlled, could be beneficial to future catalytic activity studies *via* the Fischer-Tropsch Synthesis, as well as other catalytic reactions utilizing such materials.

2.2 Experimental.

2.2.1 Materials.

All commercially available reagents were used without further purification. Iron-cobalt Prussian blue analogue precursors are potassium hexacyanoferrate ($K_3Fe(CN)_6$, Sigma, >99.0%), cobalt(II) chloride hexahydrate ($CoCl_2 \cdot 6H_2O$, Fisher Scientific, >99%) and potassium chloride (Sigma, 98%). Solvents used in the synthesis were nanopure water (4.7 Ω, Barnsted NANOpure), oleylamine (Sigma, >70%), methanol (BDH, ACS grade), toluene (Macron, ACS grade), and acetone (Macron, ACS Grade). Elemental composition analysis called for concentrated nitric acid (Sigma, Trace Grade) and nanopure water. Calibration curves were made by dissolving $FeSO_4$ x $7H_2O$ (Alfa Aesar, 99.999%) and elemental Co (Sigma, 99.99%) in 2% nitric acid and performing serial dilutions.

2.2.2 Iron-Cobalt $KCo_x[Fe_{2-x}(CN)_6]$ (FeCoPBA).

The synthesis was adapted from Talham *et al.*[71] Iron-cobalt PBAs were synthesized by co-precipitation at room temperature. First 50 mL of aqueous 20 mM $K_3Fe(CN)_6$ solution and 50 mL of aqueous 0.1 M KCl were mixed for 10 min. After stirring, 200 mL of aqueous X mM $CoCl_2$ (X=9.1, 5.1, 5, 4.75, and 4.45) was added dropwise at a rate of 5mL/min. The reaction was matured for 18 hours and the product was isolated by addition of acetone and centrifugation. The higher concentration $CoCl_2$ solution produced smaller mesocrystals while the larger mesocrystals were isolated at more dilute reaction conditions, following the tenants of nucleation theory.

2.2.3 Thermal Interconversion of $KCo_x[Fe_{2-x}(CN)_6]$ to $Fe_{3-x}Co_xC$ (Carbide) and $Fe_{2-x}Co_x$ (Bimetallic).

A round bottom was charged with 4mL of oleylamine and 40 mg of FeCo PBAs. The solution was then heated to 50 °C, degassed and stirred for 1 hour. The reaction mixture was heated to 350 °C under N_2. To isolate the carbide, the reaction was quenched at 2h, while the bimetallic is formed by quenching the reaction at 6h. under N_2 and cooled by forced air. To isolate the nanoparticle, the samples were magnetically separated and washed three times by addition of toluene and methanol. The particles were dried overnight by vacuum and stored under N_2.

2.2.4 Physical Measurements.

X-ray powder patterns were collected at RT on a Rigaku Ultima III diffractometer (Cu-$K\alpha$ source and a CCD detector). *In-situ* temperature-dependent XRD was performed at beamline 12.2.2 of the Advanced Light Source (ALS).[146-149] The powder samples were introduced into 0.7 mm quartz capillaries (Hilgenberg, Germany) and placed inside the SiC oven, which was heated using two infrared lamps (Osram 64635HLX) between room temperature and 600 °C at 10 °C/min. A N_2 gas flow of 10 NmL/min was delivered using Alicat (USA) mass flow controllers. XRD patterns were collected with 34 seconds intervals using a Perkin Elmer 1621 xN amorphous Silicon CMOS detector. The superbend beamline was operated with an incident X-ray energy of 25 keV, sample-detector distance of 330-450 mm and a spot size of 30 x 30 μm^2. The setup was calibrated with a LaB_6 standard (NIST 660b). The resulting patterns were integrated with Dioptas software V0.4.1.

Size, size dispersity, and morphology were analyzed by scanning electron microscopy (SEM) by dispersing the PBAs in MeOH and drop casting. Images were taken on a FEI Nova 400
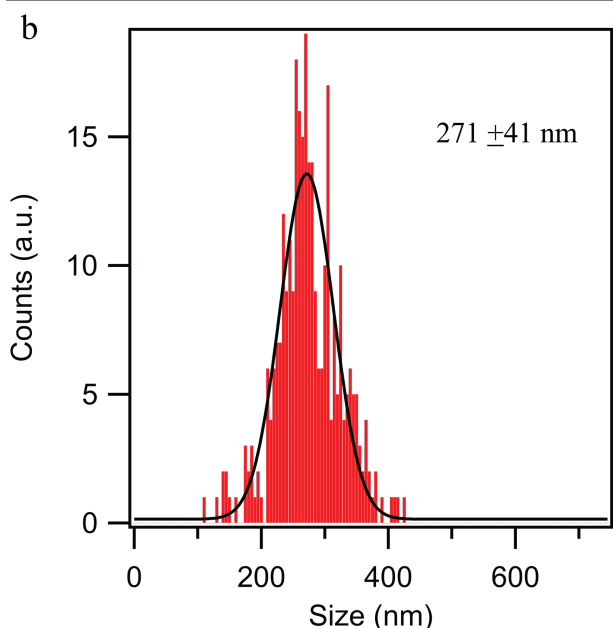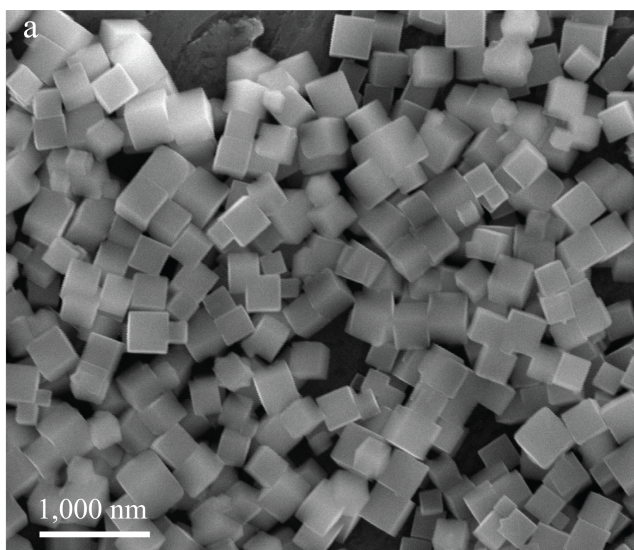
Figure 2.1. a) SEM image of 271 $\pm$ 41 nm KCo$_{1.09}$[Fe$_{0.91}$(CN)$_6$] and b) Gaussian distribution generated by measuring the cube length for >300 PBAs.

Nano SEM operating at 10.00 kV with a spot size of 2.0. Particle sizes and distributions were analyzed by measuring >300 PBAs. Size, size dispersity, and morphology for the carbide and bimetallic materials were analyzed by transmission electron microscopy (TEM) from drop casting toluene dispersed particles and drying overnight under reduced pressure. TEM measurements were carried on a JEM-ARM200cF operating at 200 kV using a carbon type A (300 mesh) on Formvar-free grids. Image analysis of >300 nanocrystals was used to generate the size distribution curves.

Elemental analysis was accomplished by digesting each sample in trace grade HNO$_3$ and injecting into an ICP-MS (Thermoscientrific, ICAP-Rq). Calibration curves were created by serial dilutions of Fe and Co in 2% HNO$_3$ with an R^2 >0.999 for each ion.

2.3 Results and Discussion.

2.3.1 Thermal Conversion of a 271 nm PBA Passivated by H_2O.

Selectively isolating the metal carbide and the metal during the thermal decomposition of a PBA should be controllable if the mechanism can be evaluated. *Ex-situ* and *in-situ* probe methods were used to follow the thermal conversion of a $KCo_{1.09}[Fe_{0.91}(CN)_6]$ PBA passivated by H_2O (FeCo PBA-H_2O). The PBA is prepared following the procedure of Talham, *et al.*[71] SEM imaging (Figure 2.1) confirms isolation of a 271 ± 41 nm FeCo PBA-H_2O mesocrystal composed of 39.8% Fe to 60.2% Co atomic percent based on ICP-MS analysis.

In-situ powder X-ray diffraction data collected on a synchrotron operating at 25 keV is shown in Figure 2.2a and Figure 2.3. Rietveld refinement of the *in-situ* XRD data set was carried out at selected temperatures to evaluate the structural changes occurring as the PBA is heated. The temperatures for the Rietveld refinement, the Rietveld refinement fits, and the structural assignments are available in the Figure 2.4 and Table 2.1

Rietveld analysis of the pattern at 18 ºC confirms the assignment to the PBA cubic *Fm-3m* structure. The low temperature (LT) cubic structure is referred to henceforth as *Fm-3m* (LT). A phase transition is identified in the TGA-DSC data (Figure 2.5a) at 119 ºC (10 ºC / min) that lacks a correlated change in diffraction pattern in the *in-situ* XRD data. The transition is associated with lattice dehydration resulting in a 21% mass loss. As the temperature is increased to 197 °C and (004) full width at half maximum (FWHM) changes over this temperature region is shown in Figure 2.5a. The structural transition is assigned to a first order phase transition, exhibiting the two phase contributions scaling inversely with increasing temperature. No mass, exothermic, or endothermic event is observed for this temperature region in the TGA-DSC. Confirming the *Pmn2₁*
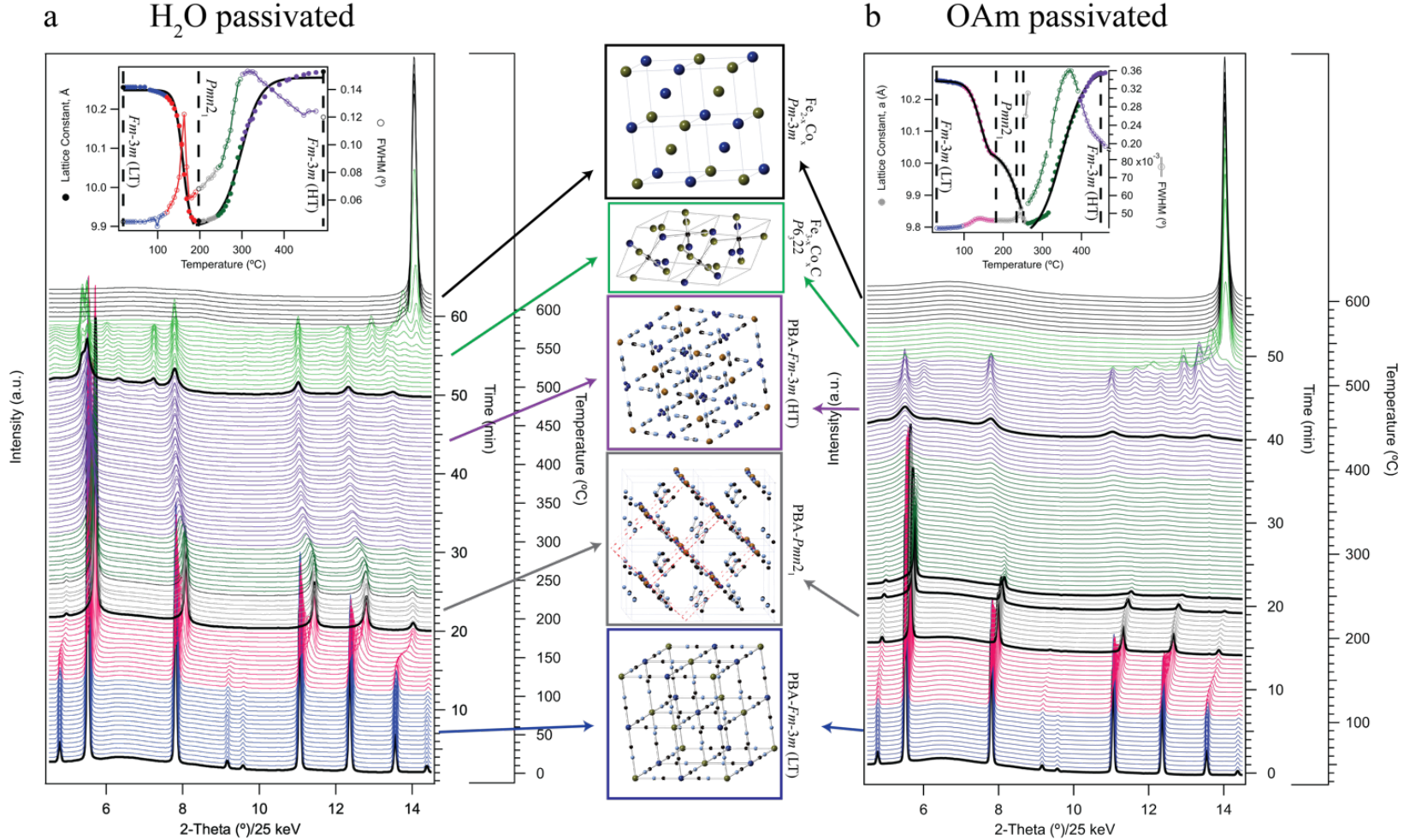
Figure 2.2. Temperature-dependent pXRD measured from 18 °C to 600 °C at 10 °C /min at 25 keV under N_2 flow. The blue is the $KCo_{1.09}[Fe_{0.91}(CN)_6]$ Fm-3m (LT) phase, the magenta traces indicates the phase transition from the cubic to orthorhombic phase, grey trace indicates the orthorhombic phase, dark green indicates disordered phases from the orthorhombic structure to the Fm-3m (HT) phase, purple represents the Fm-3m (HT) while the light green traces reveal the transition to the $Fe_{1.30}Co_{1.70}C$ phase and black is the $Fe_{0.97}Co_{1.03}$. Bolded black traces represent the patterns that were Rietveld refined. The full 2θ range is available in Figure 2.3 (PBA-H_2O) and Figure 2.9 (PBA-OAm).

crystal phase is not a metastable phase observed only in the *in-situ* XRD data, the orthorhombic phase was isolated following annealing of the PBA sample at 197 °C for 1h (Figure 2.4d).The first order phase transition from *Fm-3m* to *Pmn2*$_1$ can be envisioned as a plane rotation (screw-axis formation) inducing a canting of the cyanide bridges with the metals on ordered sites following lattice dehydration.[150, 151] The canting of the cyanide results in an overall volume reduction and a weakening of the metal-cyanide bonds due to changes in the orbital overlap. The change in orbital overlap leads to oxidative state changes as evidenced in the FT-IR data (Figure 2.6). In the *Fm-3m* (LT) phase, the M-CN stretch can be assigned based on earlier studies[152, 153] to an admixture of Fe^{III}-CN-Co^{II} species at 2159 cm^{-1} as the predominate species, and Fe^{II}-CN-Co^{III} at 2120 cm^{-1} and Fe^{II}-CN-Co^{II} at 2090 cm^{-1} as the minority contributors. Upon conversion to the *Pmn2*$_1$ phase at 197 °C, loss of the Fe^{III}-CN-Co^{II} (2159 cm^{-1}), a growth of a feature assignable to Fe^{II}CN-Co^{III} (2120 cm^{-1}), and a new mode at 2074 cm^{-1} assigned to a canted (4°) Fe-C bond is observed. The assignment of the 2074 cm^{-1} feature is based upon the observation that the orthorhombic Mn-Mn sample (solid line) in the TGA-DSC (Figure 2.5a) as the temperature is elevated from 197 °C to 493 °C. In the TGA-DSC only a small mass loss (8.2%) is observed; however, the calorimetry data exhibits an energetic transition at 266°C that corresponds with an inflection point in the (004) lattice and FWHM *vs*. temperature plot in Figure 2.2a (inset). Refinement of the *in-situ* XRD pattern at 493 °C shows two contributions in the pattern. The major contribution is assignable to a disordered *Fm-3m*, high temperature (HT) cubic phase, while the minority contribution is an amorphous phase at 11.7 wt%. The *Fm-3m* (HT) structure can be represented as being comprised of a disordered cyanide and metal network where Co[Fe(CN)$_5$]$^-$ units occupy a non-centrosymmetric site. The *Fm-3m* (HT) phase is metastable and cannot be directly isolated by heating the powder to 266 °C for extended time.
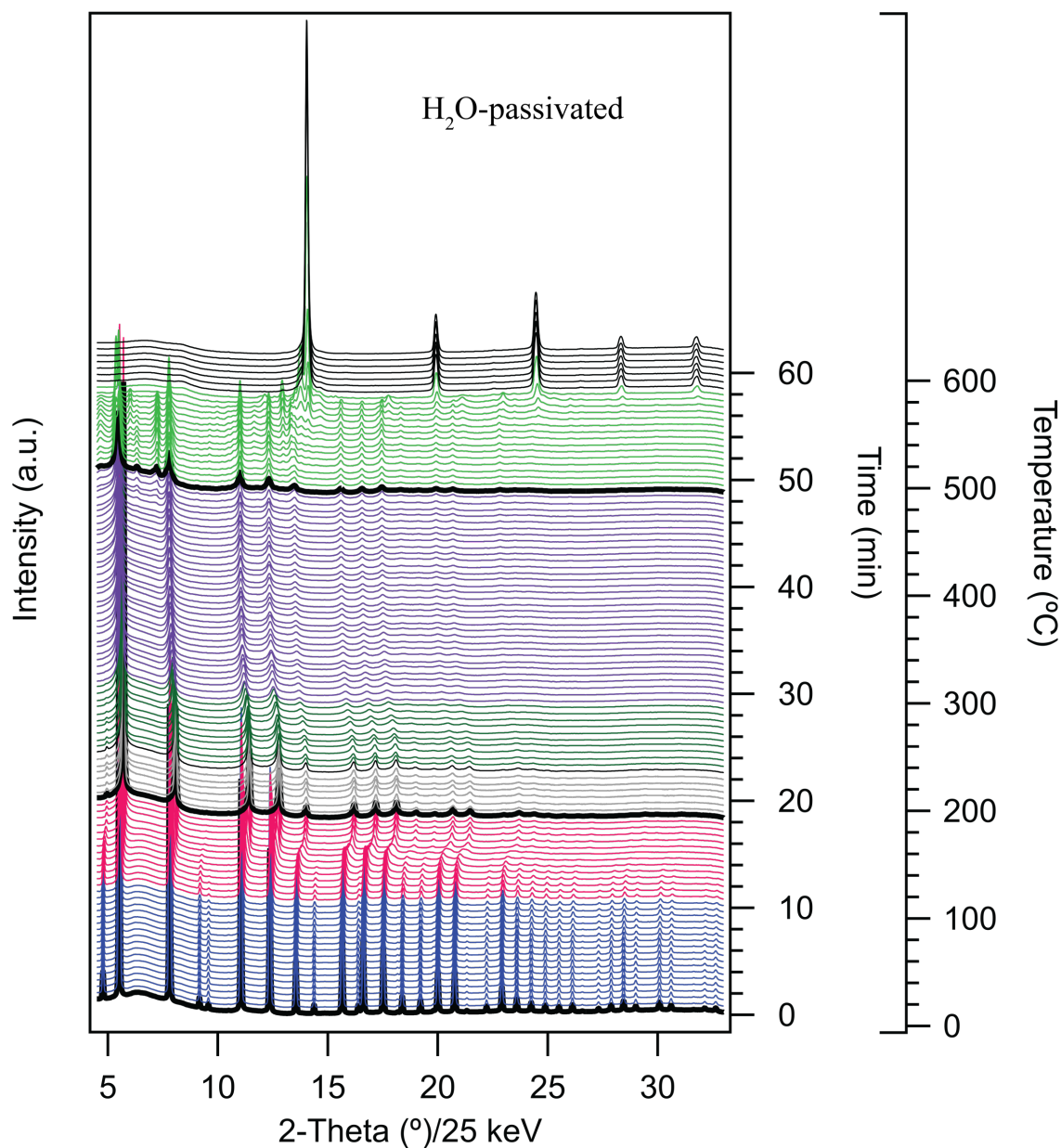
Figure 2.3. *In-situ* high-temperature powder x-ray diffraction patterns from the advanced light source operating at 25 keV of the H_2O passivated $KCo_{1.09}[Fe_{0.91}(CN)_6]$ sample. The heating ramp is 10 ºC/min from 18 ºC to 600 ºC. Data was collected every 34 seconds during the heating ramp. Nitrogen was flowing at a rate of 15 mL/min to eliminate oxidization. The blue is the $KCo_{1.09}[Fe_{0.91}(CN)_6]$, the magenta traces indicates the phase transition from the cubic to orthorhombic phase, grey trace indicates the orthorhombic phase, dark green indicates disordered phases from the orthorhombic structure to the *Fm*-3*m* (high temperature) phase, purple represents the *Fm*-3*m* (high temperature) while the light green traces reveal the transition to the $Fe_{1.30}Co_{1.70}C$ phase and black is the $Fe_{0.97}Co_{1.03}$. Bolded black traces represent the patterns that were Rietveld refined.

Figure 2.4. Rietveld refinement on ALS patterns taken at a) 18 ºC, b) 197 ºC, and c) 493 ºC. The pattern in figure (d) was collected using a Mo K_α anode after annealing the sample at 197 ºC for 1h.

Table 2.1. Parameters refined during Rietveld analysis of data taken during dynamic ALS measurements of the H_2O passivated samples.

H₂O Passivated PBA, Refined Parameters				
Temperature (ºC)	a (Å)	b (Å)	c (Å)	Phase
18	10.31654	10.31654	10.31654	*Fm-3m* (LT)
197	9.93331	6.98925	7.06601	*Pmn2₁*
493	10.35486	10.35486	10.35486	*Fm-3m* (HT)
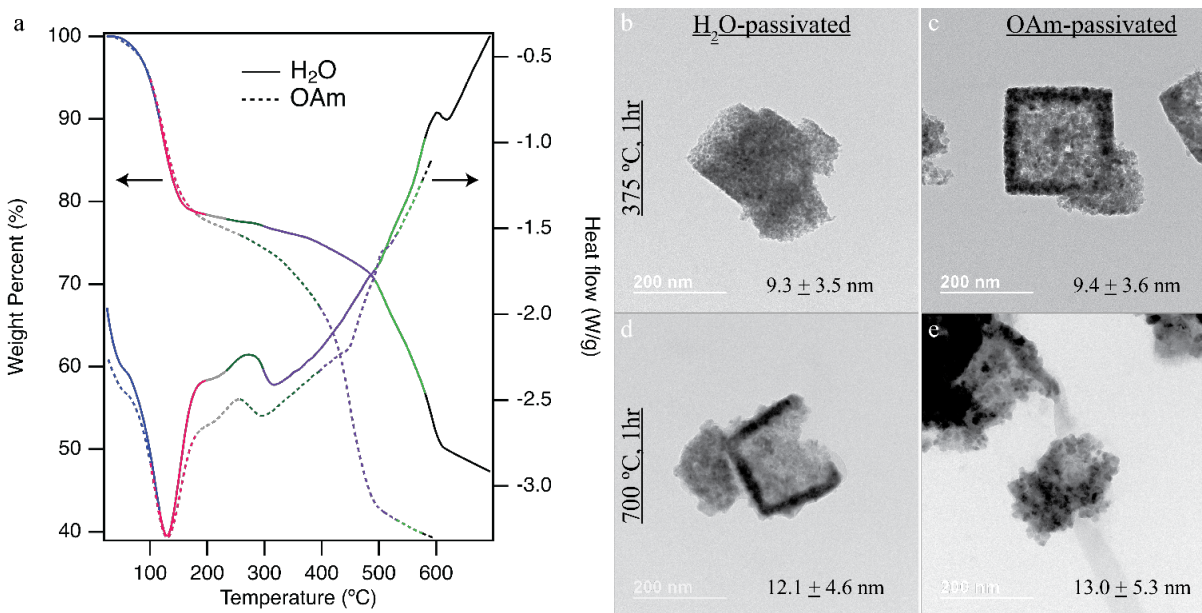
Figure 2.5. a) TGA-DSC scans of the 271 ± 41 nm $KCo_{1.09}[Fe_{0.91}(CN)_6]$ at 10 ºC/min where the solid lines represent the H_2O passivated PBAs and the dashed lines represent the OAm passivated PBAs. The trace colors correspond to the colors seen in Figure 1 on the dynamic synchrotron pXRD patterns. TEM images of a 271 ± 41 nm PBA-H_2O heated to 375 ºC (b) and 700 ºC (c) and PBA-OAm heated to 375 ºC (d) and 700 ºC (e) for 1h.

Ex-situ TEM imaging of the PBA heated to 375 ºC for 1h Figure 2.5b shows formation of a foam like structure that maintains the shape and size of the initial PBA mesocrystal. SEM-EDX line scans Figure 2.7 on the sample held at 375 ºC for 1h reveals the iron to cobalt composition is constant across the sample. Electron diffraction confirms the foam consists of aggregated nanoparticles of $Fe_{3-x}Co_xC$ with diffraction fringes assignable to the (110) plane of the $Fe_{3-x}Co_xC$ structure Figure 2.5b-e.

The experimental TGA-DSC and *in-situ* XRD data suggest that the growth of the $Fe_{3-x}Co_xC$ phase begins in the temperature region of 197 to 493 ºC through formation of cyanometallate vacancies leading to the metastable *Fm*-3*m* (HT) phase. Consistent with this hypothesis, heating
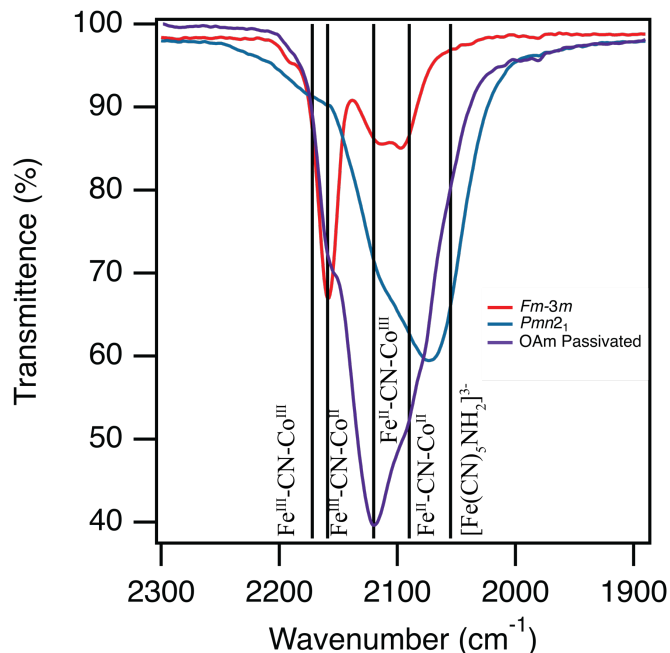
Figure 2.6. FT-IR showing the M-CN stretch of the *Fm-3m* (cubic) phase (red trace), OAm passivated *Fm-3m* (cubic) PBAs (purple trace), and *Pmn2$_1$* orthorhombic phase (blue trace).

to 580 °C (green, Figure 2.2) leads to loss of PBA features in the pXRD data and FT-IR, along with the appearance of reflections assignable to $Fe_{3-x}Co_xC$ (*P6$_3$22*) hexagonal phase. The TGA exhibits significant mass loss (20.2%) and an energetic transition is observed in the calorimetry data at 501 °C allowing assignment of the transition temperature for formation of $Fe_{3-x}Co_xC$.

2.3.2 Metal Carbide Foam to a Metal.

At higher temperatures the carbide will convert to the metal by carbon migration to the nanocrystal surface, as predicted by the phase diagram.[154] In the temperature range of 493 to 591 °C, a mixed carbide and metal pattern is observed in the *in-situ* XRD with complete transition to the bimetallic FeCo (*Pm-3m*) at 591 °C. The TGA-DSC data confirms the transition temperature for metal formation with an endothermic transition observed at 587 °C with minimal mass loss.

The temperature is identical to the report of the temperature for graphitic carbon formation at the surface of PBA nanocrystals.[74, 137]

In Figure 2.5c, a sample annealed for 1h at 700 ºC under an argon environment was investigated by TEM and shows a macroscopic aggregate is formed. The aggregate is comprised of an admixture *Pm-3m* FeCo metal and *Fd-3m* Fe_3O_4 (Figure 2.8d-f). The oxide is believed to be formed upon exposure to air prior to imaging. SEM-EDX line scans (Figure 2.7d-f) reveal the metal signal varies across the width of the sample. In the region of low contrast, the iron to cobalt signal is reduced relative to the edge; however, the iron to cobalt ratio is constant. The EDX line scans coupled to TEM and SEM imaging suggests the conversion from PBA to metal involves an etching of the PBA core followed by recrystallization of the metal at the surface of the PBA, as suggested by Lou, *et al.*[62] The result is inconsistent with the report by Yamada, *et al.*[137] of nanoparticle PBAs leading to nanoparticle metal isolation.

2.3.3 Oleylamine Assisted Conversion of a 271 nm PBA.

Coordinating ligands may lower the barrier for the structural transformations and reduce oxidation of the materials, as suggested by Yamada's study.[137] The effect of a coordinating ligand is clearly observed for a 271 nm PBA passivated by oleylamine (OAm). Passivation is achieved by ligand exchange through dissolving the PBA in neat OAm at 50 ºC for 60 min. TEM imaging shows that the PBA-OAm crystallite size remains 271 ± 41 nm and exhibits the *Fm-3m* crystallographic structure (Figure 2.11a). In the ALS data, the transition to the metal carbide and metal are observed to occur at a lower temperature for the PBA-OAm. Loss of water occurs at 122 ºC *vs*. 119 ºC with a mass loss difference of ~2% consistent with OAm replacing the H_2O on the surface of the 271 nm cube shaped PBA in the TGA-DSC data shown in Figure 2.5a.
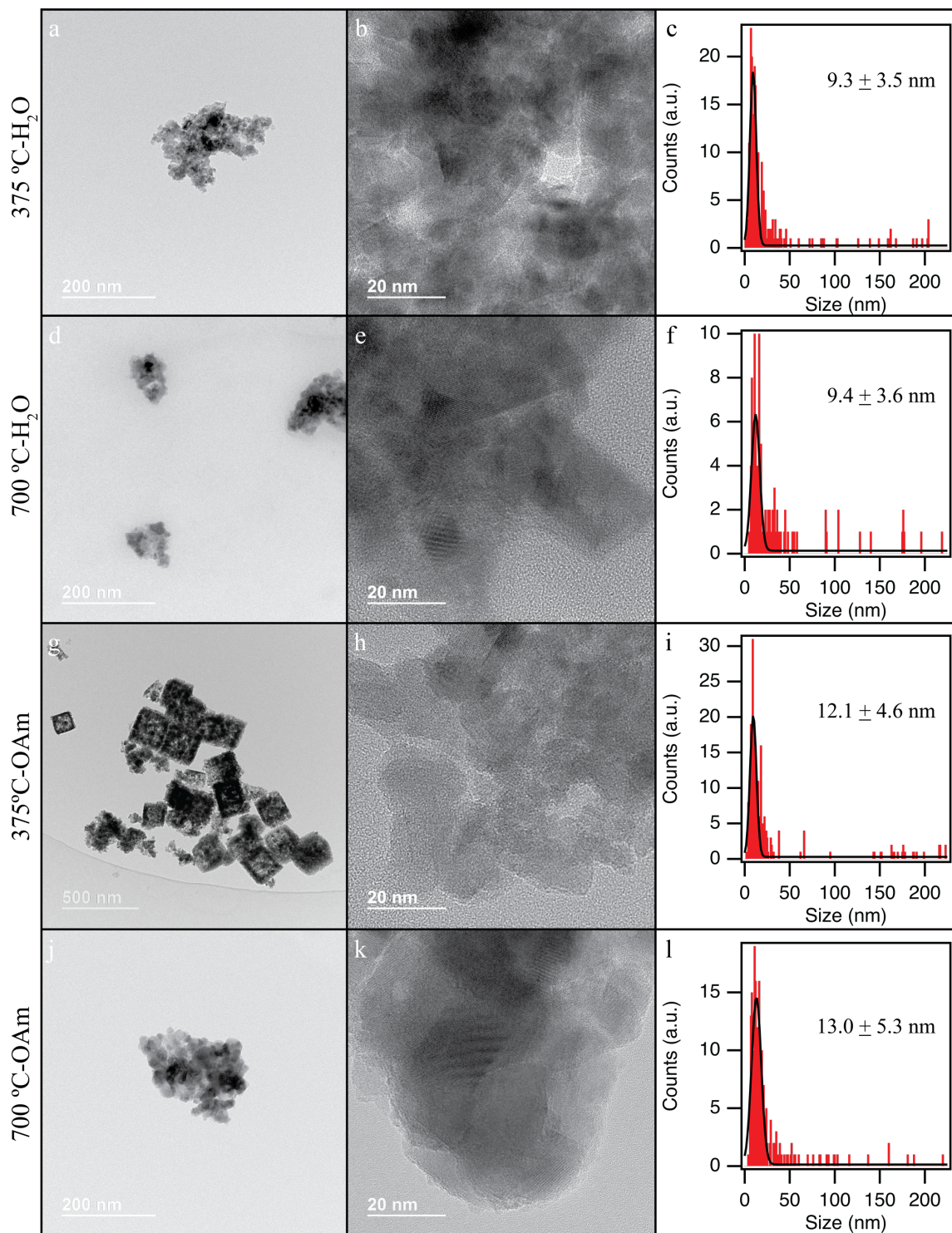
Figure 2.7. TEM images of an H_2O passivated 271 ± 41 nm $KCo_{1.09}[Fe_{0.91}(CN)_6]$ held at 375 ºC for 1 hr (a-b) and 700 ºC (d-e). Distributions of the small material are displayed in c and f. TEM images of an OAm passivated 271 ± 41 nm $KCo_{1.09}[Fe_{0.91}(CN)_6]$ held at 375 ºC for 1 hr (g-h) and 700 ºC (j-k). Distributions of the small material are displayed in i and l.

The dehydration step is followed by the first order structural phase transition from Fm-$3m$ → $Pmn2_1$ occurring at 148 ºC. Unlike in PBA-H_2O, the PBA-OAm sample exhibits a second transition between 180 and 252 ºC, with an endothermic transition observed in the TGA- DSC data at 254 ºC. The endothermic transition occurs 18 ºC lower than for the PBA-H_2O (272 ºC). Rietveld refinement (Figure 2.4) of the pXRD data at 234 ºC reveals the $Pmn2_1$ lattice is maintained during this transition but a compression of the lattice along the a and b axis (1.6% reduction along a; 2.6% along b) has occurred.

Above 300 ºC, the PBA-OAm sample exhibits significant weight loss (20%) with an exothermic transition occurring at 445 ºC in the TGA-DSC data. The mass loss is assigned to small molecule release from the PBA, and release of the OAm ligand from the surface.[155] Rietveld refinement of the at 449 ºC diffraction pattern reveals formation of the Fm-$3m$ (HT) phase with an underlying broad signal. The broad signal seen at 5.9º 2θ in the XRD pattern may arise from an amorphous carbonaceous layer that forms as carbon is ejected from the lattice, as previously suggested in the literature.[137] The transition to the $Fe_{3-x}Co_xC$ metal carbide ($P6_322$) occurs at 478 ºC. This temperature is 102 ºC lower than the H_2O passivated samples. Heating to 548 ºC produces the pure $Fe_{2-x}Co_x$ metal.

Heating of the PBA-OAm for 1h at 375 ºC and 700 ºC allows the morphology of the carbide and metal to be investigated for the OAm passivated sample. In Figure 2.5d, the $Fe_{3-x}Co_xC$ foam is observed to form, analogous to the results from PBA-H_2O. The foam is comprised of ~9.4 nm $Fe_{3-x}Co_xC$ nanocrystals. High-resolution TEM imaging reveal (110) plane with a d-spacing of 2.35 Å. The darker contrast in the edge is believed to arise from exfoliation leading to lower material
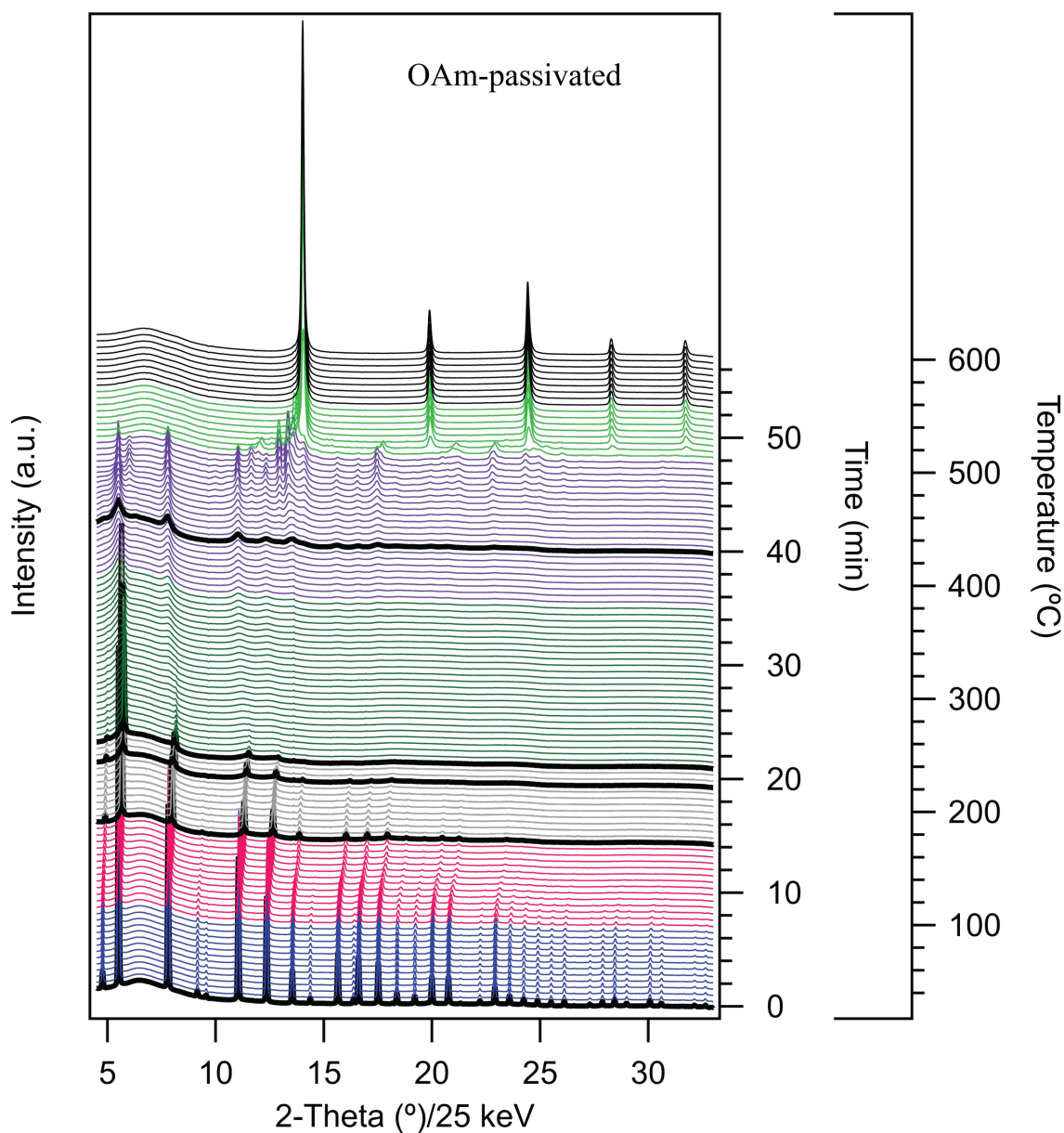
Figure 2.8. *In-situ* high-temperature powder x-ray diffraction patterns from the advanced light source operating at 25 keV of the OAm passivated $KCo_{1.09}[Fe_{0.91}(CN)_6]$ sample. The heating ramp is 10 ºC/min from 30 ºC to 600 ºC. Data was collected every 34 seconds during the heating ramp. Nitrogen was flowing at a rate of 15 mL/min to eliminate oxidization. The blue is the $KCo_{1.09}[Fe_{0.91}(CN)_6]$, the magenta traces indicates the phase transition from the cubic to orthorhombic phase, grey trace indicates the orthorhombic phase, dark green indicates disordered phases from the orthorhombic structure to the *Fm*-3*m* (high temperature) phase, purple represents the *Fm*-3*m* (high temperature) while the light green traces reveal the transition to the $Fe_{1.30}Co_{1.70}C$ phase and black is the $Fe_{0.97}Co_{1.03}$. Bolded black traces represent the patterns that were Rietveld refined.

Figure 2.9. Rietveld refinement of the OAm passivated PBA samples at a) 30 ºC, b) 181 ºC, c) 234 ºC, d) 252 ºC, e) 449 ºC. Samples were collected on the advanced light source operating at 25 KeV.

Table 2.2. Parameters refined during Rietveld analysis of data taken during dynamic ALS measurements of the OAm passivated samples.

OAm Passivated PBA, Refined Parameters				
Temperature (ºC)	a (Å)	b (Å)	c (Å)	Phase
30	10.32142	10.32142	10.32142	Fm-$3m$ (LT)
181	10.06405	7.119187	7.173005	$Pmn2_1$
234	10.02663	7.045343	7.125538	$Pmn2_1$
252	9.90216	6.935544	7.157715	$Pmn2_1$
449	10.25408	10.25408	10.25408	Fm-$3m$ (HT)
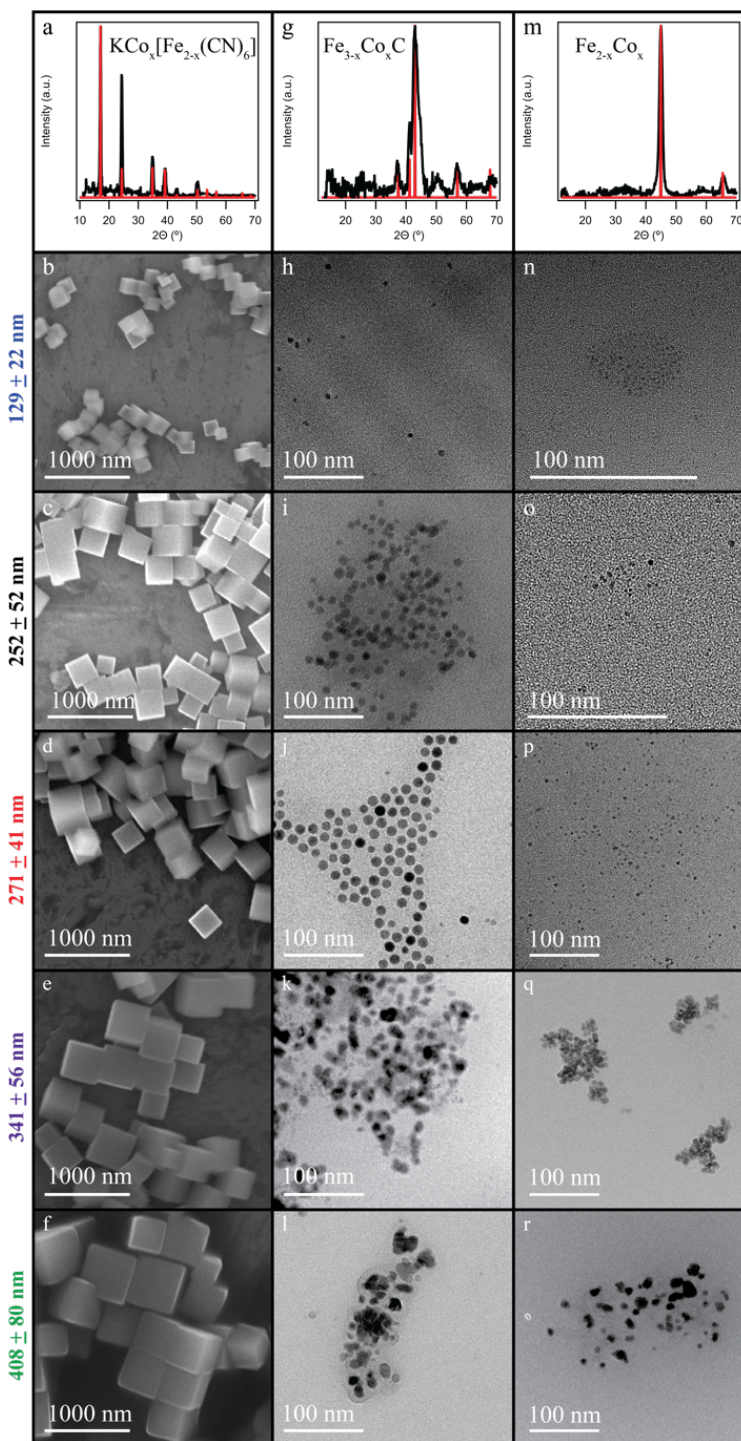
Figure 2.10. pXRD of a) $KCo_x[Fe_{2-x}(CN)_6]$, g) $Fe_{3-x}Co_xC$, and m) $Fe_{2-x}Co_x$. SEM images for the b) 129 nm, c) 252 nm, d) 271 nm, e) 341 nm, f) 408 nm PBAs. TEM images of the metal carbide nanocrystals converted from the h) 129 nm, i) 252 nm, j) 271 nm, k) 341 nm, l) 408 nm PBAs. TEM images of the isolated metal nanocrystals interconverted from n) 129 nm, o) 252 nm, p) 271 nm, q) 341nm, r) 408 nm PBAs.

density at the $Fe_{3-x}Co_xC$ foam core during sample deposition. It is believed exfoliation is due to sonication. Consistent with this picture, SEM-EDX line scans on a sample that was not sonicated (Figure 2.7) reveal the sample has a constant metal composition across the dimension of the cube. Annealing the PBA-OAm sample to 700 ºC results in the formation of a $Fe_{2-x}Co_x$ aggregate (Figure 2.5e). High-resolution TEM imaging display the (110) lattice plane with a d-spacing of 2.01Å confirming the metal is isolated. SEM-EDX line scans on the sample (Figure 2.7) shows the iron to cobalt metal ratio is constant, but a depletion of iron and cobalt form the center of the cube occurs. Unlike the H_2O passivated samples, no evidence of oxidation was observed suggesting the carbonaceous layer left by decomposition of the OAm inhibits oxidation.

2.3.4 Solvent Dispersible, Size-Controlled Carbides and Metals.

As shown in the previous section, the carbide is templated by the PBA cage and collapses to the metal following expulsion of the carbon, as anticipated by solid state phase diagrams for iron-carbide.[154] The materials do not form as discrete nanocrystals but as foam material. Carrying out the reaction on a coordinating solvent may allow nanocrystals to form due to continuous surface passivation. In addition, the use of various sized mesocrystals may lead to controlled nanocrystal formation. Size dependent conversion of a the FeCo PBA in oleylamine to evaluate the ability to isolate discrete nanocrystals from the reaction and achieve selective nanocrystal sizes was explored. A series of PBAs were prepared following the methods of Talham, *et al.*[71] yielding 129 ± 22, 252 ± 52, 271 ± 41, 341 ± 56, and 408 ± 80 nm (cube edge, Figure 3b-f) PBAs having the cubic *Fm*-3*m* (LT) structure based on pXRD measurements (Figure 2.12).

The transition from PBA-OAm to metal carbide and metal was analyzed at 350 ºC for samples heated in OAm for 2h and 6h. SEM imaging (Figure 2.11) and pXRD measurements (Figure 2.12) at 2h reveal solvent dispersible, spherical nanocrystals are formed and assignable to
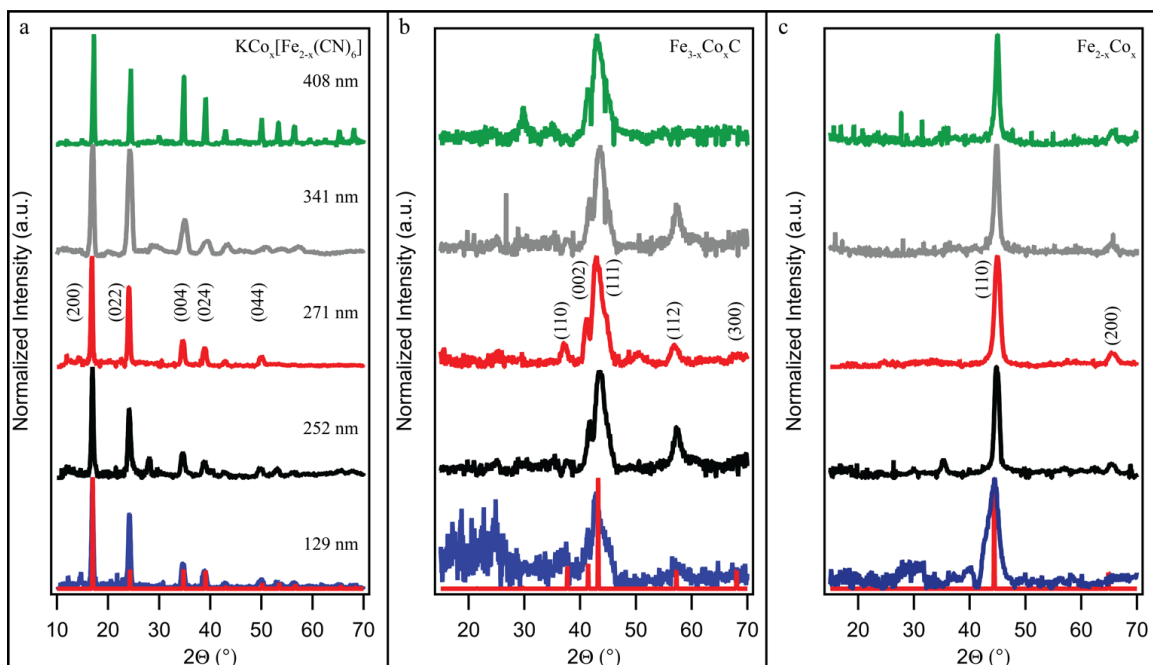
Figure 2.11. Size dependent powder diffraction patterns for a) the K[Fe$_{2-x}$Co$_x$ (CN)$_6$] b) the Fe$_{3-x}$Co$_x$C, and c) Fe$_{2-x}$Co$_x$ nanoparticles. The color of the trace indicate the material grown from the starting precursor, 129 nm K[Fe$_{2-x}$Co$_x$ (CN)$_6$] (blue), 252 nm K[Fe$_{2-x}$Co$_x$ (CN)$_6$] (black), 271 nm K[Fe$_{2-x}$Co$_x$ (CN)$_6$] (red), 341 nm K[Fe$_{2-x}$Co$_x$ (CN)$_6$] (grey), and 408 nm K[Fe$_{2-x}$Co$_x$ (CN)$_6$] (green).

$P6_3$22 Fe$_{3-x}$Co$_x$C structure with nanocrystal sizes of 4.6 $\pm$ 1.5, 8.3 $\pm$ 2.3, 10.5 $\pm$ 1.4, 10.9 $\pm$ 2.6, and 11.6 $\pm$ 2.6 nm, respectively. The samples isolated after 6h are solvent dispersible, spherical nanocrystals that can be indexed to the *Pm*-3*m* phase for a bimetallic FeCo nanocrystal, yielding 1.6 $\pm$ 0.5, 3.2 $\pm$ 1.2, 4.4 $\pm$ 0.9, 5.3 $\pm$ 2.0, and 6.3 $\pm$ 2.2 nm nanocrystals. The metal carbide and metal nanocrystal size are observed to reduce proportionally to the PBA mesocrystal size (Figure 2.15) with a R^2 value of 0.9168 for the bimetallic carbide and 0.9646 for the bimetallic nanocrystal. The linear regression allows for the prediction of the nanocrystal size from an PBA seed. Compositional analysis at each time point (0h, 2h, 6h) confirm the Fe to Co mole ratio is maintained throughout the reaction, within experimental error (Figure 2.3, Figure 2.16). To demonstrate that the elemental compositions are governed by initial PBA elemental constituents,
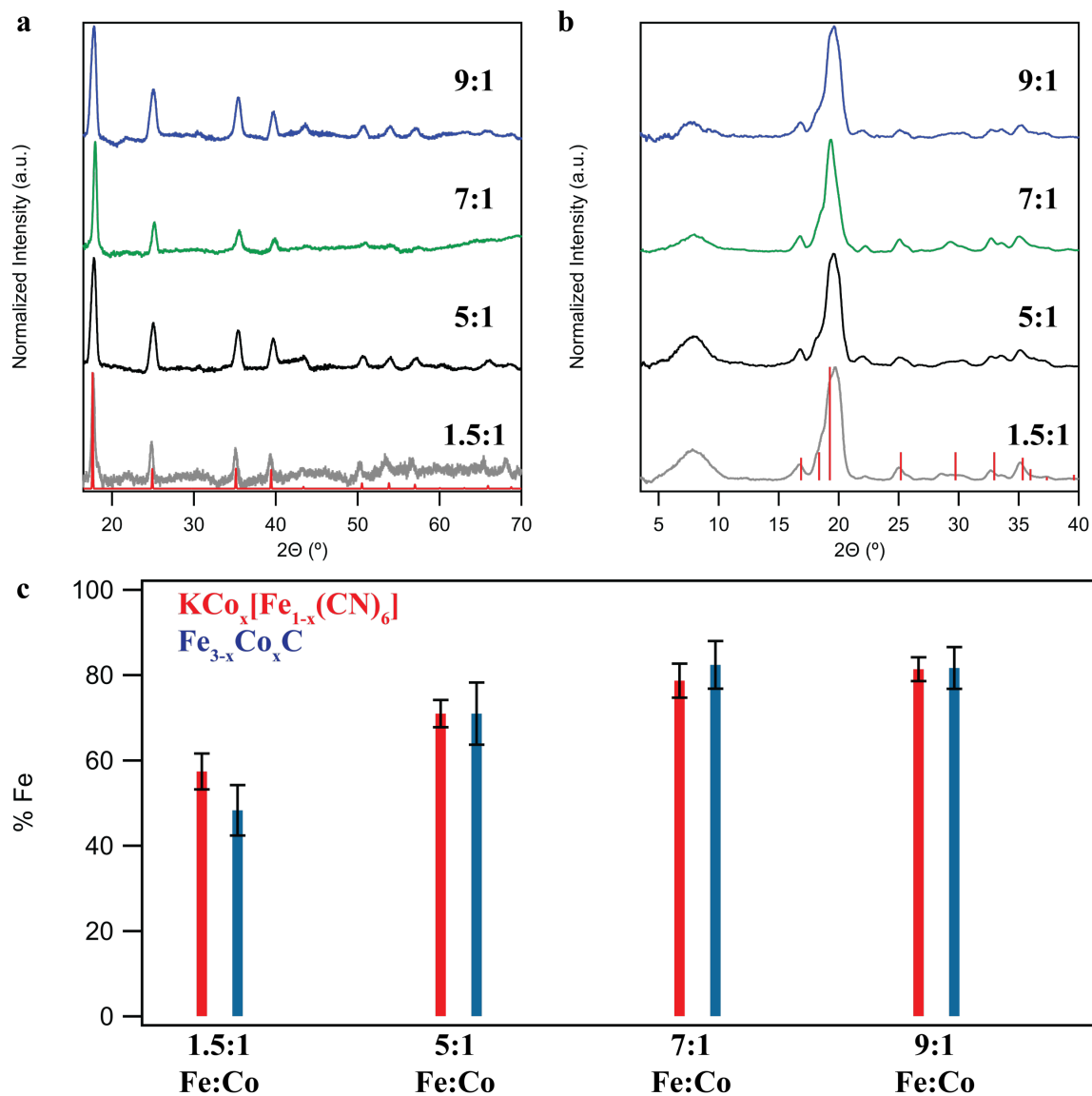
Figure 2.12. pXRD of a) PBA and b) $Fe_{3-x}Co_xC$ from PBA synthesis reactions containing 1.5:1, 5:1, 7:1, and 9:1, Fe:Co metal salts. C) ICP-MS data of the isolated PBAs and $Fe_{3-x}Co_xC$.

additional PBAs were isolated from reaction conditions with 9:1, 7:1, 5:1, and 1.5:1, Fe:Co. Following the reflux at 2h, isolation of the $Fe_{3-x}Co_xC$ metals were accomplished with elemental compositions similar to the precursor PBA (Figure 2.13). In Figure 2.14 the calculated lattice constant for the hexagonal $Fe_{3-x}Co_xC$ is shown, reflecting Vegard behavior for the nanocarbides.
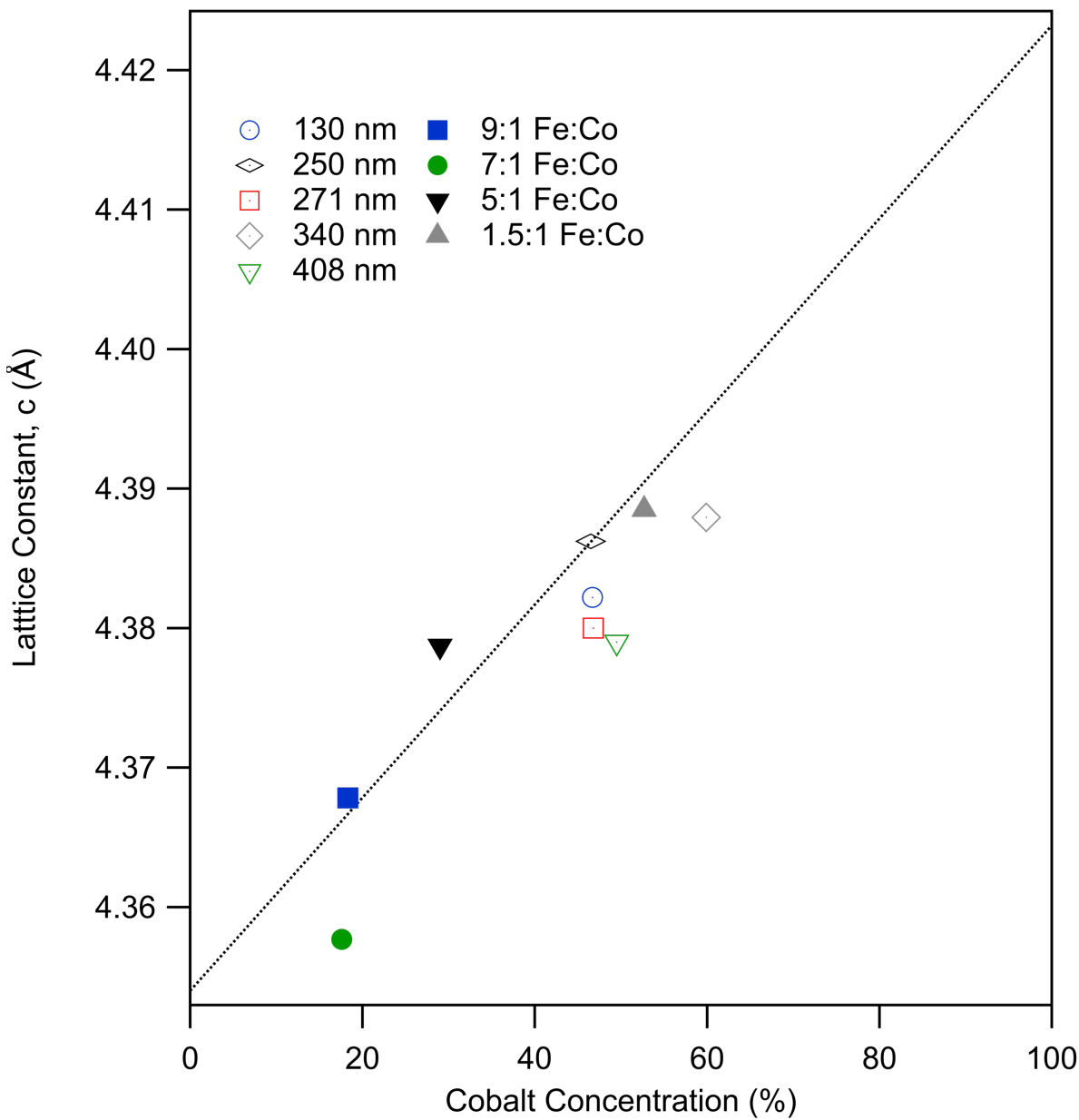
Figure 2.13. Calculated lattice constant, c, for the $Fe_{3-x}Co_xC$ where open symbols show the size dependent data whereas the shaded symbols illustrate the elemental composition-controlled samples. The observed shift of lattice constant implies alloying of the nanocarbides.

The observed error in the measurement is caused from the absence of an internal standard causing

minor changes in the pXRD reflections In the TEM images, it is worth noting that no foam
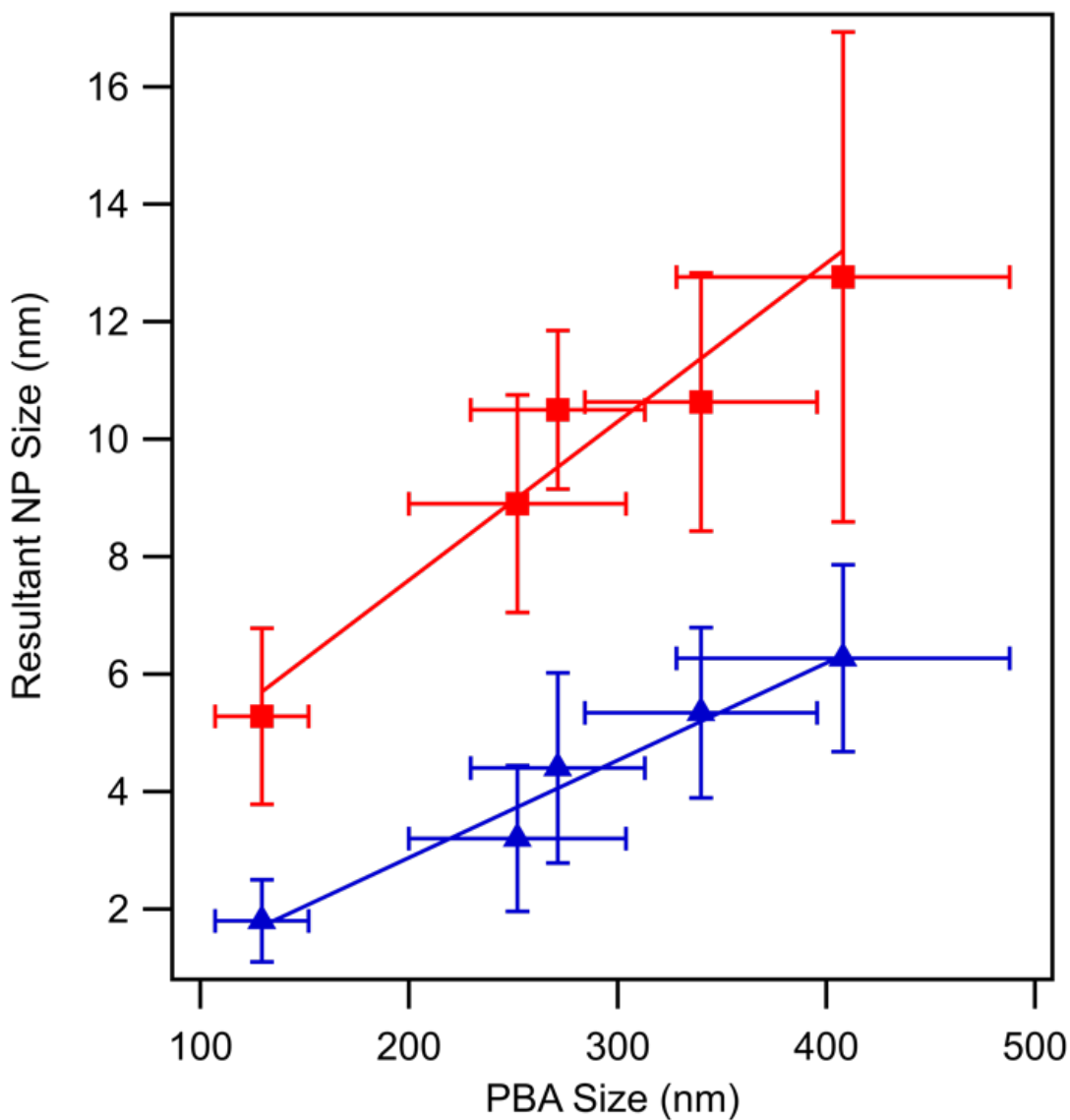
Figure 2.14. Linear relationship between $KCo_x[Fe_{2-x}(CN)_6]$ size and resultant nanoparticle size as determined from the electron microscopy images in Figure 2.11. The red squares represent the $Fe_{3-x}Co_xC$ nanoparticles while the blue triangles represent the $Fe_{2-x}Co_x$.

structures are observed at the two time points. Wider area SEM and TEM, and HR-TEM images are available in Figure 2.17-Figure 2.21.

The time and temperature dependent growth of the carbide and metal from the PBA can be more effectively analyzed by comparing the changes that occur in the FT-IR (Figure 2.24a), UV-

Table 2.3. Characterization of the $KCo_x[Fe_{2-x}(CN)_6]$, $Fe_{3-x}Co_xC$, and $Fe_{2-x}Co_x$ nanoparticles from electron microscopy images (Figure 3) and ICP-MS.

Material	129 nm PBA	252 nm PBA	271 nm PBA	341 nm PBA	408 nm PBA
$KCo_x[Fe_{2-x}(CN)_6]$ Size	129 ± 22	252 ± 52	271 ± 41	341 ± 56	408 ± 80
$KCo_x[Fe_{2-x}(CN)_6]$	39.8	42.5	45.6	43.2	44.4
% Fe (error)	(18.4%)	(4.3%)	(5.8%)	(7.4%)	(12.8%)
$Fe_{3-x}Co_xC$ Size (nm)	4.6 ± 1.5	8.3 ± 2.3	10.5 ± 1.4	10.9 ± 2.4	11.6 ± 2.6
$Fe_{3-x}Co_xC$	42.3	43.5	43.2	40.1	40.5
% Fe (error)	(12.7%)	(17.8%)	(14.3%)	(9.9%)	(17.7%)
$Fe_{2-x}Co_x$ Size (nm)	1.6 ± 0.5	3.2 ± 1.2	4.4 ± 0.9	5.3 ± 2.0	6.3 ± 2.2
$Fe_{2-x}Co_x$	48.9	39.0	48.7	39.4	41.5
% Fe (error)	(2.7%)	(5.7%)	(4.3%)	(5.5%)	(5.1%)
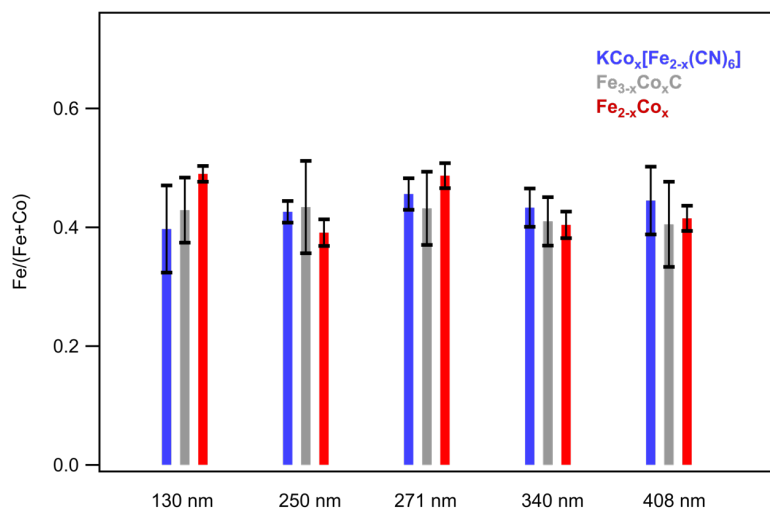
Figure 2.15. Elemental ratios determined by ICP-MS displaying percent iron in each sample. The blue traces indicate the $KCo_x[Fe_{2-x}(CN)_6]$, grey indicate $Fe_{3-x}Co_xC$, and red indicate $Fe_{2-x}Co_x$.
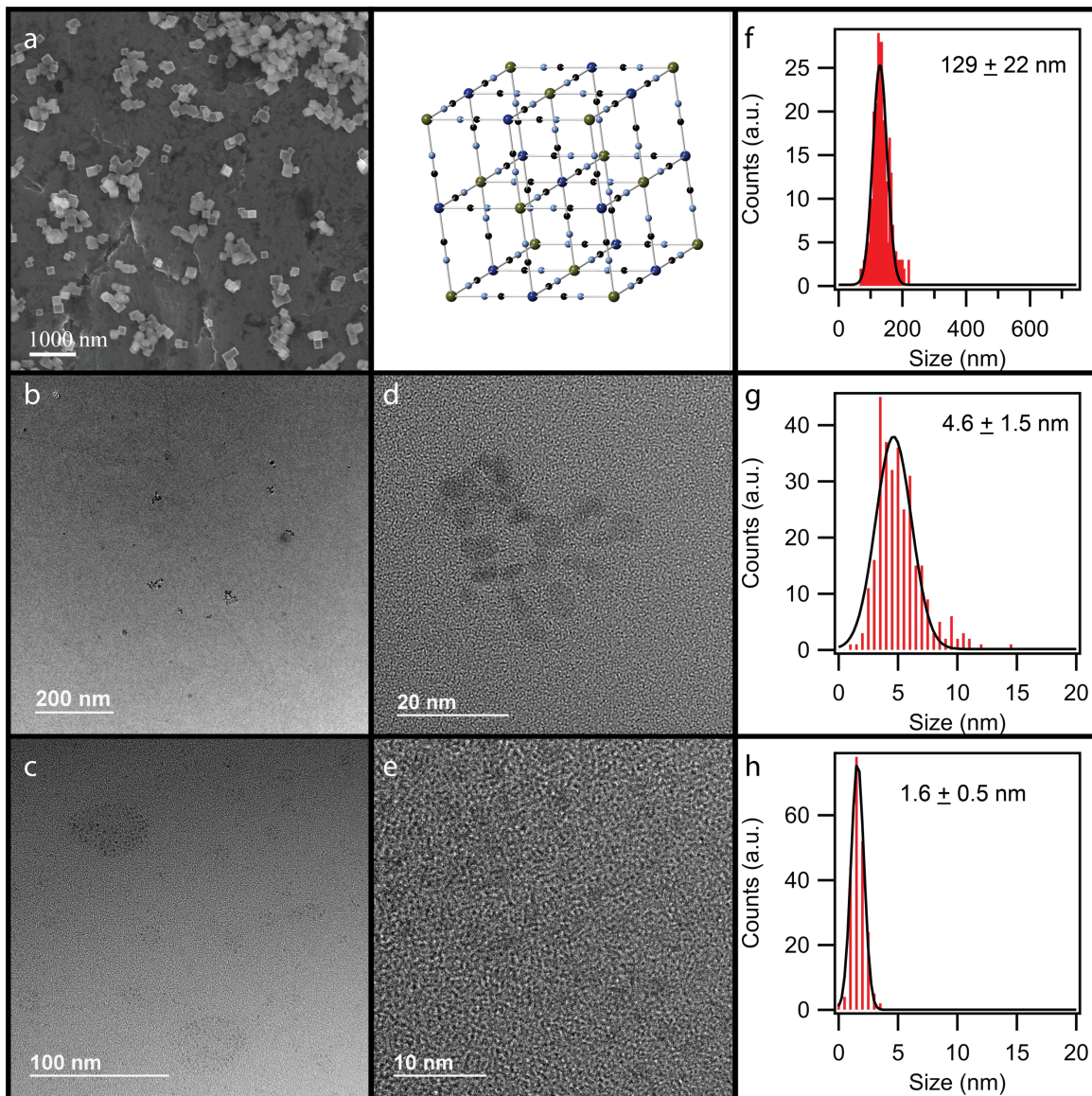
Figure 2.16. a) SEM image of the 129 nm $KCo_x[Fe_{2-x}(CN)6]$, b) low-resolution TEM image of the $Fe_{3-x}Co_xC$ from the 129 nm PBA, c) selected TEM image of the $Fe_{2-x}Co_x$ from the 129 nm PBA, d) high-resolution TEM image of $Fe_{3-x}Co_xC$, e) selected high-resolution TEM image of the $Fe_{2-x}Co_x$. Histograms and Gaussian fits for the f) $KCo_x[Fe_{2-x}(CN)6]$, g) $Fe_{3-x}Co_xC$, and h) $Fe_{2-x}Co_x$.
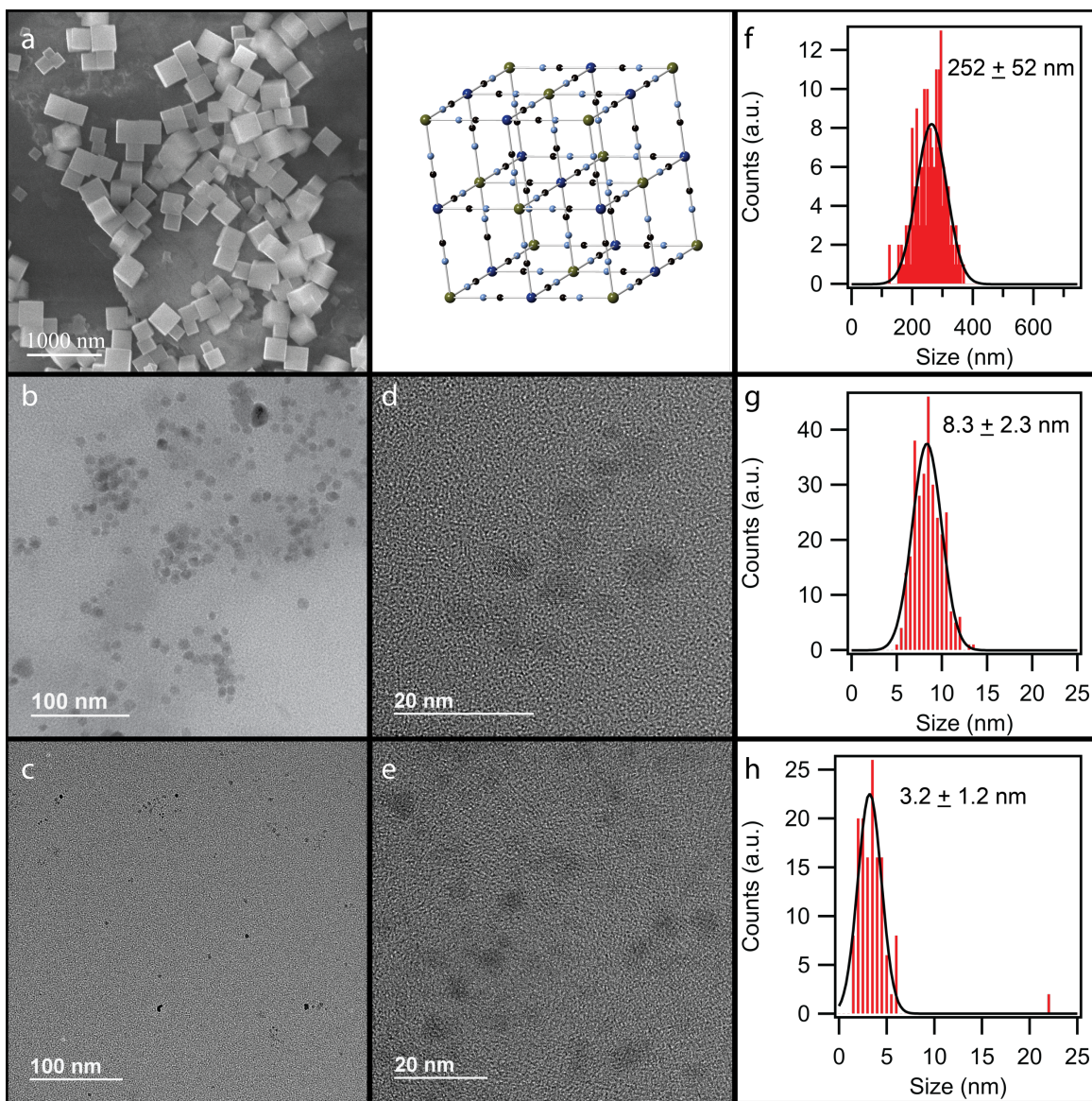
Figure 2.17. a) SEM image of the 252 nm $KCo_x[Fe_{2-x}(CN)6]$, b) low-resolution TEM image of the $Fe_{3-x}Co_xC$ from the 252 nm PBA, c) selected TEM image of the $Fe_{2-x}Co_x$ from the 252 nm PBA, d) high-resolution TEM image of $Fe_{3-x}Co_xC$, e) selected high-resolution TEM image of the $Fe_{2-x}Co_x$. Histograms and Gaussian fits for the f) $KCo_x[Fe_{2-x}(CN)6]$, g) $Fe_{3-x}Co_xC$, and h) $Fe_{2-x}Co_x$.

56
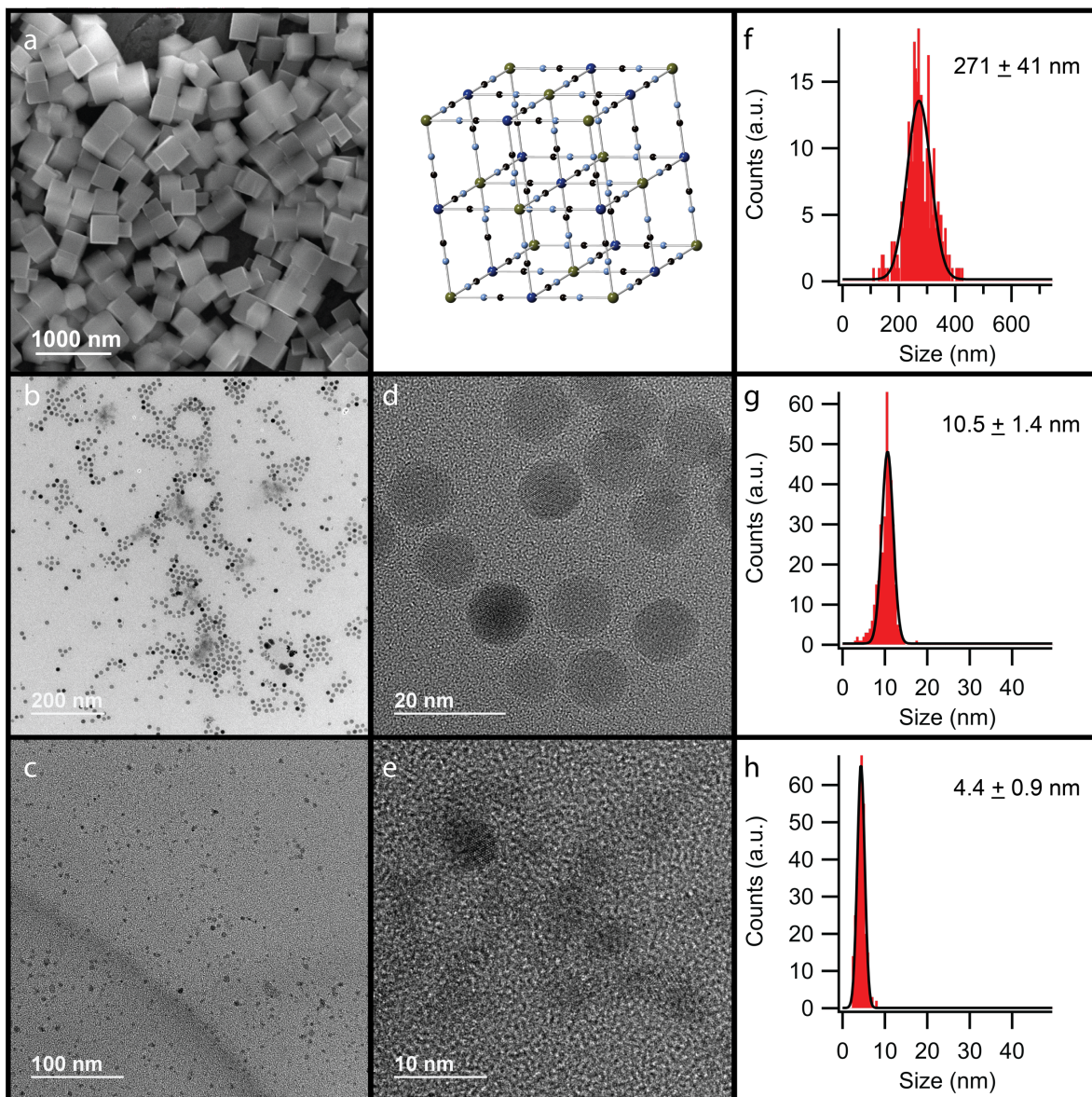
Figure 2.18. a) Selected SEM image of the 271 nm KCo$_{1.09}$[Fe$_{0.91}$(CN)$_6$], selected low-resolution TEM image of the b) Fe$_{1.30}$Co$_{1.70}$C and c) Fe$_{0.97}$Co$_{1.03}$. High-resolution TEM image of d) Fe$_{1.30}$Co$_{1.70}$C, and e) Fe$_{0.97}$Co$_{1.03}$. Histograms and Gaussian fits for the f) KCo$_{1.09}$[Fe$_{0.91}$(CN)$_6$], g) Fe$_{1.30}$Co$_{1.70}$C and h) Fe$_{0.97}$Co$_{1.03}$.
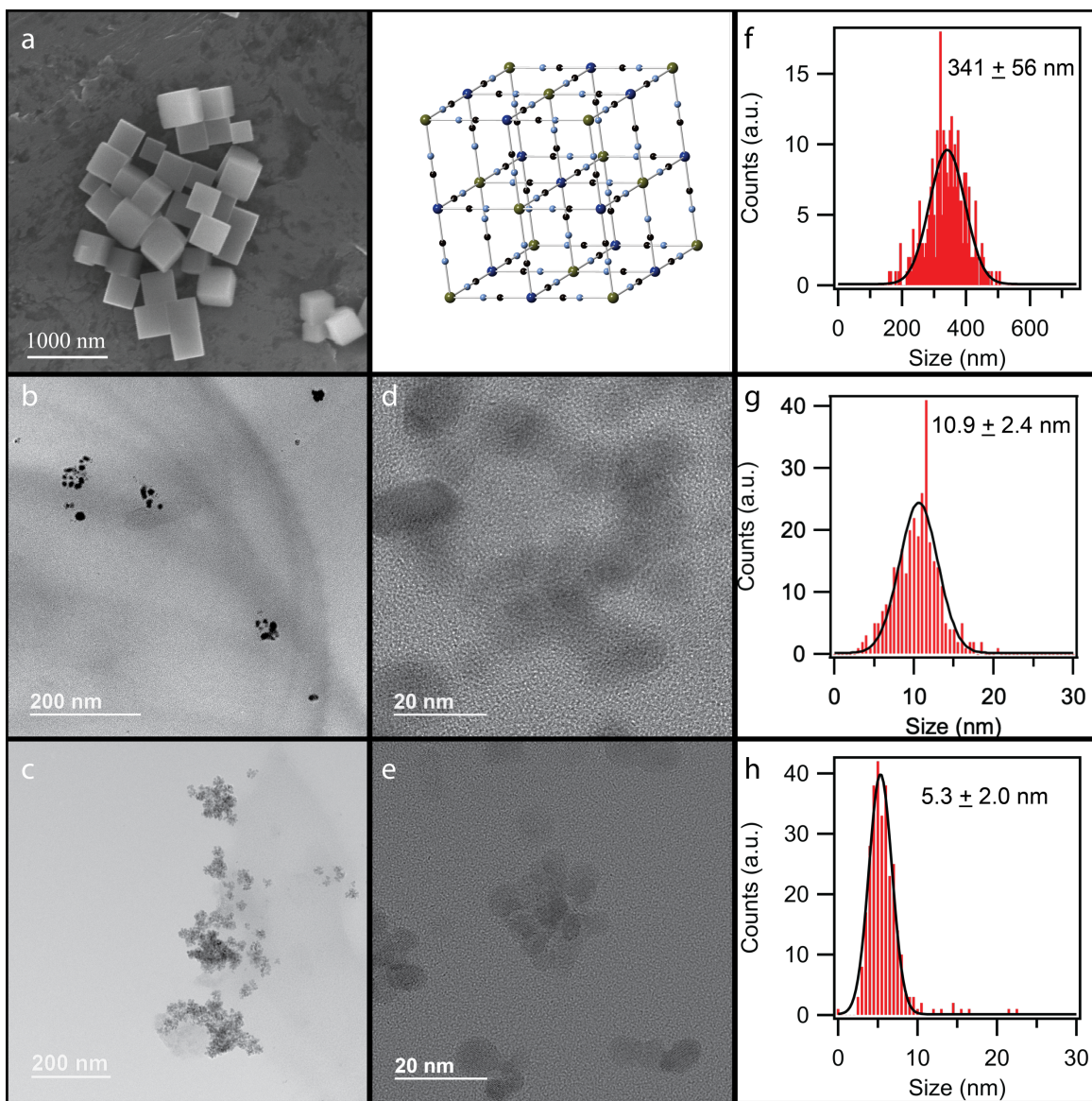
Figure 2.19. a) SEM image of the 341 nm $KCo_x[Fe_{2-x}(CN)6]$, b) low-resolution TEM image of the $Fe_{3-x}Co_xC$ from the 341 nm PBA, c) selected TEM image of the $Fe_{2-x}Co_x$ from the 341 nm PBA, d) high-resolution TEM image of $Fe_{3-x}Co_xC$, e) selected high-resolution TEM image of the $Fe_{2-x}Co_x$. Histograms and Gaussian fits for the f) $KCo_x[Fe_{2-x}(CN)6]$, g) $Fe_{3-x}Co_xC$, and h) $Fe_{2-x}Co_x$.
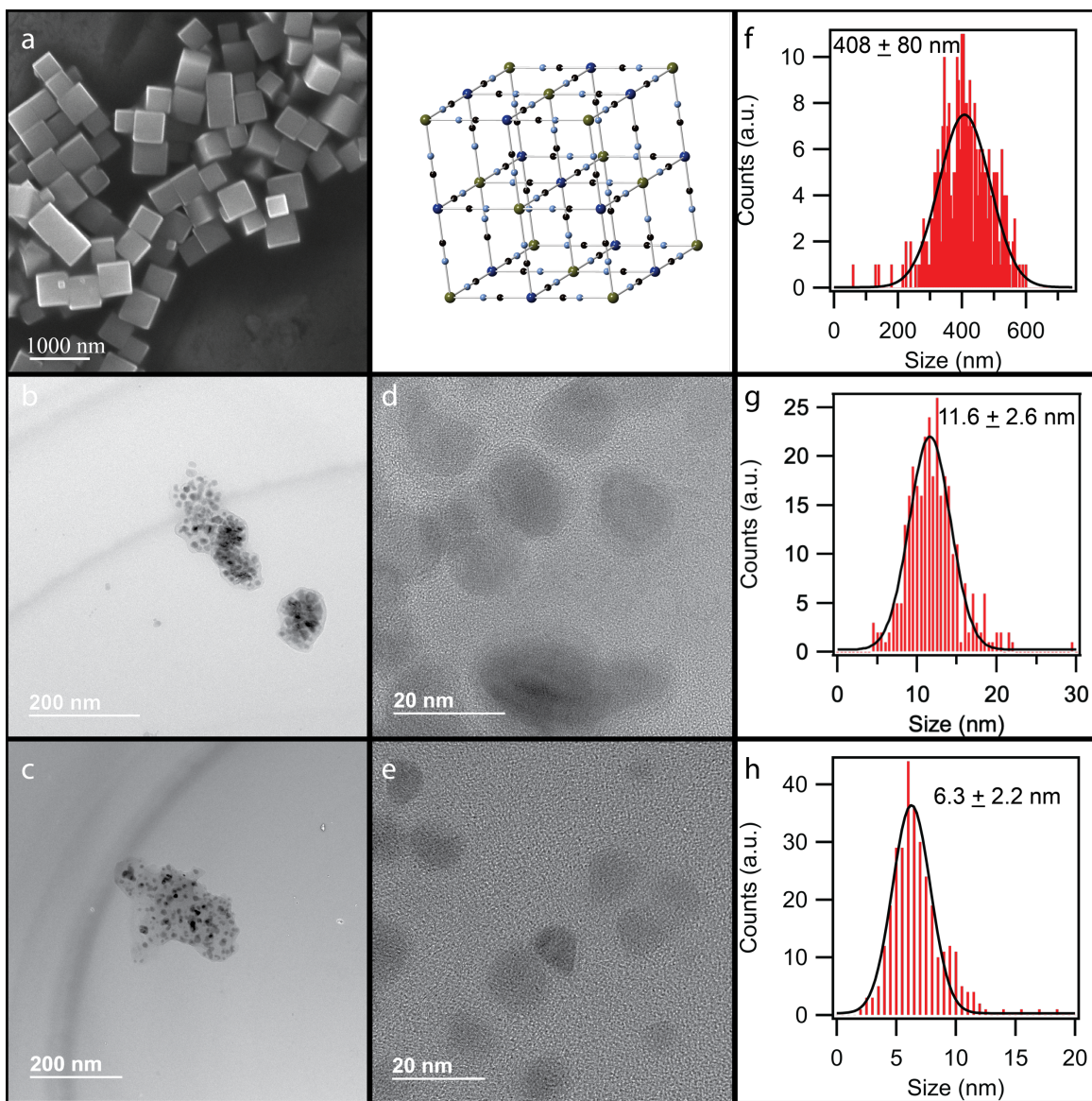
Figure 2.20. a) SEM image of the 408 nm KCo$_x$[Fe$_{2-x}$(CN)6], b) low-resolution TEM image of the Fe$_{3-x}$Co$_x$C from the 408 nm PBA, c) selected TEM image of the Fe$_{2-x}$Co$_x$ from the 408 nm PBA, d) high-resolution TEM image of Fe$_{3-x}$Co$_x$C, e) selected high-resolution TEM image of the Fe$_{2-x}$Co$_x$. Histograms and Gaussian fits for the f) KCo$_x$[Fe$_{2-x}$(CN)6], g) Fe$_{3-x}$Co$_x$C, and h) Fe$_{2-x}$Co$_x$.
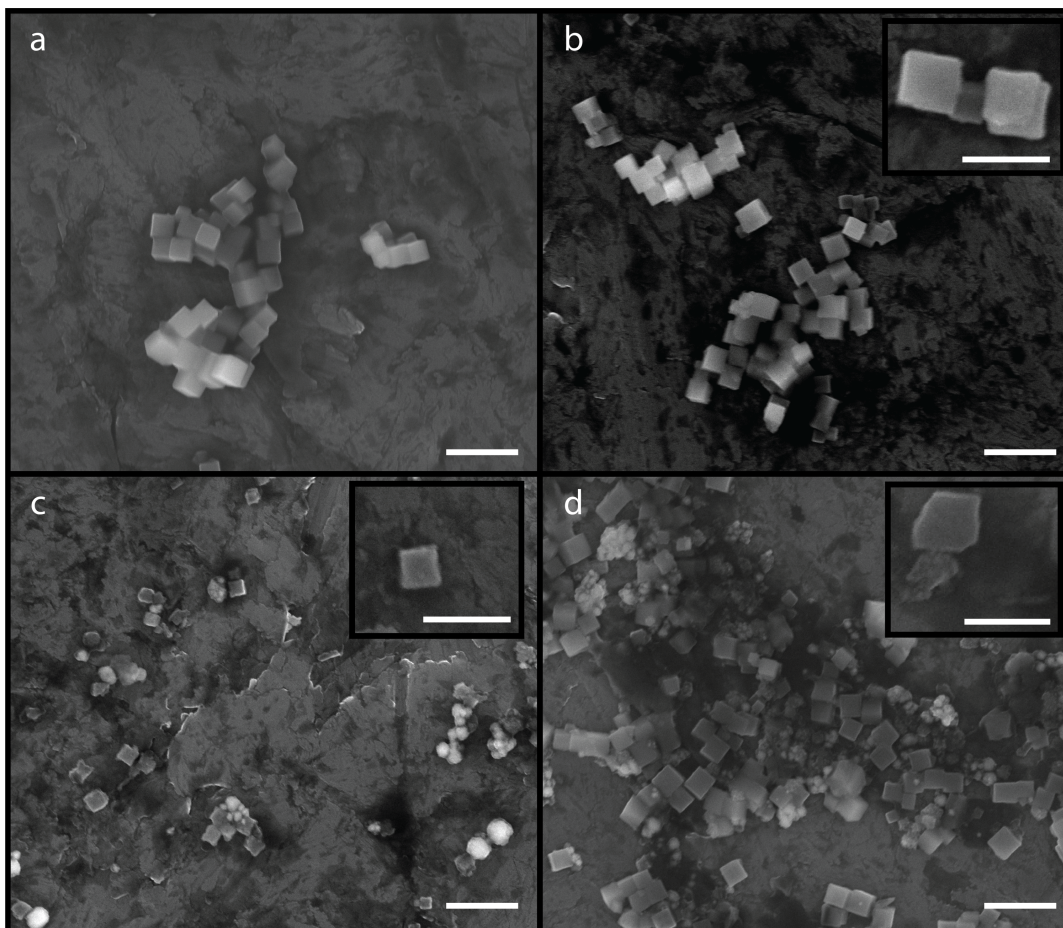
Figure 2.21. SEM images of reaction aliquots taken at 350 °C at a) 0 min, b) 15 min, c) 30 min, and d) 60 min. The scale bars for the main figures are 1,000 nm while the insets in Figures SI 5b, c, and d, are 500 nm.

Vis (Figure 2.24b), and EM (Figure 2.23 and Figure 2.24c) during the reaction. For the reaction held at 50 °C for 1h, changes in the metal oxidation state are evidenced by the loss the 2159 cm^{-1} (Fe^{III} –CN–Co^{II}) and the appearance of a 2120 cm^{-1} (Fe^{II} –CN–Co^{III}) and a 2090 cm^{-1} (Fe^{II} –CN–Co^{II}) cyanide stretches.[156, 157] No changes in the absorption data is observed and analysis of the TEM fringe d-spacing (d$_{(200)}$ = 5.0 Å) confirms the *Fm*-3*m* (LT) phase is maintained. When the reaction is heated to 350 °C, SEM images aliquots of the reaction mixture at t = 0 min (Figure 2.22) reveal no visible external morphology changes to the PBA occur; however, in TEM (Figure 2.23f-h) striations (contrast difference) appear with a width of 7.3 ± 3.0 nm. The striations grow
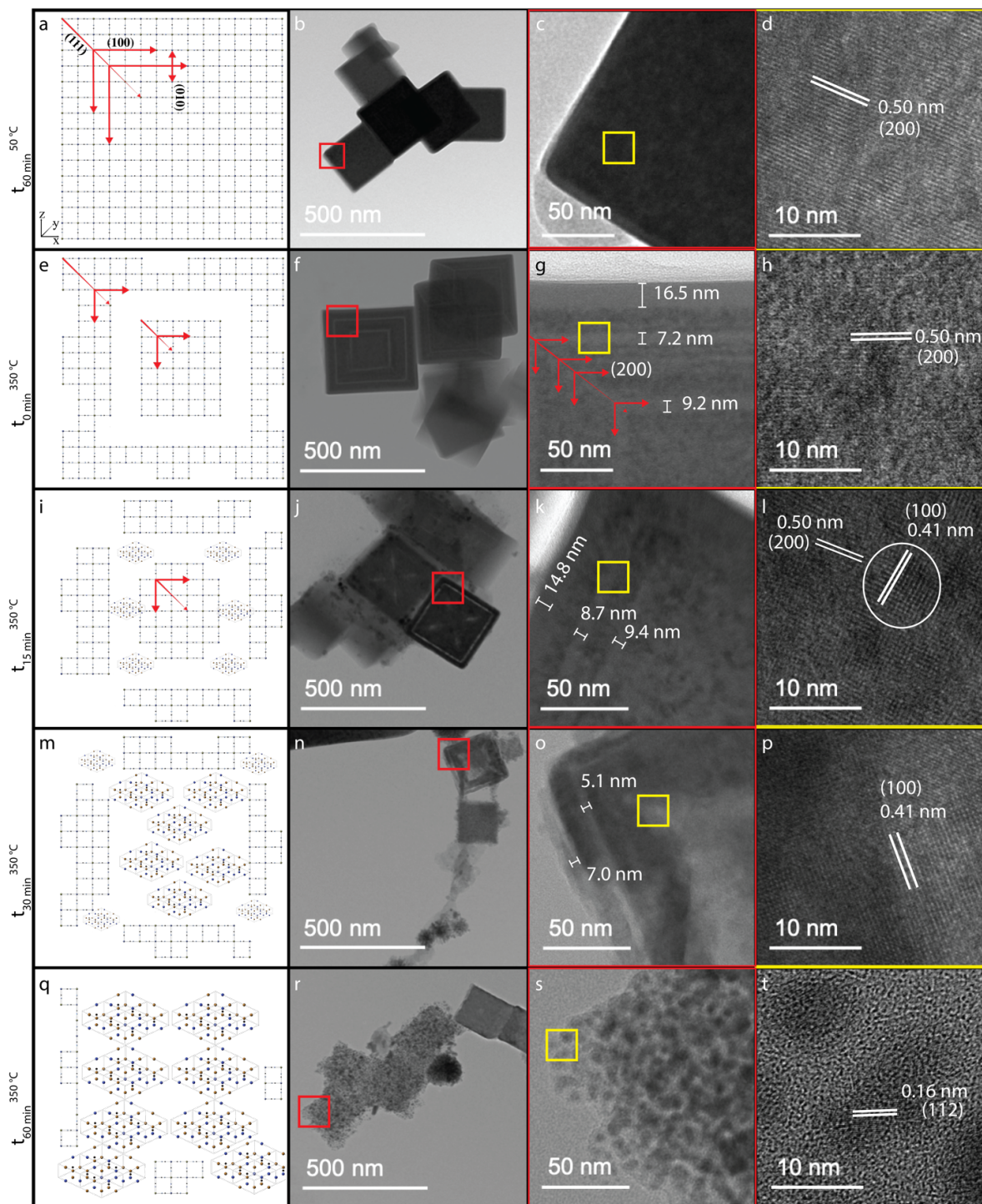
Figure 2.22. Time-dependent TEM images and the proposed PBA changes indicating direction of etching during the interconversion process. The reaction aliquots are drawn after 60 min at 50 °C (b-e), 0 min (f-h) 15 min (j-l), 30 min (n-p), and 60 min (r-t) at 350 °C. The image magnifications from left to right are (40,000x; 400,000x; and 1,000,000x). Images a ,e, i ,m and q are schematic representations at the specified time points.

61
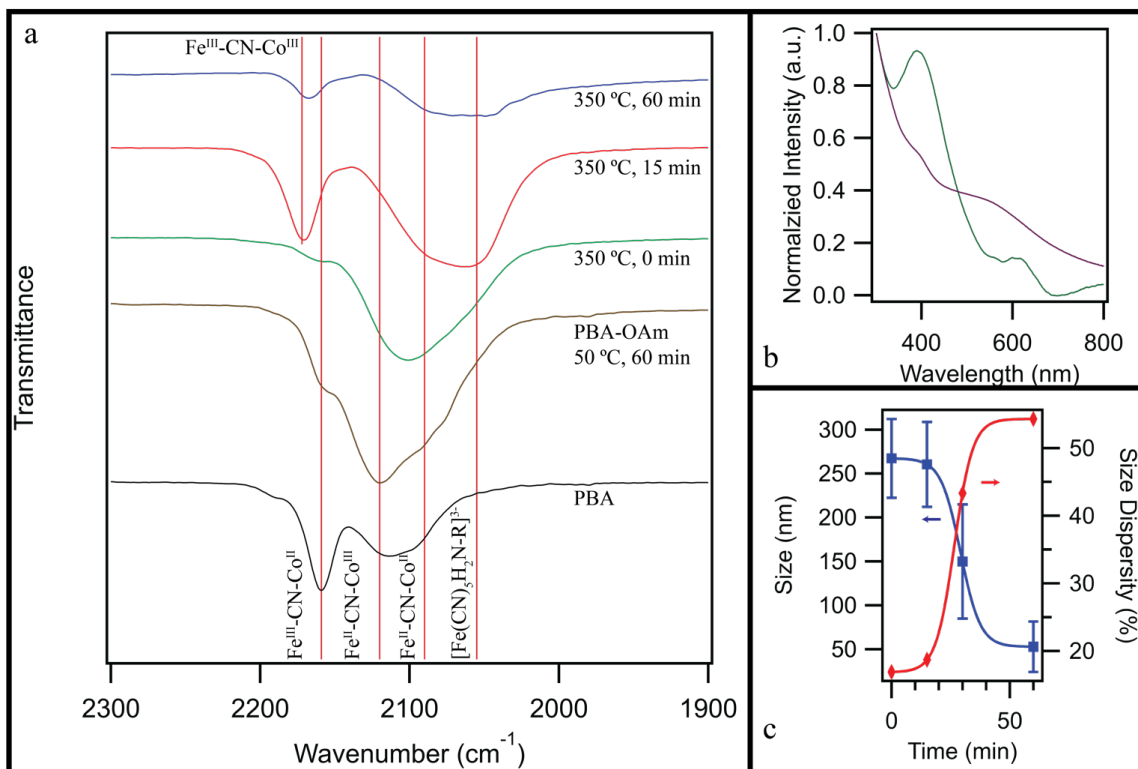
Figure 2.23. a) Time-dependent change in size and size distributions of the PBAs (blue squares) taken from SEM and the size dispersities (%, red diamonds) fit to sigmoidal curve, b) FT-IR of the ν_{CN} taken on the as-prepared (black), OAm exchanged (60 min at 50 ºC, orange), 0 min (green), 15 min (red), and 60 min (blue) at 350 °C ramped at 15 ºC/min. c) UV-Vis absorption of the as synthesized PBA (purple) (Fe^{III}-CN-Co^{II}) before being oxidized to Fe^{III}-CN-Co^{III} (green).

along the [111] and the <200> directions (indicated by the red arrows). High-resolution TEM d-space analysis allows both regions (dark and light) to be assigned to the 200) plane of the *Fm-3m* (Figure 2.23h). The striation is therefore believed to reflect redistribution of the iron and cobalt metal cyanide complexes within the PBA.

At 15 min, SEM imaging reveals that the PBA begins to decrease in size with increased size distribution (Figure 2.24a and Figure 2.22b) and morphology changes at the {111} corners and {110} edges of the PBA cube. The striation width increases to 7.9 ± 2.6 nm and can still be assigned to the (200) of the cubic *Fm-3m* phase. The morphology changes imply OAm assisted
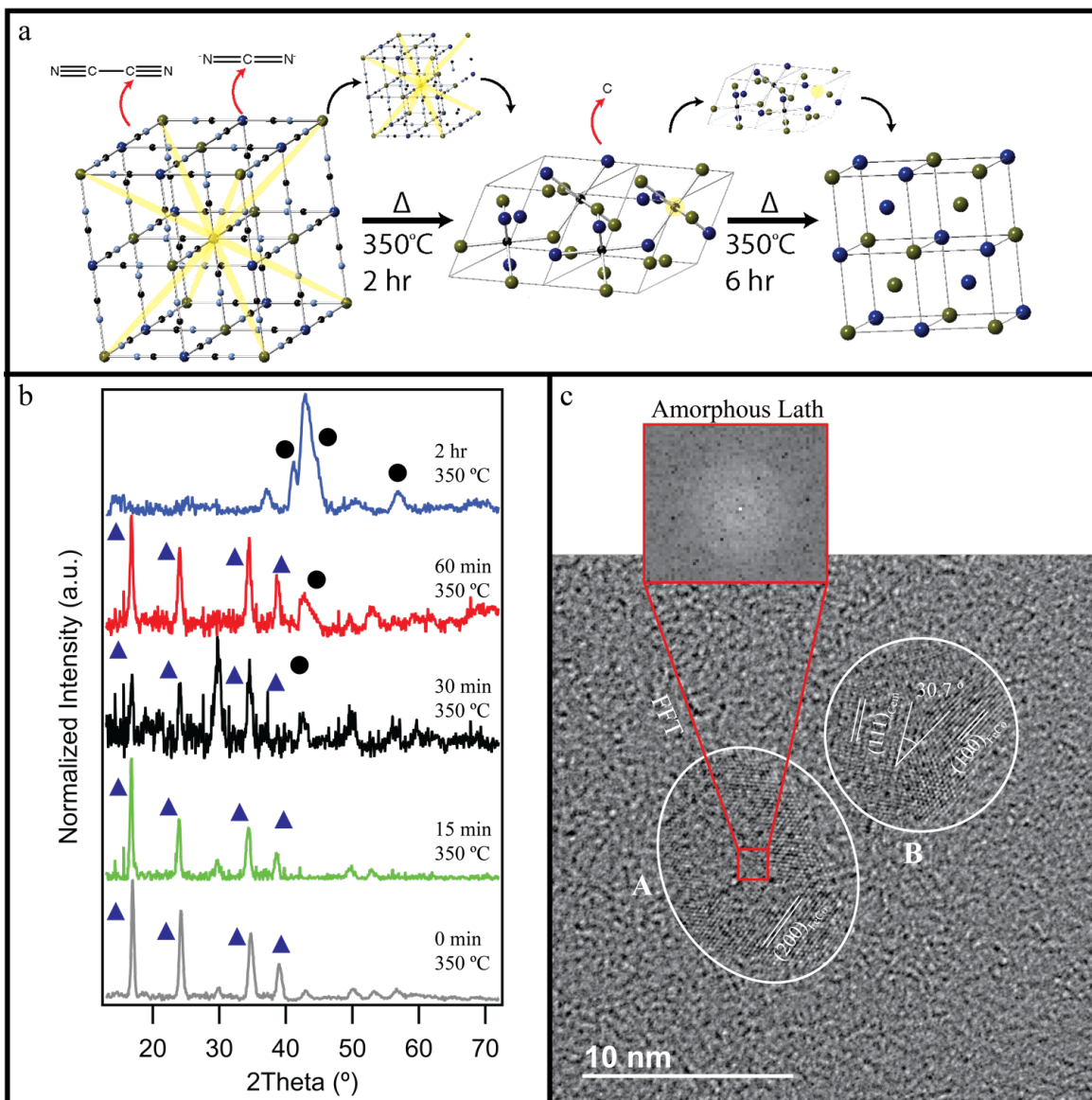
Figure 2.24. a) Proposed interconversion of a $K[Fe_{2-x}Co_x(CN)_6]$ to $Fe_{3-x}Co_xC$, and $Fe_{2-x}Co_x$ nanoparticles. b) pXRD patterns on aliquots isolated during the first 2h of reaction. The blue triangles indicate PBA lattice reflections and the black circles indicate carbide reflections. c) High-resolution TEM images catching the phase transformation to ferrite from cementite. Particle A exhibits FeCo lattice planes indexable to the (200) and an amorphous lath as evidenced by FFT of the region. Particle B shows the FeCo (100) phase nucleating at 30.7 ° to the (111) of the $Fe_{3-x}Co_xC$.

redistribution of the metal ions in the PBA lattice. The changes are coupled to the appearance of

small nanocrystals within the EM images at times > 15 min. In addition to the morphological

changes, the solution transitions from maroon to green color due to the loss of the intervalence

charge transfer band at 638 nm in the UV-Vis absorption data (Figure 2.24b). The FT-IR spectra exhibits two new cyanide stretches at 2055 cm^{-1} and 2172 cm^{-1}. The 2172 cm^{-1} is assigned to the Berlin green analogue, Fe^{III}-CN-Co^{III}, accounting for the loss of the intervalence charge transfer band[156] and the 2055 cm^{-1} feature is assigned to formation of $[Fe^{II}(CN)_5(RNH_2)]^{3-}$ species following oleylamine coordination.[158]

At t = 30 min, loss of PBA coupled to increased nanocrystal formation is evidenced in the data. The FT-IR spectra exhibits a reduction of the intensity for the cyanide stretches concurrent with the appearance of the metal carbide nanocrystal in the pXRD. In the EM imaging (Figure 2.23n- p), increased striation density and increased width of the striation is observed that is accompanied with the appearance of metal carbide nanocrystals. The pXRD patterns broaden indicative of loss of long-range order in the PBA and likely reflects nucleation and growth of carbide nanocrystals within the striation regions of the PBA, although the carbide phase cannot be definitively assigned in the pXRD. High resolution TEM d-spacing analysis conform that at t > 30 min, the PBA is polycrystalline with contributions from the metal carbide ($d_{(100)}$) and the PBA ($d_{(200)}$). The size of the carbide particles is 8.1 + 2.3, and the mean channel width is determined to be 10.4 + 3.1 nm.

As the reaction progresses to completion, the pXRD data can be assigned to a mixed PBA and metal carbide pattern at 1h, and by 2h the powder XRD confirm complete conversion of the PBA to the Fe$_{1.30}$Co$_{1.70}$C (Fiugre 2.25b). TEM images ((200) plane of the *Fm-3m* (Figure2.23h) reveal loss of the striation patterning and formation of a cube-like foam structure, with hundreds of smaller embedded particles. With longer reaction times, the nanocrystal foam structure fragments into individual nanocrystals as observed in Figure 2.11. The distribution of the smaller particles is 8.0 + 2.8 nm and HR-TEM allows assignment as the (112) lattice plane at 0.16 nm for
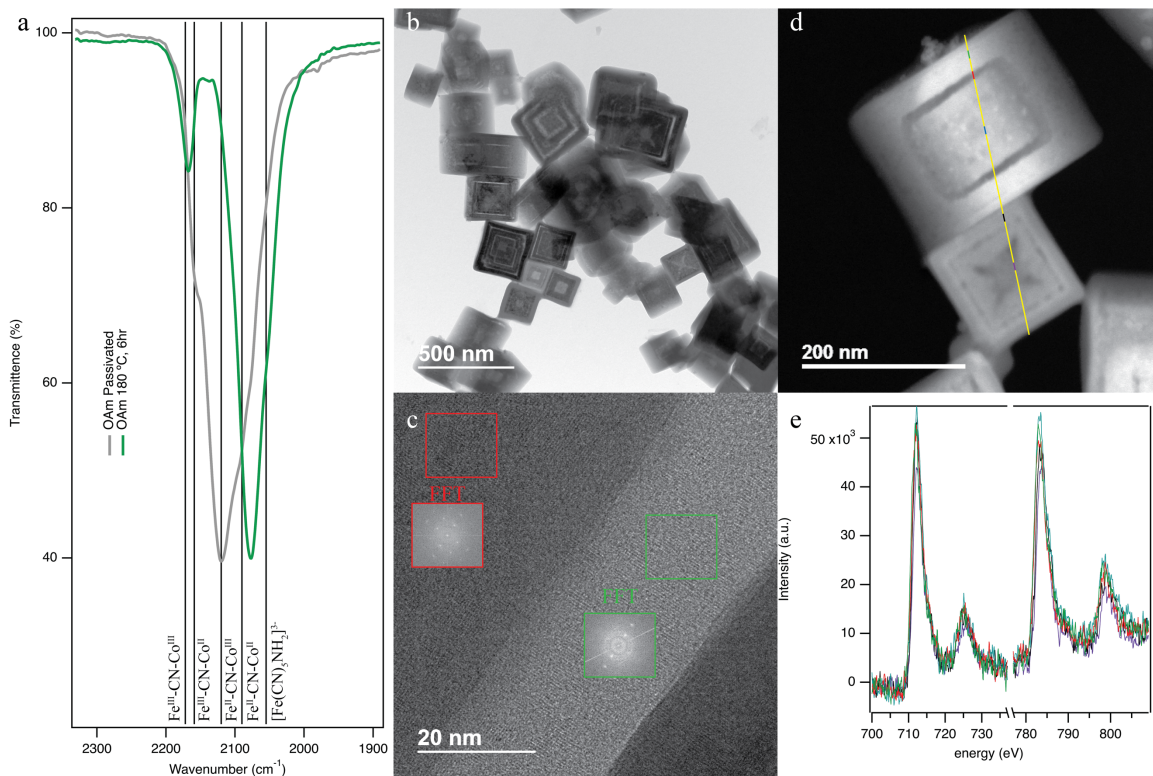
Figure 2.25. Characterization of a PBA heated to 180 ºC in OAm for 6h. a) FT-IR characterization of the M-CN stretch showing the weakened M-C bond at 2074 cm^{-1}, evident in the orthorhombic structure. Bright field TEM image (b) and high resolution TEM image showing the FFT of the light and dark regions; both regions are assigned to the orthorhombic structure. e) Dark field TEM image of a PBA cube where the yellow line represents the EELS line scan and f) data from the EELS line scan where the color of the trace represents the area from the line scan.

$Fe_{1.30}Co_{1.70}C$. No contribution from the bimetallic phase is observed within 2h. Confirming conversion of the PBA to the metal carbide, the FT-IR data at 2h exhibits only OAm features with no –CN mode observable in the spectra. Within experimental limitation, analysis of the supernatant FT-IR and UV-Vis reveal no metal cyanide coordination complexes are present. At times greater than 2h the reaction converts the metal carbide to the metal (Figure 2.11) with no change in the iron to cobalt metal ratio. The linear relationship between PBA size and metal nanocrystal is maintained (Figure 2.15).
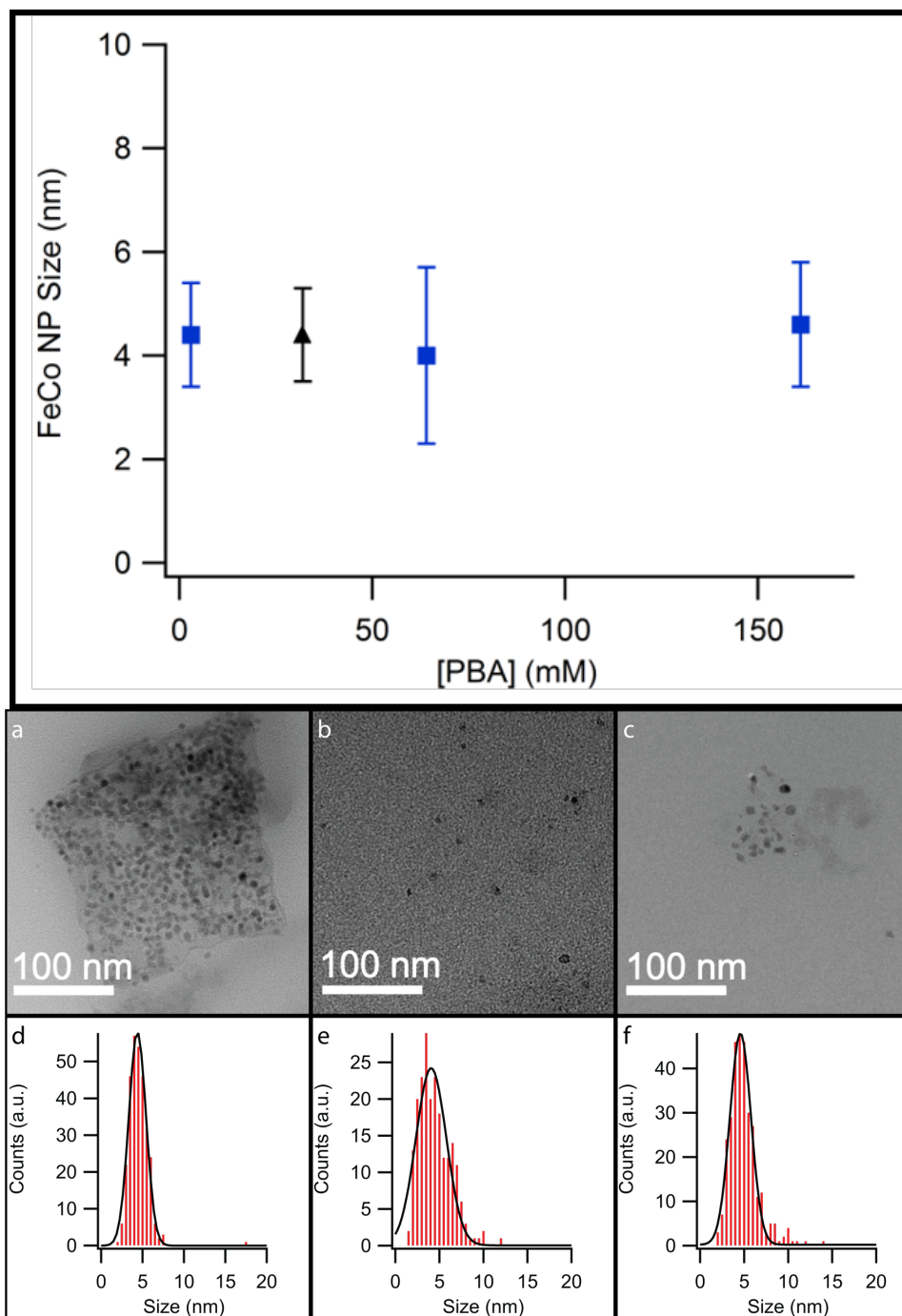
Figure 2.26. Reaction concentration *vs.* resultant nanoparticle size. Black triangle is the original collapse at 32 mM and the blue squares are collapses at 3, 64, and 161 mM. TEM images of a) 3 mM collapse, b) 64 mM collapse, and c) 161 mM collapse and accompanying histograms in d) 3mM, e) 64 mM, and f) 161 mM. Statistics were generated by analyzing >300 particles.

The data demonstrates that use of oleylamine as a solvent is critical for isolating discrete sized nanocrystals of the metal carbide and metal. The appearance and growth of the striations within the first hour of the reaction suggests that OAm is etching into the PBA along the (200) and (111) facets which can be achieved at temperatures as low as 180 °C. The etching process enhances the formation of the metal carbide through the recrystallization on the walls of the PBA. Electron energy loss spectrum (EELS) line cans across the striations for a PBA held at 180 °C for 6h (Figure 2.26), shows a reduced signal in the light contrast areas. This observation is consistent with the OAm assisted metal depletion. In support of the recrystallization process rather than complete dissociation, the line scan shows the iron to cobalt metal ratio remains constant throughout the PBA. Han, *et al.*[62] observed a similar behavior in $Ni_3[Co(CN)_6]_2$, where ammonia etching leads to controlled pore-size and pore-width within the isolated meso-PBA. The data supports a model where oleylamine acts not only to lower the barrier for conversion but also as a coordinating solvent to disperse the materials following the conversion.

2.3.5 Mechanistic Insight.

The transition from PBA to carbide is surprisingly controlled as this requires nucleation and growth of the carbide following small molecule release. The observation of the foam structures for the carbide suggest the process likely involves a templated surface mediation nucleation. An alternate mechanism would be complete dissociation of the metal precursors followed by nucleation, a metal cyanide concentration dependent mechanism. To evaluate this possibility, the effect of PBA concentration in oleylamine was analyzed for a 259 ± 50 nm (20% size dispersity) PBA held at 350 °C for 6h. In Figure 2.27it can be seen that no concentration dependence is observed for reactions carried out at 3 mM, 64 mM, and 161 mM PBA dissolved in oleylamine. The isolated nanocrystals from the concentration dependent study are 4.4 ± 1.0 nm (23%
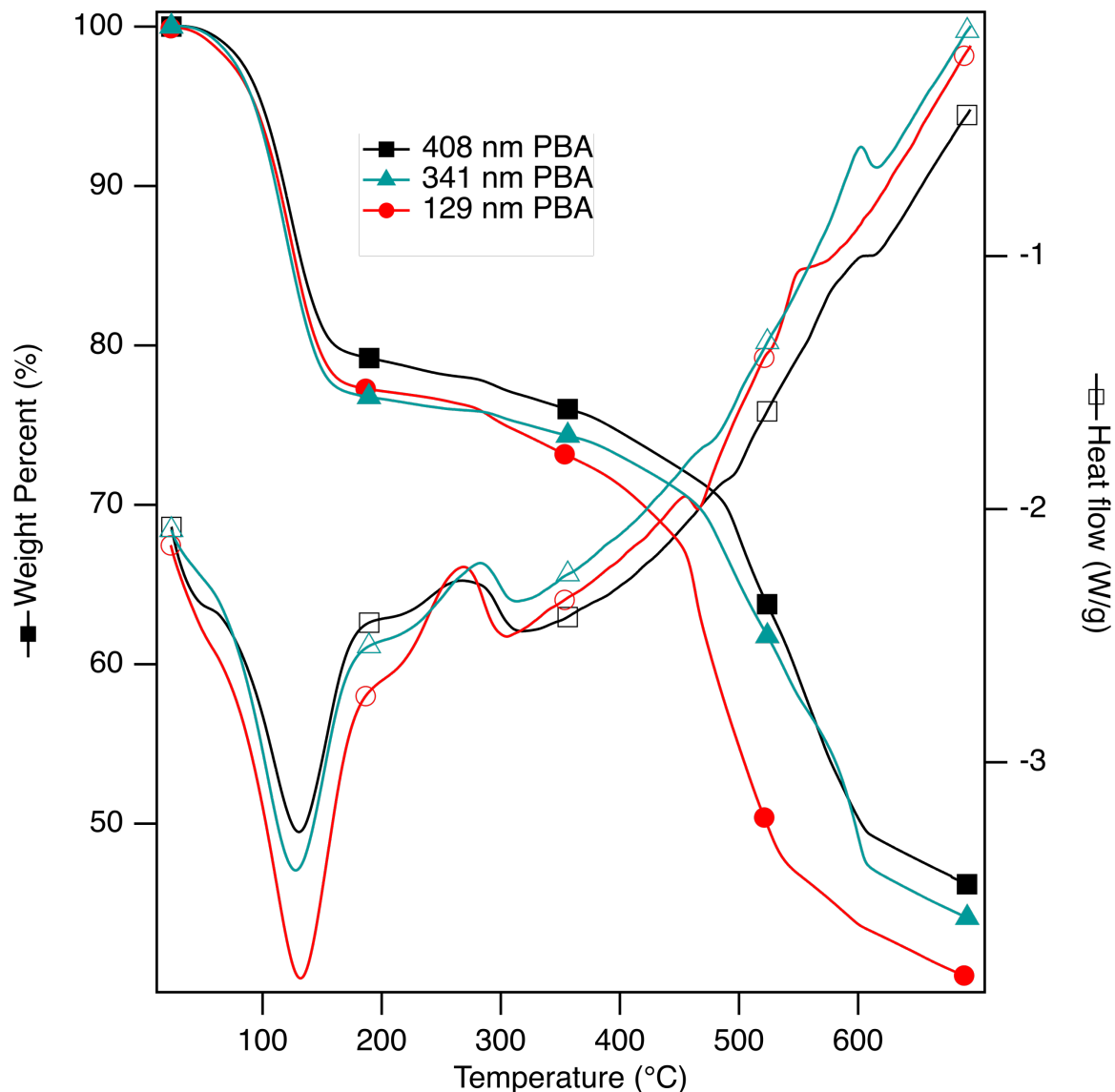
Figure 2.27. DSC-TGA measurements of a 129 ± 22 (red), 341 ± 56 (blue), and 408 ± 80 nm (black) KCo$_x$[Fe$_{2-x}$(CN)$_6$] Prussian blue analogues. The samples were heated under Ar at 10 ºC/min.

dispersity), 4.0 ± 1.7 (42% dispersity) and 4.6 ± 1.2 nm (26% dispersity), respectively. The results of the study are inconsistent with a simple dissolution and re-nucleation process, suggesting the template process is more likely.

The mechanism for PBA → metal carbide → metal is shown in Figure 2.25a. In this mechanism the PBA converts completely to the metal carbide nanocrystal during the first 2h. The formation of the carbide is believed to be initiated by the first order phase transition (cubic to

orthorhombic) observed in the TGA-DSC and *in-situ* XRD data, following lattice dehydration. The orthorhombic phase exhibits canted cyanide bridging ligands, thus reducing orbital overlap and the energetic barrier for metal cyano derivative release. Recrystallization of the metal cyano complexes on the walls of the PBA is consistent with the observation of the metal carbide foam with the macroscopic dimensions of the PBA. The size of the nanometal carbide scaling linearly with the PBA size is surprising but may relate to density of intrinsic metal cyanide vacancies that are occupied by water molecules within the crystal lattice. Metal vacancies are known in the PBA literature to charge balance the lattice for up to 1/3 of the M^{3+} sites.[65, 159] The metal cyanide vacancies can be thought of as a T-defect in the lattice leading to plastic deformation and lowering of the barrier for metal carbide formation. This observation is supported by the lowering of the phase transition temperature for the cubic to orthorhombic transition in TGA-DSC data (Figure 2.27).

The conversion of the carbide to metal after 2h of reaction occurs *via* a kinetically slow but thermodynamically favorable carbon migration to the nanoparticle surface, due to the carbide becoming hypoeutectic. The process is described by the Pitsch-Petch mechanism, and is anticipated to form lamellar sheets of ferrite and cementite in the nanocrystal with the ferrite phase growing ~59 ° to the cementite phase.[160] Consistent with the metallurgic process, the isolated nanocrystals at 3h exhibit two distinct particles in the TEM imaging (Figure 2.25c). Particle A has a crystalline and amorphous area. The crystalline area is indexable to the (111) plane of the $Fe_{0.97}Co_{1.03}$ phase at 1.46 Å. The amorphous zone at the center is attributed to lath formation following the decomposition of lamella cementite sheets. In particle B, the bcc-$Fe_{0.97}Co_{1.03}$ nanoparticle is observed to be nucleating on the $Fe_{1.30}Co_{1.70}C$ phase at 30.7°. Indexing the lattice planes allows assignment of the (111) for $Fe_{1.30}Co_{1.70}C$ at 2.09 Å and the (110) for $Fe_{0.97}Co_{1.03}$ at

2.01 Å. It is worth noting the cementite to ferrite transformation is still debated in the engineering literature and therefore, while the data fits a Pitsch-Petch process, alternate mechanisms cannot be definitively excluded.[161, 162]

2.4 Conclusion.

The experimental observation that solvent dispersible, size-controlled metal carbide nanocrystals can be isolated, while maintaining the metal ratios, following a thermal decomposition reaction of PBA is intriguing. The formation of the metal from the carbide follows classical metallurgic pathways *via* a kinetically slow carbon diffusion process,[163-166] as defined by the Pitsch-Petch relationships.[167-169] The ability to isolate high surface area metal carbides are important in catalysis, where the experimental results provide a convenient strategy to form foam like mesostructures or size-controlled nanocrystals that are potential catalyst candidates. While the isolation of metal carbide and metallic phases have been previously reported by solid state thermal decomposition routes, the ability to isolate both nanocrystal compositions and define the mechanistic attributes of the reaction when carried out lyothermally has not been reported.[137-139] Although catalysis was not investigated in this manuscript, demonstration that controlled PBA decomposition can lead to size, shape and metal ion ratio controlled metal carbide (and metal) formation provides a convenient pathway for new catalyst development. Further studies are underway to evaluate the catalytic potential of the iron-cobalt systems. The route is scalable and since a wide range of PBAs can be grown as narrow dispersity mesocrystals *(meso-PBA)*, it is believed the route offers a rich playground for materials design.[63, 64]

CHAPTER 3

BREAKING LATVA'S RULE BY ENERGY HOPPING IN A Tb(III):ZnAl$_2$O$_4$ NANOSPINEL

Latva's empirical rule states that the energy separation between a molecular sensitizer and a lanthanide excited state must lie within 2,000 to 4,000 cm^{-1} for optimal energy transfer. At energies below 2,000 cm^{-1}, back energy transfer will impact the process resulting in the reduction the photoluminescence quantum yield (PLQY). The role of excited triplet state ($^3\pi^*$) energy and intra-lanthanide ion energy hopping is assessed for a series of β-diketonate molecular sensitizers coordinated to the surface of a 2 nm 3.56% Tb(III):ZnAl$_2$O$_4$ nanospinel. It is observed that energy transfer from the β-diketonate to a 2 nm nanospinel lies within the critical radii for energy transfer and the presence of efficient energy hopping minimizes back energy transfer contributions. In contradiction to Latva's rule, the highest PLQY of 41% is achieved following sensitization by hexafluoroacetylacetonate, with an energy difference ($^3\pi^*$-^{5}D$_4$) of only 1,670 cm^{-1}. The measured PLQY is consistent with other reports of Tb(III) doped nanocrystal hosts lattices, suggesting energy hopping within the lattice enhances the Tb(III) phosphor performance. Although not measured, the energy gap plot suggests a PLQY approaching 58% may be achievable by ligand design.

3.1 Introduction.

In solid state lighting (SSL) the use of trivalent lanthanide ions, Ln(III), is common due to the high color rendering factors generated from their narrow full width half max (FWHM) emission features.[29, 30, 88, 89, 91] This allows for precise control over CIE coordinates by combining lanthanide ions to achieve white light or display technologies.[82, 91, 170, 171] Since the lanthanides

exhibit low molar extinction coefficients due to the optical selection rules, SSL applications requires the sensitization of Ln(III) by the host lattice or an appended molecular sensitizer to efficiently populate the lanthanide ion.[88, 89, 91] Our group previously observed, the efficient ligand sensitization of Eu(III) doped oxide hosts leading to enhanced photoluminescence quantum yield and the ability to use near-visible excitation wavelengths for down-shifting LED technologies.[29, 30] Other researchers have followed up on the idea showing efficient molecular sensitization in nanocrystal lattices.[172-175] To produce high PLQY nanophosphors the molecular sensitizer passivation layer must have sufficient orbital overlap, minimal radial separation between the donor and acceptor, low back energy transfer pathways, and lack low lying host trap states.[88, 90, 91, 117]

An approach to predict the optimum orbital overlap for sensitization in the nanophosphor can stem from the early reports of Latva, *et al.*[176] on Ln(III) coordination compounds. 'Latva's Rule' was defined by his conclusion that the highest sensitization efficiency from the molecular antenna to the Ln(III) ion occurs when the $^3\pi^*$ energy is between 2,000 and 4,000 cm^{-1} above the lanthanide excited state. Latva's rule suggests the maximum energy transfer sensitization is a balance between energy matching, directly related to the spectral overlap,<J>, and back energy transfer processes. Since the report of Latva,[176] several studies have supported the rule in coordination compounds,[110, 111, 177] yet it has not been translated to nanocrystalline phosphors where Ln(III)-Ln(III) hopping may occur.

To date much of the nanocrystal phosphor development has focused on Eu(III),[29, 30, 170, 178-180] a classic red emitter used commercially in fluorescent light applications.[181, 182] For lanthanides, Tb(III) is an important green emitter that is sensitive to self-quenching and site of occupation in the host,[88, 89] but has received less attention in the nanocrystal phosphor field. In this study, we evaluate the efficiency of energy transfer from an organic molecular sensitizer appended to the

surface of a 2 nm 3.56% Tb(III):ZnAl$_2$O$_4$ nanospinel. In order to evaluate the role of energy difference on the PLQY, a series of molecular sensitizing passivating ligands were bound to the surface of the Tb(III):ZnAl$_2$O$_4$ nanospinel. The ligands were chosen to have triplet energies between 22,170 - 25710 cm^{-1}, resulting in energy differences of 1,670 - 5210 cm^{-1} above the ^{5}D$_4$ excited state of Tb(III). A linear relationship between the $^3\pi^*$ and ^{5}D$_4$ energy levels was observed, with the highest quantum yield (41%) achieved for heaxfluoroacetylacetonate (hfacac) ($^3\pi^*$ 22,170 cm^{-1}, $\Delta E = 1,670$ cm^{-1}). A low lying midgap trap center associated with the host lattice is populated when the $^3\pi^*$ energy level is above 23,000 cm^{-1}. By comparison, the measured PLQY achieved in Tb(III):ZnAl$_2$O$_4$ nanospinel phosphors is at the level of the highest reported PLQY for direct host excitation of Tb incorporation into nanocrystal hosts, where values from 0.03%[183] to 43%[184] have been reported.

It is notable that a higher PLQY is observed for a smaller energy gap than predicted by Latva's rule where it was reported that significant back energy transfer contributions occurs with energy separations below 2,000 cm^{-1}.[176] It is hypothesized that Tb(III)-Tb(III) hopping within the 2 nm nanospinel reduces the contribution of back energy transfer. Contributions arising from the possibility of passivant changes to the Tb(III) center was discounted by analyzing the site sensitive ^{5}D$_4 \rightarrow {}^7$F$_6$ *vs.* ^{5}D$_4 \rightarrow {}^7$F$_5$ intensities, where no change in the blue to green ratio is observed for the different passivation group. The energy difference plot suggests the higher PLQY may be achievable at smaller triplet energy separations. The results of the study demonstrate that Latva's rule is modified by site hopping within the nanophosphor, illustrating the importance of careful passivant design to achieve the highest PLQY devices for down-shifting phosphors.

3.2 Experimental.

3.2.1 Materials.

All commercially available reagents and solvents, with the exception of dimethylformamide (DMF) were used without further purification. DMF was dried over molecular sieves. The passivating ligands was 2,4-pentanedione (acac, Alfa Aesar, 98%), 2,2,6,6-tetramethyl-3,5-heptanedione (TMHD, Alfa Aesar, 98%), 6,6,7,7,8,8,8-heptafluoro-2,2-dimethyl-3,5-octanedione (FOD, Strem Chemicals, ≥ 98%), 1,1,1-trifluoroacetylacetone (tfacac, Alfa Aesar, 98%), and 1,1,1,5,5,5-hexafluoro-2,4-pentanedione (hfacac, Alfa Aesar, 98+%). Zinc (II) undecylenate (Spectrum, 98%), oleylamine (Aldrich, 70%), nitrossium tetrafluoroborate (NOBF$_4$, Alfar Aesar, 98%), aluminum (III) 2, 4-pentanedionate (Strem Chemicals, 99%), and terbium (III) 2,4-pentanedionate hydrate (Alfa Aesar, 99.9%) were obtained from various sources.

Synthesis of 3.56% Tb(III):ZnAl$_2$O$_4$: Zinc aluminate nanospinels were synthesized by thermal decomposition of molecular precursors. Zinc undecylenate (Zn(UND)$_2$, 0.25 mmol), aluminum 2,4-pentanedionate (Al(acac)$_3$, 0.5 mmol), and terbium(III) 2,4-pentanedionate (Tb(acac)$_3$) were charged into a 10mL pyrex microwave vial with olyelamine (70% Tech grade, sigma). The reactions were heated to 280 °C for 10 minutes in an Anton Paar MW reactor and cooled with forced air cooling. The resultant nanoparticles were isolated by addition of MeOH and centrifugation. Samples were dried under reduced pressure.

3.2.2 Measurements.

Structural characterization was performed using powder X-ray diffraction (pXRD) recorded on a Rigaku DMAX 300 Ultima III Powder X-ray diffractometer (using Cu K$_\alpha$ λ = 1.5418 Å radiation). The size of the nanocrystals were measured by fitting the pXRD pattern to the Scherrer broadening equation, $L = K\lambda/\beta cos\theta$, where L is the crystallite size, K is the shape factor and assumed to be

1.0 corresponding to spherical nanocrystals, λ is the X-ray wavelength measured in nm, β is the peak width at half height at a given 2θ value, and θ is the Bragg angle. Transmission electron microscopy (TEM, JOEL, 200kV) was performed to analyze particle sizes and distributions. Samples were prepared by drop casting a dispersion of nanoparticles in toluene on a 200 mesh Au grid and dried overnight. Elemental concentrations were measured by inductively coupled plasma-mass spectrometry (ICP-MS, Thermofischer) by digesting nanoparticles in trace grade HNO_3.

3.2.3 Optical Methods.

Ligand passivation was analyzed by Fourier transform infrared (FT-IR) measured on powdered samples using a PerkinElmer Spectrum 100 FT-IR Spectrometer equipped with an attenuated total reflectance (ATR) sample chamber consisting of a ZnSe crystal over coated with diamond using a single-bounce configuration. Solution UV-Vis absorption spectra were recorded in toluene using a 1 cm quartz cuvette in a Varian Cary 50 UV-Vis spectrometer. The photoluminescence and photoluminescence excitation spectra were recorded on a Horiba Fluoromax spectrofluorimeter equipped with a 150 W CW Ozone free xenon arc lamp, Czerny-Turner monochromators with excitation grating blazed at 330 nm (1200 groove/mm) and the emission grating blazed at 500 nm (1200 grooves/mm). All spectra were corrected for the instrument response function and the intensity of the lamp. Photoluminescence quantum yield were measured by the relative method using Eu(TTA)₃Phen as a standard in EtOH. Linear regressions were generated by plotting the integrated intensity *vs.* the absorption of serial dilutions. Comparison of the slopes between the standard and the sample, allow for determination of accurate PLQYs displayed in equation (3):

$$\Phi_s = \Phi_r \left(\frac{m_s}{m_r}\right) \left(\frac{\eta_s^2}{\eta_r^2}\right) \tag{3}$$
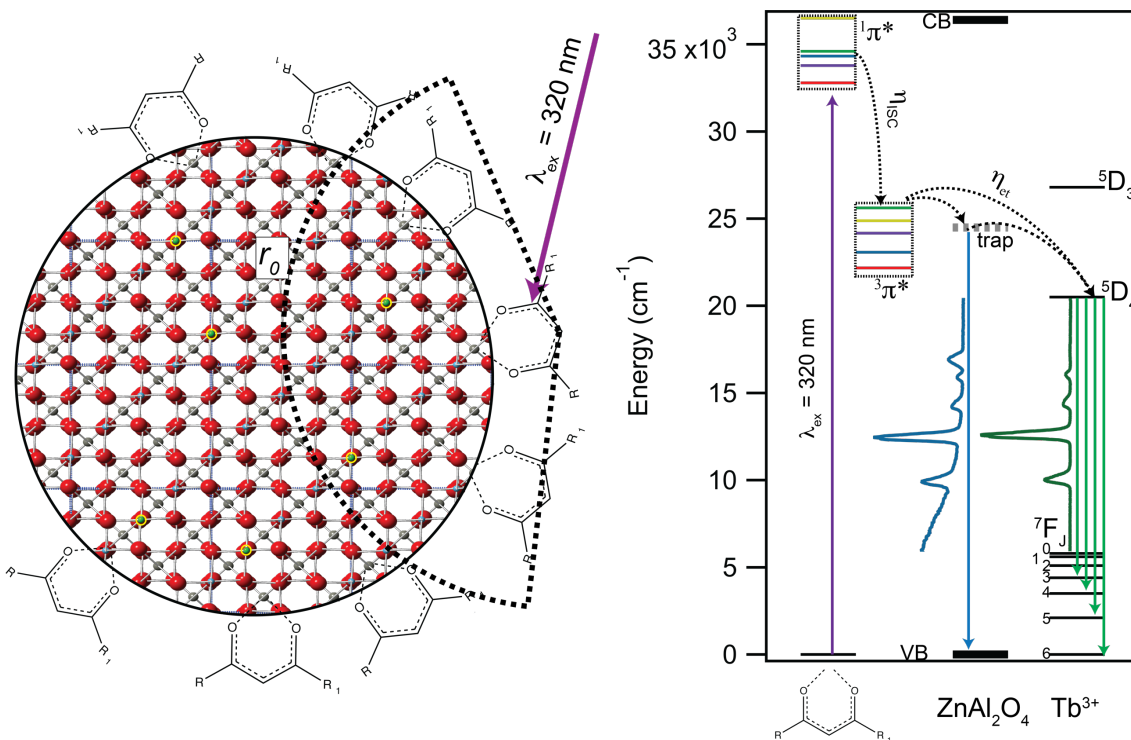
Figure 3.1. Schematic illustrating the sensitization of the surface passivated β–diketoantes with Tb(III) occupation (highlighted in yellow at the Al(III) site. In the schematic the arc represents the critical radii for energy transfer from the passivant to the Tb(III) center. The energy transfer and excited state relaxation pathways following excitation onto the $^1\pi^*$ excited state of the coordinating passivant are shown in a Jablonski diagram to the right. The energies for the $^1\pi^*$ and $^3\pi^*$ excited states are represented in the diagram by the color of the ligand where red is hfacac, blue is tfacac, purple is FOD, yellow is acac, and green is TMHD. The lattice energy levels are also drawn to scale where the dashed grey line represents the midgap trap state arising from V_{ox} defects.

Where m is the slope and η is the refractive index of the solvent. Subscripts r indicate the reference while s indicates the sample. The standard and samples were measured in EtOH at 298 K leading to the removal of the refractive index term.

Lifetime measurements were recorded on an Edinburgh Instruments LP980-KS and excited by a Continuum Nd:YAG laser coupled to an optical parametric oscillator with the resulting excitation wavelength of 320 nm. Samples were recorded in EtOH at 298 K so that radiative rates could be calculated. Lifetimes were fit to a mono-exponential equation using IGOR 8.0.

3.3 Results and Discussion.

In Figure 3.1, the $^3\pi^*$ energies for a series of β-diketonate passivants relative the Tb(III) exited state energy levels, the energy pathways for populating the Tb(III) emissive center following excitation of the passivant layer, and a schematic of the 2 nm β-diketonate passivated Tb(III):ZnAl$_2$O$_4$ spherical nanocrystal is shown. In the study, the ~2 nm spherical, β-diketonate passivated 3.56% Tb(III):ZnAl$_2$O$_4$ nanopsinel was prepared *via* a microwave assisted thermal decomposition of molecular precursors, as described previously.[2] The passivant exchange process is accomplished by employing a ligand exchange protocol developed my Murray *et al.*[185] where NOBF$_4$ removes the native OAm and acac ligands resulting in NO coordination to the nanospinel surface. Exchange of the NO for the β-diketonate of choice is accomplished by addition of a stochiometric amount of the free β-diketonate ligand to the NO-ZnAl$_2$O$_4$ nanospinel in a biphasic solution of toluene (or acetone) and DMF at 60 °C. The exchanged nanospinel is isolated by co-solvent precipitation and centrifugation following dropwise addition of polar solvents (water or MeOH) to the DMF mixture.

In Figure 3.3, the UV-Vis absorption spectrum and FT-IR or the β-diketonate exchanged Tb:ZnAl$_2$O$_4$ nanospinel are shown. In Figure 3.3a, absorption spectrum represents contributions from the $^1\pi$-π^* transition energies of the ligand. Following ligand exchange, the -CH$_2$/-CH$_3$ vibrational modes are still observable in the FT-IR spectra indicating only ~80% exchange of the native ligands is achieved, consistent with earlier reports.[185] Complete removal of native OAm is not required since it is optically inactive at the excitation wavelength of the β-diketonates. Evidence for β-diketonate coordination is evident in the FT-IR data, where the ketone stretch is observed to shift to higher frequency consistent with M-O bonding. All ketone stretches of free
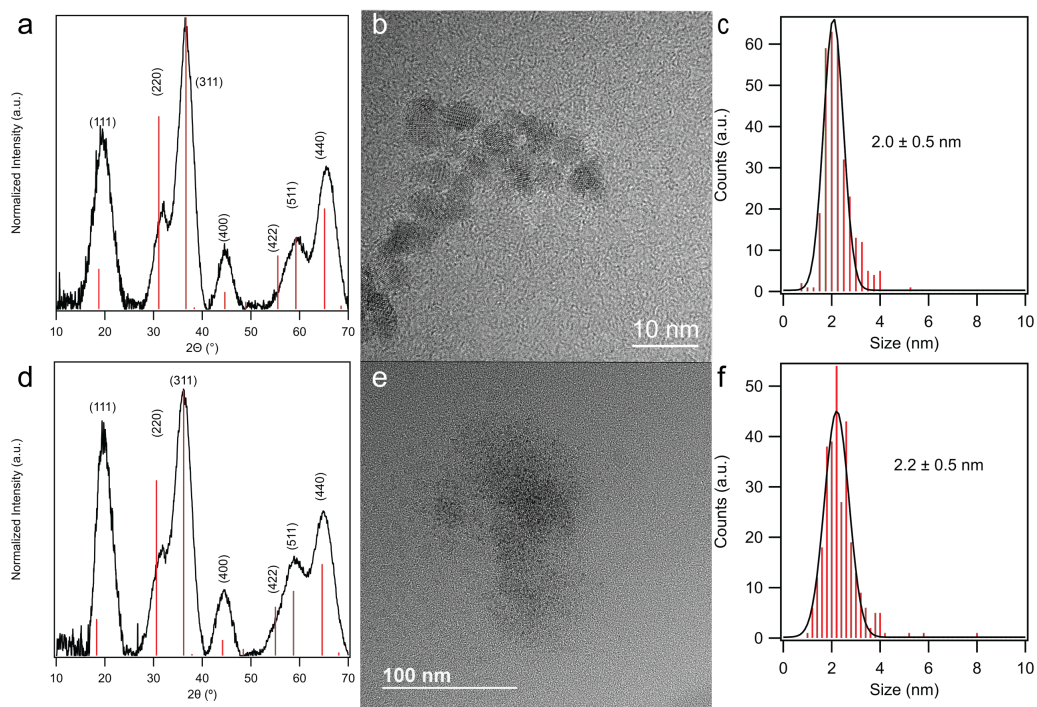
Figure 3.2. Powder X-Ray diffraction patterns indexed to the cubic - $Fd\bar{3}m$ phase (JCPDS 073-1961) for a) 0% Tb(III):ZnAl$_2$O$_4$ and d) 3.56% Tb(III):ZnAl$_2$O$_4$, b) high-resolution TEM images of 0% Tb(III):ZnAl$_2$O$_4$, Gaussian distribution of the c) 0% Tb(III):ZnAl$_2$O$_4$ and f) 3.56 % Tb(III):ZnAl$_2$O$_4$ nanospinels where statistics were generated by measuring >300 particles, and e) wide-area TEM images for 3.56 % Tb(III):ZnAl$_2$O$_4$ nanospinels.
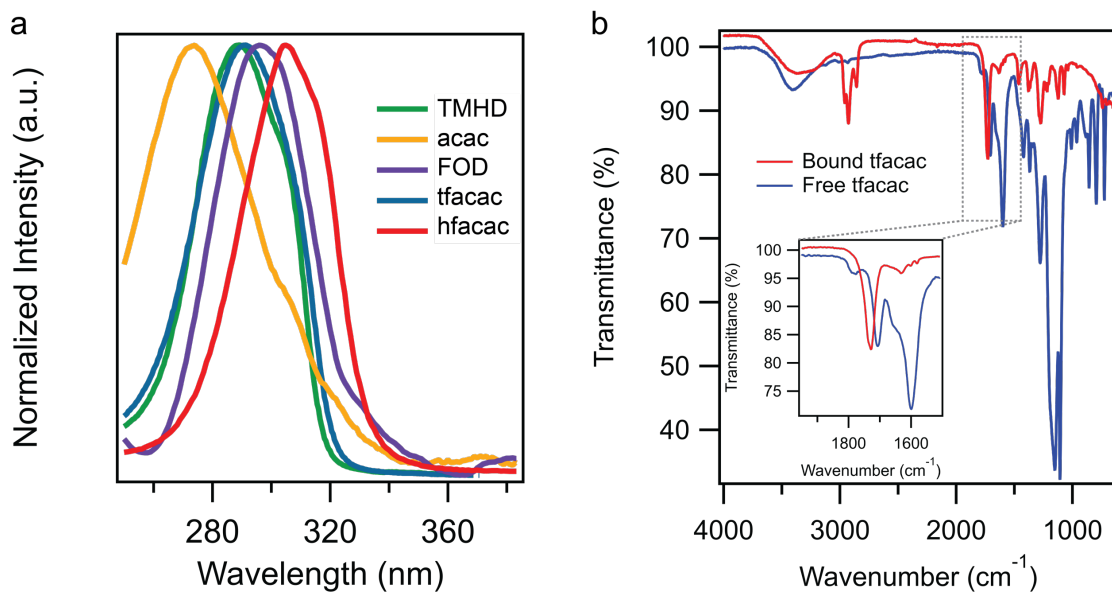
Figure 3.3. a) UV-Vis spectra at 298 K in cyclohexane for the passivated 3.567% Tb:ZnAl$_2$O$_4$ nanospinels. The $^1\pi^*$ absorption features are observed for acac (yellow), FOD (purple), hfacac (red), tfacac (blue), and TMHD (green). b) FT-IR spectra of the free tfacac ligand (blue trace) and passivated nanoparticle (red trace). The inset displays the shift in the ketone stretch.

Table 3.1. Tabulated values of free and passivated ketone stretches for the β–diekatoneate series corresponding to the data shown in Figure 3.4.

Sample	Ketone stretch frequency (cm^{-1})	
	Free ligand	Passivated Nanoparticle
hfacac	1624, 1689	1657, 1727
tfacac	1707	1730
FOD	1591, 1698	1636, 1741
acac	1709, 1728	1728, 1739
TMHD	1587, 1723	1576, 1748
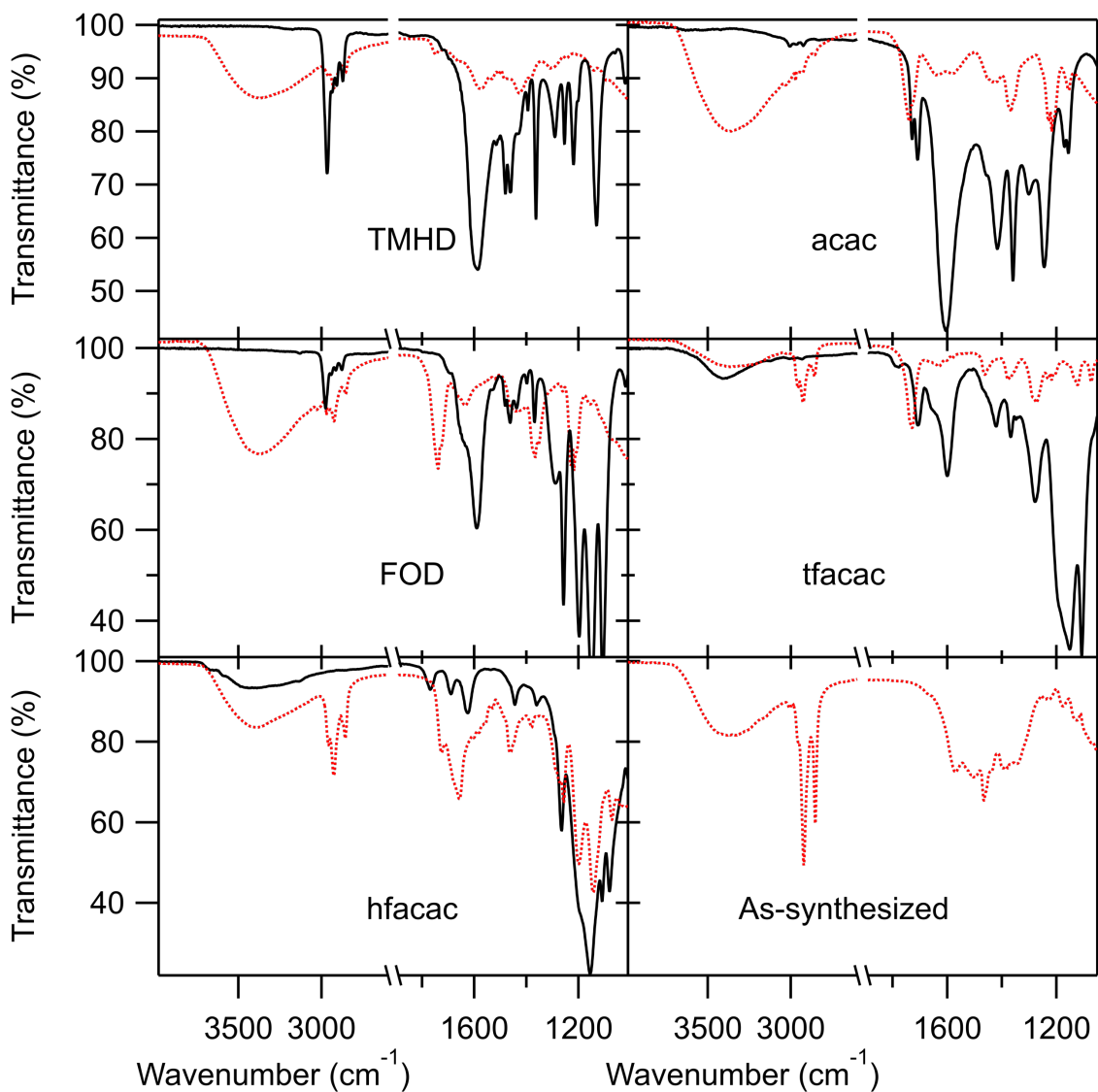
Figure 3.4. FT-IR spectra of the free ligand (black trace) and passivated 3.56% Tb(III): ZnAl$_2$O$_4$ nanospinel (red-dashed trace).

Table 3.2. Optical properties for the passivated Tb:ZnAl$_2$O$_4$ nanospinel samples

Ligand	$^3\pi^*$ (cm^{-1})	(ΔE) $^3\pi^*$ - $^5D_4$ (cm^{-1})	PLQY$_{EtOH}$ (%)	PLQY$_{EtOD}$ (%)	η_{sens} (%)
TMHD	$25{,}710 \pm 770$ [186-189]	5,210	0.47 ± 0.15	3.73 ± 0.37	4.84 ± 0.51
acac	$24{,}950 \pm 680$ [187, 188, 190-193]	4,450	3.94 ± 0.93	7.58 ± 0.91	9.83 ± 1.18
FOD	$23{,}100 \pm 1{,}100$ [186-188, 194-198]	3,030	18.27 ± 1.93	25.38 ± 1.77	32.91 ± 2.30
tfacac	$22{,}980 \pm 407$ [187, 190, 191, 199]	2,480	27.98 ± 1.97	37.72 ± 2.67	48.91 ± 3.46
hfacac	$22{,}170 \pm 590$ [186, 187, 190, 192, 193, 200, 201]	1,670	36.99 ± 2.95	41.29 ± 6.29	53.54 ± 8.16

and coordinated ligands have been tabulated in Table 3.1 and Figure 3.4. High-resolution TEM images for the 0% and 3.56% Tb(III):ZnAl$_2$O$_4$ nanocrystal along with pXRD patterns for all samples are available in the Supporting information (Figure 3.3). The TEM images confirm a spherical Tb(III):ZnAl$_2$O$_4$ nanospinel is obtained with the 0% sample being 2.0 ± 0.5 nm and the 3.56% sample being 2.2 ± 0.5 nm in size. It is worth noting that the small size and low z-number for the host lattice limit the ability to carry out accurate statistical analysis of the TEM images.

To evaluate the efficiency of the molecular photosensitization process of the Tb(III) center by the β-diketonate passivation layer, photoexcitation at 320 nm into the ligand was performed and the steady state photoluminescence (PL) recorded for all samples in toluene at 298 K (Figure 3.5). All samples display the $^5D_4 \rightarrow {}^7F_5$ transition seen at 544 nm when excited into the singlet state for the respective ligands at 320 nm. For the TMHD and acac passivated systems a large background from 400-550 nm is observed. The green ($^5D_4 \rightarrow {}^7F_5$) to blue ($^5D_4 \rightarrow {}^7F_6$) ratio for the samples is 2.53 ± 0.02 following correction for the broad emission background. The observation of a constant blue to green ratio for the samples implies no structural perturbation following ligand coordination.

The broad emission observed at high energy is attributed to either triplet ligand emission reflecting inefficient energy transfer to the lanthanide ion, or population of an emissive mid-gap trap state arising from an oxygen vacancy (V_{ox}) in the ZnAl$_2$O$_4$ lattice.[202-204] Based on time-resolved measurements in Figure 3.6, it is believed the broad emission is due to V_{ox} mid-gap state population since a roll-over feature is observed followed by a decay of 872 ns at 298 K, which is faster than typically observed for a $^3\pi^*$ emission.[205, 206] Consistent with this assumption the lifetime for triplet emission of a β-diketonate Gd(III) coordination complexes is on the order of 1.0 μs at 298 K,[207-209] while V_{ox} show lifetimes of 500 to 800 ns at 298 K.[210, 211]

As shown in Figure 3.1, the population pathways of the lanthanide excited state consist of multiple steps, each of which impacts the observed PLQY. The overall PLQY for the samples is calculated using the following expression,

$$\phi_{Ligand}^{Lanthanide} = \eta_{ISC} \times \eta_{ET} \times \phi_{Lanthanide}^{Lanthanide} = \eta_{sens} \times \phi_{Lanthanide}^{Lanthanide} \ (1),$$

where $\phi_{Lanthanide}^{Lanthanide}$ is the intrinsic quantum yield for Tb(III). The intrinsic quantum yield is estimated by comparison of the integrated intensities from direct excitation at 488 nm ($^7F_6 \rightarrow {^5D_4}$) to the Tb(III) quantum yield when populated via energy transfer from the ligand excited at 320 nm. The estimated intrinsic quantum yield for Tb(III) in the Tb(III):ZnAl$_2$O$_4$ nanospinel is 77% (Figure 3.8), which is good agreement with literature values.[212, 213]

Figure 3.5. Photoluminescence spectra of 3.56% Tb:ZnAl$_2$O$_4$ nanospinels (λ_{ex} = 320 nm, toluene, 298 K). The color of the traces represents a ligand where red traces indicate hfacac, blue traces indicate tfacac, purple traces indicate FOD, yellow traces indicate acac, and green traces indicate TMHD.

Table 3.3. Lifetime data collected in EtOH and EtOD monitoring the $^5D_4 \rightarrow ^7F_5$ transition at 544 nm following excitation at 320 nm into the singlet excited state. The values of q are derived from the Horrock's equation and the g/b ratios are the integrated intensities of the $^5D_4 \rightarrow ^7F_5/^5D_4 \rightarrow ^7F_6$.

Ligand	τ_{EtOH} (ms)	τ_{EtOD} (ms)	$k_{r, EtOH}$ (ms^{-1})	$k_{r, EtOD}$ (ms^{-1})	q	g/b
TMHD	0.746 ± 0.071	0.987 ± 0.14	0.6	3.8	0.8 ± 0.5	2.51
acac	0.681 ± 0.064	0.899 ± 0.11	5.8	8.4	0.8 ± 0.5	2.56
FOD	0.824 ± 0.021	0.936 ± 0.13	22.2	27.1	0.3 ± 0.5	2.51
tfacac	1.054 ± 0.094	1.142 ± 0.08	41.1	33.0	1.3 ± 0.5	2.56
hfacac	0.850 ± 0.068	1.083 ± 0.12	43.5	38.1	0.6 ± 0.5	2.52

λ_{ex} = 320 nm, λ_{em} = 425 nm
(τ_{obs} = 872 ns)
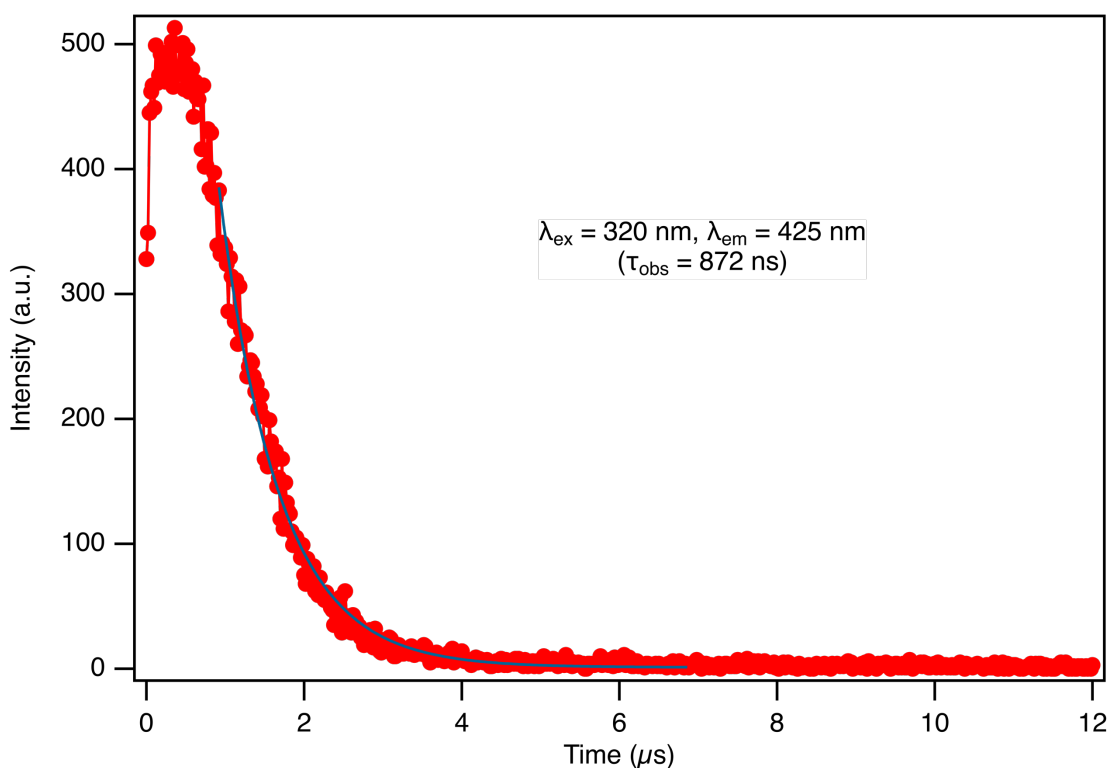
Figure 3.6. Lifetime measurements monitoring the broad emission seen at 425 nm, following excitation into acac. The rollover kinetics and short lifetime suggest population of a midgap trap state in the ZnAl$_2$O$_4$ lattice.

The efficiency of intersystem crossing (η_{ISC}) from the passivant singlet to triplet state and the efficiency of energy transfer from the passivant triplet to the Tb(III) center incorporated into the

ZnAl$_2$O$_4$ nanospinel (η_{ET}) will be governed by the spectral overlap function between the ligand

and Tb(III) excited states, as described within the Dexter mechanism[115] $k_{ent} = K < J > e^{\left(\frac{-2R_{DA}}{L}\right)}$

(2). In eqn 2, K is a pre-exponential factor in units of energy, <J> is defined as the integrated

spectral overlap function $J(v) = \frac{\int F_D(v)A_A(v)\,dv}{\int F_D(v)\,dv \int A(v)\,dv}$, R_{DA} is the radius between the donor and

acceptor, and L is the effective Bohr radius. The values of K, L, R_{DA} are invariant for the

experimental results since the nanospinel core is identical between each sample. The difference in

energy between the $^3\pi^*$ and Tb(III) $^5D_4$ level ($\Delta E_{3_{\pi^*}-Tb(III)5_{D_4}}$) is anticipated to scale with the

observed PLQY for the nanospinels. In a typical lanthanide coordination complex, the PLQY is

optimized when the energy difference (ΔE) is between 2,000 and 4,000 cm^{-1}.[176]

In , the optical properties for the series of β-diketonate passivating ligands having a $^3\pi^*$ to Tb(III) $^5D_4$ energy difference of 1,670 – 5,210 cm^{-1} is listed, along with the sensitization efficiency (η_{sens}) of the Tb(III) center, and the overall PLQY for the nanospinel samples excited at 320 nm. A plot of the PLQY vs. the energy difference between the donor and acceptor electronic states is shown in
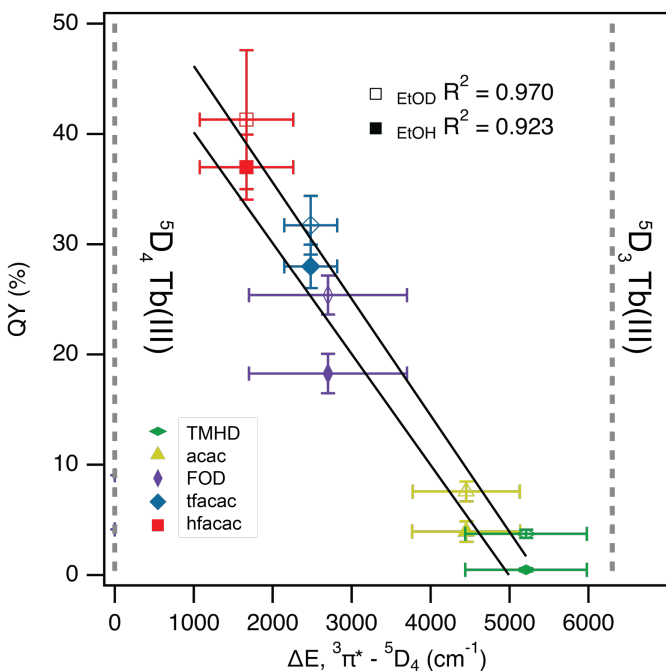
Figure 3.7. Quantum yields of 3.56% Tb vs. separation between the $^3\pi^*$ and $^5D_4$ state of the Tb(III).

Figure **3.7**. The experimental PLQY values are plotted for both the EtOH and EtOD where each can be fit
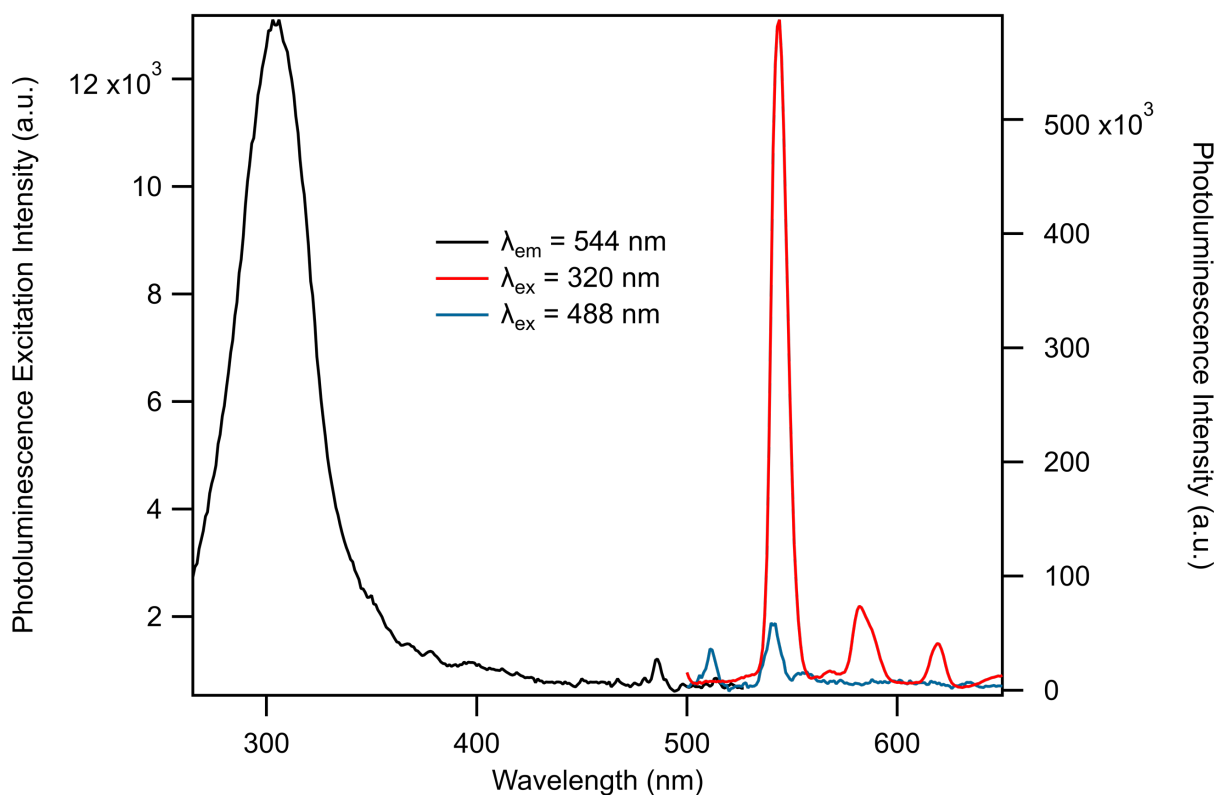
Figure 3.8. Photoluminescence excitation spectra (black trace) monitoring the $^5D_4{\rightarrow}^7F_5$ transition centered at 544 nm. Emission spectra flowing ligand excitation (red trace) at 320 nm and direct excitation (blue trace). All spectra were collected in EtOD at 298 K.

to linear regressions with a R^2 values of 0.968 and 0.990, respectively. The improved fit for the EtOD samples is unsurprising due to the elimination of quenchers (-OH) from the system which result in the higher PLQY. For the nanospinel samples, the highest PLQY was achieved when passivating the nanospinel with hfacac resulting in an experimental PLQY of 41.29 $\pm$ 6.29% in EtOD. The reported $^3\pi$* state for hfacac is ~22,170 cm^{-1} which is approximately 1,670 cm^{-1} above the $^5D_4$ excited state of the Tb(III).The linear trend is consistent with a Dexter energy transfer process in which the <J> spectral overlap integral dominates the efficiency of transfer, as observed by Latva *et al.*[176] for β-diketonate Tb(III) coordination compounds. However, the observation of
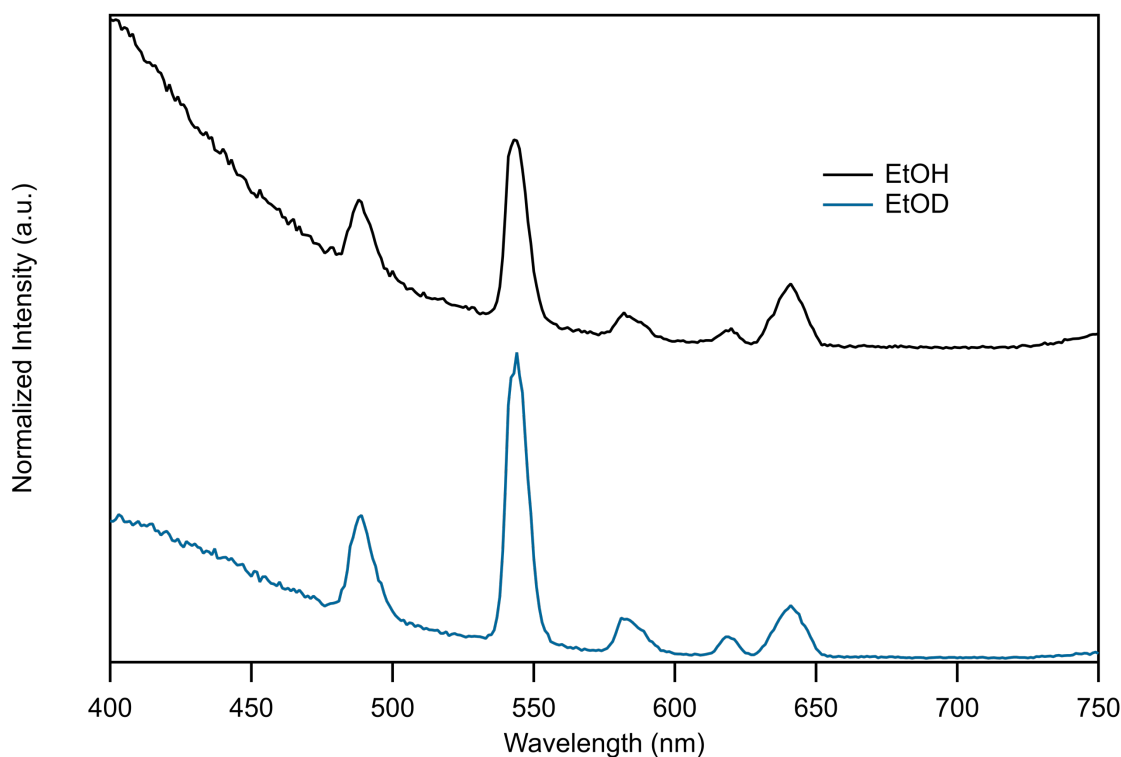
Figure 3.9. Photoluminescence spectra exciting at 320 nm into the singlet excited state of the acac passivant. The black trace represents the Photoluminescence spectra collected in EtOH where the blue trace represents EtOD as a solvent. All measurements were recorded at 298 K.

continued improvement in the PLQY when ΔE is < 2000 cm^{-1} is surprising, and contradicts Latva's rules expectation of back-energy transfer lowering the observed PLQY in this range. It is surprising that no back-energy transfer was observed in the PL as a ligand $^{3}\pi^{*}$ emission, contrary to reports in coordination complexes when $\Delta E < 2000$ cm^{-1}.

The breaking of Latva behavior may reflect loss of back-energy transfer or potentially lattice or surface changes following coordination of the β-diketonates changing the intricinsic lanthanide quantum yield. Contributions arising from surface reconstruction can be eliminated by considering the blue ($^{5}D_{4} \rightarrow {}^{7}F_{6}$) to green ($^{5}D_{4} \rightarrow {}^{7}F_{5}$) PL intensity ratio, listed in Table 3.3. The blue to green ratio is susceptible to site perturbation, and the lack of change to the b/g ratio following ligand exchange suggests reconstruction is an unlikely contributor.[93, 94] The role of
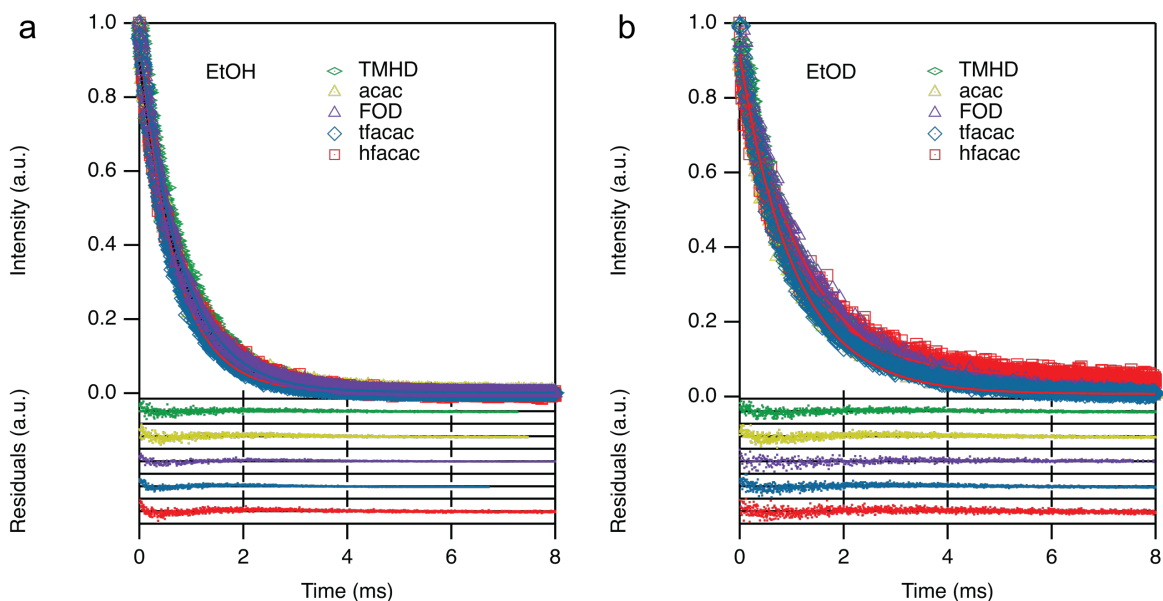
Figure 3.10. Excited state lifetimes monitoring the $^5D_4 \rightarrow {}^7F_5$ transition centered at 544 nm in a) EtOH and b) EtOD. All measurements were recorded at 298 K. The scale for the residuals are 0 ± 0.1 (a.u.) for all fits.

surface defects due to a poorer ligand coverage by the various passivants is very likely, as the appearance of a V_{ox} defect emission is clearly visible in the PL data collected in EtOH and EtOD (Figure 3.9). The presence of the defect will impact the accessibility of water to the surface, which is easily confirmed by excited state lifetime measurements using the Horrock's equation.[214-216] It is worth noting that the surface sites are more susceptible to –OH quenching than internal sites populated *via* direct energy transfer from the ligand or following a Tb(III) to Tb(III) energy migration event. In the Horrock's equation, the average bound -OH groups per nanospinel (q) is evaluated by comparison of the excited state lifetime measured in EtOH and EtOD through the expression $q = A(\tau_{EtOH}^{-1} - \tau_{EtOD}^{-1})$. In the equation A is a solvent constant available in the literature ($A_{EtOH, EtOD} = 2.3$).[217] The excited state lifetimes for each sample is listed in Table 3.3 and displayed in Figure 3.10, along with the q-value. In EtOD, the lifetimes are within experimental error as function of energy, suggesting that the ligand has no impact on the radiative rates but the nanophosphors have –OH quencher accessibility. Applying the Horrock's equation, the number of

bound -OH is less than one per nanophosphor with the exception of tfacac which has approximately 1.3 ± 0.5 coordinated quenchers (Table 3.3), suggesting that the most Tb(III) reside at within the volume of the nanoparticle. The nanospinel lattice protects the incorporated Tb(III) cations from solvent quenchers which results in the increased PLQYs. The loss of back energy transfer pathways may explain the increasing PLQY at ΔE below 200 cm$^{-1.}$ Consistent with the loss of efficient pathways for back energy transfer, the ligand $^3\pi^*$ emission is lacking form the PL plots in Figure 3.5 for the ligands with $\Delta E < 2000$ cm^{-1}. To explain the loss of back energy, transfer pathways, it is plausible in the spinel lattice that efficient Tb(III) to Tb(III) hopping in the lattice results in the Tb(III) excited state being outside the critical radii of quenching for the ligands. Further studies are underway to evaluate the hopping behavior as a function of temperature.

3.4 Conclusion.

The development of a soluble green down-shifting phosphor was achieved with photoluminescence quantum yields of 41% by incorporation of Tb(III) into a $ZnAl_2O_4$ nanospinel passivated by hfacac. The nanospinel lattice provides a thermal and radiation stable host that is optically transparent at the 320 nm, however, population of a midgap state leads to broad blue emission at the expense of Tb(III) emission state when passivated by TMHD and acac. The PLQY exhibited a linear response to energy separation between the $^3\pi^*$ and $^5D_4$ excited state of Tb(III) following fundamental photophysical behavior for energy transfer mechanisms. Latva's rule suggested that the energy separation must be between 2,000-4,000 cm^{-1} due to the propensity for back energy transfer in lanthanide coordination compounds. However, no evidence of back energy transfer was observed following the Ln(III) incorporation into a nanoparticle due to hoping events to neighboring Ln(III) cations. This can allow increased spectral overlap values to be achieved resulting in higher observed PLQYs for future nanophosphor technologies.

CHAPTER 4

STRUCTURE –FUNCTION CORRELATION: ENGINEERING HIGH QUANTUM YIELDS IN DOWN-SHIFTING NANOPHOSPHORS

Lanthanides are routinely incorporated into quantum dots to act as down-shifting and up-converting phosphors in display and lighting applications due to their high photoluminescence quantum yields (PLQY). Recent efforts in the field have demonstrated that trivalent lanthanide, Ln(III), incorporated into $ZnAl_2O_4$ spinel nanocrystals can achieve PLQYs of 50% for down-shifting nanophosphors using earth abundant materials. The high PLQY is surprising as the Al(III) site in a spinel is centrosymmetric, which should lead to poor performance for these nanophosphors. However, spinels are prone to formation of an admixture of inverse and normal spinel lattices when the cation size ratio is not optimal. Such behavior can produce local cation disorder that can influence the phosphor performance. Herein, we describe the use of Tb(III) as an optical probe to evaluate the fractional population of the inverse and normal spinel structures within $Tb_xZnAl_{2-x}O_4$. The experimental data exhibits a Tb(III) concentration dependent change in the fractional population that results in a maximum PLQY of 37% with 3.56% Tb(III) incorporation. A decrease in the degree of inversion (cation disorder) leads to larger amounts of the cubic $Fd\bar{3}m$ phase resulting in the observed photoluminescence behavior. The correlation of NMR, pXRD, and optical methods provides direct insight into the high PLQY behavior for this class of nanophosphor.

4.1 Introduction.

In the phosphor field, the incorporation of a trivalent lanthanide, Ln(III), guest ion into a metal oxide quantum dot produces materials capable of exhibiting down-shifting or up-converting

photoluminescence that can form the color center for a phosphor-converted light emitting diode (pcLED).[30, 218-223] Quantum dots have passivating ligands that can act as a molecular antenna to enhance photon capture and energy conversion of down-shifting phosphors.[29, 30] Research into the broader class of Ln(III) doped quantum dots that have molecular sensitizers have shown variable photoluminescence quantum yield (PLQY) performance depending on the host lattice structure,[224, 225] guest ion concentration,[96-98, 226, 227] and choice of sensitizer.[176, 228] The quantum yield for the down-shifting phosphor will be impacted by the sensitization efficiency from the passivant to the emitting Ln(III) center and by the site symmetry of the Ln(III) ion reflecting the optical selection rules. In non-centrosymmetric lattices, the electric dipole allowed transitions in f-orbitals become favorable and lead to higher intrinsic quantum yield,[91, 224, 225] as reported for Ln(III) incorporation into molecular sensitizer passivated Y_2O_3[29] and $NaYF_4$.[172, 229] The downshifting phosphor performance can be engineered to produce high quantum yields with improved color purity by introducing a lowered symmetry for the Ln(III) site through cation size mismatch or choice of a non-centrosymmetric lattice. Improving the optical performance by manipulating the structure-function correlation to enhance the phosphor metrics for pcLED development is a priority in solid state lighting.

In an earlier study, it was demonstrated that Eu(III) doped $ZnAl_2O_4$ spinels passivated by molecular antenna are promising nanocrystal host lattices for pc-LED applications with quantum yields of 50%.[30] The observation of high quantum yields with a high red to orange ratio is surprising when considering the substitutional (Al) site sits on an inversion center which should lead to poor performance of the phosphor.[89, 91, 230] A likely explanation lies in site distortion due to the radius mismatch ($r_{Al} = 53.5$ pm vs. $r_{Eu} = 94.7$ pm) leading to a localized lattice distortion.[231] Consistent with this hypothesis, spinels are known to exhibit cation disorder (normal $vs.$ inverse

spinel) within a crystal leading to admixtures of the cubic $Fd\overline{3}m$ and tetragonal $P4_122$ phases, as reflected in the lattice degree of inversion (DOI). The reduced symmetry associated with the admixture would lead to the removal of the inversion center accounting for the observation of a high PLQY in Eu:ZnAl$_2$O$_4$ (PLQY> 50%).[30] The enhanced red to orange ratio observed previously, is consistent with the *f-f* transitions governed by Laporte selection rules,[88, 91] wherein the ratios of the electric (ED), red, and magnetic dipoles (MD), orange, transitions report the fractional population between the two $Fd\overline{3}m$ (centrosymmetric) and $P4_122$ (non-centrosymmetric) phases. The local structural perturbations can be validated by NMR spectroscopy and correlated through changes in the lanthanide emission spectra, providing a structure-function correlation to explain the optical performance of the doped spinel family.[46, 47, 224, 225] By coupling of pXRD, ^{27}Al MAS-NMR data and the use of the Tb(III) cation as an optical probe, investigation into local site symmetry and elucidation of phases contributions is achieved, previously needing advanced theoretical and pair distribution modeling techniques to understand.[46,54]

In this work, the strain induced effect on the PLQY for a series of Tb$_x$ZnAl$_{2-x}$O$_4$ (x = 0, 0.18, 1.57, 3.56, 5.08, 7.05%) nanospinels is investigated. The results of this study lead to the development of an earth abundant green phosphor with PLQY of 37% achieved at 3.56% Tb(III) doping, where strain resulted in changes in the fractional population of the admixture of spinel phases. Analysis of optical, ^{27}Al MAS-NMR and powder X-ray diffraction (pXRD) provides a structure-function correlation to explain high PLQY and color purity achieved within a Tb(III) doped nanospinel. The results support a model wherein the Tb(III) center occupies the Al^{3+} cation site leading to a lattice distortion as reported by the lattice DOI. At low Tb(III) concentrations, increased tetragonal phase contributions lead to an increase in the PLQY with a maximum at 3.56% Tb(III). Above 3.56% Tb(III), competitive quenching processes occur through increased

interaction between neighboring lanthanides, energy migration to surface trap states, and increased contributions from the cubic phase occurs. The experimental results provide a method to use structural design to achieve an ideal phosphor for next-generation pcLED technologies. In addition, the use of hexafluoroacetylacetonate (hfacac) as a molecular sensitizer and surface passivating layer allows blending with a polymer matrix for use in additive manufacturing techniques on solid state lighting technologies.

4.2 Experimental.

4.2.1 Materials.

All commercially available reagents and solvents were used without further purification. DMF was dried over molecular sieves. The passivating ligand was 1,1,1,5,5,5-hexafluoro-2,4-pentanedione (hfacac, Alfa Aesar, 98+%). Zinc (II) undecylenate (Spectrum, 98%), oleylamine (Aldrich, 70%), $NOBF_4$ (Alfar Aesar. 98%), aluminum (III) 2, 4-pentanedionate (Strem Chemicals, 99%), and terbium (III) 2,4-pentanedionate hydrate (Alfa Aesar, 99.9%) were obtained from various sources.

4.2.2 Synthesis of $Tb_xZnAl_{2-x}O_4$ (x = 0, 0.18, 1.57, 3.56, 5.08, 7.05%).

Zinc aluminate nanospinels were synthesized by thermal decomposition of molecular precursors. Zinc undecylenate ($Zn(UND)_2$, 0.25 mmol), aluminum 2,4-pentanedionate ($Al(acac)_3$, 0.5 mmol), and terbium(III) 2,4-pentanedionate ($Tb(acac)_3$, variable mmol) were charged into a 10mL Pyrex microwave vial with olyelamine (70% Tech grade, sigma). The mmol of Tb(III) used were 0 (0%), 0.0025 (0.18%), 0.01 (1.57%), 0.02 (3.56%), 0.03 (5.08%), and 0.04 (7.05%). The reactions were heated to 280 °C for 10 minutes in an Anton Paar MW reactor and cooled with forced air cooling. The resultant nanoparticles were isolated by addition of MeOH and centrifugation. Samples were dried under reduced pressure at room temperature.

4.2.3. Measurements.

Structural characterization was performed using pXRD recorded on a Rigaku DMAX 300 Ultima III Powder X-ray diffractometer (Cu K$_\alpha$ λ = 1.5418 Å radiation). The size of the nanocrystals were measured by fitting the pXRD pattern to the Scherrer broadening equation, $L = K\lambda/\beta cos\theta$, where L is the crystallite size, K is the shape factor (0.9 corresponding to spherical nanocrystals), λ is the X-ray wavelength measured in nm, β is the peak width at half height at a given 2θ value, and θ is the Bragg angle. Transmission electron microscopy (TEM, JOEL, 200kV) was performed to analyze particle sizes and distributions. High-resolution TEM images were collected on an FEI Tecnai Osiris operating at 200 kV. The TEM grids were prepared by drop casting a dispersion of the purified nanospinels in toluene on a 300 mesh Cu grid and dried overnight. Elemental concentrations were measured by inductively coupled plasma-mass spectrometry (ICP-MS, ThermoFischer) by digesting nanoparticles in trace grade HNO$_3$. Calibration curves were generated with R^2 >0.999 using ultrapure metal salts.

4.2.4. Optical Methods.

Ligand passivation was analyzed by Fourier transform infrared (FT-IR) spectroscopy measured on powdered samples using a PerkinElmer Spectrum 100 FT-IR Spectrometer equipped with an attenuated total reflectance (ATR) sample chamber consisting of a ZnSe crystal over coated with diamond using a single-bounce configuration. Solution UV-Vis absorption spectra were recorded in toluene using a 1-cm quartz cuvette in a Varian Cary 50 UV-Vis spectrometer. The photoluminescence and photoluminescence excitation spectra were recorded on a Horiba Fluoromax spectrofluorimeter equipped with a 150 W CW Ozone free xenon arc lamp, Czerny-Turner monochromators with excitation grating blazed at 330 nm (1200 groove/mm) and the emission grating blazed at 500 nm (1200 grooves/mm). All spectra were corrected for the

instrument response function and the intensity of the lamp. Photoluminescence quantum yield were measured by the relative method using Eu(TTA)$_3$Phen as a standard in EtOH (QY = 35.6%).[99, 100] Linear regressions were generated by plotting the integrated intensity *vs.* the absorption of serial dilutions. Comparison of the slopes between the standard and the sample, allow for determination of the QYs as shown in equation (3):

$$\Phi_s = \Phi_r \left(\frac{m_s}{m_r}\right) \left(\frac{\eta_s^2}{\eta_r^2}\right) \tag{3}$$

In eqn. 3, *m* is the slope and η is the refractive index of the solvent. Subscripts *r* and *s* indicate the reference and sample, respectively. The standard and samples were both measured in EtOH at 298 K leading to the removal of the refractive index term.

Emission lifetime measurements were recorded on an Edinburgh Instruments LP980-KS and excited by a Continuum Nd:YAG laser coupled to an optical parametric oscillator with the resulting excitation wavelength of 320 nm. Samples were recorded in EtOH at 298 K so that radiative rates could be calculated. The emission lifetimes curves were fit to a monoexponential equation using IGOR 8.0.

4.3. Results and Discussion.

4.3.1. Physical Characterization.

In Figure 4.1, a schematic of the Tb$_x$ZnAl$_{2-x}$O$_4$ nanospinel and the possible structural phases that form for the normal *vs.* the inverted spinel lattice are shown. In Table 1, the characterization data for all Tb$_x$ZnAl$_{2-x}$O$_4$ nanospinels is summarized. The series of ~2 nm, spherical hexafluoroacetylacetonate (hfacac) Tb$_x$:ZnAl$_{2-x}$O$_4$ (x = 0 to 7.05) spinel nanocrystals were prepared by thermal decomposition of metal coordination complexes at 280 °C in oleylamine using a 2.45 GHz microwave reactor operating at 300 W. The nanospinels were ligand exchanged with hfacac by treatment with NOBF$_4$ followed by hfacac at 60 °C in acetone, as described by
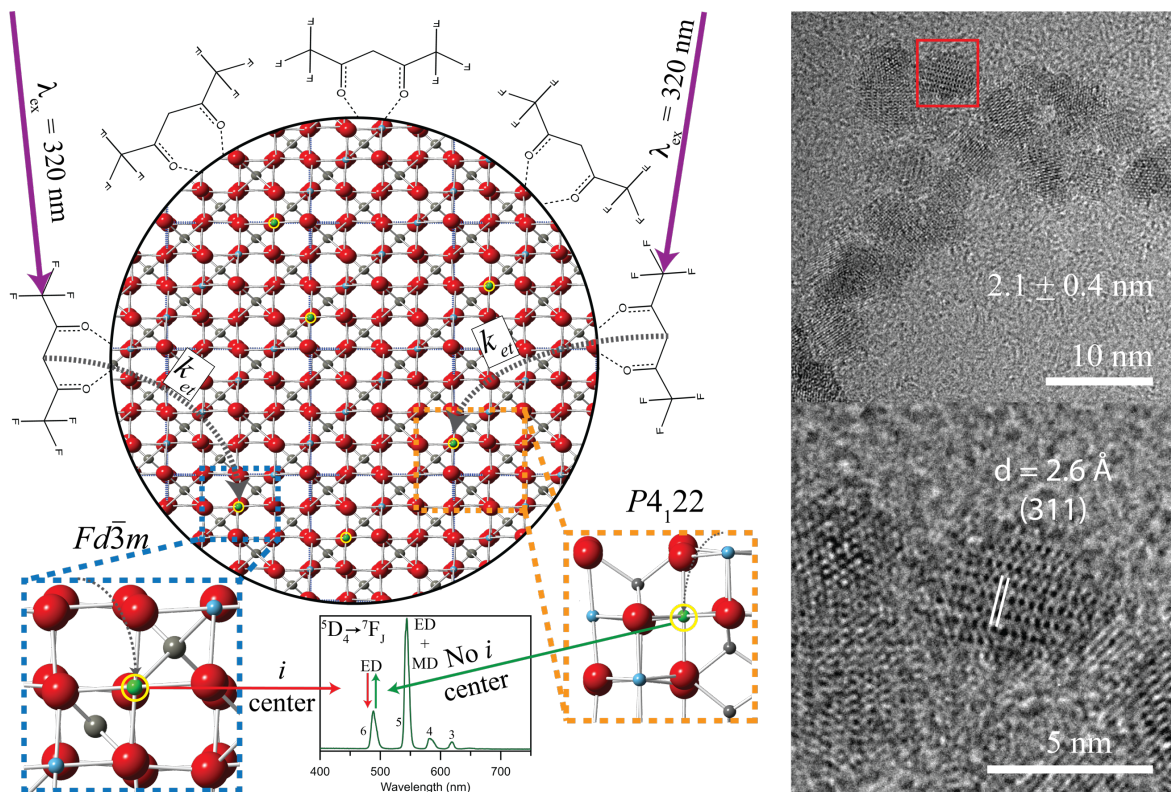
Figure 4.1. Schematic illustrating the incorporation of Tb(III) into a 2.1 nm $ZnAl_2O_4$ lattice passivated with hfacac ligands to sensitize the Tb(III) emission and high resolution-TEM of the parent $ZnAl_2O_4$ nanospinel with an average size and size distribution of 2.1 ± 0.4 nm. The red, grey, blue and green spheres are oxygen, Zn(II), Al(III), and Tb(III) respectively. In the spinel the Al(III) occupies two non-equivalent octahedral sites, shown as dark (Al-1) and light (Al-2) blue atoms.

Murray, *et al.*[185] The nanospinel is isolated using selective precipitation/centrifugation protocols.[30]

FT-IR spectroscopy confirms passivant exchange at > 80%, consistent with reports by Murray, *et. al.*[185] (Figure 4.2).

In Figure 4.1 high resolution TEM is shown for the parent $ZnAl_2O_4$ nanocrystal. TEM analysis of the $Tb_xZnAl_{2-x}O_4$ nanocrystal is difficult due to low z-number; however, low magnification imaging allows the nanocrystal size and size distributions to be analyzed for 300 nanocrystals on a single grid (Figure 4.3, Table 1). High resolution imaging of the parent $ZnAl_2O_4$

Table 4.1. Characterization of $Tb_xZnAl_{2-x}O_4$

% Tb(III)	[Tb^{3+}] (%)	Size (nm)		X-ray parameters			NMR
	ICP-MS	TEM	pXRD	% $P4_122$	ε, (%)	a, (Å)	λ (%)
0%	-	2.1 ± 0.4	2.8	35	1.45	8.06	44
0.18%	0.18	1.9 ± 0.5	2.2	17	1.92	8.12	19
1.57%	1.57	2.4 ± 0.6	2.2	14	1.93	8.14	17
3.56%	3.56	2.2 ± 0.5	2.0	7	2.08	8.15	6
5.08%	5.08	2.2 ± 0.4	1.7	6	2.41	8.16	3
7.05%	7.05	2.1 ± 0.5	1.7	4	2.56	8.17	2

nanocrystal shows a spinel lattice is formed as a faceted particle with a size of 2.1 ± 0.4 nm. Lattice fringes for the parent spinel are assignable in the high-resolution image as the (311) plane ($d_{(311)}$ = 2.6 Å).

In Figure 4.4a, the pXRD patterns for $Tb_xZnAl_{2-x}O_4$ are indexed to the $Fd\bar{3}m$ phase (JCPDS 073-1961). The pXRD diffraction peaks exhibit a shift in 2θ and a change in the FWHM as Tb(III) concentration is increased. Non-Vegard law behavior is expected as substituting the Tb(III) (92.3 pm) into a smaller Al(III) (53.5 pm)[231] site is not favorable, resulting in lattice strain and changes to the DOI. A plot of the calculated lattice constant *vs.* Tb(III) concentration confirms non-Vegard law behavior is observed for the $Tb_xZnAl_{2-x}O_4$ nanospinel samples. The plot of the predicted Vegard law behavior is shown as a dashed line in Figure 4.5.

The lattice strain can be evaluated from the observed pXRD pattern FWHM and peak shape using the Williamson-Hall (W-H) relationship, $\beta_{hkl}cos\Theta = \frac{K\lambda}{D} + 4\varepsilon \sin \theta$. In the W-H relationship the peak shape is calculated as a Lorentzian function varying as 1/cosθ if size is the dominant contributor. In the presence of strain the peak shape will be Gaussian and can be related
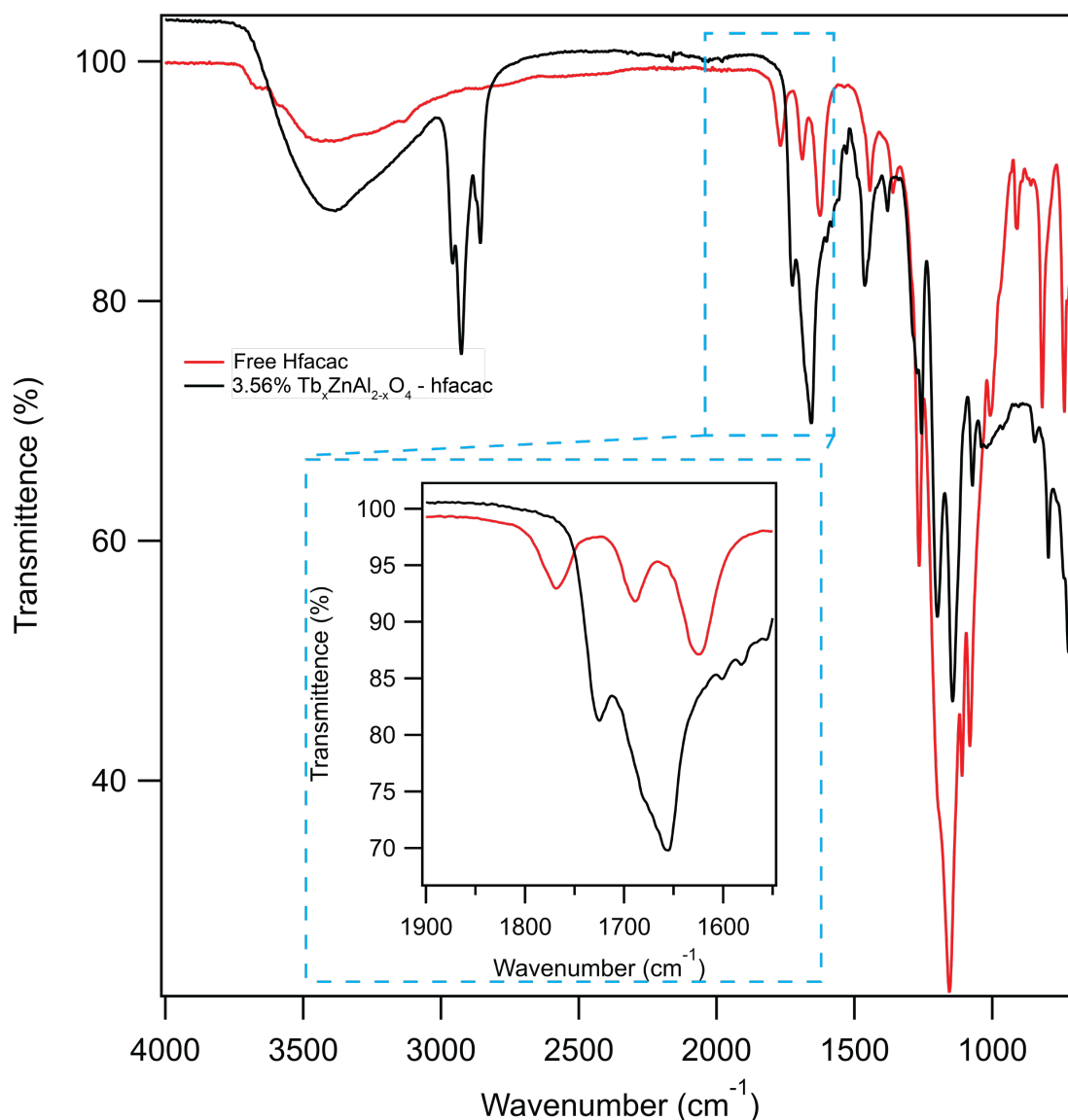
Figure 4.2. FT-IR spectra taken of the free hfacac ligand and the hfacac passivated 3.56 % Tb:ZnAl₂O₄ samples. The inset shows the ketone stretch showing a shift in the frequency and symmetry following coordination to the nanospinel. The red trace is the free ligand while the black trace is the hfacac passivated nanospinel.

to the trigonometric tangent relationship, $\sin\theta/\cos\theta$.[232, 233] The β_{hkl} term is the FWHM of the peak, $\cos\theta$ and $\sin\theta$ are the trigonometric function of the peak position expressed in radians, K is the shape factor (typically 0.9 for spherical nanoparticles), λ is the wavelength of X-ray, D is the particle size, and ε is strain. To deconvolute the strain and size parameters from the pXRD patterns, the size of the nanocrystal must be estimated from the TEM measurements. Using the W-H
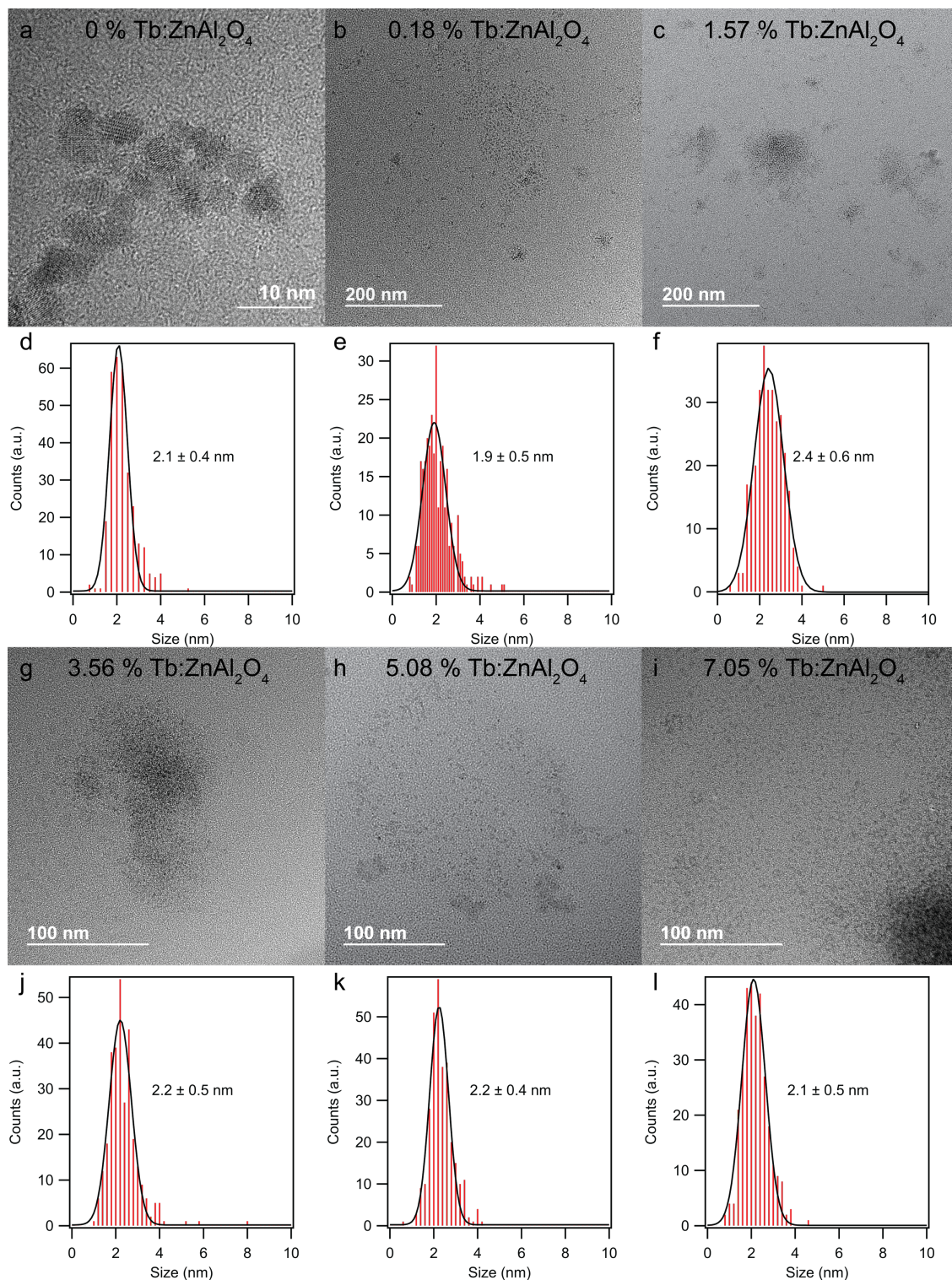
Figure 4.3. TEM images of a) 0% Tb:ZnAl$_2$O$_4$, b) 0.18% Tb:ZnAl$_2$O$_4$, c) 1.57% Tb:ZnAl$_2$O$_4$, g) 3.56% Tb:ZnAl$_2$O$_4$, h) 5.08% Tb:ZnAl$_2$O$_4$, and i) 7.05% Tb:ZnAl$_2$O$_4$. Size and size dispersiteis statistics were generated by measuring over 300 particles where the histograms are displayed in d) 0% Tb:ZnAl$_2$O$_4$, e) 0.18% Tb:ZnAl$_2$O$_4$, f) 1.57% Tb:ZnAl$_2$O$_4$, k) 3.56% Tb:ZnAl$_2$O$_4$, l) 5.08% Tb:ZnAl$_2$O$_4$, and m) 7.05% Tb:ZnAl$_2$O$_4$.

97
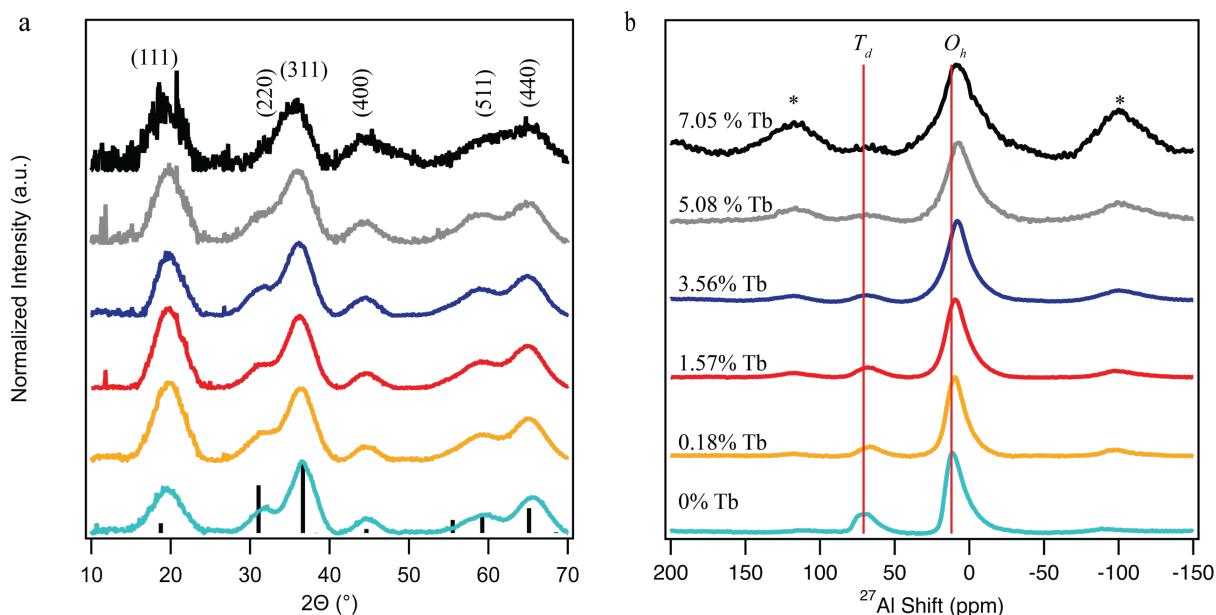
Figure 4.4. a) Powder X-Ray diffraction patterns and b) ^{27}Al MAS-NMR for x% $Tb_xZnAl_{2-x}O_4$ where (*) indicate spinning side bands. The color of the trace represents the Tb(III) concentration where 0% Tb is light blue, 0.18% Tb is yellow, 1.57% Tb (red), 3.56% Tb is dark blue, 5.08% Tb is grey, and 7.05% Tb is black.

relationship, the calculated lattice strain value (ε) is listed in Table 1 and represents the average strain value for the analysis of the (311), (400), (511), and (440) reflections.

The structural changes occurring within the nanospinel lattice with increasing Tb(III) content can be analyzed by comparing the observed strain (ε), phase purity, and DOI for the samples. In Figure 4.6a, a plot of the average strain (ε) *vs.* Tb(III) concentration shows increased strain in the lattice is evident as the Tb(III) concentration increases. Likewise, the phase purity is observed to be inversely proportional to Tb(III) concentration (Figure 4.6b). The phase purity is evaluated by whole pattern fitting of the pXRD to extract the fractional population of $Fd\bar{3}m$ and $P4_122$ in each sample, shown in Figure 4.7. Changes in $P4_122$ fraction in the lattice will be reflected in the O_h to T_d site occupation of the Al(III) site, or the degree of inversion (DOI) for the spinel. The DOI is evaluated by the change in area for the ^{27}Al resonance for the two sites through
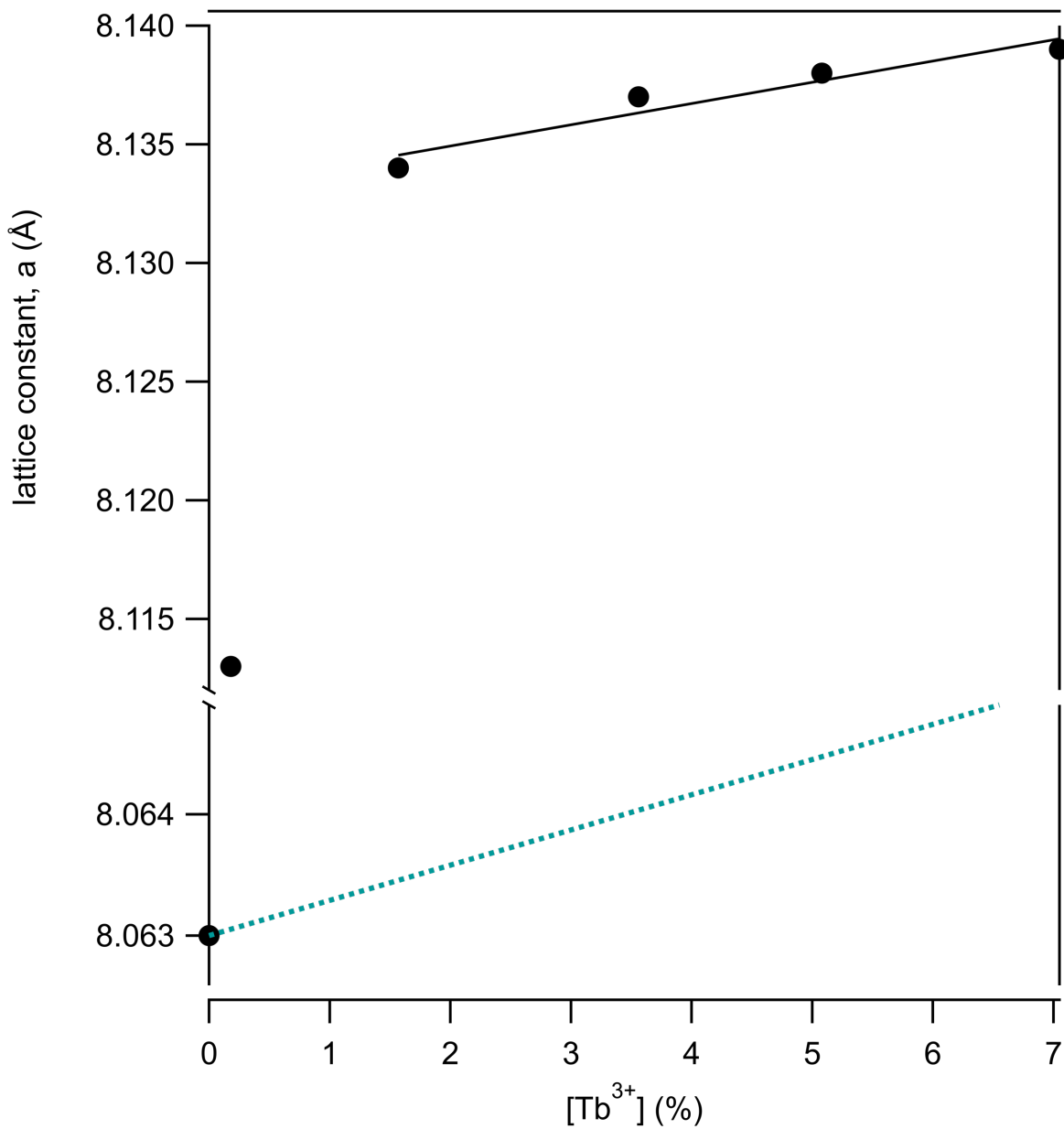
Figure 4.5. Calculated lattice constant shown in black circles showing non-Vegard behavior. The dashed line represents the calculated shift in lattice constant as a function of Tb(III) concentration.

the following relationship, $I_{Td}/I_{Oh} = \lambda/(2 - \lambda)$.[42, 44, 48, 49, 234, 235] In the relationship, I_{Td} and I_{Oh}

are the integrated areas for the T_d and O_h peaks, respectively. In Figure 4.4b, the ^{27}Al NMR spectra

is shown for the $Tb_xZnAl_{2-x}O_4$ samples. From the $ZnAl_2O_4$ (x = 0) sample the T_d site is assigned

to 69.3 ppm and the O_h site is assigned to 11.5 ppm. As the concentration increases a Fermi contact
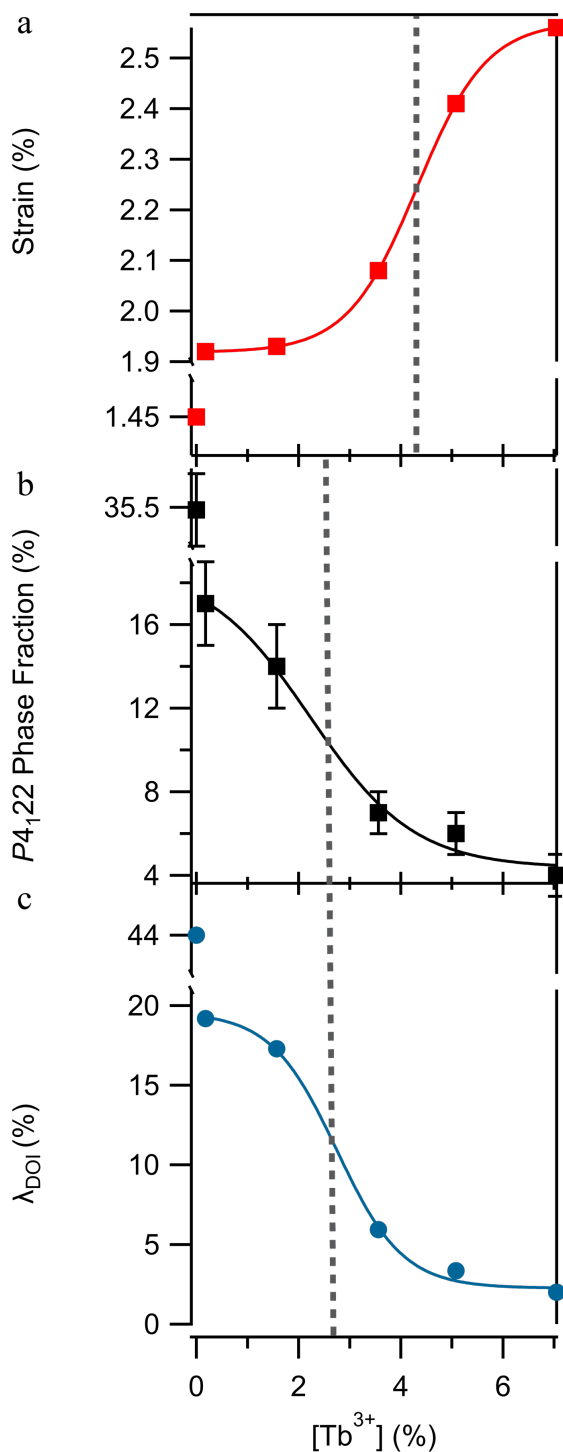
Figure 4.6. A plot of the a) strain, b) $P4_122$ phase fractions and c) degree of inversion *vs.* Tb(III) concentration. The dashed line is an aid to see the change in inflection points seen throughout the types of analysis.

shift due to the paramagnetic Tb(III) ions is observed along with a pseudo contact shift as evidenced by the increasing spinning side band intensity with increasing Tb(III) incorporation.[236-238] The observed behavior is consistent with uniform Tb(III) incorporation.

In Figure 4.6c, the change in T_d/ O_h line intensity, or degree of inversion (DOI) for the spinel lattice, is shown by plotting the ^{27}Al integrated area for $I(O_h)$ / $I(T_d)$ *vs.* Tb(III) concentration. A plot of the ^{27}Al chemical shift *vs.* Tb(III) concentration is provided in Figure 4.8. The plots in Figure 4.6 and Figure 4.8 all fit to sigmoidal functions with 4.32% Tb(III), the $P4_122$ phase fraction has an inflection point at 2.23%, the DOI exhibits an inflection point at 2.81%, and the inflection points. The strain (ε) plot exhibits an inflection point occurring at O_h chemical shift has an inflection at 2.54%. The sigmoidal relationships suggest similar a first-order
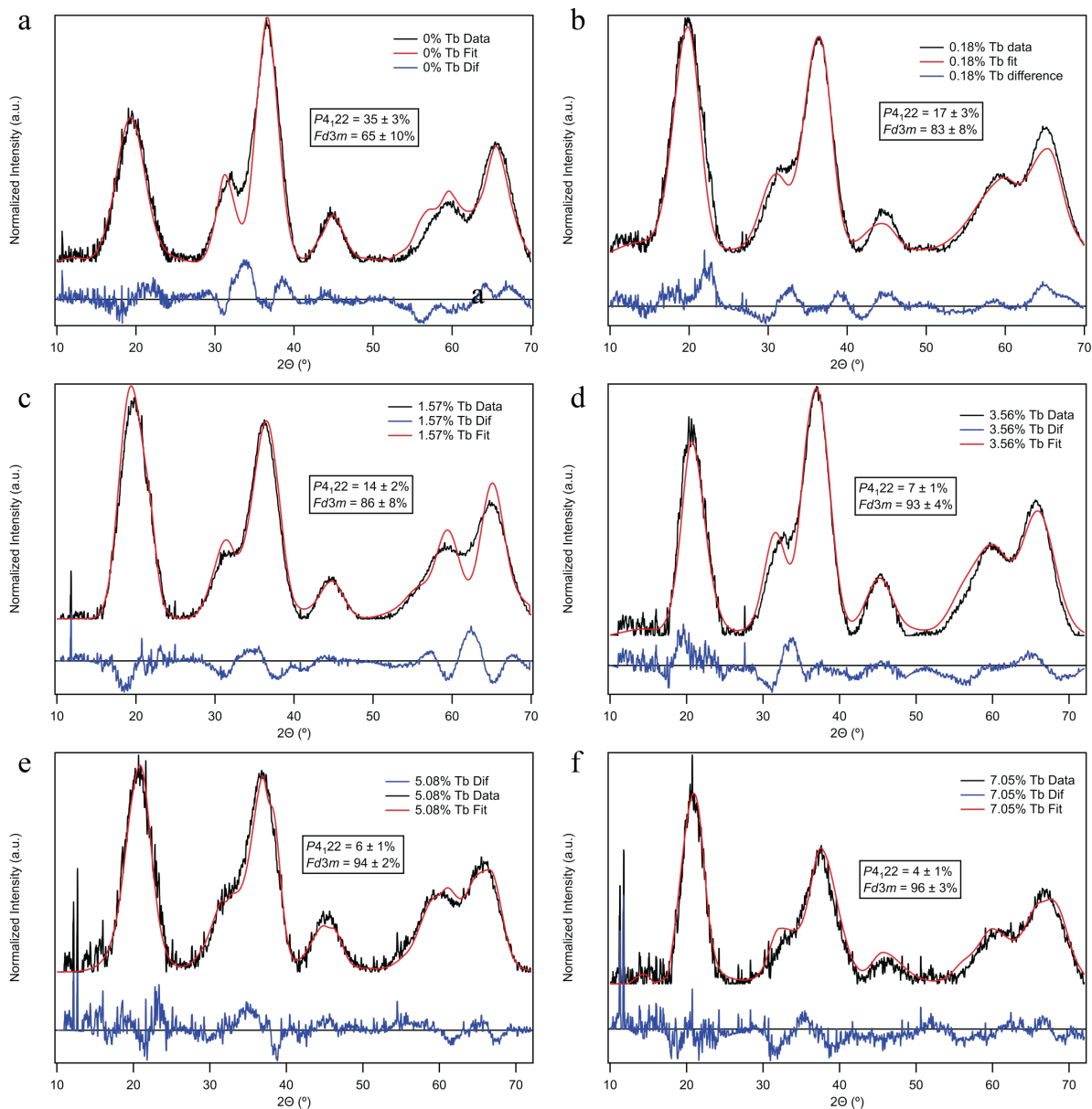
Figure 4.7. Whole pattern fitting of the a) 0% Tb:ZnAl₂O₄, b) 0.18% Tb:ZnAl₂O₄, c) 1.57% Tb:ZnAl₂O₄, d) 3.56% Tb:ZnAl₂O₄,e) 5.08% Tb:ZnAl₂O₄, and 7.05% Tb:ZnAl₂O₄. The black trace is the pXRD data, red trace is the fit, and the blue trace is the difference pattern.

phase transition within the material is occurring with increasing Tb(III) content. As anticipated, local changes in structure are observed in the fractional population of the tetragonal phase, the DOI, and the chemical shift, where the inflection point is within experimental error. The strain parameter (ε) inflection is shifted to higher concertation reflecting normal spinel domain
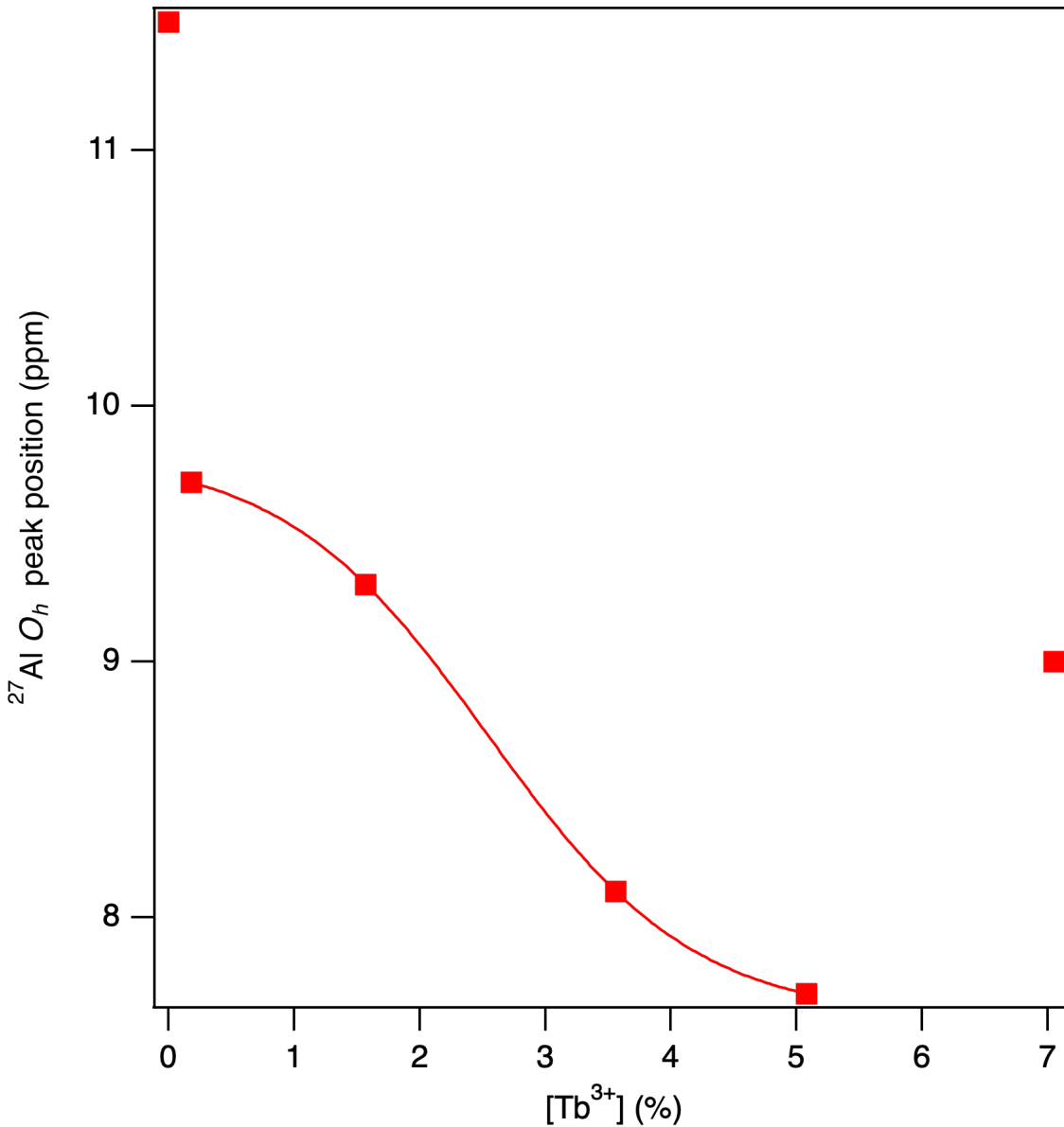
Figure 4.8. O_h peak position determined from the ^{27}Al MAS-NMR *vs.* Tb(III) concentration.

coalescence within the nanocrystal occurs first to accommodate the large cation size mismatch between Al(III) and Tb(III).

The postulate that a phase transition is induced by localized strain due to cation size mismatch has been reported previously in spinel lattices. Stevanović and Zunger, *et al.*[54] postulated that all inverse spinel oxides nucleate as the pure $P4_122$ tetragonal structure based upon cation pairing energies. As the cation radius rules lead to a normal spinel, a lower degree of inversions is
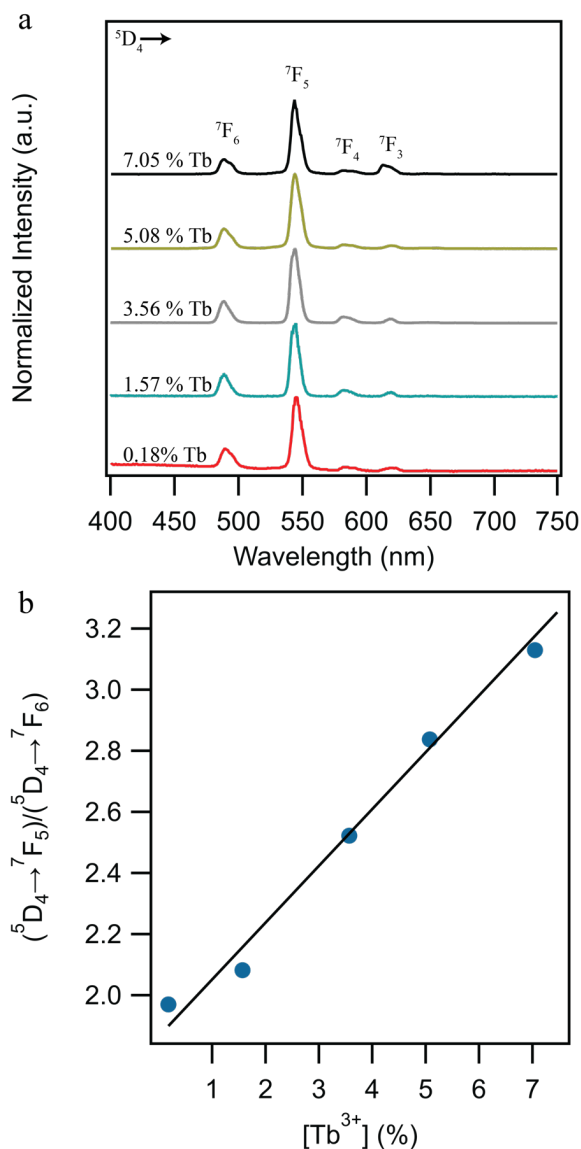
Figure 4.9. a) Photoluminescence emission spectra of hfacac passivated $Tb_xZnAl_{2-x}O_4$ nanospinels in EtOH excited at 320 nm at 298 K and b) displays the ratio of the $(^5D_4 \rightarrow {}^7F_5)/ (^5D_4 \rightarrow {}^7F_6)$ transitions, noted as the green/blue ratio.

observed but can be theoretically treated as the incorporation of cubic sites as an admixture as the lattice transitions to a normal spinel. Experimentally, Lang, *et al.*[46] observed the appearance of an admixture of cubic and tetragonal phases in $Mg_xNi_{1-x}Al_2O_4$ with increasing Ni(II) content. The experimental studies observed that higher DOI values correlate with an increase in the tetragonal (inverse) $P4_122$ phase fraction. The literature results and experimental observations support a model wherein cation size mismatch leads to increasing strain in the nanocrystal samples driving structural disorder in the spinel. The structural disorder will break the site symmetry for the Tb(III), which is anticipated to lead to changes in the optical properties, including a shift in the color purity and the PLQY.

4.3.2. Optical Properties.

For the Tb(III) cation, the site symmetry around the Tb(III) guest ion arising from the admixture of $P4_122$ and $Fd\bar{3}m$ within the nanocrystal lattice will be observable in the intensity of the Judd-Ofelt (JO) allowed transitions for Tb(III).[239, 240] An electric dipole (ED) transition is allowed for a Ln(III) site occupying a non-centrosymmetric site

Table 4.2. Optical properties of x% $Tb_xZnAl_{2-x}O_4$.

Sample	G/B	PLQY (%)	τ (ms)	k_r (ms)	k_{nr} (ms)
0%	-	-	-	-	-
0.18%	1.97	5.3 (0.5)	0.857	0.062	1.105
1.57%	2.08	20.9 (2.8)	0.756	0.209	1.046
3.56%	2.52	37.0 (3.1)	0.746	0.496	0.845
5.08%	2.83	19.1 (2.2)	0.733	0.261	1.104
7.05%	3.13	4.2 (0.9)	0.718	0.058	1.334

and forbidden for a centrosymmetric site. The magnetic dipole (MD) transition allowedness is independent of the site symmetry. The allowedness of the JO transitions reflect the selection rules for the ED and MD transitions. The selection rules for assigning ED transitions are $|\Delta J| \leq 6$, $|\Delta J| = 2, 4, 6$ and $|\Delta L| \leq 6$, whereas MD transitions are assigned when $\Delta J = 0, \pm 1$ and $\Delta L = 0$. For both MD and ED transitions the spin selection rule dictates that spin must be conserved ($|\Delta S| = 0$).

In Figure 4.1, the ED and MD character of the main intensity line for Tb(III) are shown. For Tb(III), the most intense feature at 544 nm is assigned as the $^5D_4 \rightarrow {}^7F_5$ and has contributions from both MD and ED transitions making it less sensitive to site symmetry.[94, 218, 241] The $^5D_4 \rightarrow$ $^7F_6$ transition is a pure ED transition ($|\Delta J| = 2$, $|\Delta L| = 1$) and therefore the intensity of the transition is strongly susceptible to the local environment.[93, 94] The symmetry sensitivity of the JO lines allows the ratio of the integrated intensity for the MD to ED transitions , often termed the blue-green ratio, to act as a convenient probe of lanthanide site symmetry. In $Tb_xZnAl_{2-x}O_4$ the blue-green ratio will act as an internal validator of the lattice transitions form a tetragonal (0%) to a cubic (7.05%) lattice and provide optical evidence of the observed lattice strain caused by the incorporation of the Tb(III) onto the Al(III) site.

In Figure4.9a, it is observed that excitation into hfacac (λ_{ex} = 320 nm) leads to population of the Tb(III) $^5D_4$ excited state levels. The population of the $^5D_4$ levels occurs through a Dexter
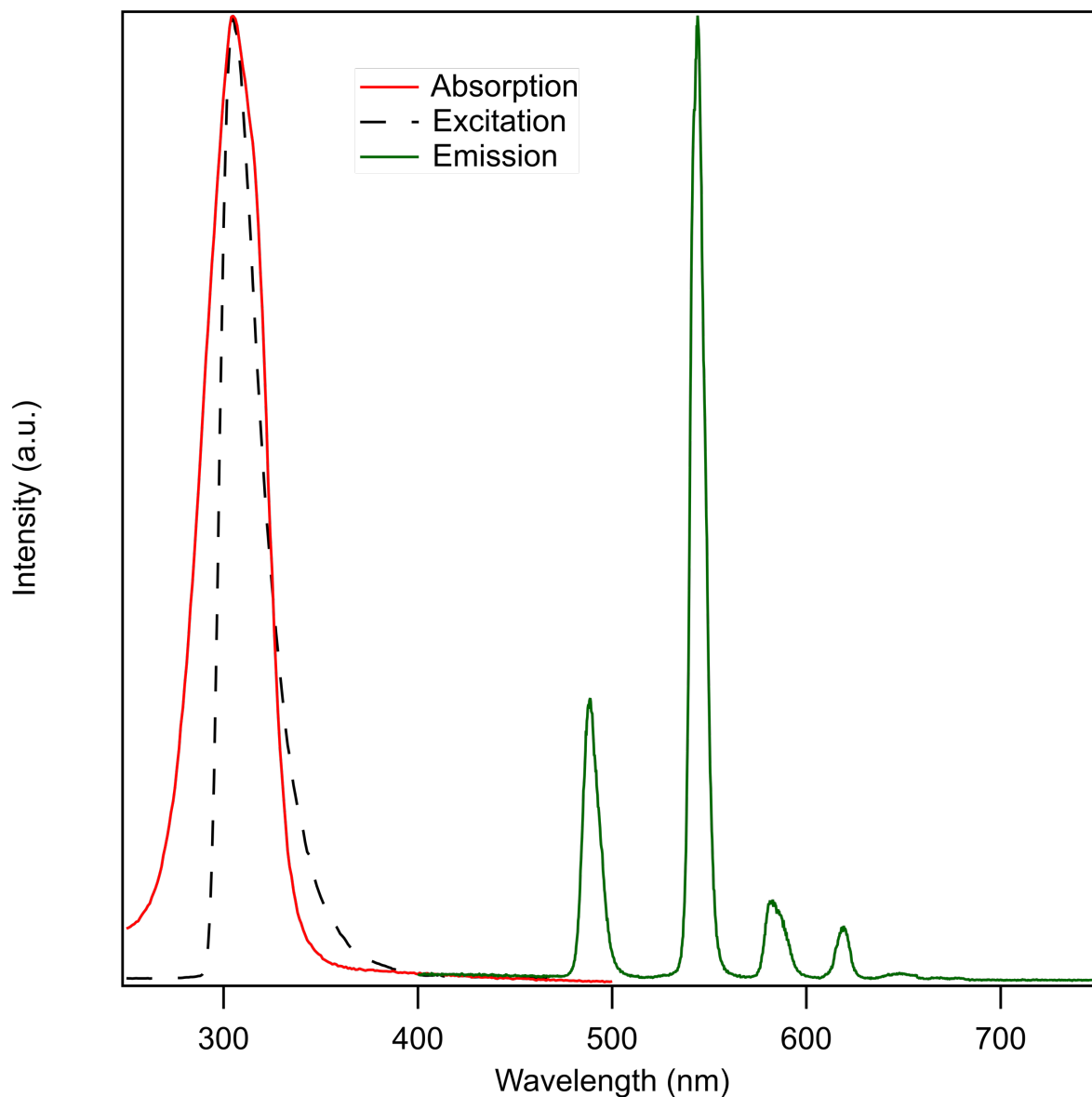
Figure 4.10. Photoluminescence spectra of the hfacac passivated 0.18% Tb:ZnAl$_2$O$_4$ exciting at λ_{ex} = 320 nm (green trace). Photoluminescence excitation spectra monitoring the $^5D_4 \rightarrow {}^7F_5$ transition at 544 nm (dashed, black trace) and UV-Vis absorption shown in the red trace. All spectra were collected at 298 K and in cyclohexane.

energy transfer molecular antenna sensitization process.[30, 115] Photoluminescence excitation spectra obtained by monitoring the $^5D_4 \rightarrow {}^7F_5$ line confirms hfacac acts as a molecular sensitizer for the Tb(III) centers due to the overlap of the absorption and excitation spectra and is available in Figure 4.10. The observed steady state photoluminescence (PL) emission for all samples are
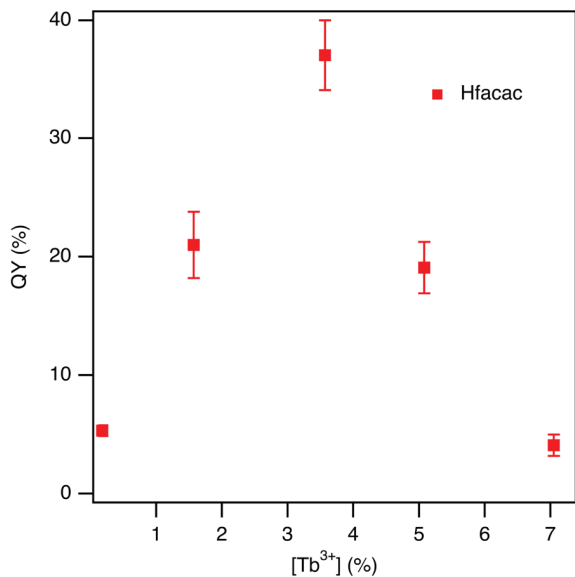
Figure 4.11. Photoluminescence quantum yields of the hfacac passivated $Tb_xZnAl_{2-x}O_4$ nanospinels excited at 320 nm at 298 K in EtOH.

assignable to the discrete $^5D_4 \rightarrow {}^7F_J$ transitions (^7F_J assignments are labeled in Figure 4.9a). The optical data for the $Tb_xZnAl_{2-x}O_4$ samples collected at $\lambda_{ex} = 320$ nm is listed in Table 4.2.

The concentration dependent PLQY for the $Tb_xZnAl_{2-x}O_4$ samples is plotted in Figure 4.11 and exhibits a maximum PLQY value (37%) at a Tb(III) concentration of 3.56%. As the concentration increases above 3.56% Tb(III), a quenching behavior is observed to coincide with the increased contribution of the cubic ($Fd\bar{3}m$) spinel. Since a Tb(III) sitting on an inversion center will have a lower quantum yield than a Tb(III) occupying a non-centrosymmetric site, the PLQY for the sample will decrease with increasing Tb(III) content due to the increasing site population for the centrosymmetric Tb(III) center in the cubic lattice (Figure 4.11). The competitive influences explain the observed peak PLQY of 37% observed in Figure 4.11 for the 3.65% Tb(III) in the $Tb_xZnAl_{2-x}O_4$ nanospinels. The Tb(III) excited state lifetime exhibits no maximum value but exhibits a decrease with increasing concentration, as shown in Table 2 and Figure 4.12. The observed 16% decrease in lifetime may arise from a reduced radiative rate concurrent with the increase in cubic phase arising from the increasing symmetry about the Tb(III) cation or from concentration dependent Tb-Tb nearest neighbor self-quenching. The self-quenching effect has been previously observed for Tb(III) phosphors.[97, 98 96-98, 226, 227]
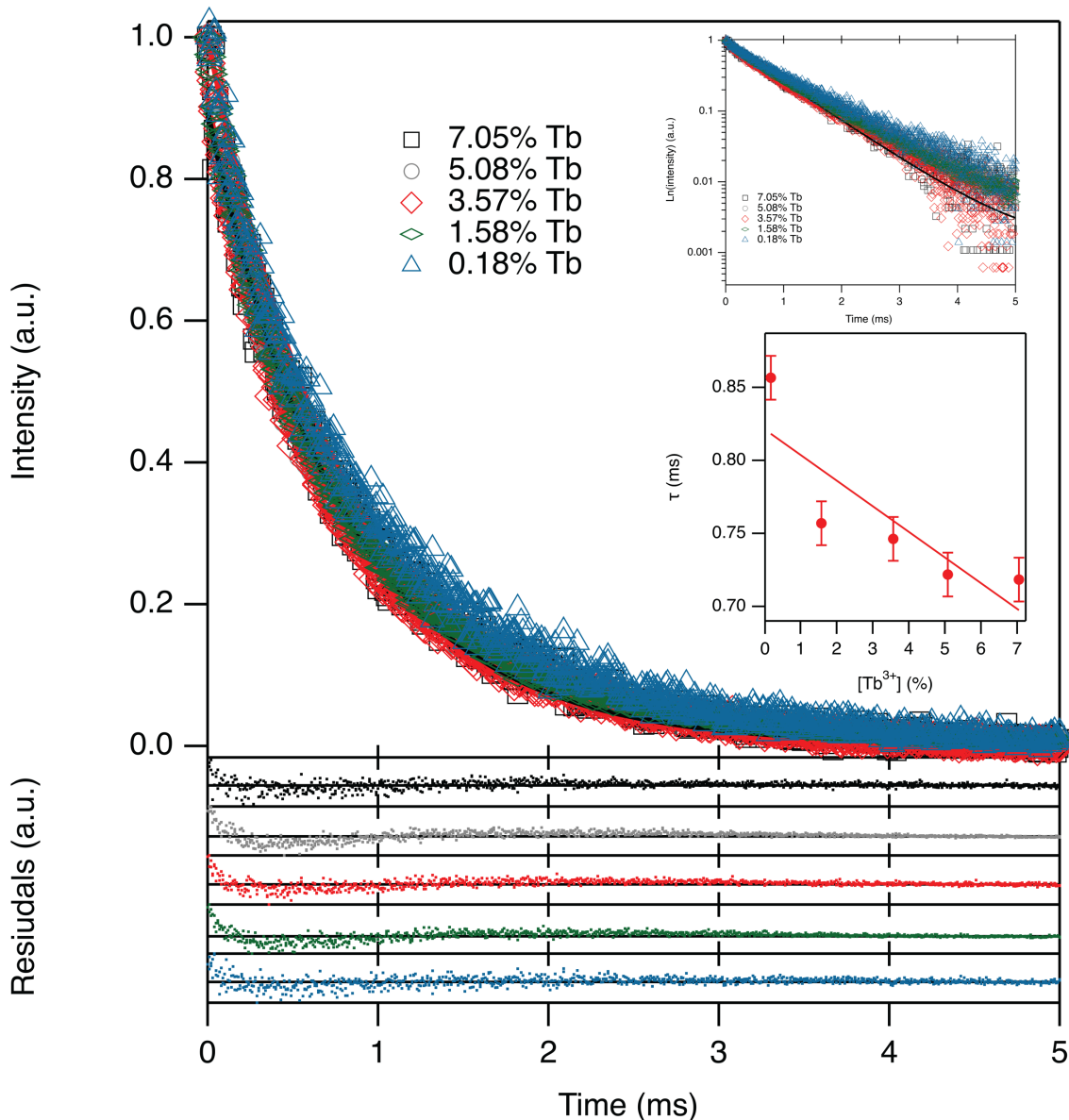
Figure 4.12. Lifetimes of the x% Tb:ZnAl$_2$O$_4$ nanospinels monitoring the $^5D_4 \rightarrow ^7F_5$ transition at 544 nm. Data was collected at 298 K in EtOH under ambient conditions with a Nd:YAG laser operating at 1 Hz. The data was fit to a mono-exponential decay curve where the observed lifetimes *vs*. concentration are plotted in the inset.

In Figure 4.9b, a plot of the ($^5D_4 \rightarrow ^7F_5$) / ($^5D_4 \rightarrow ^7F_6$) ratio *vs*. the Tb(III) concentration exhibits a linear increase proportional to the Tb(III) concentration. Lower ($^5D_4 \rightarrow ^7F_5$) to ($^5D_4 \rightarrow ^7F_6$) ratios imply a non-centrosymmetric site (no inversion center) while higher ($^5D_4 \rightarrow ^7F_5$) to ($^5D_4 \rightarrow ^7F_6$) ratios imply the appearance of an inversion center.[93, 94] The change in symmetry leads to a

switch from non-centrosymmetric to centrosymmetric site occupation for the Tb(III) ion induced by strain associated with the larger Tb(III) center occupying the smaller Al(III) site. The symmetry changes are reported as an enhancement of the PLQY and a redistribution in the intensities of the green ($^5D_4 \rightarrow {}^7F_5$) and blue ($^5D_4 \rightarrow {}^7F_6$) transitions. The change in ($^5D_4 \rightarrow {}^7F_5$) to ($^5D_4 \rightarrow {}^7F_6$) ratio further confirms the concentration dependent increase in the centrosymmetric site for Tb(III) in $Tb_xZnAl_{2-x}O_4$, as evidenced in the PLQY, the NMR DOI, and the pXRD refinement (Table 2). The optical response of the $Tb_xZnAl_{2-x}O_4$ is correlated to changes in the physical properties determined from the characterization by pXRD and ^{27}Al NMR data.

4.4. Conclusion.

The functional properties of the down-shifting phosphor, $Tb_xZnAl_{2-x}O_4$, as illustrated by the enhancement of PLQY, reduction in lifetime, and enhancement of green-blue intensity ratio can be directly linked to the structural changes occurring within the nanospinel due to cation radius mismatch and the flexibility of spinel lattices to accommodate strain through changes in the DOI.[48] In the case of the Tb(III) emission, the transition from $P4_122$ phase transitions to the $Fd\overline{3}m$ phase increases the site symmetry from a trigonally distorted octahedron to a normal octahedron with the appearance of an inversion center leading the activation of the Laporte selection rule, reducing the intrinsic QY of the Tb(III) nanophoshor.

The use of optical probes to interrogate the site symmetry for a substitutional ion is a powerful tool for evaluating nanocrystals. [219, 242-244] In the case of phosphors, the lanthanide ion can not only act as the luminophore but also as a probe of the structure due to the sensitivity of the electric and magnetic dipoles for *f-f* centered transitions. Analysis of the optical data confirms that the Tb(III) site symmetry in $Tb_xZnAl_{2-x}O_4$ is distorted with increasing Tb(III) concentration. The data is in agreement with the ^{27}Al NMR and whole pattern fitting analysis of the samples, where a

sigmoidal change in DOI is observed with increasing Tb(III) content. A maximum of 37% PLQY was observed at 3.56% Tb(III) followed by a severe quenching behavior caused by the increased cubic spinel phase contributions. These observations are supported by the reports of Stevanović *et al.*[54] and Lang *et al.*[46] where theoretical and experimental results suggest that spinels are comprised of an admixture of tetragonal and cubic lattices. Strain induced lattice effects are an underexplored quenching mechanism in lanthanide doped down-shifting nanoparticles with a few reports based upon the $NaYF_4$ lattice. As the demand to reduce Y(III) content increases, researchers are challenged with the development of tomorrow's technology with earth abundant compositions.

CHAPTER 5

SPECTRALLY ENGINEERING A 2-COLOR NANOPHOSPHOR THROUGH CONTROL OF ENERGY TRANSFER, OCTAHEDRAL TILTING, AND QUADRUPOLE-QUADRUPOLE COUPLING

Control of the energy transfer pathways in a 2-color phosphor was explored for a 2 nm $Tb_xEu_{0.07-x}$:$ZnAl_{2-x}O_4$ nanospinel. The phosphor exhibits a photoluminescence quantum yield of 45% and can be spectrally engineered through doping concentration and excitation wavelength. Excitation into the $^1\pi^*$ energy level of the β-diketonate passivating layer leads to a competitive population of the Tb(III) and Eu(III) centers *via* a Dexter energy transfer process, while excitation into the Tb(III) $^7F_6 \rightarrow ^5D_4$ absorption populates the Eu(III) through quadrupole-quadrupole resonant coupling. Time resolved emission measurements allow the elucidation of the individual population of the emitting states, the role of octahedral tilt in the nanospinel lattice, and the nature of resonant energy coupling that lead to spectral tuning. Fitting the decay data to a stretched exponential function that incorporates the quadrupole-quadrupole orientation within the spinel lattice, the degree of octahedral tilting to reduce lattice strain following lanthanide incorporation onto the Al(III) cation site in the spinel can be directly visualized. Interestingly, the tilt for the core and surface are unique, implying reconstruction of the surface following hfacac passivation may be present. The results of the study open a strategy that allows spectral engineering of a 2-color phosphor potentially useable for future smart-LED downshifting lighting.

5.1 Introduction.

Solid state lighting has advanced through design of new down-shifting phosphors that reduce rare earth content to reduce cost,[30, 170, 245, 246] isolation as nanophosphors to reduce scattering losses,[247, 248] and the use of a passivating shell to enhance dissolution in the lens materials, as well

as a molecular antenna to enhance the conversion efficiency.[29, 30, 172] As lighting technology continues to progress, the capacity to spectrally engineer a down-shifting phosphor by controlling color coordinates through changes in excitation wavelength can lead to smart-LED based solid state lighting capable to adapting to environmental changes and user perception. This is particularly important in night-lighting where blue can lower visual acuity.[249] While many approaches to address this problem exist,[250-253] one plausible strategy for a single phosphor is to manipulate the energy transfer pathways within a single host lattice containing coupled emitters.

In this manuscript we explore the ability to spectrally engineer the color of a 2 nm nanophosphor containing Tb(III) and Eu(III) doped into an earth abundant host lattice based on the $ZnAl_2O_4$ spinel lattice. The phosphor is surface passivated by hexafluoracetylacetonate (hfacac) to act as a molecular antenna that enhances the photon absorption cross section since the host lattice is optically transparent in the >350 nm range. In addition, hfacac promotes dissolution in non-polar and polar solvents making it a viable phosphor for dispersion in LED lenses. Spectral tuning in these phosphors arises from competitive energy transfer pathways within the co-doped nanospinel. Excitation into the hfacac passivant leads to a competitive population of the Tb(III) and Eu(III) emitting centers that scales with dopant concentration and the efficiency for Dexter energy transfer from the passivant π^* excited state to the Judd-Ofelt (J-O) levels of the lanthanides. Excitation into the Tb(III) J-O levels at 488 nm leads to population of both Tb(III) and Eu(III) via quadrupole-quadrupole resonant coupling between the lanthanide ions, while excitation at 394 nm into the Eu(III) levels leads to only Eu(III) allowed J-O level population. Consistent with the population through energy transfer pathways, the efficiency is dictated by the separation distance of the dopants and the quadrupole orientation within the spinel lattice. The wavelength dependent population allows selective tuning of the green to red ratio in the single 2 nm nanospinel.

In co-doped Tb(III)/Eu(III) containing nanophosphors, assignment of the nature of the electric field in the energy transfer process between the Ln(III) cations is controversial with reports of dipole-dipole,[118-120] dipole-quadrupole,[119, 252, 254, 255] or quadrupole-quadrupole[105-107] resonant coupling. For the $Tb_xEu_{0.07-x}$:$ZnAl_{2-x}O_4$ samples, the emission process involves a series of coupled energy transfer pathways. Fitting the Tb(III) decay to a stretched exponential allow a direct measure of the electric field coupling (β-value), as well as an orientation term for the octahedral sites containing the lanthanide ions. Excitation into the Tb(III) centers leads to a β-value of 0.3 consistent with a quadrupole-quadrupole interaction, confirming the observation of others. Analysis of the octahedral tilt from the κ-value indicates a distortion of the Al(III) site occurs in the spinel. It is believed this is due to cation radii mismatch ($r_{Al(III)}$ = 53.5 vs. $r_{Eu(III)}$ = 94.7 , $r_{Tb(III)}$ = 92.3 pm)[231] leading to lattice distortion. The resultant distortion produces a nanophosphor with 45% PLQY due to breaking of the centrosymmetric symmetry at the Al(III) site in the nanospinel. The observation of octahedral tiling upon lanthanide incorporation into $ZnAl_2O_4$ PLQYs of 50% and 42% for single doping of Eu(III)[30] and Tb(III),[228] respectively.

5.2 Experimental.

5.2.1 Materials.

All commercially available reagents and solvents, with the exception of dimethylformamide (DMF) were used without further purification. DMF was dried over molecular sieves. The passivating ligand was 1,1,1,5,5,5-hexafluoro-2,4-pentanedione (hfacac, Alfa Aesar, 98+%). Zinc (II) undecylenate (Spectrum, 98%), oleylamine (Aldrich, 70%), Nitrosonium tetrafluoroborate ($NOBF_4$, Alfar Aesar, 98%), aluminum (III) 2, 4-pentanedionate (Strem Chemicals, 99%), europium (III) 2,4-pentanedionate hydrate (Alfa Aesar, 99.9%), and terbium (III) 2,4-pentanedionate hydrate (Alfa Aesar, 99.9%) were obtained from various sources.

5.2.2 Synthesis of $Tb_x, Eu_{0.07-x}:ZnAl_{2-x}O_4$ (x=0, 0.007, 0.015, 0.022, 0.049, 0.051, 0.070).

Zinc aluminate nanospinels were synthesized by thermal decomposition of molecular precursors. Zinc undecylenate ($Zn(UND)_2$, 0.25 mmol), aluminum 2,4-pentanedionate ($Al(acac)_3$, 0.5 mmol), europium (III) 2,4-pentanedionate hydrate ($Eu(acac)_3$), and terbium(III) 2,4-pentanedionate ($Tb(acac)_3$) were added to a 10mL pyrex microwave vial with olyelamine (70% Tech grade, sigma). The reaction vial was heated to 280 °C for 10 minutes in a 2.45GHz Anton Paar MW reactor operating at 300W. To isolate the materials, the reaction vessel is cooled with forced air cooling, and the nanospinels isolated by addition of MeOH and centrifugation. Samples were dried under reduced pressure.

5.2.3 Characterization.

Structural characterization was performed using powder X-ray diffraction (pXRD) recorded on a Rigaku DMAX 300 Ultima III Powder X-ray diffractometer (using Cu K_α $\lambda = 1.5418$ Å radiation). The size of the nanocrystals were measured by fitting the pXRD pattern to the Scherrer broadening equation, $L = K\lambda/\beta cos\theta$, where L is the crystallite size, K is the shape factor and assumed to be 1.0 corresponding to spherical nanocrystals, λ is the X-ray wavelength measured in nm, β is the peak width at half height at a given 2θ value, and θ is the Bragg angle. Transmission electron microscopy (TEM, JOEL, 200kV) was performed to analyze particle sizes and distributions. Samples were prepared by drop casting a dispersion of nanoparticles in toluene on a 300 mesh Cu grid and dried overnight. Elemental concentrations were measured by inductively coupled plasma-mass spectrometry (ICP-MS, Thermofischer) by digesting nanoparticles in trace grade HNO_3.

Figure 5.1. Jablonski diagram of a hexafluoroacetylacetonate passivated $Tb_xEu_{0.07-x}:ZnAl_{2-x}O_4$ illustrating the multiple energy transfer pathways within the nanophosphor. The schematic to the right shows the crystallographic unit cell with the octahedral sites for Al(III) highlighted along with the trigonometric relationships for the quadrupoles on the Tb(III) and Eu(III) centers. A simplified projection of the θ_D, θ_A, θ_T and r is shown below the unit cell to highlight the role of the orientation factor (κ^2) in resonant energy transfer coupling.

5.2.4 Optical Methods.

Ligand passivation was analyzed by Fourier transform infrared (FT-IR) measured on powdered samples using a PerkinElmer Spectrum 100 FT-IR Spectrometer equipped with an attenuated total reflectance (ATR) sample chamber consisting of a ZnSe crystal over coated with diamond using a single-bounce configuration. Solution UV-Vis absorption spectra were recorded in toluene using a 1-cm quartz cuvette in a Varian Cary 50 UV-Vis spectrometer. The photoluminescence (PL) and photoluminescence excitation (PLE) spectra were recorded on a Horiba Fluoromax spectrofluorimeter equipped with a 150 W CW Ozone free xenon arc lamp,
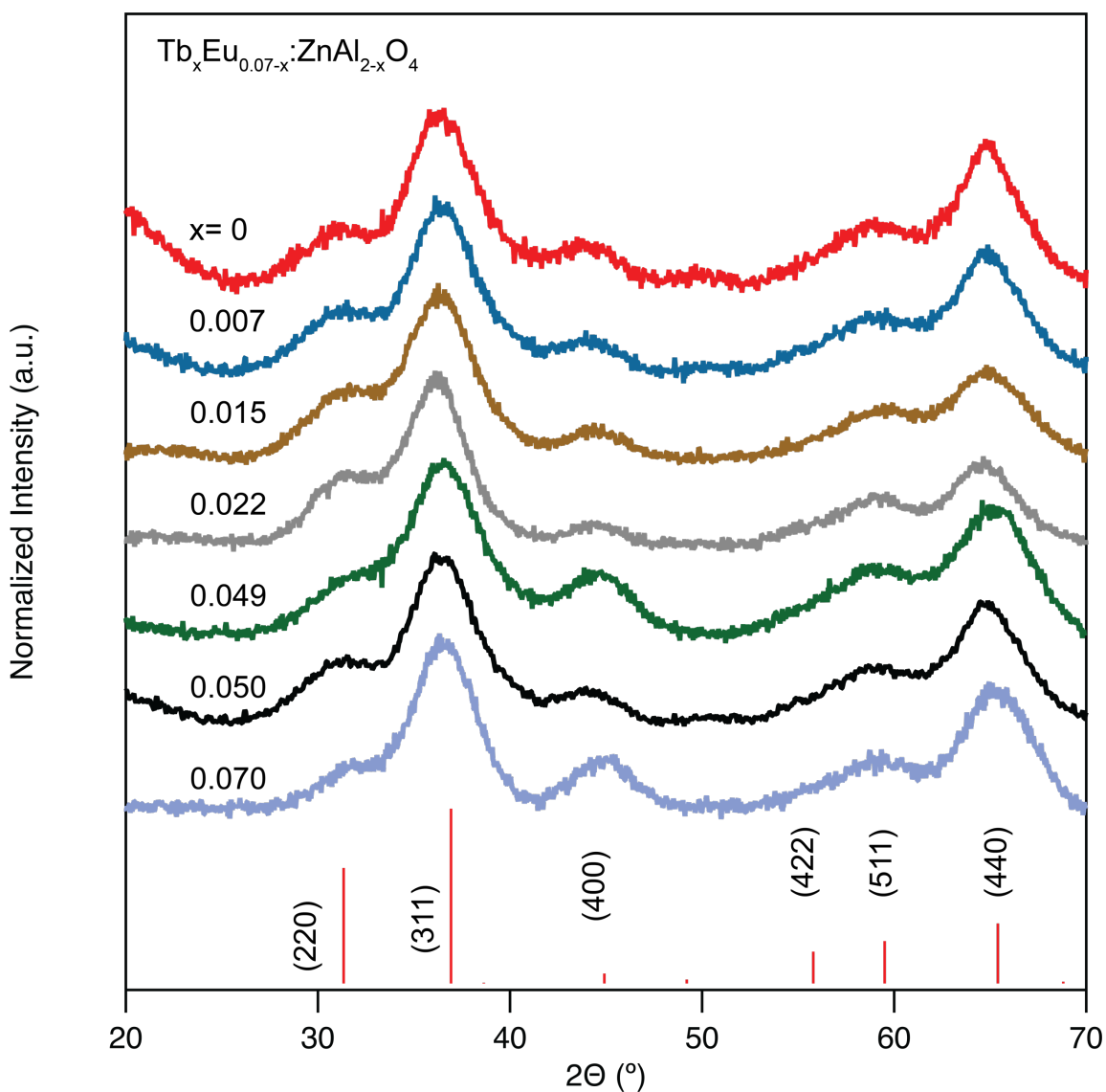
Figure 5.2. Powder X-Ray diffraction patterns indexed to the cubic - $Fd\bar{3}m$ phase (JCPDS 073-1961) for the $Tb_xEu_{0.07-x}:ZnAl_2O_4$

Czerny-Turner monochromators with excitation grating blazed at 330 nm (1200 groove/mm) and the emission grating blazed at 500 nm (1200 grooves/mm). The PL and PLE measurements wee carried out on N_2 sparged samples.

All spectra were corrected for the instrument response function and the intensity of the lamp. Photoluminescence quantum yield were measured by the relative method using thenoyltrifluoroacetonato 1,10-phenanthroline europium(III) complex (Eu(TTA)$_3$phen) as a

standard in EtOD. Linear regressions were generated by plotting the integrated intensity *vs.* the absorption of serial dilutions. Comparison of the slopes between the standard and the sample, allow for determination of accurate QYs displayed in equation (3):

$$\Phi_s = \Phi_r \left(\frac{m_s}{m_r}\right) \left(\frac{\eta_s^2}{\eta_r^2}\right) \tag{3}$$

Where *m* is the slope and η is the refractive index of the solvent. Subscripts *r* indicate the reference while *s* indicates the sample. The standard and samples were measured in EtOD at 298 K leading to the removal of the refractive index term.

Lifetime measurements were recorded on an Edinburgh Instruments LP980-KS and excited by a Continuum Nd:YAG laser coupled to an optical parametric oscillator with the resulting excitation wavelength of 320 nm or 488 nm. Samples were recorded in N_2 sparged EtOD at 298 K so that radiative rates could be calculated. Lifetimes were fit to a stretched exponential equation using Mathematica and IGOR 8.0.

5.3 Results and Discussion.

5.3.1 Preparation of 2-Color Nanospinel.

To evaluate the spectral tuning and the energy transfer pathways, a series of $Tb_xEu_{0.07-x}:ZnAl_{2-x}O_4$ nanospinels were prepared using previously reported protocols based upon microwave induced thermal decomposition of zinc undecylenate and aluminum acetylacetonate (acac) in the presence of the lanthanide acac complexes in oleylamine (OAm) at 280 ℃ (10 min, 300W). The OAm/acac passivated nanospinels were isolated by addition of methanol and centrifuged prior to ligand exchange to hfacac coordinated to the surface of the $ZnAl_2O_4$ nanospinel *via* the Murray nitrosonium tetrafluoroborate (NOBF₄) protocol.[185] The isolated nanospinel pXRD pattern can be fit to cubic Fd3m, JCPDS #073-1961 (Figure 5.2).
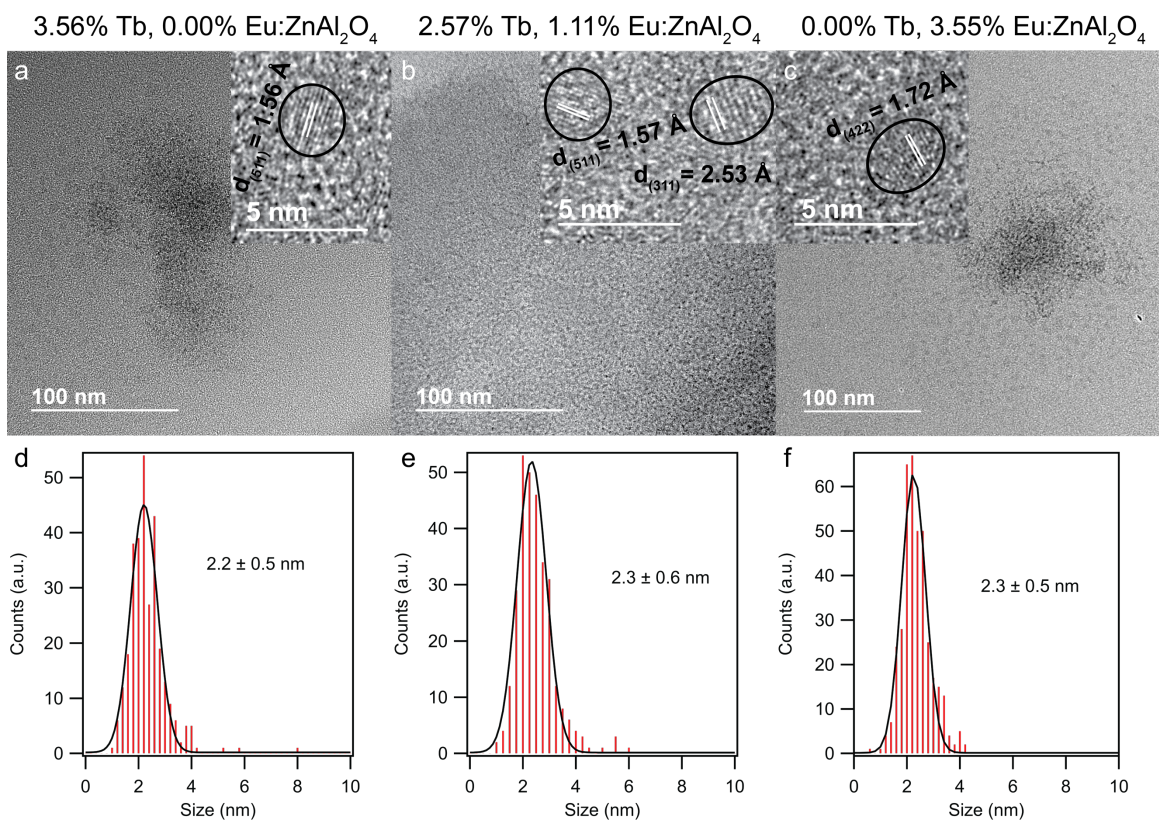
Figure 5.3. Low resolution TEM images for a) 3.56% Tb, 0.00% Eu:$ZnAl_2O_4$, b) 2.57% Tb, 1.11% Eu:$ZnAl_2O_4$, and c) 0.00% Tb, 3.55% Eu:$ZnAl_2O_4$ nanospinels where the insets display high resolution TEM images showing fringes assignable to the $ZnAl_2O_4$ lattice. The size dispersity was determined by analysis of >300 nanoparticles and are reported in d) 3.56% Tb, 0.00% Eu:$ZnAl_2O_4$, e) 2.57% Tb, 1.11% Eu:$ZnAl_2O_4$, and f) 0.00% Tb, 3.55% Eu:$ZnAl_2O_4$.

Table 5.1. Elemental compositions determined from ICP-MS following digestion of $Tb_xEu_{0.07-x}$:$ZnAl_{2-x}O_4$ in trace grade HNO_3.

Tb$_x$Eu$_{0.07-x}$:ZnAl$_2$O$_4$			
x =	[Tb^{3+}] (%)	[Eu^{3+}] (%)	[Zn^{2+}]:[Al^{3+}] (mol)
0	0	3.55	1.00:1.98
0.007	0.37	2.52	1.00:1.91
0.015	0.76	2.37	1.00:1.93
0.022	1.11	2.57	1.00:1.90
0.049	2.43	0.80	1.00:1.99
0.050	2.51	0.23	1.00:1.97
0.070	3.56	0	1.00:2.01
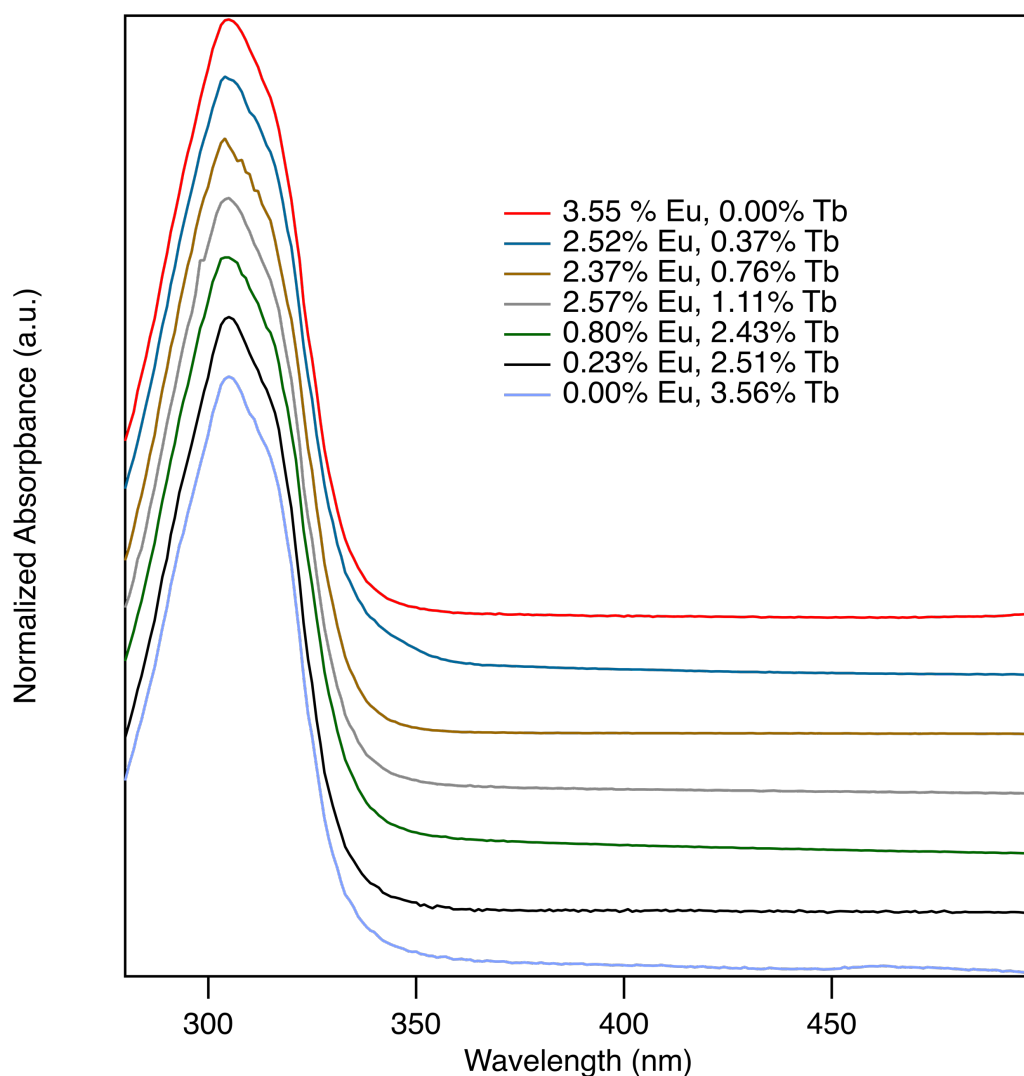
Figure 5.4. UV-Vis absorption of the hfacac exchanged $Tb_xEu_{0.07-x}:ZnAl_{2-x}O_4$ nanospinel phosphors in toluene at 298 K. The feature centered at 304 nm is assignable to the hfacac $^1(\pi \rightarrow \pi^*)$ transition.

TEM imaging reveals the isolation of ~2nm spherical nanospinel, consistent with earlier reports and are shown in Figure 5.3.[30, 228] The composition of the spinel for Tb(III) and Eu(III) measured by ICP-MS is listed in Table 5.1 as a function of *x* for the $Tb_xEu_{0.07-x}:ZnAl_{2-x}O_4$ nanospinels. Complete characterization data for the hfacac-passivated $Tb_xEu_{0.07-x}:ZnAl_{2-x}O_4$ nanospinels including powder X-ray diffraction, TEM, ICP-MS, UV-Vis, FTIR, and PLE are shown in Figure 5.2, Figure 5.3, Table 5.1, Figure 5.4 Figure 5.5 and Figure 5.8, respectively.
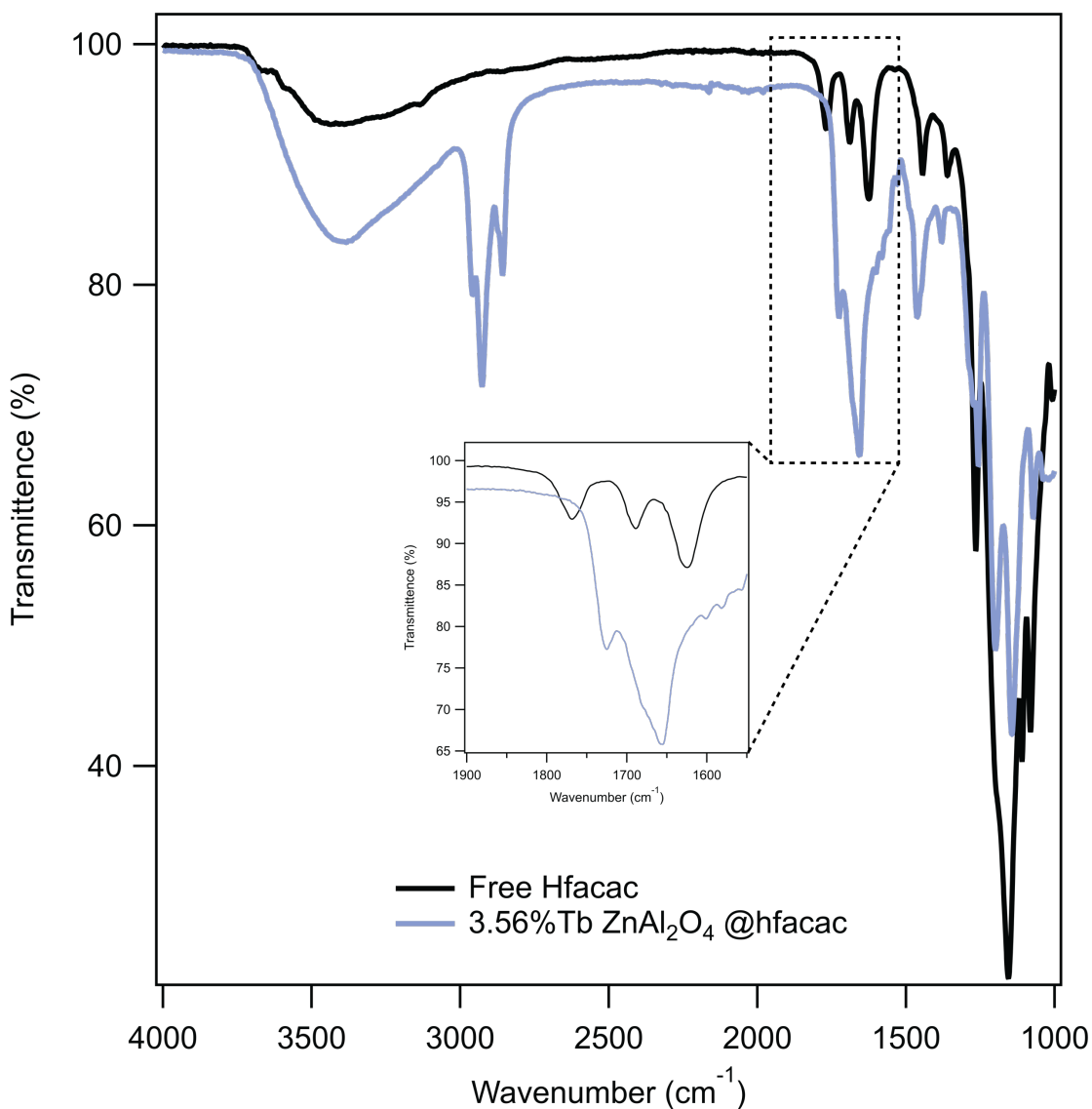
Figure 5.5. FTIR spectra of the free hfacac (black trace) and hfacac exchanged 3.56% Tb:ZnAl$_2$O$_4$ nanospinels (purple trace). The shift in ketone frequency confirms coordination and a change in symmetry to the ketone stretch following the passivation of the nanospinel (inset).

5.3.2 Energy Transfer Pathways.

For a Tb(III) and Eu(III) doped host lattice the red to green ratio will be modified by the concentration of acceptors and the sensitization efficiency for population via multiple energy transfer pathways. As shown in Figure 5.1, the ability to spectrally tune the color of a phosphor,
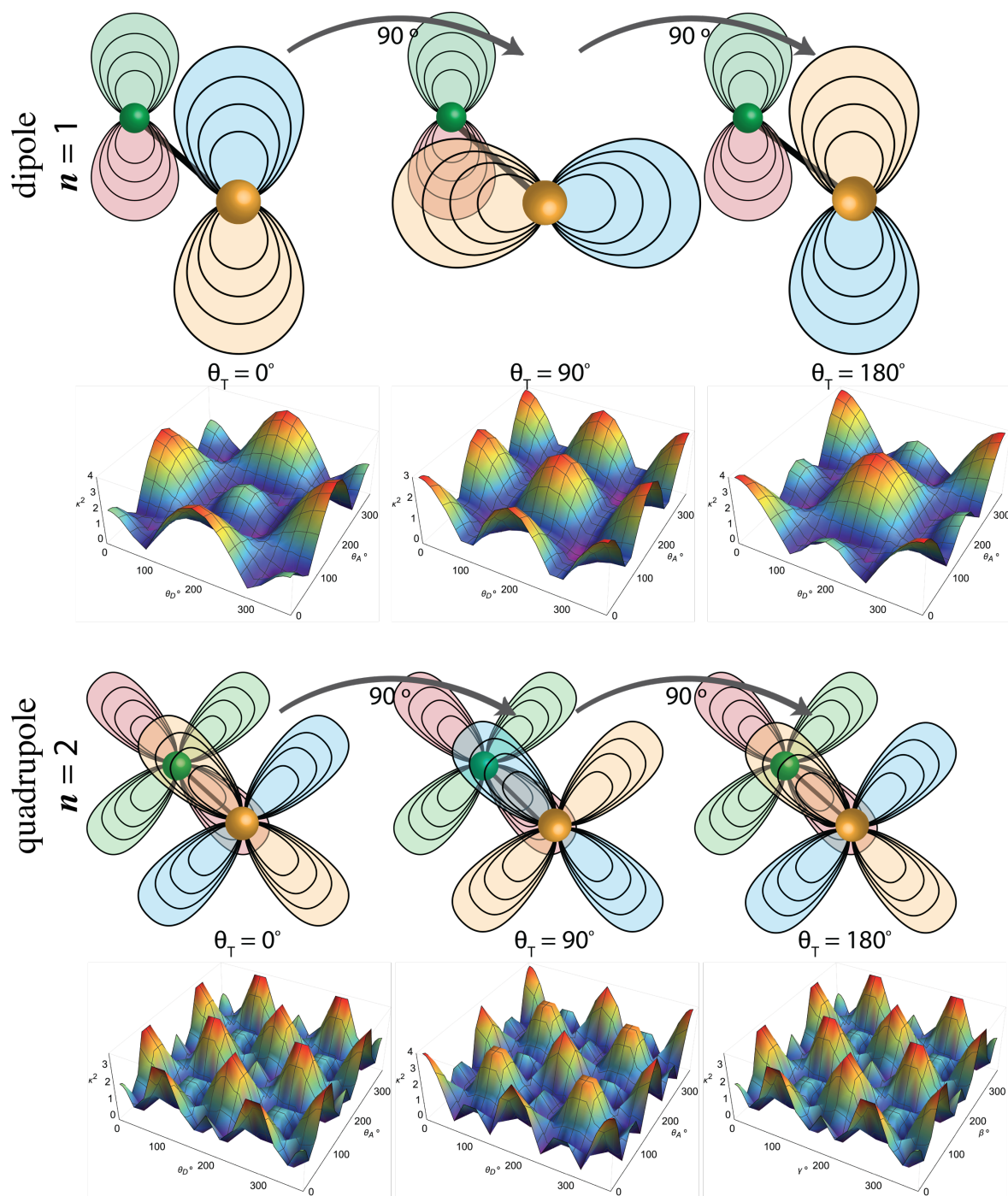
Figure 5.6. Theoretical prediction of the orientation κ^2 value for a dipole-dipole vs quadrupole-quadrupole coupling process when θ_T 0, 90, 180°. The projections illustrate the change in value with octahedral tilting within the spinel lattice between illustrating differences of dipole and quadrupole calculations.

effect control the CIE coordinates for a material, can be achieved by controlling the excited state population of two acceptors within a nanocrystal lattice through the manipulation of the energy coupling pathways shown in the Jablonski diagram. The overall quantum yield for the co-doped nanospinel phosphor will be dictated by the efficiency of energy probability for population of the individual pathways, the contribution to the PL from the Tb(III) and Eu(III) sites will change the color coordinate in a CIE plot. The effect is easily shown by considering the various quantum efficiencies involved. The sensitization of the lanthanide by themolecular passivant is a Dexter process that has been fully described previously.[115] The columbic interactions within the Dexter mechanism lead to an exponential dependency on distance between the donor and acceptor shown as, $k_{ent} = K <J> e^{-\frac{2R_{DA}}{L}}$, where K is the pre-exponential factor, R_{DA} is the separation between the donor and acceptor, and L is the effective Bohr radius. The ligand to the lanthanide sensitization for a single nanospinel size will therefore be governed by the spectral overlap function, $<J>$, and the number of donors within the spinel lattice, as the number dictates the distance (R_{DA}) for ligand to lanthanide energy sensitization. The passivating ligand, hfacac, has a triplet energy level that is 1,670 cm^{-1} above the $^5D_4$ excited state of the Tb(III) cation and 3,150 cm^{-1} above $^5D_1$ excited state level of the Eu(III) cation.

Energy transfer between the Tb(III) and Eu(III) centers has been reported to be governed by resonant energy transfer *via* dipole-dipole,[118-120] dipole-quadrupole,[119, 254] or quadrupole-quadrupole.[256-258] When considering the effect of dipole-dipole vs. quadrupole-quadrupole electric field interactions, the sensitization efficiency will vary with the angular dependence for resonant coupling as shown schematically in Figure 5.1b and Figure 5.6. The significant change in the magnitude of the κ value landscape for a dipole-dipole vs. quadrupole-quadrupole interaction is shown in Figure 5.6. For a dipole ($n = 1$) vs. quadrupole ($n = 2$) the resonance condition will be

influenced due to a second vector associated with the quadrupole.[92] When $n = 1$, the orientation of the dipoles is coherent at 0 and 2π, and perpendicular at $\pi/2$ and $3\pi/2$. At $n = 2$, the quadrupoles are coherent at 0, π, and 2π, and perpendicular at $\pi/4$, $3\pi/4$, $5\pi/4$, and $7\pi/4$. For the quadrupole, the net moment is zero and produces additional nodes shown in the 3D plots in Figure 5.6. As shown in Figure 5.6, the efficiency of energy transfer between the Tb(III) and Eu(III) ions incorporated into the nanospinel lattice are anticipated to be governed by, concentration and lattice structure influencing the donor-acceptor pair distances (R_{DA});[88, 89, 259] and the angles $(\theta_D, \theta_A, \theta_T)$[260] of the electric field, which are directly dependent of the lattice structure and strain induced by size mismatch.

The nature of resonant energy coupling can be described analogously to FRET allowing the energy coupling efficiency to be related to separation distance and can be mathematically described in terms of a critical distance (R_0), $R_0 = \left(\frac{9000(ln10)\kappa^2\emptyset}{128\pi^5 N_A n^4} J(\lambda)\right)^{1/(c)}$ where R_o is the distance at which there is an equal probability for energy to transfer to the acceptor or emit form the donor. In the expression, $\emptyset$ is the quantum yield of the donor, N_A is Avogadro's number, n is the refractive index of the media, (1.7940 for $ZnAl_2O_4$[122, 123]), c is the coupling constant either 6 (dipole-dipole), 8 (dipole-quadrupole), or 10 (quadrupole-quadrupole), and κ is the orientation factor of the electric field between the donor and acceptor described by $\kappa^2 = (cos(n * \theta_T) - 3cos(n * \theta_D)cos(n * \theta_A))^2$.[259, 261] Values for κ are constrained between 0-4 where values of 0 when the electric fields are perpendicular to each other, and 4 when the electric fields are parallel and collinear.[260-262] In molecular energy transfer system, a value of $2/3$ is assumed reflecting the random orientation in time for the dipoles;[14, 16] however, in a solid state material the κ is dependent on the doping site and lattice structure, since the lanthanides are not free to re-orient.

The theoretical treatment leads to an expectation of rollover kinetics in the Eu(III) PL time dependent decay if the energy transfer is slow and no rollover kinetics if fast. For a slow energy transfer the Inokuti-Hirayama model[254, 263-267] is employed, while for a fast transfer the stretched exponential function, $y = y_0 + A * e^{\left(-\frac{x}{\tau}\right)^{\beta * \kappa^2}}$, is used to account for the distribution in distance and the resonant coupling mechanism through the β-value and the orientation of the electric field through the κ^2-value. It is anticipated that the κ^2 values for a fixed overall concentration of Ln(III) within the nanospinel lattice. For the 3-dimmensonal spherical nanoparticle the β terms are constrained to $^3/_6$ (dipole-dipole), $^3/_8$ (dipole-quadrupole), and $^3/_{10}$ (quadrupole-quadrupole). [103, 104] [105-107] Evaluating the excited state decay for Eu(III) in the nanospinel samples should therefore allow a statistical discrimination between the various resonant coupling pathways (β-value) and octahedral tilt orientation (κ^2) for the lanthanides incorporated onto Al(III) sites in the nanospinel lattice.

In a simplified model where a singly doped nanoparticle is passivated by one passivant the overall PLQY will governed by equation 1:

$$\phi_{Ligand}^{Ln(III)} = \eta_{ISC} \times \eta_{ET} \times \phi_{Ln(III)}^{Ln(III)} = \eta_{sens \cdot Ligand} \times \phi_{Ln(III)}^{Ln(III)} \tag{1}$$

Where η_{ISC} is the efficiency of intersystem crossing and η_{ET} is the efficiency of energy transfer, which follows a Dexter energy transfer mechanism from ligand to lanthanide. The quantum yield $(\phi_{Ln(III)}^{Ln(III)})$ for the directly excited Ln(III) ion is influenced by the presence of excited state quenchers and by local lattice strain. For a system containing two lanthanides which are both sensitized by a surface passivant, the overall PLQY will be additive reflecting the sensitization of each cation independently. Additionally, if an energy transfer pathway is occurring between lanthanides in the system, this will also show an additive effect to the total quantum yield. Taken
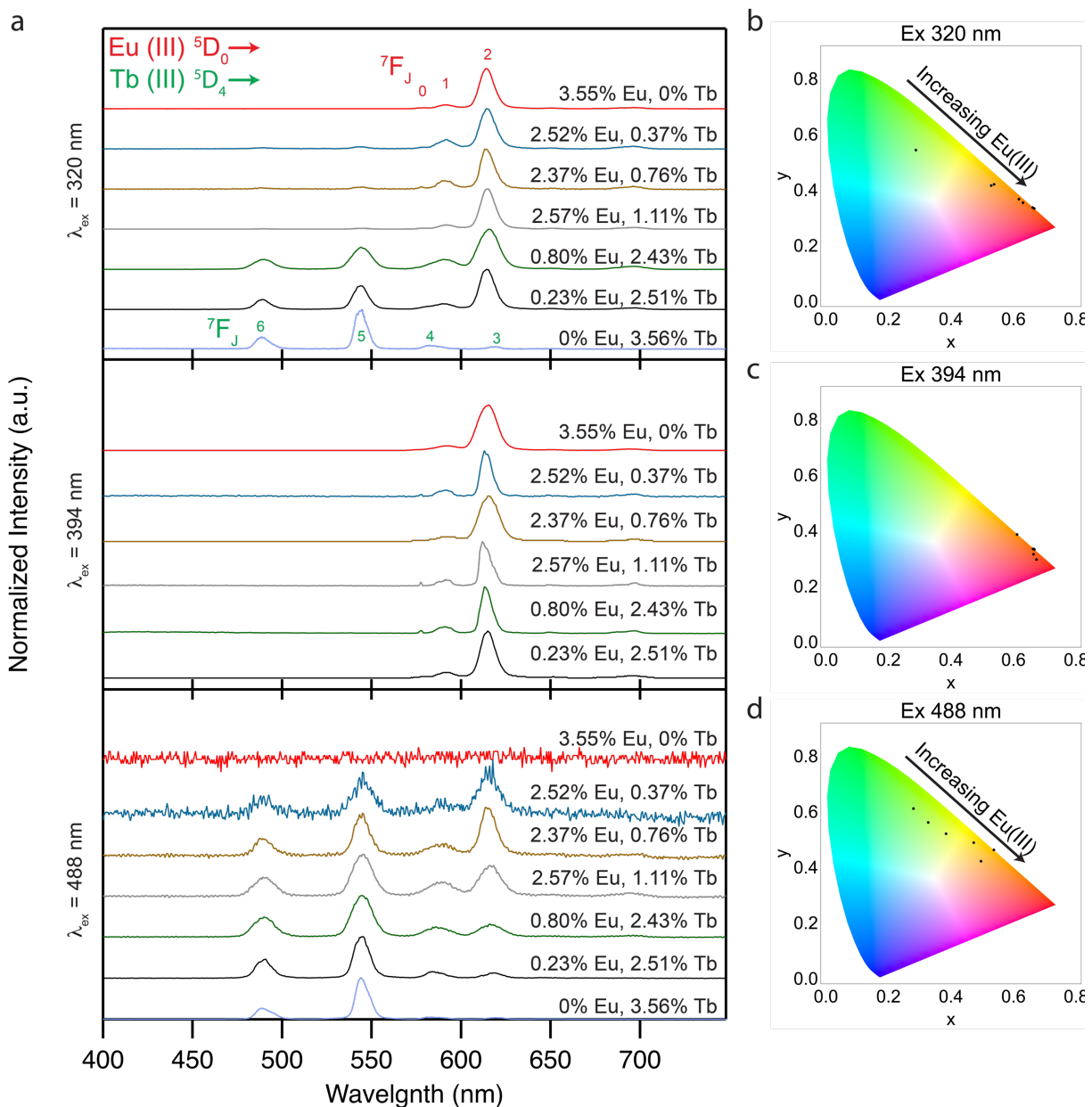
Figure 5.7. Photoluminescence spectra of the co-doped Eu(III), Tb(III): ZnAl$_2$O$_4$ samples at 298 K in toluene when excited into the ligand at a) 320 nm and the $^7F_6 \rightarrow {}^5D_4$ absorption of the Tb(III) cation at b) 488 nm. The calculated CIE coordinates are shown to the right of the PL figures in b, c, and d.

124
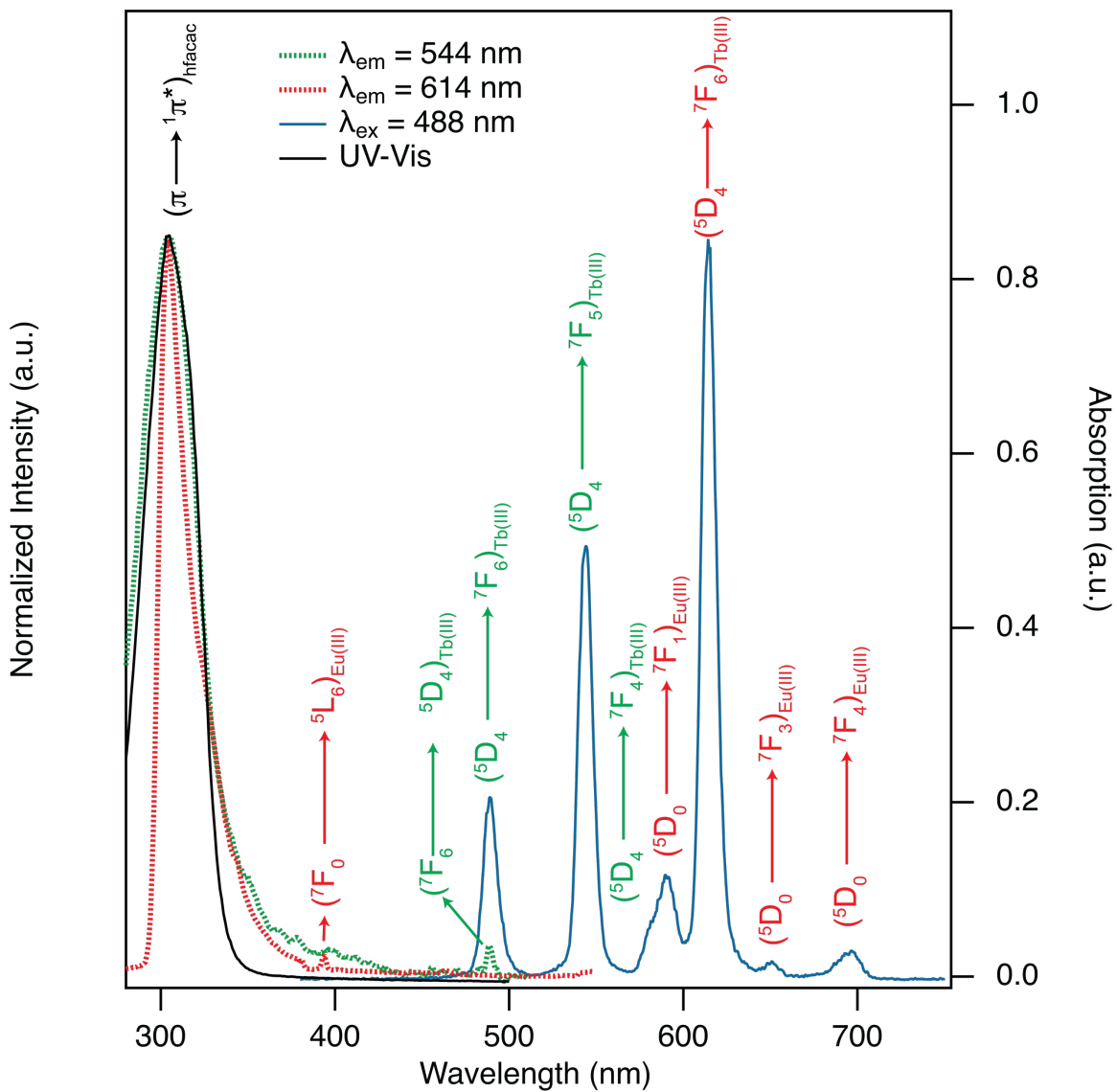
Figure 5.8. Photoluminescence excitation spectra monitoring the Tb(III) emission at 544 nm (green-dashed trace) or the Eu(III) emission at 614 nm (red-dashed trace) and the photoluminescence spectra following direct Tb(III) excitation at 488 nm. The black trace represents the UV-Vis absorption data showing the singlet absorption feature. All spectra were recorded at 298 K in toluene.

together the overall PLQY for the sample will depend on excitation and can be written as:

$$\phi_{tot} = \left(\eta_{sens.Ligand}^{Tb(III)} \times \phi_{Tb(III)}^{Tb(III)} \right) + \left(\eta_{sens.Ligand}^{Eu(III)} \times \phi_{Eu(III)}^{Eu(III)} \right) + \left(\eta_{sens.Tb(III)\rightarrow Eu(III)}^{Eu(III)} \times \phi_{Eu(III)}^{Eu(III)} \right) \quad (2)$$

Where $\eta_{sens.Ligand}^{Ln(III)}$ is the efficiency of sensitization either cations from the ligand while

$\eta_{sens.Tb(III)\rightarrow Eu(III)}^{Eu(III)}$ is the sensitiztion efficieny from Tb(III) to Eu(III) and $\phi_{Ln(III)}^{Ln(III)}$ is the intrsinsic

quantum yield of the lanthanides, described previously. The efficiency of energy transfer,

$\eta_{sens.Tb(III)\rightarrow Eu(III)}^{Eu(III)}$, will be dictated by the electric field involved in the coupling (dipole vs.

quadrupole) and the distance of separation (r) between the appropriate donor and acceptor.

5.3.3 Optical Analysis of 2-Color Nanospinels.

The UV-Vis data (Figure 5.4) for all nanospinel samples in toluene exhibit a strong

absorption feature assignable to the $^1(\pi-\pi^*)$ transition in hfacac at 304 nm. The Eu(III) and Tb(III)

transitions cannot be observed in the UV-Vis reflecting their low concertation and extinction

coefficients. The bandgap absorption for the parent $ZnAl_2O_4$ nanospinel host occurs above 280

nm.

In Figure 5.8, the photoluminescence excitation (PLE) spectra monitored at the Tb(III)

$^5D_4 \rightarrow {}^7F_5$ (λ_{em} =544 nm) exhibits the $^7F_6 \rightarrow {}^5D_4$ feature at 488 nm, while monitoring at the $^5D_0 \rightarrow {}^7F_2$

(λ_{em} =614 nm) allows assignment of the $^7F_0 \rightarrow {}^5L_6$ for Eu(III) at 394 nm. When monitoring the

Eu(III) $^5D_0 \rightarrow {}^7F_2$ PL line, the Tb(III) $^7F_6 \rightarrow {}^5D_4$ feature at 488 nm is not observed.

In Figure 5.7, the solution phase photoluminescence (PL) spectra for 1 x 10^{-4} M $Tb_xEu_{0.07-}$

$_x$:$ZnAl_{2-x}O_4$ samples dissolved in toluene at 298K are plotted following ligand sensitization (λ_{ex} =

320 nm), direct excitation into the $^7F_6 \rightarrow {}^5D_4$ absorption for Tb(III) (λ_{ex} = 488 nm), and direct

excitation into $^7F_0 \rightarrow {}^5L_6$ for Eu(III) (λ_{ex} = 394 nm) transitions. The PL spectra in Figure 5.7 displays

sharp features assignable to specific overlapping lanthanide centered transitions attributed to the

Table 5.2. Optical properties for Tb,Eu:ZnAl$_2$O$_4$ nanospionels following ligand (λ_{ex} = 320 nm) or Tb(III) (λ_{ex} = 488 nm) excitation.

Tb$_x$Eu$_{0.07-x}$:ZnAl$_2$O$_4$			I_{Eu}/I_{Tb}	I_{Eu}/I_{Tb}	$\phi_{Ln}{}^{Ln}$	$\phi_{L}{}^{Ln}$
x =	[Tb^{3+}] (%)	[Eu^{3+}] (%)	$\lambda_{320\ nm}$	$\lambda_{488\ nm}$	(%)	(%)
0	0	3.55	-	-	48 $\pm$ 2	45 $\pm$ 7
0.007	0.37	2.52	19.32	1.38	-	40 $\pm$ 5
0.015	0.76	2.37	23.81	0.77	-	29 $\pm$ 3
0.022	1.11	2.57	6.31	3.50	-	32 $\pm$ 5
0.049	2.43	0.80	1.84	3.25	-	30 $\pm$ 5
0.050	2.51	0.23	1.82	8.15	-	31 $\pm$ 5
0.070	3.56	0	-	-	77 $\pm$ 8	41 $\pm$ 6

individual Eu(III) $^5D_0 \rightarrow {}^7F_J$ and Tb(III) $^5D_4 \rightarrow {}^7F_J$ Judd-Olfelt (J-O) allowed transitions. The spectra exhibit no observable $^3\pi^*$ emission for all samples regardless of excitation wavelength. The hypersensitive transition for the Eu(III) is centered at 614 nm and is assigned to the $^5D_0 \rightarrow {}^7F_2$ transition, while the dominant transition of Tb(III) is centered at 544 nm and reflects the $^5D_4 \rightarrow {}^7F_5$ transition. The intensity contributions for the Tb(III) and Eu(III) is observed to depend on the excitation energy. Eu(III) emission is observed at all excitation wavelengths, while Tb(III) emission is observed only when excited into the ligand or directly into the Tb(III) center, suggesting no back energy transfer from Eu(III) to Tb(III) or Eu(III) to hfacac is occurring when excited at 394 nm.

The PLQY and CIE coordinates for the nanospinels excited into the hfacac $^1\pi^*$ transition at 320 nm are listed in Table 5.2 and 5.3. The highest PLQY is seen for the single doped samples (x =0, x=0.07) with a PLQY for Tb$_x$Eu$_{0.07-x}$:ZnAl$_{2-x}$O$_4$ (x = 0) of 45 $\pm$ 7 % in EtOD leading to a CIE coordinate at 14.3, 7.2, 0. The Tb$_x$Eu$_{0.07-x}$:ZnAl$_{2-x}$O$_4$ (x = 0.07) has a measured value of 41 $\pm$ 6 % with a CIE coordinate at 6.1, 11.6, 3.6. For the samples containing both Tb(III) and Eu(III) (0.07 > x > 0), the PLQY is ~30 $\pm$ 5% for all samples with CIE coordinates that vary with the lanthanide ratios (Figure 5.7b). The relative ratio of the $^5D_4 \rightarrow {}^7F_5$, Tb(III), to $^5D_0 \rightarrow {}^7F_2$, Eu(III),

Table 5.3. *x, y, z* CIE coordinates for Tb,Eu:ZnAl$_2$O$_4$ nanospionels following ligand ($\lambda_{ex} = 320$ nm) or Tb(III) ($\lambda_{ex} = 488$ nm) excitation that correspond to the CIE plots in Figure 5.7.

Tb$_x$Eu$_{0.07-x}$:ZnAl$_2$O$_4$	CIE cords. (x,y,z)		
x =	$\lambda_{320\ nm}$	$\lambda_{394\ nm}$	$\lambda_{488\ nm}$
0	14.3,7.2,0	16.6,8.4,0.1	-
0.007	16.8,9.5,0.4	8.7,4.1,0.3	7.5,12.9,2.6
0.015	14.5,7.4,0.0	17.2,8.6,0.0	14.0,18.9,3.4
0.022	16.6,9.9,0.4	11.8,7.5,0.0	21.6,22.4,1.8
0.049	22.2,17.3,1.7	8.4,3.4,0.4	25.4,21.6,4.2
0.050	18.0,14.2,1.9	15.5,7.8,0.0	21.5,18.5,0.1
0.070	6.1,11.6,3.6	-	5.6,12.1,2.2

transition intensity is observed to vary with the respective lanthanide concentration; however, the Eu(III) $^5D_0 \rightarrow {}^7F_2$ transition dominates the spectrum for all samples regardless of the Tb(III) concentration. This is evidenced in the CIE coordinates for the sample (Figure 5.7b).

Direct excitation into the Eu(III) and Tb(III) *f-f* absorption lines lead to very different PL spectral profiles (Figure 5.7a). Exciting at 394 nm into the Eu(III) $^7F_0 \rightarrow {}^5L_6$ for samples with x > 0 results in a PL spectrum assignable to only the Eu(III) J-O allowed transitions. The CIE coordinates vary with the x-value for the Tb$_x$Eu$_{0.07-x}$:ZnAl$_{2-x}$O$_4$, with an average value of (15.1, 8.9, 0.1). The lack of Tb(III) and hfacac $^3\pi^*$ emission supports the assumption of no back-energy transfer to ligand or to Tb(III) when Eu(III) is excited in the nanospinel. Direct excitation into the Tb(III) $^7F_6 \rightarrow {}^5D_4$ absorption feature at 488 nm leads to the observed population of both the Tb(III) and Eu(III) energy levels for all samples with x < 0.07.[268] A loss of S/N in the PL spectra with decreasing Tb(III) content is observed as expected due to the lower optical cross section for the $^7F_6 \rightarrow {}^5D_4$ transition. As a control, in Figure 5.7 no Eu(III) emission lines are observed in the x = 0 Tb$_x$Eu$_{0.07-x}$:ZnAl$_{2-x}$O$_4$ sample (pure Eu(III)) when excited at 488 nm. The CIE coordinates for the samples excited at 488 nm spans the green to red region of the chart, reflecting the change in
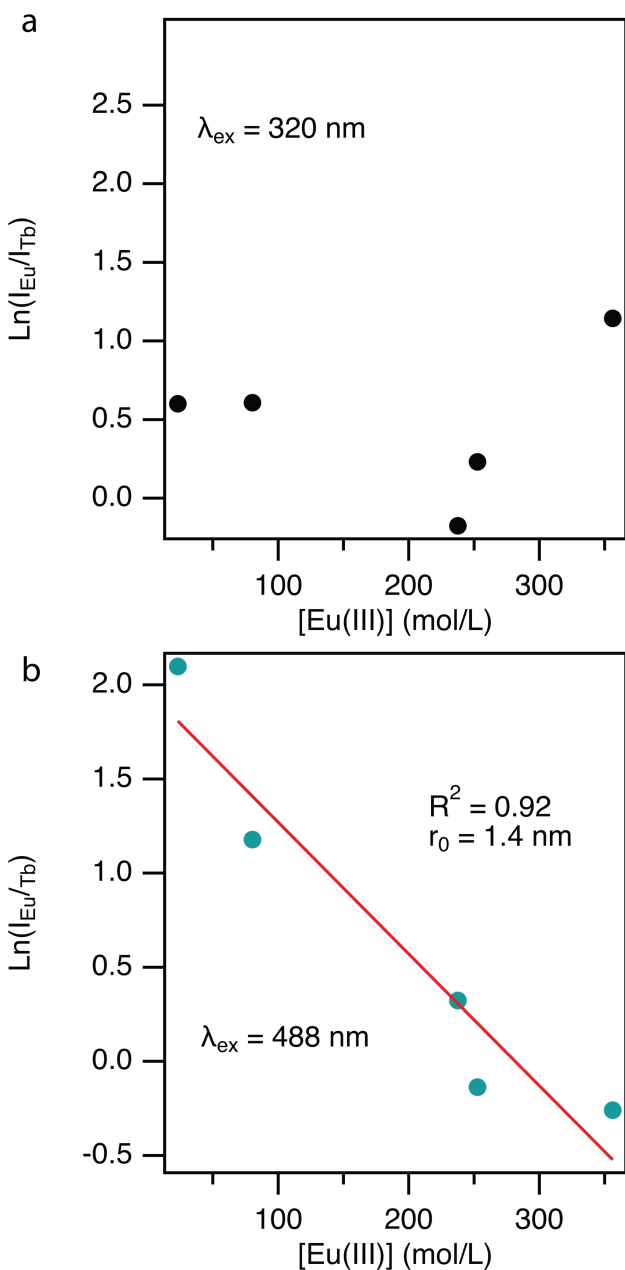
Figure 5.9. The PL intensity ratio of Eu(III) to Tb(II) vs. concertation Perrin plot for emission extracted from the PL data measured in toluene at 298K. The intensities are measured at the most intense electric dipole allowed transition for each ion (Eu(III) $^5D_0 \rightarrow {}^7F_2$, Tb(III) $^5D_4 \rightarrow {}^7F_5$). The Perrin plot is calculated for excitation into hfacac at a) 320 nm and b) 488 nm.

population of the Tb(III) and Eu(III) emitting centers implying energy transfer is occurring form Tb(III) → Eu(III) in the nanospinel phosphors through a down-shifting process.

5.3.4 Evaluating the Energy Transfer Pathways.

Comparison of the CIE coordinate plots for the various excitation wavelengths in Figure 5.7 clearly show the population of the Eu(III) and Tb(III) centers (Figure 5.1) is sensitive to the excitation wavelength due to the efficiency of down-shifting sensitization. As discussed in the theory section and schematically shown in Figure 5.1, the population of Eu(III) and Tb(III) by direct energy transfer from the ligand to the lanthanide is determined by the spectral overlap function $<J>$. As reported by Raymond, et al lanthanide sensitization from the passivant occurs through a Dexter energy transfer process and will be more efficient for Tb(III) when hfacac is the

Table 5.4. Experimental fitting parameters for excited state decay in nanospinels.

Sample	λ_{em} = 544 nm (stretched exponential)					
Tb$_x$Eu$_{0.07-x}$:ZnAl$_2$O$_4$	λ_{ex} = 320 nm			λ_{ex} = 488 nm		
x =	τ_{544} (ms)	κ^2	β_{544}	τ_{614} (ms)	κ^2	β_{614}
0	-	-	-	-	-	-
0.007	0.396	1.86	0.309	0.864	2.11	0.305
0.015	0.226	1.70	0.316	1.010	2.07	0.300
0.022	0.464	2.01	0.314	1.089	2.10	0.303
0.049	0.355	1.84	0.319	1.183	2.21	0.319
0.050	0.357	1.93	0.334	1.457	2.12	0.313
0.070	1.083	-	1.0	1.414	-	1

Sample	λ_{ex} = 320 nm		
x =			
0	1.279	1.014	-
0.007	1.117	1.176	1.166
0.015	1.124	1.149	1.194
0.022	1.154	1.288	1.435
0.049	1.263	1.364	1.577
0.050	1.409	1.123	1.323
0.070	-	-	-

passivating ligand based on evaluation of $<J>$.[115] The down-shifting energy transfer between the lanthanides is dependent on the separation distance (R$_{DA}$) between the dopants and is describable as a non-diffusional energy transfer problem within a three dimensional sphere.[11] For non-diffusional energy transfer in a nanocrystal, the distance is proportional to the lanthanide cation concentration.[29, 30, 121]

A Perrin non-diffusional energy transfer model is a convenient approach to evaluating the critical radius for Tb(III) to Eu(III) energy transfer. The Perrin model predicts the PL intensity of the Eu(III) center will vary as $\ln\left(\frac{I_{Eu(III)}}{I_{Tb(III)}}\right) = -VN_A[Eu(III)]$, where V is the volume of the quenching sphere ($V = \frac{4}{3}\pi R_0^3$), N_A is Avogadro's number, and [Eu(III)] is molar concentration. The Perrin model assumes only one energy transfer pathway (Tb(III)→Eu(III)) is present. A plot

of the $\ln\left(\frac{I_{Eu(III)}}{I_{Tb(III)}}\right)$ *vs.* the [Eu(III)] following excitation at 320 nm (hfacac excitation) is shown in

Figure 5.9a. The plot is non-linear, implying multiple pathways for Eu(III) population are present, consistent with the earlier assumption that a combination of ligand and Tb(III) sensitization of Eu(III) likely occurs in the nanospinel samples. In Figure 5.9b, excitation at 488 nm (Tb(III) direct excitation) yields a linear dependence with Eu(III) concentration (R^2 = 0.92). consistent with down-shifting energy transfer from Tb(III) to Eu(III) being an allowed pathway for Eu(III) population. From the slope in Figure 5.9b, the sphere of quenching for Tb(III) population of Eu(III) with a 50% probability is R_0 =1.4 nm indicating efficient sensitization over the entire nanospinel occurs, agreeing with previous literature reports.[120, 269]

In Figure 5.10, the excited decay profiles for the series of $Tb_xEu_{0.07-x}:ZnAl_{2-x}O_4$ nanospinels excited into the hfacac (λ_{ex} = 320 nm) and directly into the Tb(III) center (λ_{ex} = 488 nm) is shown for samples in N_2 sparged EtOD at 298K. Excited state decay profiles for excitation into the Eu(III) center at 394 nm is shown in Figure 5.11. EtOD is used to eliminate –OH and O_2 quenching in the samples. No experimental evidence of roll-over kinetics in the Eu(III) data is observed at short time scales indicating energy transfer is occurring in the sub-ps time regime allowing use of the stretched exponential function rather than the Inokuti-Hirayama expression. The lifetimes therefore are fit to a stretched exponential function as detailed in theory section of the manuscript and the fit parameters are tabulated in Table 5.4, allowing extraction of the β-value to identify the nature of energy coupling between Tb(III) and Eu(III) (dipole-dipole vs dipole-quadrupole vs quadrupole-quadrupole) and the κ^2 orientation term for the octahedral tilting in the nanospinel lattice.

Monitoring the Eu(III) $^5D_0 \rightarrow {}^7F_2$ transition centered at 614 nm, the lifetimes can be fit to a monoexponential decay with a lifetime of 1.0 – 1.5 μs regardless of excitation wavelength. Fitting
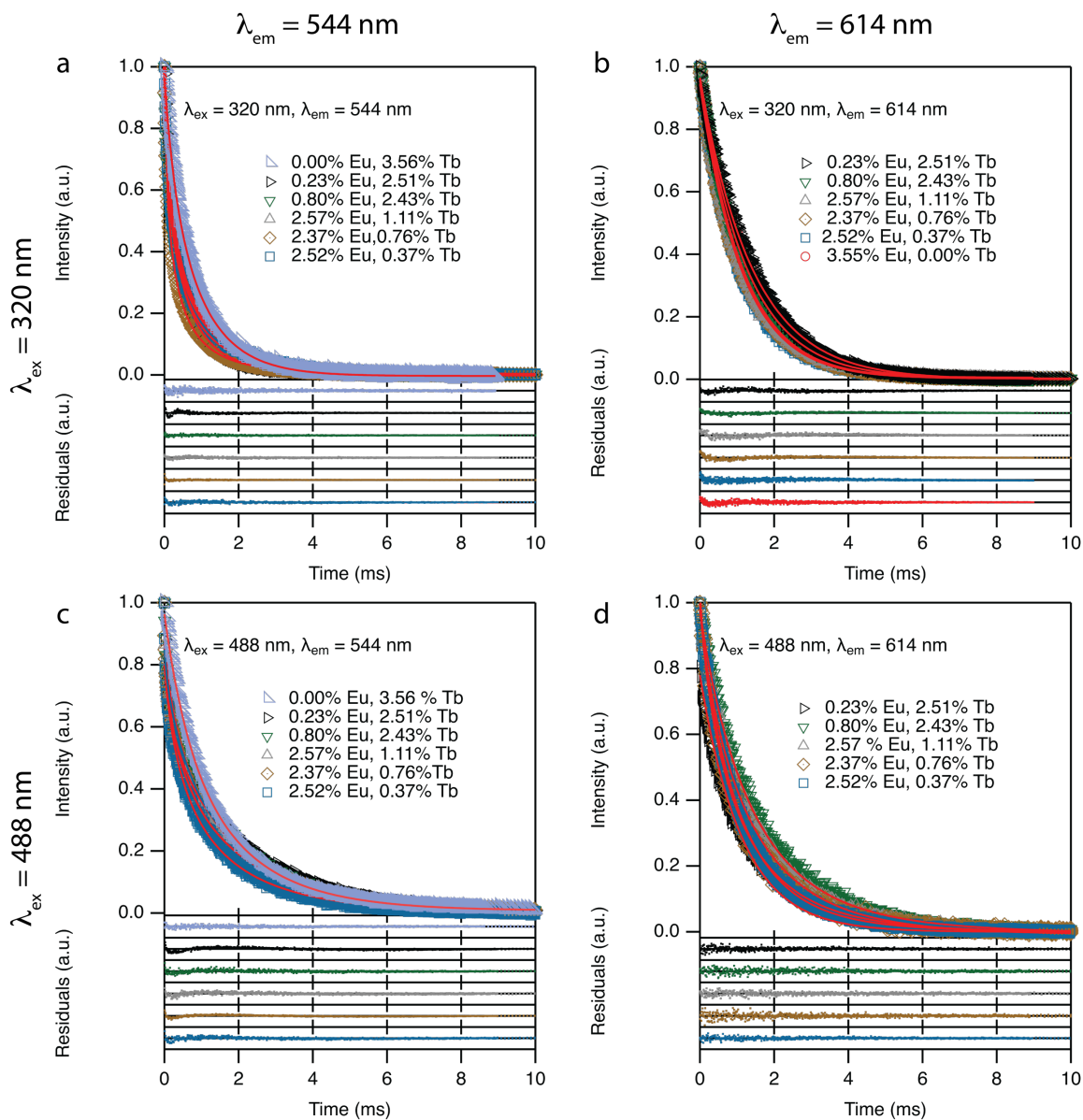
Figure 5.10. Excited state lifetime decays recorded at 298 K in N₂ sparged EtOD monitoring Tb(III) emission (a & c) and Eu(III) (b & d) following ligand excitation (a & b) and direct excitation (c & d).

to a stretched exponential yields a β = 1 value confirming mono-exponential. The observation of invariant lifetime values, regardless of excitation wavelength is consistent with the anticipated lack of perturbation of the Eu(III) site in the lattice and the participation of all Eu(III) centers. The excited state lifetime of the Tb(III) centers is more complex and is dependent on excitation
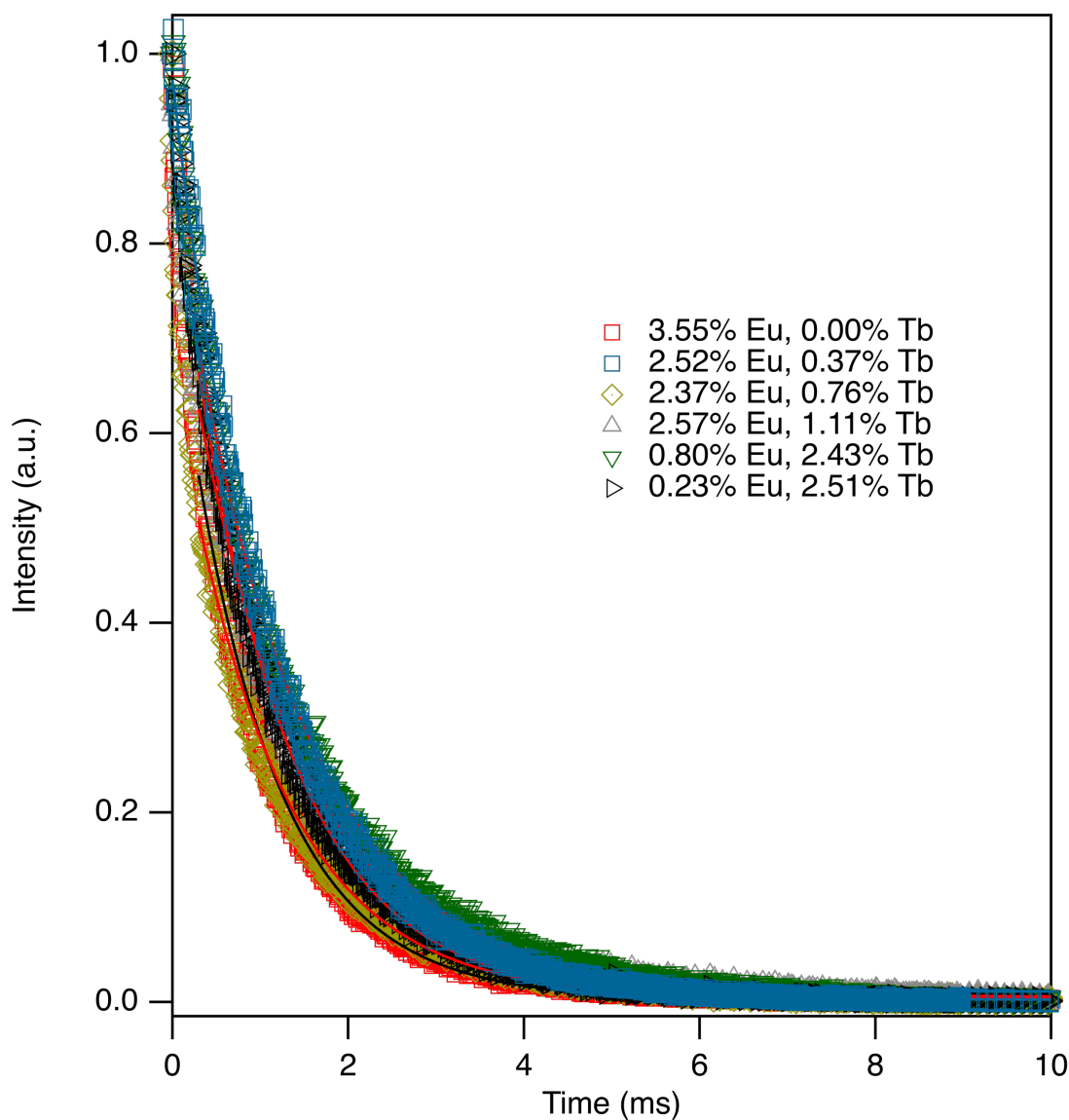
Figure 5.11. Excited state lifetime decays recorded at 298 K in N$_2$ sparged EtOD monitoring Eu(III) emission following direct excitation of Eu(III) at 394 nm.

wavelength. The Tb(III) lifetimes are fit to a stretched exponential function. Excitation at 320nm (hfacac) results in the observation of quenched Tb(III) lifetimes when Eu(III) is present (τ = 0.23 – 0.46 μs) compared to the lifetime for the x = 0.07 sample (τ = 1.08 μs, β = 1.0). The β-value ranges from 0.31 to 0.33 for all samples containing Eu(III). Excitation into the Tb(III) *f-f* absorption at 488 nm leads to shorter τ's with increasing Eu(III) to Tb(III) content. The β-values

range from 0.30 – 0.32 for all samples containing Eu(III) centers. The x = 0.07 sample (pure Tb(III)) exhibits a lifetime that is 23% quenched (1.083 ms) when hfacac is excited as compared to direct Tb(III) excitation (1.414 ms). The Tb(III) excited state fitting parameters provide insight into the coupling mechanism and the role of orientation in the energy transfer process. The β values will reflect the Tb(III)-Eu(III) coupling with values of $^3/_6$, $^3/_8$, or $^3/_{10}$ for 3D dipole-dipole, 3D dipole-quadrupole, and 3D quadrupole-quadrupole coupling, respectively. The observed β values between 0.305 and 0.324 for Tb(III) decay supports 3D quadrupole-quadrupole coupling, agreeing with the previous report that Tb(III) to Eu(III) is a quadrupole-quadrupole process.[256-258]

In a solid state lattice, it is reasonable to assume the orientation of the quadrupoles associated with the emissive center will be dictated by the lattice. In the nanospinel lattice, two Al(III) sites exist in the tetragonal phase. Assuming the occupation of Tb(III) and Eu(III) are equally probable at the two sites, trigonometry allows us to experimentally determine a theoretical κ_{theory}-value using the angular orientation terms for the tetragonal lattice, $\theta_T = 16.5$, $\theta_A = 1.8°$, and $\theta_D = 2.2°$. From the angular terms, the κ_{theory}-value is calculated to be 2.15 for the tetragonal lattice. By comparison, solving for the experimental κ^2_{exptl}-value by fitting the stretched exponential function for the direct excitation into Tb(III) leads to a value of 2.14 + 0.07. The difference in the theory and experimental values is believed to arise from Al(III) lattice site distortion due to the large size difference for Al(III) compared to Tb(III) and Eu(IIII). Back calculating from the orientation factor, the two Ln(III) octahedral sites should have a net tilt of ~4-7° with respect to the vector containing the donor and acceptor. The angle (θ_T) between the donor and acceptor was found to be ~ 13-15°.

Surprisingly, evaluating the value of κ^2_{exptl} when the hfacac is excited yields a different value even though the β-values are within experimental error. The change in κ may arise form

lattice realization of the nanospinel surface following passivation, as suggested previously. [270-272] Similarly, lattice relaxation has been reported to occur in CdSe quantum dots.[273] The presence of surface emitting sites being unique to core emitting sites also has been reported for Eu(III) doped Y_2O_3.[29] If we assume the change in κ^2_{exptl} is due to surface reconstruction, an estimate of the octahedral tilt change can be calculated. The average κ^2 value extracted by fitting the stretched exponential decay excited at 320 nm was found to be 1.81 ± 0.20. Converting the change in κ^2 to a tilt parameter yields an estimated value of θ_T of 20º for the surface associated sites as compared to 13-15º for the internal sites. The extracted values are remarkable close to the reported tilts in the inverse spinel, Fe_3O_4, where surface canting was reported to have net values between 23 and 42º.[272] The role of surface reconstruction of the physical properties of these materials is critical for 2 nm nanospinels and the estimates imply an inversion may occur at the surface upon passivation. Further studies are underway to evaluate this possibility of surface reconstruction and its role on optical properties in these phosphors.

5.4 Conclusion.

Spectral engineering was achieved through the sensitization of co-doped $Tb_xEu_{0.07-x}:ZnAl_{2-x}O_4$ nanospinels passivated by hexafluoroacetylacetonate. The high sensitization efficiency of Eu(III) leads to higher red contributions upon incorporation of Eu(III) into the nanospinel, although spectral features exhibit concentration and excitation dependencies that reflect the energy transfer efficiencies within the system. Inspection of the lifetimes and Perrin plots allow for the assignment of a competitive energy transfer pathway involving hfacac to both Eu(III) and Tb(III), as well as direct Tb(III) to Eu(III) process occurring over the whole volume of the nanospinel. No evidence of back energy transfer is observed, as evidenced by the lack of hfacac triplet emission or Tb(III) emission when the Eu(III) center is excited. Based upon the lifetime findings, the likely

energy transfer mechanism is a quadrupole-quadrupole coupling due to the β values $\sim {}^3/_{10}$. The stretched exponential allows the extraction of the octahedral titling within the nanospinel by solving for the orientation factor (κ) yielding values for canting that are in a good agreement with angles determined from the crystallographic information. The orientation factor also identified enhanced octahedral tilting at the surface of the nanospinel suggesting lattice reconstruction or inverse spinel formation at the passivation-nanospinel interface may occur.

CHAPTER 6

CONCLUSIONS & OUTLOOK

While the work completed within this dissertation provides tools for next generation technology, future work is necessary to implement this material into tangible applications. The phosphor work has shown that spectral engineering is achieved by systematic manipulation of Ln(III) concentration, quadrupole-quadrupole coupling, and the octahedral tilt where the Ln(III) are sensitized by a surface passivating ligand and Eu(III) was demonstrated to be sensitized by a neighboring Tb(III) cation. In addition, the optimization of the nanophosphor spinels was accomplished demonstrating that the efficiency of energy transfer is governed orbital overlap of the ligand's triplet state and lanthanide excited state where hfacac passivated nanophosphors produced PLQYs up to 41.3% in EtOD. Concentration optimization was accomplished and in Chapter 3 where we observed a quenching event that coincides with the strain exerted on the lattice upon Tb(III) incorporation into the $ZnAl_2O_4$ nanospinel. Additionally, Chapter 2 described a new approach to isolate templated nanocrystals that have applications in catalysis such as the Fischer-Tropsch Synthesis (FTS) and the water gas shift reaction. This chapter provides future outlook for all materials listed in this dissertation to produce catalytic material, and smart nanophosphors.

6.1 Developing Smart Nanophosphors.

6.1.1 Dual-Ligand Systems for Selective Sensitization.

The co-doped Tb(III), Eu(III):$ZnAl_2O_4$ described in Chapter 5 provide a route to isolate 2 nm nanophosphors that are capable of exhibiting changes in the spectral features that can be induced by altering the excitation wavelength or external presser exerted on the system. The work shown in Chapter 5 show a single ligand system that sensitized both the Eu(III) and Tb(III)
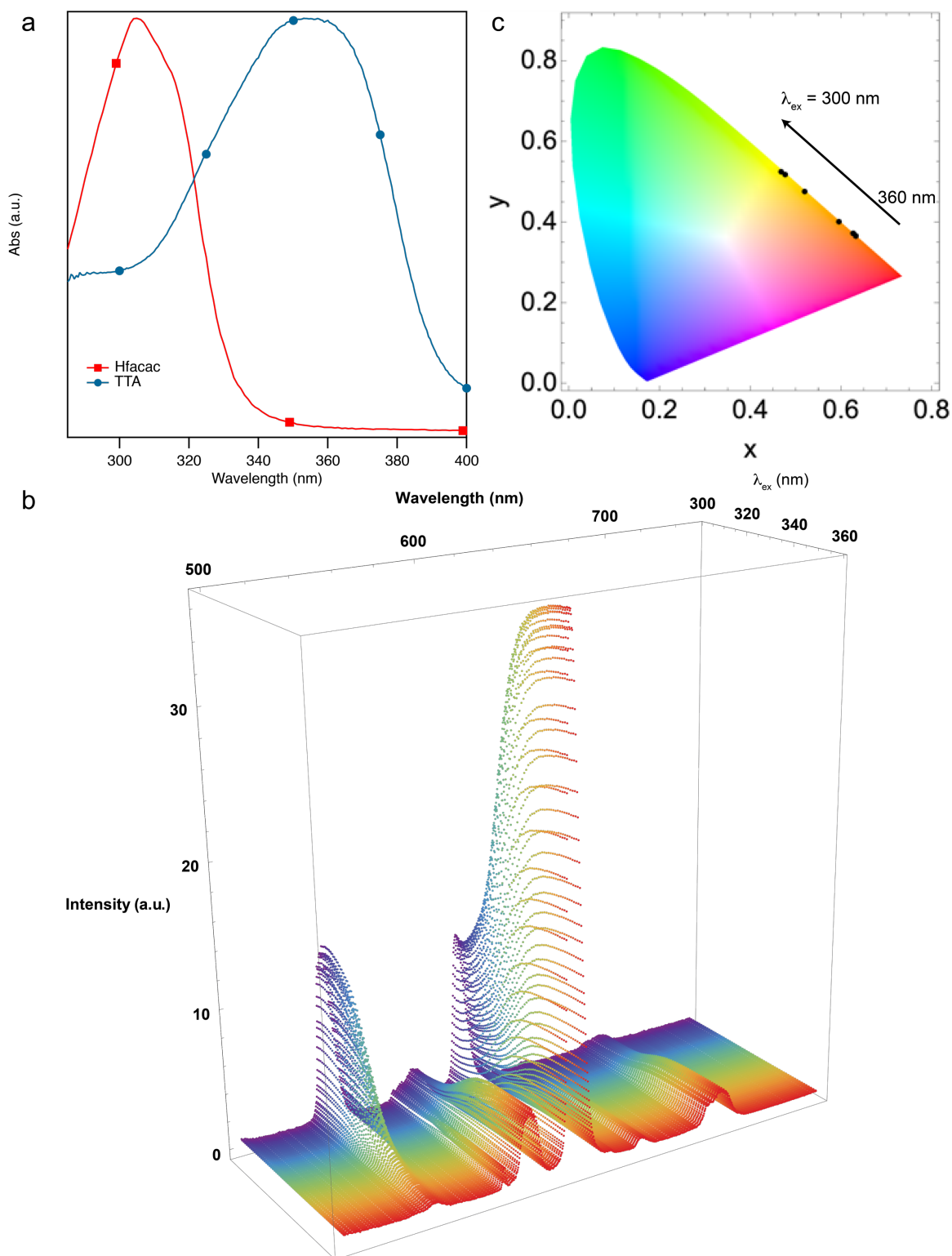
Figure 6.1. a) UV-Vis absorption of TTA and hfacac passivated nanospinel phosphors in toluene, b) predicted emission profile as a function of excitation wavelength generated from the absorption features in 6.1a, and c) CIE response of the predicted emission profiles showing a linear shift in CIE coordinates.

following excitation at 320 nm. The Tb(III) $^5D_4$ and Eu(III) $^5D_0$ excited state energies are 20,500 and 17,293 cm^{-1}, respectively therefore Eu(III) can be populated selectively at through passivation of a ligand with a lower triplet energy. Previous work in the group has demonstrated that quantum yields of 50% can be achieved from a Eu(III):ZnAl$_2$O$_4$ when sensitized by 2-theyonyltrifluoroacetone (TTA).[30] The triplet energy of TTA is ~19,000 cm^{-1}, 1,500 cm^{-1} below the Tb(III) $^5D_4$. Employing a dual-ligand system will allow for the selective sensitization, thus resulting in spectral feature changes.

It is proposed in Figure 6.1 that passivation by hfacac and TTA will produce a smart nanophosphor that will reflect change from red to orange phosphor dependent upon the excitation wavelength. Figure 6.1a displays the normalized UV-Vis absorption data of a TTA and hfacac passivated nanospinels where Figure 6.1b shows the predicted 3D plot illustrating the spectral changes as a function of excitation wavelength from 360 to 300 nm. The emission spectra shown in Figure 6.1b are corrected for the observed PLQY for a hfacac passivated nanopahosnor where 5.08% Tb(III):ZnAl$_2$O$_4$ is 19% and 5% Eu(III): ZnAl$_2$O$_4$ is 37%, reflecting the higher sensitization efficiency of Eu(III). The modeled emission spectra exhibit a linear response in the calculated CIE coordinates shown in Figure 6.1c. Current InGaN LED pumps exhibit a red shift with decreasing voltage and a blue shift with decreasing current of up to 15-20 nm (*i.e.* 460 $\pm$ 20 nm), the tunable emission of the LED is also observed in red and green LEDs.[274] The proposed work will expand the optical cross section of the nanophosnors by employing two ligands capable of selective sensitization. The work will require careful consideration of molar extinction coefficients for the respective ligands, determination of the intersystem crossing efficiencies, and systematic control over ligand passivation.

6.1.2 Spectral Engineering Through External Pressures.

In Chapter 4, we demonstrated that the Ln(III) is a reporter of lattice strain that causes different ratios of the magnetic and electric dipole transitions. Wisser *et al.*[230] has demonstrated that the external pressures exerted on the system are reflected in the Ln(III) transitions for upconverting nanoscrystals. Lis *et al.*[275] observed a linear red shift up to 50 nm and increase in FWHM as pressure increased to 30 GPa in Ce(III):$Y_6Ba_4(SiO_4)_6F_2$ powders. It is anticipated that pressure induced spectral changes in for Ce(III) will also impact the ability to sensitize neighboring Ln(III) cations due to changes in the spectral overlap between the donor and acceptor. Thus the energy transfer rates can be calculated by evaluating a series of pressure and temperature dependent studies. Development of a smart nanosphosnor can use the work described within this dissertation and the literature to spectrally engineer the emission through the application of external pressures. This capability will allow for precise tuning of Ce(III) (blue), Tb(III) (green), and Eu(III) (red), nanophsnors through compression of the crystal field about the Ln(III) cations.

6.1.3 Additional Sensitization Pathways.

Historically, Ln(III) have been sensitized by a molecular antenna that is coordinated to the cation, however, recent work has shown efficient sensitization may occur through inorganic antennas that have a large optical cross section. Incorporation of Ce(III) and Tb(III) into Lanthanum phosphate have reported overall PLQYs up to 84% when co-doping is achieved.[276, 184, 277] The increased PLQY is due to the blue Ce(III) emission and sensitization of Tb(III) through dipole-quadrupole coupling from the Ce(III) $5d^1 \rightarrow {}^7F_{5/2,\ 7/2}$ transition.[276] Other cations such as Bi(III)[180, 278, 279] provide up to a 3-fold increase in the internal PLQY following excitation *circa* 320 nm. The energy transfer mechanism from Bi(III) to Eu(III) is currently debated to be dipole-dipole[278] or dipole-quadrupole coupling,[180] however, since dipole transitions are forbidden in the
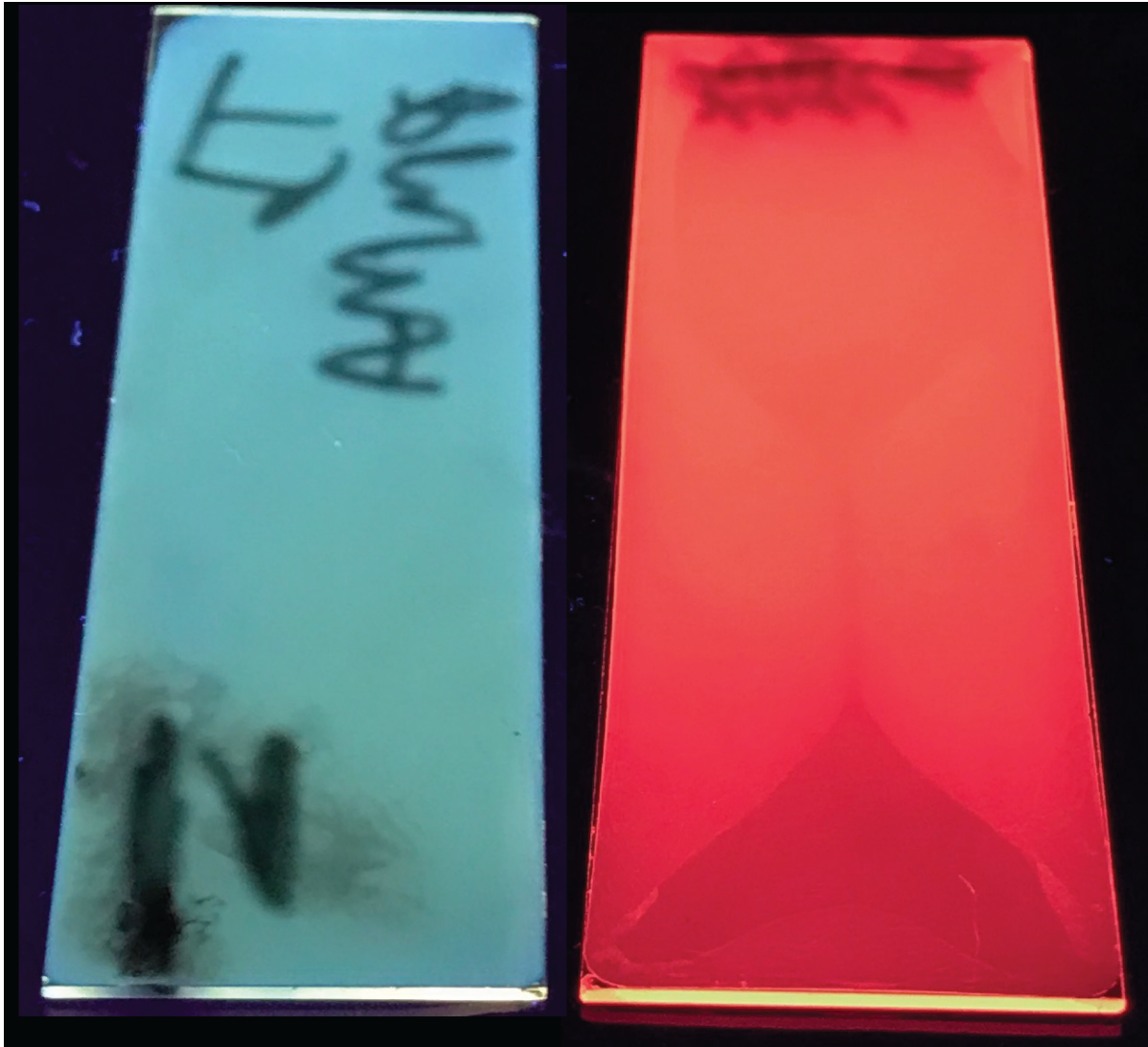
Figure 6.2. Blending of Tb(III):ZnAl$_2$O$_4$ @ hfacac (left) and Eu(III):ZnAl$_2$O$_4$ @ TTA nanophosphors into a PMMA matrix.

f-f transitions, it is likely to follow a dipole-quadrupole mechanism that has a distance dependence of R$_{DA}^{-8}$. Likewise, Mn(II) can be employed to sensitize lanthanide photoluminescence,[170, 280, 281] albeit it was postulated that a maximum sensitization efficiency of 33% could be achieved.[170] The inorganic antenna may also be coupled to the molecular antenna to further increase the optical cross section and allow for selective sensitization. Furthermore, the incorporation of the inorganic antenna will allow for Ln(III) access throughout the nanophosphor, in contrast to the molecular antenna that can only access 75% of the nanophosphor.

6.1.4 Additive Manufacturing of Nanophosphor Composites.

Additive manufacturing protocols allow for the mass production of solid-state lighting material that can be printed into the desired specifications. The ability to passivate the nanospinel allow for enhanced solubility into a polymer matrix such as polymethyl methacrylate (PMMA) shown in Figure 6.2. However, distribution of the nanopsinels within the extruded polymer needs to be addressed and optimized. This can be achieved by extruding a filament containing the blended nanoparticles in PMMA using screw extrusion methods and examining the cross section using SEM. This technique can allow for EDAX mapping of the filament as well as the ability to use back scattered electrons to examine the solubility of the nanoparticles within the matrix.

6.2 Understanding the Catalytic Behavior.

Chapter 2 outlined a synthetic protocol to isolate nanoparticle catalysts for the Fischer-Tropsch Synthesis and the water gas shift reaction. The numerous reaction pathways that occur in the FTS will provide difficulty in development of a systematic study aimed to study the catalytic response of the mixed-metal carbides and bimetallic nanocrystals. First, it is necessary to understand fundamental catalytic activity such as the water gas shift (WGS). Iron based systems are more susceptible to the WGS, whereas Co containing systems are less reactive. The results in Chapter 2 suggest that the elemental composition is maintained throughout the reaction and these results are supported by previous work from Yamada *et al.*[137] Thus, systematic studies through control of reaction precursors ($FeCl_2$/ $CoCl_2$) in the initial PBA reaction will produce a correlated response observed in the WGS and subsequently in the FTS. This work can also be expanded to investigate the role of turnover frequency and its relationship to nanocrystal size. The optimization should demonstrate selective isolation of liquid fuels through systematic control of nanoparticle size and elemental composition.

BIBLIOGRAPHY

1.   Pattison, M.; Bardsley, N.; Elliot, C.; Hansen, M.; Lee, K.; Pattison, L.; Tsao, J.; Yamada, M., 2018 Solid-State Lighting R&D Opportunities. U.S. Department of Energy, 2019.

2.   Gas-to-liquid plants face challenges in the U.S. market. https://www.eia.gov/todayinenergy/detail.php?id=15071.

3.   Moyer, M. M.; Karakaya, C.; Kee, R. J.; Trewyn, B. G., In Situ Formation of Metal Carbide Catalysts. *ChemCatChem* **2017,** *9* (16), 3090-3101.

4.   Chang, Q.; Zhang, C.; Liu, C.; Wei, Y.; Cheruvathur, A. V.; Dugulan, A. I.; Niemantsverdriet, J. W.; Liu, X.; He, Y.; Qing, M.; Zheng, L.; Yun, Y.; Yang, Y.; Li, Y., Relationship between Iron Carbide Phases (ε-Fe$_2$C, Fe$_7$C$_3$, and χ-Fe$_5$C$_2$) and Catalytic Performances of Fe/SiO$_2$ Fischer–Tropsch Catalysts. *ACS Catalysis* **2018,** *8* (4), 3304-3316.

5.   Wang, P.; Chen, W.; Chiang, F.-K.; Dugulan, A. I.; Song, Y.; Pestman, R.; Zhang, K.; Yao, J.; Feng, B.; Miao, P.; Xu, W.; Hensen, E. J. M., Synthesis of stable and low-CO$_2$ selective ε-iron carbide Fischer-Tropsch catalysts. *Science Advances* **2018,** *4* (10), eaau2947.

6.   Xiong, H.; Moyo, M.; Motchelaho, M. A.; Tetana, Z. N.; Dube, S. M. A.; Jewell, L. L.; Coville, N. J., Fischer–Tropsch synthesis: Iron catalysts supported on N-doped carbon spheres prepared by chemical vapor deposition and hydrothermal approaches. *Journal of Catalysis* **2014,** *311*, 80-87.

7.   Yang, C.; Zhao, H.; Hou, Y.; Ma, D., Fe$_5$C$_2$ Nanoparticles: A Facile Bromide-Induced Synthesis and as an Active Phase for Fischer–Tropsch Synthesis. *Journal of the American Chemical Society* **2012,** *134* (38), 15814-15821.

8.   Calderone, V. R.; Shiju, N. R.; Ferre, D. C.; Rothenberg, G., Bimetallic catalysts for the Fischer–Tropsch reaction. *Green Chemistry* **2011,** *13* (8), 1950-1959.

9.   Liu, Y.; Chen, J.-F.; Bao, J.; Zhang, Y., Manganese-Modified Fe3O4 Microsphere Catalyst with Effective Active Phase of Forming Light Olefins from Syngas. *ACS Catalysis* **2015,** *5* (6), 3905-3909.

10.   Li, S.; Ren, P.; Yang, C.; Liu, X.; Yin, Z.; Li, W.; Yang, H.; Li, J.; Wang, X.; Wang, Y.; Cao, R.; Lin, L.; Yao, S.; Wen, X.; Ma, D., Fe$_5$C$_2$ nanoparticles as low-cost HER electrocatalyst: the importance of Co substitution. *Science Bulletin* **2018,** *63* (20), 1358-1363.

11.   Li, S.; Yang, J.; Song, C.; Zhu, Q.; Xiao, D.; Ma, D., Iron Carbides: Control Synthesis and Catalytic Applications in CO$_x$ Hydrogenation and Electrochemical HER. *Advanced Materials* **2019,** *0* (0), 1901796.

12.   Yang, C.; Zhao, B.; Gao, R.; Yao, S.; Zhai, P.; Li, S.; Yu, J.; Hou, Y.; Ma, D., Construction of Synergistic Fe$_5$C$_2$/Co Heterostructured Nanoparticles as an Enhanced Low Temperature Fischer–Tropsch Synthesis Catalyst. *ACS Catalysis* **2017,** *7* (9), 5661-5667.

13.   Yadav, T. P.; Yadav, R. M.; Singh, D. P., Mechanical milling: a top down approach for the synthesis of nanomaterials and nanocomposites. *Nanoscience and Nanotechnology* **2012,** *2* (3), 22-48.

14.   Ashley, B.; Vakil, P. N.; Lynch, B. B.; Dyer, C. M.; Tracy, J. B.; Owens, J.; Strouse, G. F., Microwave Enhancement of Autocatalytic Growth of Nanometals. *ACS Nano* **2017,** *11* (10), 9957-9967.

15.   Gerbec, J. A.; Magana, D.; Washington, A.; Strouse, G. F., Microwave-Enhanced Reaction Rates for Nanoparticle Synthesis. *Journal of the American Chemical Society* **2005,** *127* (45), 15791-15800.

16.   Lovingood, D. D.; Strouse, G. F., Microwave induced in-situ active ion etching of growing InP nanocrystals. *Nano letters* **2008,** *8* (10), 3394-3397.

17.   Hardy, D. A.; Nguyen, E. T.; Parrish, S. E.; Schriber, E. A.; Schlicker, L.; Gili, A.; Kamutzki, F.; Hohman, J. N.; Strouse, G. F., Prussian blue iron-cobalt mesocrystals as a template for the growth of Fe/Co carbide (cementite) and Fe/Co nanocrystals. *Chemistry of Materials* **2019**.

18.   Thanh, N. T.; Maclean, N.; Mahiddine, S., Mechanisms of nucleation and growth of nanoparticles in solution. *Chemical reviews* **2014,** *114* (15), 7610-7630.

19.   Watzky, M. A.; Finke, R. G., Transition Metal Nanocluster Formation Kinetic and Mechanistic Studies. A New Mechanism When Hydrogen Is the Reductant: Slow, Continuous Nucleation and Fast Autocatalytic Surface Growth. *Journal of the American Chemical Society* **1997,** *119* (43), 10382-10400.

20.   Mondloch, J. E.; Yan, X.; Finke, R. G., Monitoring supported-nanocluster heterogeneous catalyst formation: Product and kinetic evidence for a 2-step, nucleation and autocatalytic growth mechanism of Pt (0) n formation from H_2PtCl_6 on Al_2O_3 or TiO_2. *Journal of the American Chemical Society* **2009,** *131* (18), 6389-6396.

21.   Lin, C.-S.; Khan, M. R.; Lin, S. D., The preparation of Pt nanoparticles by methanol and citrate. *Journal of colloid and interface science* **2006,** *299* (2), 678-685.

22.   Finney, E. E.; Finke, R. G., The four-step, double-autocatalytic mechanism for transition-metal nanocluster nucleation, growth, and then agglomeration: metal, ligand, concentration, temperature, and solvent dependency studies. *Chemistry of Materials* **2008,** *20* (5), 1956-1970.

23.   Gaikwad, A. V.; Rothenberg, G., In-situ UV-visible study of Pd nanocluster formation in solution. *Physical Chemistry Chemical Physics* **2006,** *8* (31), 3669-3675.

24.   Stiegman, A., Loss Mechanisms and Microwave-Specific Effects in Heterogeneous Catalysis. *Advances in Organometallic Chemistry and Catalysis* **2016**.

25.   Abdelsayed, V.; Shekhawat, D.; Smith, M. W.; Link, D.; Stiegman, A. E., Microwave-assisted pyrolysis of Mississippi coal: A comparative study with conventional pyrolysis. *Fuel* **2018,** *217*, 656-667.

26.   Duangkamol, C.; Batsomboon, P.; Stiegman, A. E.; Dudley, G. B., Microwave heating outperforms conventional heating for a thermal reaction that produces a thermally labile product: Observations consistent with selective microwave heating. *Chemistry–An Asian Journal*.

27.   Kappe, C. O., Controlled microwave heating in modern organic synthesis. *Angewandte Chemie International Edition* **2004,** *43* (46), 6250-6284.

28.   Levin, E. E.; Grebenkemper, J. H.; Pollock, T. M.; Seshadri, R., Protocols for High Temperature Assisted-Microwave Preparation of Inorganic Compounds. *Chemistry of Materials* **2019**.

29.   Dai, Q.; Foley, M. E.; Breshike, C. J.; Lita, A.; Strouse, G. F., Ligand-Passivated Eu:Y_2O_3 Nanocrystals as a Phosphor for White Light Emitting Diodes. *Journal of the American Chemical Society* **2011,** *133* (39), 15475-15486.

30.   Foley, M. E.; Meulenberg, R. W.; McBride, J. R.; Strouse, G. F., Eu^{3+}-Doped ZnB_2O_4 (B = Al^{3+}, Ga^{3+}) Nanospinels: An Efficient Red Phosphor. *Chemistry of Materials* **2015,** *27* (24), 8362-8374.

31.   Carnevale, D. J. a. S. M. a. S. G. F., Ligand Passivated Core–Shell FePt@Co Nanomagnets Exhibiting Enhanced Energy Product. *Chemistry of Materials* **2016,** *28* (15), 5480-5487.

32.   Vakil, P. N.; Muhammed, F.; Hardy, D.; Dickens, T. J.; Ramakrishnan, S.; Strouse, G. F., Dielectric Properties for Nanocomposites Comparing Commercial and Synthetic Ni- and Fe_3O_4-Loaded Polystyrene. *ACS Omega* **2018,** *3* (10), 12813-12823.

33.   Vakil, P. N.; Hardy, D. A.; Strouse, G. F., Synthesis of Highly Uniform Nickel Multipods with Tunable Aspect Ratio by Microwave Power Control. *ACS Nano* **2018,** *12* (7), 6784-6793.

34.   Lee, H.-W.; Muralidharan, P.; Ruffo, R.; Mari, C. M.; Cui, Y.; Kim, D. K., Ultrathin Spinel LiMn2O4 Nanowires as High Power Cathode Materials for Li-Ion Batteries. *Nano Letters* **2010,** *10* (10), 3852-3856.

35.   Foley, M. E.; Meulenberg, R. W.; McBride, J. R.; Strouse, G. F., Eu^{3+}-Doped ZnB_2O_4 (B = Al^{3+}, Ga^{3+}) Nanospinels: An Efficient Red Phosphor. *Chem. Mater.* **2015,** *27* (24), 8362-8374.

36.   Wang, S. F.; Sun, G. Z.; Fang, L. M.; Lei, L.; Xiang, X.; Zu, X. T., A Comparative Study of $ZnAl_2O_4$ Nanoparticles Synthesized from Different Aluminum Salts for Use as Fluorescence Materials. *Sci. Rep.* **2015,** *5*.

37.   Kumar, M.;   Gupta, S. K.; Kadam, R. M., Near White Light Emitting $ZnAl_2O_4$:Dy^{3+} Nanocrystals: Sol–Gel Synthesis and Luminescence Studies. *Mater. Res. Bull.* **2016,** *74*, 182-187.

38.   Jantzen, C. M. a. B. K. G., Predicting the Spinel–Nepheline Liquidus for Application to Nuclear Waste Glass Processing. Part I: Primary Phase Analysis, Liquidus Measurment, and Quasicrystalline Approach. *Journal of the American Ceramic Society* **2007,** *90* (6), 1866--1879.

39.   Donald, I. W.; Metcalfe, B. L.; Taylor, R. N. J., The immobilization of high level radioactive wastes using ceramics and glasses. *Journal of Materials Science* **1997,** *32* (22), 5851-5887.

40.   Wiss, T.; Matzke, H.; Rondinella, V. V.; Sonoda, T.; Assmann, W.; Toulemonde, M.; Trautmann, C., Damage produced in magnesium aluminate spinel by high energy heavy ions including fission products of fission energy: microstructure modifications. *Progress in Nuclear Energy* **2001,** *38* (3), 281-286.

41.   Zinkle, S. J.; Was, G. S., Materials challenges in nuclear energy. *Acta Materialia* **2013,** *61* (3), 735-758.

42.   Duan, X.; Yuan, D.; Yu, F., Cation Distribution in Co-Doped $ZnAl_2O_4$ Nanoparticles Studied by X-ray Photoelectron Spectroscopy and ^{27}Al Solid-State NMR Spectroscopy. *Inorganic Chemistry* **2011,** *50* (12), 5460-5467.

43.   Redfern, S. A.; Harrison, R. J.; O'Neill, H. S. C.; Wood, D. R., Thermodynamics and kinetics of cation ordering in $MgAl_2O_4$ spinel up to 1600 C from in situ neutron diffraction. *American Mineralogist* **1999,** *84* (3), 299-310.

44.   Dwibedi, D.; Murugesan, C.; Leskes, M.; Barpanda, P., Role of annealing temperature on cation ordering in hydrothermally prepared zinc aluminate ($ZnAl_2O_4$) spinel. *Materials Research Bulletin* **2018,** *98*, 219-224.

45.   Van Minh, N.; Yang, I.-S., A Raman study of cation-disorder transition temperature of natural $MgAl_2O_4$ spinel. *Vibrational spectroscopy* **2004,** *35* (1-2), 93-96.

46.   O'Quinn, E. C.; Shamblin, J.; Perlov, B.; Ewing, R. C.; Neuefeind, J.; Feygenson, M.; Gussev, I.; Lang, M., Inversion in $Mg_{1-x}Ni_xAl_2O_4$ Spinel: New Insight into Local Structure. *Journal of the American Chemical Society* **2017,** *139* (30), 10395-10402.

47.   Schmocker, U.; Boesch, H. R.; Waldner, F., A direct determination of cation disorder in $MgAl_2O_4$ spinel by ESR. *Physics Letters A* **1972,** *40* (3), 237-238.

48.   Pellerin, N.; Dodane-Thiriet, C.; Montouillout, V.; Beauvy, M.; Massiot, D., Cation Sublattice Disorder Induced by Swift Heavy Ions in $MgAl_2O_4$ and $ZnAl_2O_4$ Spinels: ^{27}Al Solid-State NMR Study. *The Journal of Physical Chemistry B* **2007,** *111* (44), 12707-12714.

49.   Sepelak, V.; Bergmann, I.; Indris, S.; Feldhoff, A.; Hahn, H.; Becker, K. D.; Grey, C. P.; Heitjans, P., High-resolution ^{27}Al MAS NMR spectroscopic studies of the response of spinel aluminates to mechanical action. *Journal of Materials Chemistry* **2011,** *21* (23), 8332-8337.

50.   Blaakmeer, E. S.; Rosciano, F.; van Eck, E. R. H., Lithium Doping of $MgAl_2O_4$ and $ZnAl_2O_4$ Investigated by High-Resolution Solid State NMR. *The Journal of Physical Chemistry C* **2015,** *119* (14), 7565-7577.

51.   van der Laag, N. J.; Snel, M. D.; Magusin, P. C. M. M.; de With, G., Structural, elastic, thermophysical and dielectric properties of zinc aluminate ($ZnAl_2O_4$). *Journal of the European Ceramic Society* **2004,** *24* (8), 2417-2424.

52.   Bragg, W. H., The Structure of Magnetite and the Spinels. *Nature* **1915,** *95* (2386), 561-561.

53.   Nishikawa, S. H.; Ocirc; Ji, Structure of Some Crystals of Spinel Group. *Tokyo Sugaku-Buturigakkwai Kizi Dai 2 Ki* **1915,** *8* (7), 199-209_1.

54.   Stevanović, V.; d'Avezac, M.; Zunger, A., Universal Electrostatic Origin of Cation Ordering in A_2BO_4 Spinel Oxides. *Journal of the American Chemical Society* **2011,** *133* (30), 11649-11654.

55.   Wojtowicz, P. J., Theoretical model for tetragonal-to-cubic phase transformations in transition metal spinels. *Physical Review* **1959,** *116* (1), 32.

56.   Cheng, F.; Shen, J.; Peng, B.; Pan, Y.; Tao, Z.; Chen, J., Rapid room-temperature synthesis of nanocrystalline spinels as oxygen reduction and evolution electrocatalysts. *Nature chemistry* **2011,** *3* (1), 79.

57.   Errandonea, D.; Kumar, R. S.; Manjón, F.; Ursaki, V.; Rusu, E., Post-spinel transformations and equation of state in $ZnGa_2O_4$: determination at high pressure by in situ x-ray diffraction. *Physical Review B* **2009,** *79* (2), 024103.

58.   Ware, M., Prussian blue: Artists' pigment and chemists' sponge. ACS Publications: 2008.

59.   Itaya, K.; Uchida, I., Nature of intervalence charge-transfer bands in Prussian blues. *Inorganic Chemistry* **1986,** *25* (3), 389-392.

60.   Itaya, K.; Ataka, T.; Toshima, S., Spectroelectrochemistry and electrochemical preparation method of Prussian blue modified electrodes. *Journal of the American Chemical Society* **1982,** *104* (18), 4767-4772.

61.   Liu, S.; Li, H.; Jiang, M.; Li, P., Platinum hexacyanoferrate: A novel Prussian Blue analogue with stable electroactive properties. *Journal of Electroanalytical Chemistry* **1997,** *426* (1), 27-30.

62.   Han, L.; Yu, X. Y.; Lou, X. W., Formation of Prussian-Blue-Analog Nanocages via a Direct Etching Method and their Conversion into Ni–Co-Mixed Oxide for Enhanced Oxygen Evolution. *Advanced Materials* **2016,** *28* (23), 4601-4605.

63.   Lee, J. H.; Ali, G.; Kim, D. H.; Chung, K. Y., Metal-Organic Framework Cathodes Based on a Vanadium Hexacyanoferrate Prussian Blue Analogue for High-Performance Aqueous Rechargeable Batteries. *Advanced Energy Materials* **2017,** *7* (2).

64.   Nie, P.; Yuan, J.; Wang, J.; Le, Z.; Xu, G.; Hao, L.; Pang, G.; Wu, Y.; Dou, H.; Yan, X.; Zhang, X., Prussian Blue Analogue with Fast Kinetics Through Electronic Coupling for Sodium Ion Batteries. *ACS Applied Materials & Interfaces* **2017,** *9* (24), 20306-20312.

65.   Kaye, S. S.; Long, J. R., Hydrogen Storage in the Dehydrated Prussian Blue Analogues $M_3[Co(CN)_6]_2$ (M = Mn, Fe, Co, Ni, Cu, Zn). *Journal of the American Chemical Society* **2005,** *127* (18), 6506-6507.

66.   Kaye, S. S.; Long, J. R., The role of vacancies in the hydrogen storage properties of Prussian blue analogues. *Catalysis Today* **2007,** *120* (3), 311-316.

67.   Reguera, L.; Krap, C. P.; Balmaseda, J.; Reguera, E., Hydrogen Storage in Copper Prussian Blue Analogues: Evidence of H2 Coordination to the Copper Atom. *The Journal of Physical Chemistry C* **2008,** *112* (40), 15893-15899.

68.   Lavaud, C.; Kajdan, M.; Compte, E.; Maurel, J.-C.; Lai Kee Him, J.; Bron, P.; Oliviero, E.; Long, J.; Larionova, J.; Guari, Y., In situ synthesis of Prussian blue nanoparticles within a biocompatible reverse micellar system for in vivo Cs^+ uptake. *New Journal of Chemistry* **2017,** *41* (8), 2887-2890.

69.   Liu, J.; Li, X.; Rykov, A. I.; Fan, Q.; Xu, W.; Cong, W.; Jin, C.; Tang, H.; Zhu, K.; Ganeshraja, A. S.; Ge, R.; Wang, X.; Wang, J., Zinc-modulated Fe–Co Prussian blue analogues with well-controlled morphologies for the efficient sorption of cesium. *Journal of Materials Chemistry A* **2017,** *5* (7), 3284-3292.

70.   Nielsen, P.; Fischer, R.; Heinrich, H.; Pfau, A., Prevention of enteral radiocesium absorption by hexacyanoferrates (II) in piglets. *Experientia* **1988,** *44* (6), 502-504.

71.   Andrus, M. J.; Calm, Y. M.; Knowles, E. S.; Dumont, M. F.; Abboud, K. A.; Meisel, M. W.; Talham, D. R., Influence of particle size on the phase behavior associated with the thermal spin transition of the Prussian blue analogue $K_{0.4}Co_{1.3}[Fe(CN)_6]\cdot4.4H_2O$. *Polyhedron* **2013,** *64*, 289-293.

72.   Vaucher, S.; Li, M.; Mann, S., Synthesis of Prussian blue nanoparticles and nanocrystal superlattices in reverse microemulsions. *Angewandte Chemie* **2000,** *112* (10), 1863-1866.

73.   Dumont, M. F.; Risset, O. N.; Knowles, E. S.; Yamamoto, T.; Pajerowski, D. M.; Meisel, M. W.; Talham, D. R., Synthesis and Size Control of Iron(II) Hexacyanochromate(III) Nanoparticles and the Effect of Particle Size on Linkage Isomerism. *Inorganic Chemistry* **2013,** *52* (8), 4494-4501.

74.   Zakaria, M. B.; Chikyow, T., Recent advances in Prussian blue and Prussian blue analogues: synthesis and thermal treatments. *Coordination Chemistry Reviews* **2017,** *352*, 328-345.

75.   Uemura, T.; Ohba, M.; Kitagawa, S., Size and Surface Effects of Prussian Blue Nanoparticles Protected by Organic Polymers. *Inorganic Chemistry* **2004,** *43* (23), 7339-7345.

76.   Li, Z.; Zhang, J.; Mu, T.; Du, J.; Liu, Z.; Han, B.; Chen, J., Preparation of polyvinylpyrrolidone-protected Prussian blue nanocomposites in microemulsion. *Colloids and Surfaces A: Physicochemical and Engineering Aspects* **2004,** *243* (1-3), 63-66.

77.   Cumberland, S. L.; Hanif, K. M.; Javier, A.; Khitrov, G. A.; Strouse, G. F.; Woessner, S. M.; Yun, C. S., Inorganic Clusters as Single-Source Precursors for Preparation of CdSe, ZnSe, and CdSe/ZnS Nanomaterials. *Chemistry of Materials* **2002,** *14* (4), 1576-1584.

78.   Agrawal, A.; Cho, S. H.; Zandi, O.; Ghosh, S.; Johns, R. W.; Milliron, D. J., Localized surface plasmon resonance in semiconductor nanocrystals. *Chemical reviews* **2018,** *118* (6), 3121-3207.

79.   Gabr, A. M.; Wheeldon, J. F.; Beal, R. M.; Walker, A.; Sacks, J.; Savidge, R. M.; Hall, T. J.; Kleiman, R. N.; Hinzer, K. In *Modeling down-conversion and down-shifting for photovoltaic applications*, Photovoltaic Specialists Conference (PVSC), 2012 38th IEEE, IEEE: 2012; pp 000048-000052.

80.   Bardsley, N.; Hansen, M.; Pattison, L.; Pattison, M.; Stober, K.; Taylor, V.; Tsao, J.; Yamada, M., Solid-State Lighting R&D Plan. Energy, U. S. D. o., Ed. 2016.

81.   Yang, Z.; Li, X.; Yang, Y.; Li, X., The influence of different conditions on the luminescent properties of YAG:Ce phosphor formed by combustion. *Journal of Luminescence* **2007,** *122*, 707-709.

82.   Xia, Z.; Xu, Z.; Chen, M.; Liu, Q., Recent developments in the new inorganic solid-state LED phosphors. *Dalton Transactions* **2016,** *45* (28), 11214-11232.

83.   Murphy, J. E. a. G.-S. F. a. S. A. A. a. S. S. S., 62.4: PFS, K_2SiF_6:Mn^{4+}: the Red-line Emitting LED Phosphor behind GE's TriGain Technology™ Platform. *SID Symposium Digest of Technical Papers* **2015,** *46* (1), 927--930.

84.   Murphy, J. E.; Garcia-Santamaria, F.; Setlur, A. A.; Sista, S. In *62.4: PFS, K_2SiF_6: Mn^{4+}: the Red-line Emitting LED Phosphor behind GE's TriGain Technology™ Platform*, SID Symposium Digest of Technical Papers, Wiley Online Library: 2015; pp 927-930.

85.   Garcia-Santamaria, F.; Murphy, J.; Setlur, A.; Sista, S., Concentration quenching in K_2SiF_6: Mn^{4+} phosphors. *ECS Journal of Solid State Science and Technology* **2018,** *7* (1), R3030-R3033.

86.   Bauer, D.; Diamond, D.; Li, J.; Sandalow, D.; Telleen, P.; Wanner, B., US Department of Energy critical materials strategy. **2010**.

87.   Sastri, V. S.; BÜNzli, J.-C.; Rao, V. R.; Rayudu, G. V. S.; Perumareddi, J. R., chapter 1 - INTRODUCTION. In *Modern Aspects of Rare Earths and Their Complexes*, Sastri, V. S.; BÜNzli, J.-C.; Rao, V. R.; Rayudu, G. V. S.; Perumareddi, J. R., Eds. Elsevier: Amsterdam, 2003; pp 1-72.

88.   Bünzli, J.-C. G.; Eliseeva, S. V., Basics of Lanthanide Photophysics. In *Lanthanide Luminescence: Photophysical, Analytical and Biological Aspects*, Hänninen, P.; Härmä, H., Eds. Springer Berlin Heidelberg: Berlin, Heidelberg, 2011; pp 1-45.

89.   Bunzli, J.-C. G.; Piguet, C., Taking advantage of luminescent lanthanide ions. *Chemical Society Reviews* **2005,** *34* (12), 1048-1077.

90.   Bunzli, J.-C. G.; Eliseeva, S. V., Intriguing aspects of lanthanide luminescence. *Chemical Science* **2013,** *4* (5), 1939-1949.

91.   de Bettencourt-Dias, A., *Luminescence of lanthanide ions in coordination compounds and nanomaterials*. John Wiley & Sons: 2014.

92.   Binnemans, K., Interpretation of europium (III) spectra. *Coordination Chemistry Reviews* **2015,** *295*, 1-45.

93.   Ahmed, Z.; Iftikhar, K., Efficient Layers of Emitting Ternary Lanthanide Complexes for Fabricating Red, Green, and Yellow OLEDs. *Inorganic Chemistry* **2015,** *54* (23), 11209-11225.

94.   Duhamel-Henry, N.; Adam, J.; Jacquier, B.; Linares, C., Photoluminescence of new fluorophosphate glasses containing a high concentration of terbium (III) ions. *Optical Materials* **1996,** *5* (3), 197-207.

95.   Zhang, Y.; Liu, X., Nanocrystals: Shining a light on upconversion. *Nat Nano* **2013,** *8* (10), 702-703.

96.   Tver'yanovich, Y. S., Concentration Quenching of Luminescence of Rare-Earth Ions in Chalcogenide Glasses. *Glass Physics and Chemistry* **2003,** *29* (2), 166-168.

97.   Johnson, N. J. J.; He, S.; Diao, S.; Chan, E. M.; Dai, H.; Almutairi, A., Direct Evidence for Coupled Surface and Concentration Quenching Dynamics in Lanthanide-Doped Nanocrystals. *Journal of the American Chemical Society* **2017,** *139* (8), 3275-3282.

98.   Stouwdam, J. W.; van Veggel, F. C. J. M., Near-infrared Emission of Redispersible Er^{3+}, Nd^{3+}, and Ho^{3+} Doped LaF$_3$ Nanoparticles. *Nano Letters* **2002,** *2* (7), 733-737.

99.   Nockemann, P.; Beurer, E.; Driesen, K.; Van Deun, R.; Van Hecke, K.; Van Meervelt, L.; Binnemans, K., Photostability of a highly luminescent europium β-diketonate complex in imidazolium ionic liquids. *Chemical Communications* **2005,** (34), 4354-4356.

100.   Brouwer, A. M., Standards for photoluminescence quantum yield measurements in solution (IUPAC Technical Report). *Pure and Applied Chemistry* **2011,** *83* (12), 2213-2228.

101.   D'Aléo, A.; Moore, E. G.; Xu, J.; Daumann, L. J.; Raymond, K. N., Optimization of the Sensitization Process and Stability of Octadentate Eu(III) 1,2-HOPO Complexes. *Inorganic Chemistry* **2015,** *54* (14), 6807-6820.

102.   de Lill, D. T.; de Bettencourt-Dias, A.; Cahill, C. L., Exploring Lanthanide Luminescence in Metal-Organic Frameworks: Synthesis, Structure, and Guest-Sensitized Luminescence of a Mixed Europium/Terbium-Adipate Framework and a Terbium-Adipate Framework. *Inorganic Chemistry* **2007,** *46* (10), 3960-3965.

103.   Berberan-Santos, M.; Bodunov, E.; Valeur, B., Mathematical functions for the analysis of luminescence decays with underlying distributions 1. Kohlrausch decay function (stretched exponential). *Chemical Physics* **2005,** *315* (1-2), 171-182.

104.   Inokuti, M.; Hirayama, F., Influence of energy transfer by the exchange mechanism on donor luminescence. *The journal of chemical physics* **1965,** *43* (6), 1978-1989.

105.   Berberan-Santos, M.; Bodunov, E.; Martinho, J., Luminescence quenching in fractal media accelerated by migration. *Optics and Spectroscopy* **1996,** *81* (2), 217-221.

106.   Berberan-Santos, M.; Bodunov, E.; Martinho, J., Kinetics of luminescence of porous media: The effective fractal dimensionality and penetration depth of chromophores. *OPTICS AND SPECTROSCOPY C/C OF OPTIKA I SPEKTROSKOPIIA* **1999,** *87*, 66-69.

107.   Bodunov, E. N.; Simões Gamboa, A. L., Luminescence Decay of Colloidal Quantum Dots and Stretched Exponential (Kohlrausch) Relaxation Function. *Semiconductors* **2018,** *52* (5), 587-589.

108.   Moore, E. G.; Samuel, A. P. S.; Raymond, K. N., From Antenna to Assay: Lessons Learned in Lanthanide Luminescence. *Accounts of Chemical Research* **2009,** *42* (4), 542-552.

109.   Daumann, L. J.; Tatum, D. S.; Snyder, B. E. R.; Ni, C.; Law, G.-l.; Solomon, E. I.; Raymond, K. N., New Insights into Structure and Luminescence of EuIII and SmIII Complexes of the 3,4,3-LI(1,2-HOPO) Ligand. *Journal of the American Chemical Society* **2015,** *137* (8), 2816-2819.

110.   Daumann, L. J.; Werther, P.; Ziegler, M. J.; Raymond, K. N., Siderophore inspired tetra- and octadentate antenna ligands for luminescent Eu(III) and Tb(III) complexes. *Journal of Inorganic Biochemistry* **2016,** *162*, 263-273.

111.   Viswanathan, S.; de Bettencourt-Dias, A., Eu(III) and Tb(III) Luminescence Sensitized by Thiophenyl-Derivatized Nitrobenzoato Antennas. *Inorganic Chemistry* **2006,** *45* (25), 10138-10146.

112.   N. Berberan Santos, M., External heavy-atom effect on fluorescence kinetics. *PhysChemComm* **2000,** *3* (5), 18-23.

113.   Kasha, M., Collisional Perturbation of Spin-Orbital Coupling and the Mechanism of Fluorescence Quenching. A Visual Demonstration of the Perturbation. *The Journal of Chemical Physics* **1952,** *20* (1), 71-74.

114.   McClure, D. S., Spin-Orbit Interaction in Aromatic Molecules. *The Journal of Chemical Physics* **1952,** *20* (4), 682-686.

115.   Mara, M. W.; Tatum, D. S.; March, A.-M.; Doumy, G.; Moore, E. G.; Raymond, K. N., Energy Transfer from Antenna Ligand to Europium(III) Followed Using Ultrafast Optical and X-ray Spectroscopy. *Journal of the American Chemical Society* **2019,** *141* (28), 11071-11081.

116.   Dexter, D. L., A Theory of Sensitized Luminescence in Solids. *The Journal of Chemical Physics* **1953,** *21* (5), 836-850.

117.   Ward, M. D., Mechanisms of sensitization of lanthanide (III)-based luminescence in transition metal/lanthanide and anthracene/lanthanide dyads. *Coordination chemistry reviews* **2010,** *254* (21-22), 2634-2642.

118.   Joshi, B., Enhanced Eu^{3+} emission by non-radiative energy transfer from Tb^{3+} in zinc phosphate glass. *Journal of non-crystalline solids* **1995,** *180* (2-3), 217-220.

119.   Van Uitert, L., Characterization of energy transfer interactions between rare earth ions. *Journal of the electrochemical society* **1967,** *114* (10), 1048-1053.

120.   Zhou, J.; Xia, Z., Multi-color emission evolution and energy transfer behavior of $La_3GaGe_5O_{16}$: Tb^{3+}, Eu^{3+} phosphors. *Journal of Materials Chemistry C* **2014,** *2* (34), 6978-6984.

121.   Perrin, F., Law of decrease in the fluorescent power according to concentration. *CR Acad. Sci. Paris* **1924,** *178*, 1978-1980.

122.   Medenbach, O.; Siritanon, T.; Subramanian, M.; Shannon, R.; Fischer, R.; Rossman, G. R., Refractive index and optical dispersion of In_2O_3, $InBO_3$ and gahnite. *Materials Research Bulletin* **2013,** *48* (6), 2240-2243.

123.   Skoog, D. A.; Holler, F. J.; Crouch, S. R., *Principles of instrumental analysis*. Cengage learning: 2017.

124.   Jahangiri, H.; Bennett, J.; Mahjoubi, P.; Wilson, K.; Gu, S., A review of advanced catalyst development for Fischer–Tropsch synthesis of hydrocarbons from biomass derived syn-gas. *Catalysis Science & Technology* **2014,** *4* (8), 2210-2229.

125.   Krylova, A. Y., Products of the Fischer-Tropsch synthesis (A Review). *Solid Fuel Chemistry* **2014,** *48* (1), 22-35.

126.   10.2.   Fischer-Tropsch   Synthesis | netl.doe.gov. https://www.netl.doe.gov/research/coal/energy-systems/gasification/gasifipedia/ftsynthesis.

127.   Ralston, W. T.; Liu, W.-C.; Alayoglu, S.; Melaet, G., Bimetallic Cobalt Nanoparticles (Co–M): Synthesis, Characterization, and Application in the Fischer–Tropsch Process. *Topics in Catalysis* **2018,** *61* (9-11), 1002-1015.

128.   Gnanamani, M. K.; Hamdeh, H. H.; Jacobs, G.; Qian, D.; Liu, F.; Hopps, S. D.; Thomas, G. A.; Shafer, W. D.; Xiao, Q.; Hu, Y.; Davis, B. H., Fischer–Tropsch synthesis: effect of Cu, Mn and Zn addition on activity and product selectivity of cobalt ferrite. *RSC Advances* **2016,** *6* (67), 62356-62367.

129.   Liu, J.-X.; Wang, P.; Xu, W.; Hensen, E. J. M., Particle Size and Crystal Phase Effects in Fischer-Tropsch Catalysts. *Engineering* **2017,** *3* (4), 467-476.

130.   Mabaso, E.; Van Steen, E.; Claeys, M., Fischer-Tropsch synthesis on supported iron crystallites of different size. *DGMK Tagungsbericht* **2006,** *4*, 93-100.

131.   Liu, Y.; Chen, J.-F.; Zhang, Y., The effect of pore size or iron particle size on the formation of light olefins in Fischer–Tropsch synthesis. *RSC Advances* **2015,** *5* (37), 29002-29007.

132.   Giordano, C.; Antonietti, M., Synthesis of crystalline metal nitride and metal carbide nanostructures by sol–gel chemistry. *Nano Today* **2011,** *6* (4), 366-380.

133.   Wang, X.; Zhang, P.; Gao, J.; Chen, X.; Yang, H., Facile synthesis and magnetic properties of Fe3C/C nanoparticles via a sol–gel process. *Dyes and Pigments* **2015,** *112*, 305-310.

134.   Wang, C.; Wang, Q.; Sun, X.; Xu, L., CO Hydrogenation to Light Alkenes Over Mn/Fe CatalystsPrepared by Coprecipitation and Sol-gel Methods. *Catalysis Letters* **2005,** *105* (1), 93-101.

135.   Wei, J.; Liang, Y.; Hu, Y.; Kong, B.; Zhang, J.; Gu, Q.; Tong, Y.; Wang, X.; Jiang, S. P.; Wang, H., Hydrothermal Synthesis of Metal–Polyphenol Coordination Crystals and Their Derived Metal/N-doped Carbon Composites for Oxygen Electrocatalysis. *Angewandte Chemie International Edition* **2016,** *55* (40), 12470-12474.

136.   Kumar, R.; Choudhary, H. K.; Pawar, S. P.; Bose, S.; Sahoo, B., Carbon encapsulated nanoscale iron/iron-carbide/graphite particles for EMI shielding and microwave absorption. *Physical Chemistry Chemical Physics* **2017,** *19* (34), 23268-23279.

137.   Yamada, M.; Okumura, S.-j.; Takahashi, K., Synthesis and Film Formation of Magnetic FeCo Nanoparticles with Graphitic Carbon Shells. *The Journal of Physical Chemistry Letters* **2010,** *1* (13), 2042-2045.

138.   Pechenyuk, S. I.; Domonov, D. P.; Shimkin, A. A.; Ivanov, Y. V., Thermal decomposition of iron cyano complexes in an inert atmosphere. *Russian Chemical Bulletin* **2015,** *64* (2), 322-328.

139.   Aparicio, C.; Machala, L.; Marusak, Z., Thermal decomposition of Prussian blue under inert atmosphere. *Journal of Thermal Analysis and Calorimetry* **2012,** *110* (2), 661-669.

140.   Ingham, B.; Lim, T. H.; Dotzler, C. J.; Henning, A.; Toney, M. F.; Tilley, R. D., How nanoparticles coalesce: an in situ study of Au nanoparticle aggregation and grain growth. *Chemistry of Materials* **2011,** *23* (14), 3312-3317.

141.   Hardy, D. A.; Nguyen, E. T.; Parrish, S. E.; Schriber, E. A.; Schlicker, L.; Gili, A.; Kamutzki, F.; Hohman, J. N.; Strouse, G. F., Prussian Blue Iron–Cobalt Mesocrystals as a Template for the Growth of Fe/Co Carbide (Cementite) and Fe/Co Nanocrystals. *Chemistry of Materials* **2019,** *31* (19), 8163-8173.

142.   Mehdad, A.; Jentoft, R. E.; Jentoft, F. C., Single-phase mixed molybdenum-niobium carbides: Synthesis, characterization and multifunctional catalytic behavior in toluene conversion. *Journal of Catalysis* **2017,** *351*, 161-173.

143.   Leclercq, L.; Provost, M.; Pastor, H.; Grimblot, J.; Hardy, A. M.; Gengembre, L.; Leclercq, G., Catalytic properties of transition metal carbides: I. Preparation and physical characterization of bulk mixed carbides of molybdenum and tungsten. *Journal of Catalysis* **1989,** *117* (2), 371-383.

144.   Luc, W.; Jiao, F., Synthesis of Nanoporous Metals, Oxides, Carbides, and Sulfides: Beyond Nanocasting. *Accounts of Chemical Research* **2016,** *49* (7), 1351-1358.

145.   Liu, X.-W.; Cao, Z.; Zhao, S.; Gao, R.; Meng, Y.; Zhu, J.-X.; Rogers, C.; Huo, C.-F.; Yang, Y.; Li, Y.-W., Iron Carbides in Fischer–Tropsch Synthesis: Theoretical and Experimental Understanding in Epsilon-Iron Carbide Phase Assignment. *The Journal of Physical Chemistry C* **2017,** *121* (39), 21390-21396.

146.   Kunz, M.; MacDowell, A. A.; Caldwell, W. A.; Cambie, D.; Celestre, R. S.; Domning, E. E.; Duarte, R. M.; Gleason, A. E.; Glossinger, J. M.; Kelez, N.; Plate, D. W.; Yu, T.; Zaug, J. M.; Padmore, H. A.; Jeanloz, R.; Alivisatos, A. P.; Clark, S. M., A beamline for high-pressure studies at the Advanced Light Source with a superconducting bending magnet as the source. *Journal of Synchrotron Radiation* **2005,** *12* (5), 650-658.

147.   Doran, A.; Schlicker, L.; Beavers, C. M.; Bhat, S.; Bekheet, M. F.; Gurlo, A., Compact low power infrared tube furnace for in situ X-ray powder diffraction. *Review of Scientific Instruments* **2017,** *88* (1), 013903.

148.   Schlicker, L.; Doran, A.; Schneppmüller, P.; Gili, A.; Czasny, M.; Penner, S.; Gurlo, A., Transmission in situ and operando high temperature X-ray powder diffraction in variable gaseous environments. *Review of Scientific Instruments* **2018,** *89* (3), 033904.

149.   Gili, A.; Schlicker, L.; Bekheet, M. F.; Görke, O.; Penner, S.; Grünbacher, M.; Götsch, T.; Littlewood, P.; Marks, T. J.; Stair, P. C.; Schomäcker, R.; Doran, A.; Selve, S.; Simon, U.; Gurlo, A., Surface Carbon as a Reactive Intermediate in Dry Reforming of Methane to Syngas on a 5% Ni/MnO Catalyst. *ACS Catalysis* **2018,** *8* (9), 8739-8750.

150.   Chapman, K. W.; Chupas, P. J.; Kepert, C. J., Compositional dependence of negative thermal expansion in the prussian blue analogues MIIPtIV (CN) 6 (M= Mn, Fe, Co, Ni, Cu, Zn, Cd). *Journal of the American Chemical Society* **2006,** *128* (21), 7009-7014.

151.   Shi, N.; Gao, Q.; Sanson, A.; Li, Q.; Fan, L.; Ren, Y.; Olivi, L.; Chen, J.; Xing, X., Negative thermal expansion in cubic FeFe (CN) 6 Prussian blue analogues. *Dalton Transactions* **2019**.

152.   Sugimoto, M.; Yamashita, S.; Akutsu, H.; Nakazawa, Y.; DaSilva, J. G.; Kareis, C. M.; Miller, J. S., Increase in the Magnetic Ordering Temperature (Tc) as a Function of the Applied Pressure for $A_2Mn[Mn(CN)_6]$ (A = K, Rb, Cs) Prussian Blue Analogues. *Inorganic Chemistry* **2017,** *56* (17), 10452-10457.

153.   Her, J.-H.; Stephens, P. W.; Kareis, C. M.; Moore, J. G.; Min, K. S.; Park, J.-W.; Bali, G.; Kennon, B. S.; Miller, J. S., Anomalous Non-Prussian Blue Structures and Magnetic Ordering of $K_2Mn^{II}[Mn^{II}(CN)_6]$ and $Rb_2Mn^{II}[Mn^{II}(CN)_6]$. *Inorganic Chemistry* **2010,** *49* (4), 1524-1534.

154.   Clayton, C. R., Materials science and engineering: An introduction: by WD Callister Jr.; published by Wiley, Chichester, West Sussex, 1985; 602 pp.; price,£ 40.40. Elsevier: 1987.

155.   Georgiadou, V.;   Kokotidou, C.;   Le Droumaguet, B.;   Carbonnier, B.;   Choli-Papadopoulou, T.; Dendrinou-Samara, C., Oleylamine as a beneficial agent for the synthesis of CoFe2O4 nanoparticles with potential biomedical uses. *Dalton Transactions* **2014,** *43* (17), 6377-6388.

156.   Kulesza, P. J.;   Malik, M. A.;   Denca, A.; Strojek, J., In Situ FT-IR/ATR Spectroelectrochemistry of Prussian Blue in the Solid State. *Analytical Chemistry* **1996,** *68* (14), 2442-2446.

157.   Kettle, S. F. A.;   Diana, E.;   Marchese, E. M. C.;   Boccaleri, E.; Stanghellini, P. L., The vibrational spectra of the cyanide ligand revisited: the ν(CN) infrared and Raman spectroscopy of Prussian blue and its analogues. *Journal of Raman Spectroscopy* **2011,** *42* (11), 2006-2014.

158.   Zhilinskaya, V. V.; Gol'tsov, Y. G.; Glukhoi, A. M.; Korol, É. N., Study of pentacyanide complexes of iron by mass spectrometry with bombardment by fast atoms. *Theoretical and Experimental Chemistry* **1989,** *25* (6), 675-679.

159.   Chapman, K. W.;   Chupas, P. J.;   Maxey, E. R.; Richardson, J. W., Direct observation of adsorbed H_2-framework interactions in the Prussian Blue analogue $Mn^{II}_3[Co^{III}(CN)_6]_2$: The relative importance of accessible coordination sites and van der Waals interactions. *Chemical Communications* **2006,** (38), 4013-4015.

160.   Shtansky, D. V.;   Nakai, K.; Ohmori, Y., Mechanism and crystallography of ferrite precipitation from cementite in an Fe-Cr-C alloy during austenitization. *Philosophical Magazine A* **1999,** *79* (7), 1655-1669.

161.   Kim, J.;   Kang, K.; Ryu, S., Characterization of the misfit dislocations at the ferrite/cementite interface in pearlitic steel: An atomistic simulation study. *International Journal of Plasticity* **2016,** *83*, 302-312.

162.   Guziewski, M.;   Coleman, S. P.; Weinberger, C. R., Atomistic investigation into the mechanical properties of the ferrite-cementite interface: The Bagaryatskii orientation. *Acta Materialia* **2018,** *144*, 656-665.

163.   Ivanisenko, Y.;   Lojkowski, W.;   Valiev, R.; Fecht, H.-J., The mechanism of formation of nanostructure and dissolution of cementite in a pearlitic steel during high pressure torsion. *Acta Materialia* **2003,** *51* (18), 5555-5570.

164.   Sauvage, X.; Ivanisenko, Y., The role of carbon segregation on nanocrystallisation of pearlitic steels processed by severe plastic deformation. *Journal of Materials Science* **2007,** *42* (5), 1615-1621.

165.   Karmakar, A.; Mandal, M.; Mandal, A.; Basiruddin Sk, M.; Mukherjee, S.; Chakrabarti, D., Effect of Starting Microstructure on the Grain Refinement in Cold-Rolled Low-Carbon Steel During Annealing at Two Different Heating Rates. *Metallurgical and Materials Transactions A* **2016,** *47* (1), 268-281.

166.   Kapp, M. W.; Hohenwarter, A.; Wurster, S.; Yang, B.; Pippan, R., Anisotropic deformation characteristics of an ultrafine- and nanolamellar pearlitic steel. *Acta Materialia* **2016,** *106*, 239-248.

167.   Shtansky, D. V.; Nakai, K.; Ohmori, Y., Pearlite to austenite transformation in an Fe–2.6Cr–1C alloy. *Acta Materialia* **1999,** *47* (9), 2619-2632.

168.   Mangan, M. A.; Shiflet, G. J., The pitsch-petch orientation relationship in ferrous pearlite at small undercooling. *Metallurgical and Materials Transactions A* **1999,** *30* (11), 2767-2781.

169.   Kante, S.; Leineweber, A., EBSD characterization of the eutectic microstructure in hypoeutectic Fe-C and Fe-C-Si alloys. *Materials Characterization* **2018,** *138*, 274-283.

170.   Song, E.; Zhao, W.; Dou, X.; Zhu, Y.; Yi, S.; Min, H., Nonradiative energy transfer from Mn^{2+} to Eu^{3+} in $K_2CaP_2O_7$:Mn^{2+},Eu^{3+} phosphor. *Journal of Luminescence* **2012,** *132* (6), 1462-1467.

171.   George, N. C.; Denault, K. A.; Seshadri, R., Phosphors for Solid-State White Lighting. *Annual Review of Materials Research* **2013,** *43* (1), 481-501.

172.   Agbo, P.; Abergel, R. J., Ligand-Sensitized Lanthanide Nanocrystals: Merging Solid-State Photophysics and Molecular Solution Chemistry. *Inorganic Chemistry* **2016,** *55* (20), 9973-9980.

173.   Wang, X.; Valiev, R. R.; Ohulchanskyy, T. Y.; Ågren, H.; Yang, C.; Chen, G., Dye-sensitized lanthanide-doped upconversion nanoparticles. *Chemical Society Reviews* **2017,** *46* (14), 4150-4167.

174.   Vats, B. G.; Shafeeq, M.; Singhal, P.; Neogy, S., Organic Soluble $LaPO_4$: Eu^{3+} Nanorods: Sensitization of Surface Eu^{3+} Ions and Phase Transfer in Water. *ChemistrySelect* **2018,** *3* (17), 4930-4938.

175.   Samanta, T.; Jana, S. K.; Praveen, A. E.; Mahalingam, V., Ligand sensitized strong luminescence from Eu^{3+}-doped $LiYF_4$ nanocrystals: a photon down-shifting strategy to increase solar-to-current conversion efficiency. *Dalton Transactions* **2017,** *46* (29), 9646-9653.

176.   Latva, M.; Takalo, H.; Mukkala, V.-M.; Matachescu, C.; Rodríguez-Ubis, J. C.; Kankare, J., Correlation between the lowest triplet state energy level of the ligand and lanthanide (III) luminescence quantum yield. *Journal of Luminescence* **1997,** *75* (2), 149-169.

177.   Listkowski, A.; Osińska, W.; Mohanraj, J.; Pietraszkiewicz, M.; Dutkiewicz, G.; Borowiak, T., Synthesis and photoluminescence properties of novel lanthanide complexes based on pyrazolone Schiff bases. *Synthetic Metals* **2012,** *162* (13), 1285-1291.

178. Liu, J.; Lian, H.; Shi, C., Improved optical photoluminescence by charge compensation in the phosphor system $CaMoO_4$:Eu^{3+}. *Optical Materials* **2007,** *29* (12), 1591-1594.

179. Hong, W. T.; Lee, J. H.; Jang, H. I.; Park, S. J.; Joo, J. S.; Yang, H. K. In *Orange-red light emitting europium doped calcium molybdate phosphor prepared by high energy ball milling method*, 2015 20th Microoptics Conference (MOC), 25-28 Oct. 2015; 2015; pp 1-2.

180. Xie, W.; Mo, Y.; Zou, C.; Kang, F.; Sun, G., Broad color tuning and Eu^{3+}-related photoemission enhancement via controllable energy transfer in the La_2MgGeO_6:Eu^{3+},Bi^{3+} phosphor. *Inorganic Chemistry Frontiers* **2018,** *5* (5), 1076-1084.

181. Huang, C.-H.; Kuo, T.-W.; Chen, T.-M., Thermally stable green $Ba_3Y(PO_4)_3$:Ce^{3+}, Tb^{3+} and red $Ca_3Y(AlO)_3(BO_3)_4$:Eu^{3+} phosphors for white-light fluorescent lamps. *Optics express* **2011,** *19* (101), A1-A6.

182. Tang, Y.-S.; Hu, S.-F.; Lin, C. C.; Bagkar, N. C.; Liu, R.-S., Thermally stable luminescence of $KSrPO_4$:Eu^{2+} phosphor for white light UV light-emitting diodes. *Applied Physics Letters* **2007,** *90* (15), 151108.

183. Chengelis, D. A.; Yingling, A. M.; Badger, P. D.; Shade, C. M.; Petoud, S., Incorporating Lanthanide Cations with Cadmium Selenide Nanocrystals: A Strategy to Sensitize and Protect Tb(III). *Journal of the American Chemical Society* **2005,** *127* (48), 16752-16753.

184. Kömpe, K.; Borchert, H.; Storz, J.; Lobo, A.; Adam, S.; Möller, T.; Haase, M., Green-Emitting $CePO_4$:Tb/$LaPO_4$ Core–Shell Nanoparticles with 70 % Photoluminescence Quantum Yield. *Angewandte Chemie International Edition* **2003,** *42* (44), 5513-5516.

185. Dong, A.; Ye, X.; Chen, J.; Kang, Y.; Gordon, T.; Kikkawa, J. M.; Murray, C. B., A Generalized Ligand-Exchange Strategy Enabling Sequential Surface Functionalization of Colloidal Nanocrystals. *Journal of the American Chemical Society* **2011,** *133* (4), 998-1006.

186. H. V. Werts, M.; A. Duin, M.; W. Hofstraat, J.; W. Verhoeven, J., Bathochromicity of Michler's ketone upon coordination with lanthanide(III) β-diketonates enables efficient sensitisation of Eu^{3+} for luminescence under visible light excitation†. *Chemical Communications* **1999,** (9), 799-800.

187. Villata, L. S.; Wolcan, E.; Féliz, M. R.; Capparelli, A. L., Competition between Intraligand Triplet Excited State and LMCT on the Thermal Quenching in β-Diketonate Complexes of Europium(III). *The Journal of Physical Chemistry A* **1999,** *103* (29), 5661-5666.

188. Bulgakov, R. G.; Eliseeva, S. M.; Galimov, D. I., The first registration of a green liquid-phase chemiluminescence of the divalent Eu^{2+} ion in interaction of β-diketonate complexes $Eu(acac)_3 \cdot H_2O$, $Eu(dpm)_3$, $Eu(fod)_3$ and $Eu(CH_3COO)_3 \cdot 6H_2O$ with Bui_2AlH in THF with the participation of oxygen. *RSC Advances* **2015,** *5* (64), 52132-52140.

189. Berry, M. T.; May, P. S.; Xu, H., Temperature Dependence of the Eu^{3+} $^5D_0$ Lifetime in Europium Tris(2,2,6,6-tetramethyl-3,5-heptanedionato). *The Journal of Physical Chemistry* **1996,** *100* (22), 9216-9222.

190.   Sager, W. F.; Filipescu, N.; Serafin, F. A., Substituent Effects on Intramolecular Energy Transfer. I. Absorption and Phosphorescence Spectra of Rare Earth β-Diketone Chelates. *The Journal of Physical Chemistry* **1965,** *69* (4), 1092-1100.

191.   Zheng, Y.; Liang, Y.; Zhang, H.; Lin, Q.; Chuan, G.; Wang, S., Red electroluminescent device with europium 1,1,1-trifluoroacetylacetonate complex as emissive center. *Materials Letters* **2002,** *53* (1), 52-56.

192.   Katagiri, S.; Hasegawa, Y.; Wada, Y.; Yanagida, S., Thermo-sensitive Luminescence Based on the Back Energy Transfer in Terbium(III) Complexes. *Chemistry Letters* **2004,** *33* (11), 1438-1439.

193.   Marciniak, B.; Elbanowski, M.; Lis, S., Quenching of the triplet state of benzophenone by lanthanide 1,3-diketonate chelates in solutions. *Monatshefte für Chemie / Chemical Monthly* **1988,** *119* (6), 669-676.

194.   Dao, P.; Twarowski, A. J., The photophysics of gas phase europium chelates. I. Temperature dependence of luminescence. *The Journal of chemical physics* **1986,** *85* (12), 6823-6827.

195.   dos Santos, E. R.; Freire, R. O.; da Costa, N. B.; Paz, F. A. A.; de Simone, C. A.; Júnior, S. A.; Araújo, A. A. S.; Nunes, L. A. O.; de Mesquita, M. E.; Rodrigues, M. O., Theoretical and Experimental Spectroscopic Approach of Fluorinated $Ln^{3+}-$β-Diketonate Complexes. *The Journal of Physical Chemistry A* **2010,** *114* (30), 7928-7936.

196.   Wolcan, E.; Villata, L.; Capparelli, A. L.; Féliz, M. R., Temperature effects on the quenching of the $^5D_0 \rightarrow {}^7F_2$ emission of Eu(6,6,7,7,8,8,8-heptafluoro-2,2-dimethyl-3,5-octanedionate)$_3$ by a Cu(II) macrocycle. *Photochemical & Photobiological Sciences* **2004,** *3* (3), 322-327.

197.   Huang, Y.-J.; Ke, C.; Fu, L.-M.; Li, Y.; Wang, S.-F.; Ma, Y.-C.; Zhang, J.-P.; Wang, Y., Excitation Energy-Transfer Processes in the Sensitization Luminescence of Europium in a Highly Luminescent Complex. *ChemistryOpen* **2019,** *8* (3), 388-392.

198.   Kazakov, V. P.; Voloshin, A. I.; Shavaleev, N. M., Chemiluminescence in visible and infrared spectral regions and quantum chain reactions upon thermal and photochemical decomposition of adamantylideneadamantane-1,2-dioxetane in the presence of chelates Pr(dpm)$_3$ and Pr(fod)$_3$. *Journal of Photochemistry and Photobiology A: Chemistry* **1998,** *119* (3), 177-186.

199.   Ilmi, R.; Iftikhar, K., Optical emission studies of new europium and terbium dinuclear complexes with trifluoroacetylacetone and bridging bipyrimidine. Fast radiation and high emission quantum yield. *Polyhedron* **2015,** *102*, 16-26.

200.   Congiu, M.; Alamiry, M.; Moudam, O.; Ciorba, S.; Richardson, P. R.; Maron, L.; Jones, A. C.; Richards, B. S.; Robertson, N., Preparation and photophysical studies of [Ln(hfac)$_3$DPEPO], Ln = Eu, Tb, Yb, Nd, Gd; interpretation of total photoluminescence quantum yields. *Dalton Transactions* **2013,** *42* (37), 13537-13545.

201.   Strasser, A.; Vogler, A., Phosphorescence of gadolinium(III) chelates under ambient conditions. *Inorganica Chimica Acta* **2004,** *357* (8), 2345-2348.

202.   He, X.; Liu, X.; Li, R.; Yang, B.; Yu, K.; Zeng, M.; Yu, R., Effects of local structure of Ce^{3+} ions on luminescent properties of $Y_3Al_5O1_2$:Ce nanoparticles. *Scientific Reports* **2016,** *6*, 22238.

203.   Ahemen, I.; Dejene, F. B., The role of traps in the blue–green emission of ZrO_2:Ce^{3+}, Tb^{3+} co-doped phosphors. *Journal of Materials Science: Materials in Electronics* **2018,** *29* (3), 2140-2150.

204.   Zych, E.; Brecher, C.; Glodo, J., Kinetics of cerium emission in a YAG:Ce single crystal: the role of traps. *Journal of Physics: Condensed Matter* **2000,** *12* (8), 1947-1958.

205.   Penconi, M.; Cazzaniga, M.; Kesarkar, S.; Baldoli, C.; Mussini, P. R.; Ceresoli, D.; Bossi, A., β-Diketonate ancillary ligands in heteroleptic iridium complexes: a balance between synthetic advantages and photophysical troubles. *Photochemical & Photobiological Sciences* **2018,** *17* (9), 1169-1178.

206.   DeRosa, C. A.; Samonina-Kosicka, J.; Fan, Z.; Hendargo, H. C.; Weitzel, D. H.; Palmer, G. M.; Fraser, C. L., Oxygen Sensing Difluoroboron Dinaphthoylmethane Polylactide. *Macromolecules* **2015,** *48* (9), 2967-2977.

207.   Chen, J.; Teng, T.; Kang, L.; Chen, X.-L.; Wu, X.-Y.; Yu, R.; Lu, C.-Z., Highly Efficient Thermally Activated Delayed Fluorescence in Dinuclear Ag(I) Complexes with a Bis-Bidentate Tetraphosphane Bridging Ligand. *Inorganic Chemistry* **2016,** *55* (19), 9528-9536.

208.   Chan, K. T.; Tong, G. S. M.; To, W.-P.; Yang, C.; Du, L.; Phillips, D. L.; Che, C.-M., The interplay between fluorescence and phosphorescence with luminescent gold(I) and gold(I) complexes bearing heterocyclic arylacetylide ligands. *Chemical Science* **2017,** *8* (3), 2352-2364.

209.   Kim, J.-H.; Kim, S.-Y.; Cho, Y.-J.; Son, H.-J.; Cho, D. W.; Kang, S. O., A Detailed Evaluation for the Nonradiative Processes in Highly Phosphorescent Iridium(III) Complexes. *The Journal of Physical Chemistry C* **2018,** *122* (7), 4029-4036.

210.   Kang, F.; Yang, X.; Peng, M.; Wondraczek, L.; Ma, Z.; Zhang, Q.; Qiu, J., Red Photoluminescence from Bi^{3+} and the Influence of the Oxygen-Vacancy Perturbation in $ScVO_4$: A Combined Experimental and Theoretical Study. *The Journal of Physical Chemistry C* **2014,** *118* (14), 7515-7522.

211.   Ghodsi, V.; Jin, S.; Byers, J. C.; Pan, Y.; Radovanovic, P. V., Anomalous Photocatalytic Activity of Nanocrystalline γ-Phase Ga_2O_3 Enabled by Long-Lived Defect Trap States. *The Journal of Physical Chemistry C* **2017,** *121* (17), 9433-9441.

212.   Aebischer, A.; Gumy, F.; Bünzli, J.-C. G., Intrinsic quantum yields and radiative lifetimes of lanthanide tris(dipicolinates). *Physical Chemistry Chemical Physics* **2009,** *11* (9), 1346-1353.

213.   Sardar, D. K.; Nash, K. L.; Yow, R. M.; Gruber, J. B.; Valiev, U. V.; Kokanyan, E. P., Absorption intensities and emission cross sections of Tb^{3+} ($4f^8$) in $TbAlO_3$. *Journal of Applied Physics* **2006,** *100* (8), 083108.

214.   Supkowski, R. M.; Horrocks, W. D., On the determination of the number of water molecules, q, coordinated to europium(III) ions in solution from luminescence decay lifetimes. *Inorganica Chimica Acta* **2002,** *340* (Supplement C), 44-48.

215.   Horrocks, W. D.; Sudnick, D. R., Lanthanide ion luminescence probes of the structure of biological macromolecules. *Accounts of Chemical Research* **1981,** *14* (12), 384-392.

216.   Horrocks, W. D.; Sudnick, D. R., Lanthanide ion probes of structure in biology. Laser-induced luminescence decay constants provide a direct measure of the number of metal-coordinated water molecules. *Journal of the American Chemical Society* **1979,** *101* (2), 334-340.

217.   Dissanayake, P.; Mei, Y.; Allen, M. J., Luminescence-Decay as an Easy-to-Use Tool for the Study of Lanthanide-Containing Catalysts in Aqueous Solutions. *ACS Catalysis* **2011,** *1* (10), 1203-1212.

218.   Shionoya, S.; Yen, W. M.; Yamamoto, H., *Phosphor handbook*. CRC press: 2018.

219.   Menon, S. G.; Hebbar, D. N.; Kulkarni, S. D.; Choudhari, K.; Santhosh, C., Facile synthesis and luminescence studies of nanocrystalline red emitting $Cr:ZnAl_2O_4$ phosphor. *Materials Research Bulletin* **2017,** *86*, 63-71.

220.   Singh, D. K.; Manam, J., Structural and photoluminescence studies of red emitting $CaTiO_3:Eu^{3+}$ perovskite nanophosphors for lighting applications. *Journal of Materials Science: Materials in Electronics* **2016,** *27* (10), 10371-10381.

221.   Komuro, N.; Mikami, M.; Shimomura, Y.; Bithell, E. G.; Cheetham, A. K., Synthesis, structure and optical properties of cerium-doped calcium barium phosphate - a novel blue-green phosphor for solid-state lighting. *Journal of Materials Chemistry C* **2015,** *3* (1), 204-210.

222.   Liu, X.; Lü, Y.; Chen, C.; Luo, S.; Zeng, Y.; Zhang, X.; Shang, M.; Li, C.; Lin, J., Synthesis and Luminescence Properties of $YNbO_4:A$ (A = Eu^{3+} and/or Tb^{3+}) Nanocrystalline Phosphors via a Sol–Gel Process. *The Journal of Physical Chemistry C* **2014,** *118* (47), 27516-27524.

223.   Boyer, J.-C.; Cuccia, L. A.; Capobianco, J. A., Synthesis of Colloidal Upconverting $NaYF_4:Er^{3+}/Yb^{3+}$ and Tm^{3+}/Yb^{3+} Monodisperse Nanocrystals. *Nano Letters* **2007,** *7* (3), 847-852.

224.   Fujihara, S.; Tokumo, K., Multiband orange-red luminescence of Eu^{3+} ions based on the pyrochlore-structured host crystal. *Chemistry of materials* **2005,** *17* (22), 5587-5593.

225.   Gupta, S. K.; Mohapatra, M.; Godbole, S.; Natarajan, V., On the unusual photoluminescence of Eu^{3+} in α-$Zn_2P_2O_7$: a time resolved emission spectrometric and Judd–Ofelt study. *RSC Advances* **2013,** *3* (43), 20046-20053.

226. Chan, E. M.; Levy, E. S.; Cohen, B. E., Rationally designed energy transfer in upconverting nanoparticles. *Advanced Materials* **2015,** *27* (38), 5753-5761.

227. Auzel, F., Upconversion and Anti-Stokes Processes with f and d Ions in Solids. *Chemical Reviews* **2004,** *104* (1), 139-174.

228. Hardy, D. A.; Tigaa, R. A.; McBride, J. R.; Strouse, G. F., Breaking Latva's rule by energy hopping in a Tb(III):ZnAl$_2$O$_4$ nanospinel. *In Review*, 2019.

229. Dong, H.; Du, S.-R.; Zheng, X.-Y.; Lyu, G.-M.; Sun, L.-D.; Li, L.-D.; Zhang, P.-Z.; Zhang, C.; Yan, C.-H., Lanthanide Nanoparticles: From Design toward Bioimaging and Therapy. *Chemical Reviews* **2015,** *115* (19), 10725-10815.

230. Wisser, M. D.; Chea, M.; Lin, Y.; Wu, D. M.; Mao, W. L.; Salleo, A.; Dionne, J. A., Strain-Induced Modification of Optical Selection Rules in Lanthanide-Based Upconverting Nanoparticles. *Nano Letters* **2015,** *15* (3), 1891-1897.

231. Revised effective ionic radii and systematic studies of interatomic distances in halides and chalcogenides. *Acta Crystallographica Section A* **1976,** *32* (5), 751--767.

232. Kibasomba, P. M.; Dhlamini, S.; Maaza, M.; Liu, C.-P.; Rashad, M. M.; Rayan, D. A.; Mwakikunga, B. W., Strain and grain size of TiO$_2$ nanoparticles from TEM, Raman spectroscopy and XRD: The revisiting of the Williamson-Hall plot method. *Results in Physics* **2018,** *9*, 628-635.

233. Khorsand Zak, A.; Majid, W. H. A.; Ebrahimizadeh Abrishami, M.; Yousefi, R.; Parvizi, R., Synthesis, magnetic properties and X-ray analysis of Zn$_{0.97}$X$_{0.03}$O nanoparticles (X = Mn, Ni, and Co) using Scherrer and size–strain plot methods. *Solid State Sciences* **2012,** *14* (4), 488-494.

234. Fabian, M.; Bottke, P.; Girman, V.; Duvel, A.; Da Silva, K. L.; Wilkening, M.; Hahn, H.; Heitjans, P.; Sepelak, V., A simple and straightforward mechanochemical synthesis of the far-from-equilibrium zinc aluminate, ZnAl$_2$O$_4$, and its response to thermal treatment. *RSC Advances* **2015,** *5* (67), 54321-54328.

235. Sreeja, V.; Smitha, T.; Nand, D.; Ajithkumar, T.; Joy, P., Size dependent coordination behavior and cation distribution in MgAl$_2$O$_4$ nanoparticles from ^{27}Al solid state NMR studies. *The Journal of Physical Chemistry C* **2008,** *112* (38), 14737-14744.

236. Chapter 5 - Transition Metal Ions: Shift and Relaxation. In *Current Methods in Inorganic Chemistry*, Bertini, I.; Luchinat, C.; Parigi, G., Eds. Elsevier: 2001; Vol. 2, pp 143-203.

237. Zhang, Y.; Castets, A.; Carlier, D.; Ménétrier, M.; Boucher, F., Simulation of NMR fermi contact shifts for lithium battery materials: The need for an efficient hybrid functional approach. *The Journal of Physical Chemistry C* **2012,** *116* (33), 17393-17402.

238. Rodriguez-Fortea, A.; Alemany, P.; Ziegler, T., Density Functional Calculations of NMR Chemical Shifts with the Inclusion of Spin−Orbit Coupling in Tungsten and Lead Compounds. *The Journal of Physical Chemistry A* **1999,** *103* (41), 8288-8294.

239.   Judd, B. R., Optical absorption intensities of rare-earth ions. *Physical review* **1962,** *127* (3), 750.

240.   Ofelt, G., Intensities of crystal spectra of rare-earth ions. *The journal of chemical physics* **1962,** *37* (3), 511-520.

241.   Tucto Salinas, K. Y.; Flores Escalante, L. F.; Guerra Torres, J. A.; Grieseler, R.; Kups, T.; Pezoldt, J.; Osvet, A.; Batentschuk, M.; Weingärtner, R., Effect of Post-Annealing Treatment on the Structure and Luminescence Properties of AlN:Tb^{3+} Thin Films Prepared by Radio Frequency Magnetron Sputtering. *Materials Science Forum* **2017,** *890*, 299-302.

242.   Basavaraju, N.; Priolkar, K. R.; Gourier, D.; Sharma, S. K.; Bessière, A.; Viana, B., The importance of inversion disorder in the visible light induced persistent luminescence in Cr^{3+} doped AB_2O_4 (A= Zn or Mg and B= Ga or Al). *Physical Chemistry Chemical Physics* **2015,** *17* (3), 1790-1799.

243.   Bindra, J. K.; Kurian, G.; Christian, J. H.; Van Tol, J.; Singh, K.; Dalal, N. S.; Mochena, M. D.; Stoian, S. A.; Strouse, G. F., Evidence of Ferrimagnetism in Fe-Doped CdSe Quantum Dots. *Chemistry of Materials* **2018,** *30* (23), 8446-8456.

244.   Zheng, W.; Wang, Z.; Wright, J.; Goundie, B.; Dalal, N. S.; Meulenberg, R. W.; Strouse, G. F., Probing the Local Site Environments in Mn:CdSe Quantum Dots. *The Journal of Physical Chemistry C* **2011,** *115* (47), 23305-23314.

245.   Uheda, K.; Maruyama, T.; Takizawa, H.; Endo, T., Synthesis and long-period phosphorescence of $ZnGa_2O_4$:Mn^{2+} spinel. *Journal of Alloys and Compounds* **1997,** *262*, 60-64.

246.   Zhu, H.; Lin, C. C.; Luo, W.; Shu, S.; Liu, Z.; Liu, Y.; Kong, J.; Ma, E.; Cao, Y.; Liu, R.-s.; Chen, X., Highly efficient non-rare-earth red emitting phosphor for warm white light-emitting diodes. *Nature Communications* **2014,** *5*, 4312.

247.   Mueller, G. O.; Mueller-Mach, R. B.; Bertram, D.; Juestel, T.; Schmidt, P. J.; Opitz, J., Light-emitting devices utilizing nanoparticles. Google Patents: 2005.

248.   Wang, S.; Westcott, S.; Chen, W., Nanoparticle Luminescence Thermometry. *The Journal of Physical Chemistry B* **2002,** *106* (43), 11203-11209.

249.   Association, A. M., AMA adopts guidance to reduce harm from high intensity street lights. 2016.

250.   Li, J.; Ding, J.; Cao, Y.; Zhou, X.; Ma, B.; Zhao, Z.; Wang, Y., Color-Tunable Phosphor $[Mg_{1.25}Si_{1.25}Al_{2.5}]O_3N_3$:$Eu^{2+}$—A New Modified Polymorph of AlON with Double Sites Related Luminescence and Low Thermal Quenching. *ACS Applied Materials & Interfaces* **2018,** *10* (43), 37307-37315.

251.   Im, W. B.; George, N.; Kurzman, J.; Brinkley, S.; Mikhailovsky, A.; Hu, J.; Chmelka, B. F.; DenBaars, S. P.; Seshadri, R., Efficient and color-tunable oxyfluoride solid solution phosphors for solid-state white lighting. *Advanced Materials* **2011,** *23* (20), 2300-2305.

252. Jiao, M.; Jia, Y.; Lü, W.; Lv, W.; Zhao, Q.; Shao, B.; You, H., $Sr_3GdNa(PO_4)_3F:Eu^{2+}$, Mn^{2+}: a potential color tunable phosphor for white LEDs. *Journal of Materials Chemistry C* **2014,** *2* (1), 90-97.

253. Wu, L.; Zhang, Y.; Gui, M.; Lu, P.; Zhao, L.; Tian, S.; Kong, Y.; Xu, J., Luminescence and energy transfer of a color tunable phosphor: Dy^{3+}-, Tm^{3+}-, and Eu^{3+}-coactivated $KSr_4(BO_3)_3$ for warm white UV LEDs. *Journal of Materials Chemistry* **2012,** *22* (13), 6463-6470.

254. Nakazawa, E.; Shionoya, S., Energy Transfer between Trivalent Rare-Earth Ions in Inorganic Solids. *The Journal of Chemical Physics* **1967,** *47* (9), 3211-3219.

255. Liu, X.; Wang, X.; Wang, Z., Selectively excited emission and Tb^{3+}, Ce^{3+} energy transfer in yttrium aluminum garnet. *Physical Review B* **1989,** *39* (15), 10633-10639.

256. Yang, J.; Wang, X.; Song, L.; Luo, N.; Dong, J.; Gan, S.; Zou, L., Tunable luminescence and energy transfer properties of $GdPO_4:Tb^{3+}$, Eu^{3+} nanocrystals for warm-white LEDs. *Optical Materials* **2018,** *85*, 71-78.

257. Guo, N.; Liang, Q.; Li, S.; Ouyang, R.; Lü, W., Triple energy transfer and color tuning in Tb^{3+} and Eu^{3+}-coactivated apatite-type gadolinium-containing phosphors. *Optical Materials* **2017,** *73*, 570-576.

258. Yang, D.; Liao, L.; Guo, Q.; Mei, L.; Liu, H.; Zhou, T.; Ye, H., Luminescence properties and energy transfer of $K_3LuF_6:Tb^{3+},Eu^{3+}$ multicolor phosphors with a cryolite structure. *RSC Advances* **2019,** *9* (8), 4295-4302.

259. Főrster, T., 10th Spiers Memorial Lecture. Transfer mechanisms of electronic excitation. *Discussions of the Faraday Society* **1959,** *27* (0), 7-17.

260. Scholes, G. D.; Andrews, D. L., Resonance energy transfer and quantum dots. *Physical Review B* **2005,** *72* (12), 125331.

261. van der Meer, B. W.; van der Meer, D. M.; Vogel, S. S., Optimizing the Orientation Factor Kappa-Squared for More Accurate FRET Measurements. *FRET – Förster Resonance Energy Transfer* **2013**, 63-104.

262. Curutchet, C.; Franceschetti, A.; Zunger, A.; Scholes, G. D., Examining Forster energy transfer for semiconductor nanocrystalline quantum dot donors and acceptors. *The Journal of Physical Chemistry C* **2008,** *112* (35), 13336-13341.

263. Llanos, J.; Espinoza, D.; Castillo, R., Energy transfer in single phase Eu^{3+}-doped Y_2WO_6 phosphors. *RSC Advances* **2017,** *7* (25), 14974-14980.

264. Morgan, J. R.; El-Sayed, M. A., Temporal and temperature dependence of the energy transfer process among europium (3+) in an amorphous solid. *The Journal of Physical Chemistry* **1981,** *85* (24), 3566-3568.

265. Luo, Y.; Liu, Z.; Wong, H. T.; Zhou, L.; Wong, K. L.; Shiu, K. K.; Tanner, P. A., Energy Transfer between Tb^{3+} and Eu^{3+} in $LaPO_4$: Pulsed versus Switched-off Continuous Wave Excitation. *Advanced Science* **2019,** *6* (10), 1900487.

266. García-Rosales, G.; Mercier-Bion, F.; Drot, R.; Lagarde, G.; Roques, J.; Simoni, E., Energy transfer from Tb^{3+} to Eu^{3+} ions sorbed on SrTiO3 surface. *Journal of Luminescence* **2012,** *132* (5), 1299-1306.

267. Vetrone, F.; Boyer, J.-C.; Capobianco, J. A.; Speghini, A.; Bettinelli, M., A spectroscopic investigation of trivalent lanthanide doped Y_2O_3nanocrystals. *Nanotechnology* **2003,** *15* (1), 75-81.

268. Due to the low extinction coefficients of the lanthanides a Nd:YAG laser coupled to an optical parametric oscillator was used to excite at 488 nm (3.6 m J). The PL spectra displayed in Figure 5.7, was recorded from 400-750 nm 10 ns after the Nd:YAG pulse and collected over a 1 ms window.

269. Guo, N.; Song, Y.; You, H.; Jia, G.; Yang, M.; Liu, K.; Zheng, Y.; Huang, Y.; Zhang, H., Optical properties and energy transfer of $NaCaPO_4$:Ce^{3+},Tb^{3+} phosphors for potential application in light-emitting diodes. *European Journal of Inorganic Chemistry* **2010,** *2010* (29), 4636-4642.

270. Chen, L. X.; Liu, T.; Thurnauer, M. C.; Csencsits, R.; Rajh, T., Fe_2O_3 Nanoparticle Structures Investigated by X-ray Absorption Near-Edge Structure, Surface Modifications, and Model Calculations. *The Journal of Physical Chemistry B* **2002,** *106* (34), 8539-8546.

271. Chattot, R.; Le Bacq, O.; Beermann, V.; Kühl, S.; Herranz, J.; Henning, S.; Kühn, L.; Asset, T.; Guétaz, L.; Renou, G.; Drnec, J.; Bordet, P.; Pasturel, A.; Eychmüller, A.; Schmidt, T. J.; Strasser, P.; Dubau, L.; Maillard, F., Surface distortion as a unifying concept and descriptor in oxygen reduction reaction electrocatalysis. *Nature Materials* **2018,** *17* (9), 827-833.

272. Krycka, K. L.; Borchers, J. A.; Booth, R. A.; Ijiri, Y.; Hasz, K.; Rhyne, J. J.; Majetich, S. A., Origin of Surface Canting within Fe_3O_4 Nanoparticles. *Physical Review Letters* **2014,** *113* (14), 147203.

273. Lovingood, D. D.; Achey, R.; Paravastu, A. K.; Strouse, G. F., Size- and Site-Dependent Reconstruction in CdSe QDs Evidenced by $^{77}Se\{1H\}$ CP-MAS NMR Spectroscopy. *Journal of the American Chemical Society* **2010,** *132* (10), 3344-3354.

274. Dyble, M.; Narendran, N.; Bierman, A.; Klein, T. In *Impact of dimming white LEDs: Chromaticity shifts due to different dimming methods*, Fifth international conference on solid state lighting, International Society for Optics and Photonics: 2005; p 59411H.

275. Runowski, M.; Woźny, P.; Stopikowska, N.; Guo, Q.; Lis, S., Optical Pressure Sensor Based on the Emission and Excitation Band Width (fwhm) and Luminescence Shift of Ce3+-Doped Fluorapatite—High-Pressure Sensing. *ACS Applied Materials & Interfaces* **2019,** *11* (4), 4131-4138.

276.   Wang, Z.; Zhu, Q.; Wang, X.; Li, X.; Sun, X.; Kim, B.-N.; Li, J.-G., Multi-Color Luminescent m-LaPO$_4$:Ce/Tb Monospheres of High Efficiency via Topotactic Phase Transition and Elucidation of Energy Interaction. *Inorganic Chemistry* **2019,** *58* (1), 890-899.

277.   Riwotzki, K.; Meyssamy, H.; Schnablegger, H.; Kornowski, A.; Haase, M., Liquid-Phase Synthesis of Colloids and Redispersible Powders of Strongly Luminescing LaPO$_4$:Ce,Tb Nanocrystals. *Angewandte Chemie International Edition* **2001,** *40* (3), 573-576.

278.   Dang, P.; Liang, S.; Li, G.; Lian, H.; Shang, M.; Lin, J., Broad color tuning of Bi^{3+}/Eu^{3+}-doped (Ba,Sr)$_3$Sc$_4$O$_9$ solid solution compounds via crystal field modulation and energy transfer. *Journal of Materials Chemistry C* **2018,** *6* (37), 9990-9999.

279.   Dang, P.; Liang, S.; Li, G.; Wei, Y.; Cheng, Z.; Lian, H.; Shang, M.; Ho, S. J.; Lin, J., Controllable optical tuning and improvement in Li$^+$, Eu^{3+}-codoped BaSc$_2$O$_4$:Bi^{3+} based on energy transfer and charge compensation. *Journal of Materials Chemistry C* **2018,** *6* (24), 6449-6459.

280.   Luchechko, A.; Kravets, O.; Kostyk, L.; Tsvetkova, O., Luminescence spectroscopy of Eu^{3+} and Mn^{2+} ions in MgGa$_2$O$_4$ spinel. *Radiation Measurements* **2016,** *90*, 47-50.

281.   Xia, H.; Lei, L.; Hong, W.; Xu, S., A novel Ce^{3+}/Mn^{2+}/Eu^{3+} tri-doped GdF$_3$ nanocrystals for optical temperature sensor and anti-counterfeiting. *Journal of Alloys and Compounds* **2018,** *757*, 239-245.

BIOGRAPHICAL SKETCH

Education

Ph.D. in Chemistry, Florida State University   2018-2019
M.Sc. in Chemistry, Florida State University   2015-2018
B. Sc. in Chemistry, The University of Tampa   2011-2015

Experience

PH.D. RESEARCH ASSISTANT, FLORIDA STATE UNIVERSITY — 8/2016-PRESENT
Geoffrey F. Strouse Group
• Developed nano-material with applications in solid-state lighting, photonics, and catalysis.
• Secured a 3-year $450,000 NSF research grant and provided annual reports to funding agencies.
•Acted as lab manager which required contacting vendors, balancing multiple budgets, maintaining lab instruments, overseeing inventory and implementing safety protocols.
• Devised a novel, top down approach to make soluble, surface passivated magnetic nanoparticles.

TEACHING ASSISTANT, FLORIDA STATE UNIVERSITY — 8/2015-8/2016
• Taught new topics and techniques to undergraduate students in General and Organic Chemistry labs with a class size of 20 students.
• Graded and maintained confidential records of students' progress.
• Wrote letters of recommendations for students applying to post-baccalaureate programs.

RESEARCH FELLOW, THE UNIVERSITY OF TAMPA — 5/2014-5/2015
• Conducted research in lanthanide extraction from nuclear waste streams.
• Developed a new analytical method to quantify extraction efficiencies by ICP-OES.
• Published research papers.

Skills

Synthesis Skills
-Bottom-up Nanoparticle Growth
-Top-down Nanoparticle Synthesis
-Microwave-Assisted Synthesis
-Surface Functionalization
-Nanocomposite Preparation

Instrumentation and Methods
-TEM
-SEM
-Energy Dispersive X-ray Spectroscopy

-pXRD
-High-Temperature pXRD
-X-ray Fluorescence
-UV-Vis -NIR Spectroscopy
-Fluorescence Microscopy
-Photoluminescence Lifetime
-IR spectroscopy
-Laser Spectroscopy
-TGA
-TGA-Mass spectrometry
-ICP-MS
-ICP-OES
-Microwave Synthesis

Software Packages
- Microsoft Office Suite

-Igor Pro 8.0
-OriginPro 8.5
-Image J & Gatan DM3
-Adobe Creative Suite
-EndNote
-Mathematica

Soft Skills
-Leadership
-Project Management
-Lab Management
-Team Management
-Communication
-Collaboration & Teamwork
-Data Analysis

Publications

Hardy, D.A. ;Foley, M.E.; Parrish, S.E.; Chien, P.; McBride J.R.; Chen, B.; Hu, Y.; Strouse, G.F.; Rapid Microwave Synthesis of Nanospinels. *In Preparation*

Hardy, D.A.; Tigaa, R.A.; Ortega, R.E.; Mcbride, J.R.; Strouse, G.F.; Tb(III) as an optical probe of lattice disorder in Tb(III):$ZnAl_2O_4$ nanospinels. *In Review*

Hardy, D.A.; Strouse, G.F.; Spectral Engineering in Eu(III) and Tb(III) co-doped $ZnAl_2O_4$ nanospinels. *In Review*

Hardy, D.A.; Tigaa, R.A.; Mcbride, J.R.; Strouse, G.F.; Breaking Latva's Rule by Energy Hopping in a Tb(III):$ZnAl_2O_4$ Nanospinel. *In Review*

Hardy, D.A.; Nguyen, E.T.; Parrish, S.E.; Schriber, E.A.; Schlicker, L.; Gili, A.; Kamutzki, F.; Hohman, J.N.; Strouse, G.F.; Prussian blue iron-cobalt mesocrystals as a template for the growth of Fe/Co carbide (cementite) and Fe/Co nanocrystals. *Chem. Mater*. **2019,** 31 (19), 8163-8173.

Vakil, P. N.; Muhammed, F.; **Hardy, D. A.;** Dickens, T. J.; Ramakrishann, S.; Strouse, G. F.; Nanoparticle loaded polystyrene as a potential printable low-k hybrid material. *ACS Omega*. **2018** 3 (10) 12813-12823

Vakil, P. N.; **Hardy, D. A.**; Strouse, G. F., Synthesis of Highly Uniform Nickel Multipods With Tunable Aspect Ratio by Microwave Power Control. *ACS Nano*, **2018** 12 (7), 6784-6793

Coburn, K. M.; **Hardy, D. A.**; Patterson, M. G.; McGraw, S. N.; Peruzzi, M. T.; Boucher, F.; Beelen, B.; Sartain, H. T.; Neils, T.; Lawrence, C. L., f-Element coordination and extraction selectivity of a carbamoylmethylphosphine oxide ligand based on a tripodal phosphine oxide scaffold. *Inorganica Chimica Acta* **2016,** *449*, 96-106.

Presentations (Oral and Poster)

E. T. Nguyen, **D. A. Hardy**, G. F. Strouse "Prussian blue analogues for templated nanoparticle growth." Oral presentation at the 258th ACS National Meeting and Exposition. San Diego, CA, August 2019.

D. A. Hardy, G. F. Strouse, "The formation of a nanoparticle: exploring microwave methods for phosphors and templated synthesis of carbides and metals." Oral presentation at Florida State University, Department of Chemistry and Biochemistry, Materials Seminar. Tallahassee, FL April 2018.

D. A. Hardy, R. A. Tigaa, G. F. Strouse "Interrogating, J, spectral overlap in terbium(III) doped nano-spinels as green emitters for solid-state lighting." Oral presentation at the 257th ACS National Meeting and Exposition. Orlando, FL, April 2019.

C. Conti, **D. A. Hardy,** G. F. Strouse "Manipulating plasmon resonances in In_2O_3 by bandgap tuning and dual-doping." Poster presentation at the 257th ACS National Meeting and Exposition. Orlando, FL, April 2019.

E. T. Nguyen, **D. A. Hardy**, G. F. Strouse "Understanding the thermal conversion of Prussian blue analogues." Oral presentation at the 257th ACS National Meeting and Exposition. Orlando, FL, April 2019.

D. A. Hardy, S. E. Parrish, G. F. Strouse "Size dependent thermal decomposition of prussian blue analogue as precursors for magnetic nanoparticles." Oral presentation at the 256th ACS National Meeting and Exposition. Boston, MA, August 2018.

E. T. Nguyen, **D. A. Hardy,** R. A. Tigaa, G. F. Strouse "Synthesis and characterization of lead halide perovskites for solid state lighting." Poster presentation at the 256th ACS National Meeting and Exposition. Boston, MA, August 2018.

M. C. Ellis, **D. A. Hardy**, R. A. Tigaa, S. McGill, G. F. Strouse, N. S. Dalal "Magnetic effect on photoluminescence in lanthanide-doped nanospinels." Poster presentation at the 256th ACS National Meeting and Exposition. Boston, MA, August 2018.

D. A. Hardy, G. F. Strouse "Terbium(III) doped nano-spinels as green emitters for solid state lighting." Oral presentation at Florida Annual Meeting and Exposition (FAME 2018), Tampa, FL, May 2018.

C. M. Dyer **D. A. Hardy**, G. F. Strouse "Prussian blue analogues as a template for bimetallic carbides." Poster presentation at Florida Annual Meeting and Exposition (FAME 2018), Tampa, FL, May 2018.

E. T. Nguyen, **D. A. Hardy,** G. F. Strouse "Synthesis and Characterization of Lead Halide Perovskite for Solid State Lighting." Oral presentation at Florida Annual Meeting and Exposition (FAME 2018), Tampa, FL, May 2018.

M. C. Ellis, **D. A. Hardy,** R. A. Tigaa, S. McGill, G. F. Strouse "Magneto-optical properties of lanthanide-doped nanospinels." Poster presentation at Florida Annual Meeting and Exposition (FAME 2018), Tampa, FL, May 2018.

E. B. Curling, **D. A. Hardy**, G. F. Strouse, "Lanthanide Doped Phosphors for Solid State Lighting." Poster presentation at Florida State University, Undergraduate research symposium. Tallahassee, FL, March 2018.

D. A. Hardy, S. E. Parrish, G. F. Strouse, "Thermal decomposition of Prussian blue analogue as precursors for magnetic nanoparticles." Oral presentation at the 255th ACS National Meeting and Exposition. New Orleans, LA, March 2018

P. N. Vakil, **D. A. Hardy**, G. F. Strouse, "Pulsed microwave energy: A kinetic control approach to highly branched nickel multipod nanostructures." Oral presentation at the 255th ACS National Meeting and Exposition. New Orleans, LA, March 2018

S. E. Parrish, **D. A. Hardy,** G. F. Strouse, "Thermal Decomposition of Prussian Blue Analogues as Precursors for Magnetic Nanoparticles." Poster Presentation at Florida Undergraduate Research Conference (FURC). Cocoa ,FL. February 2018

D. A. Hardy, G. F. Strouse "Advancements in Solid State Lighting." Oral presentation for Ph. D. Candidacy, Florida State University, Tallahassee, FL, December 2017.

D. A. Hardy, G. F. Strouse, "Synthesis of prussian blue analogues as precursors for magnetic nanoparticles." Oral presentation at Southeast Regional ACS conference (SERMACS) 2017. Charlotte, NC. November 2017

L. A. Saucedo, D. J. Carnevale, J. Lengyel, **D. A. Hardy**, M. Shatruk, G. F. Strouse, "Synthesis of FeSe and Fe_3Se_4 nanoparticles from molecular precursors." Poster presentation at Florida Inorganic and Materials Symposium (FIMS) 2017. Gainesville, FL. October 2017

D. A. Hardy, G. F. Strouse, "Synthesis of lanthanide doped nano-spinels as hosts for down-shifting phosphors." Oral presentation at 254th ACS National Meeting and Exposition. Washington D.C. August 2017

P. N. Kurek, **D. A. Hardy**, G. F. Strouse, "Red and green down-shifting phosphors for LED lighting using Eu^{3+} and Tb^{3+} -doped nanospinels." Poster presentation at NSF-REU site: Sunshine Institute for the interaction of light with matter. Tallahassee, FL August 2017

D. A. Hardy, G. F. Strouse, "Lanthanide Doped Nanospinels for Solid State Lighting" Oral presentation at Florida State University, Department of Chemistry and Biochemistry, Materials Seminar. Tallahassee, FL September 2016

D. A. Hardy, M. E. Foley, G. F. Strouse, "Blue down-shifting phosphors for LED lighting using a Tm^{3+}-doped nanospinel." Poster presentation at 252nd ACS National Meeting and Exposition. Philadelphia, PA August 2016

D. A. Hardy, M. E. Foley, G. F. Strouse, "Synthesis of Tm^{3+}-doped nanospinel for blue down-shifting LED phosphors." Oral presentation at ACS Florida Annual Meeting and Exposition (FAME). Tampa, FL May 2016

M. Patterson, **D. A. Hardy**, S. M, Biros, E. J. Werner, "Tripodal CMPO ligands as potential lanthanide extractants: A systematic study of ligand structure and selectivity in acidic aqueous media." Poster presentation at 251st ACS National Meeting and Exposition. San Diego, CA March 2016

E. J. Werner, S. M, Biros, M. Patterson, **D. A. Hardy**, "Design and evaluation of selective CMPO-based extractants for f-element separations." Oral presentation at 251st ACSNational Meeting and Exposition. San Diego, CA March 2016

D. A. Hardy, M. T. Peruzzi, S. N. McGraw, S. M, Biros, E. J. Werner, " Luminescence and extraction properties of novel tripodal CMPO ligands." Poser presentation at 249th ACS National Meeting and Exposition. Denver, CO March 2015

E.J. Werner, S.M. Biros, S.N. McGraw, **D. A. Hardy**, H.T. Sartain, "Tripodal carbamoylmethylphosphine oxide (CMPO) ligands for f-element chelation: Solution photophysical studies and lanthanide/actinide extraction properties." Oral presentation at 249th ACS National Meeting and Exposition. Denver, CO March 2015

D. A. Hardy, M. T. Peruzzi, S. N. McGraw, S. M, Biros, E. J. Werner, "Determination of Lanthanide Extraction Efficiencies of Multimodal CMPO ligands." Poser presentation at Florida Undergraduate Research Conference (FURC). Daytona Beach, FL February 2015

Awards, Honors, and Professional Memberships

- Summer Research Fellow, The University of Tampa, (Summer 2014)
- American Chemical Society (Division of Inorganic Chemistry)
- Member of the President's Leadership Fellows at the University of Tampa (8/2011-5/2015)
- Boy Scouts of America - Eagle Scout

Outreach/Volunteer Experience

- Volunteer Panel Member of Graduate School Reality Check, Part I and Part II at the ACS 257th National Meeting and Exposition.
- Volunteer Judge at the 2019 Capital Regional Science and Engineering Fair (Feb. 2019)
- Volunteer Panel Member of Graduate School Reality Check, Part I and Part II at the ACS 256th National Meeting and Exposition.
- Volunteer Judge at the 2018 Capital Regional Science and Engineering Fair (Feb. 2018)
- Volunteer Panel Member of Graduate School Reality Check, Part I and Part II at the ACS 252nd National Meeting and Exposition.
- Train five undergraduate students to conduct research in nanoparticle synthesis and characterization who have matriculated to graduate, medical, and pharmaceutical programs across the nation.